

SANDIA REPORT

S A N D 2 0 0 8 - 6 0 6 6

Unlimited Release

Printed September 2008

Development of Advanced Continuum Models that Incorporate Nanomechanical Deformation into Engineering Analysis

Jonathan A. Zimmerman, Reese E. Jones, Jeremy A. Templeton, David L. McDowell, Jason R. Mayeur, Garritt J. Tucker, Douglas J. Bammann and Huajian Gao

Prepared by
Sandia National Laboratories
Albuquerque, New Mexico 87185 and Livermore, California 94550

Sandia is a multiprogram laboratory operated by Sandia Corporation, a Lockheed Martin Company, for the United States Department of Energy's National Nuclear Security Administration under Contract DE-AC04-94-AL85000.

Approved for public release; further dissemination unlimited.

Issued by Sandia National Laboratories, operated for the United States Department of Energy by Sandia Corporation.

NOTICE: This report was prepared as an account of work sponsored by an agency of the United States Government. Neither the United States Government, nor any agency thereof, nor any of their employees, nor any of their contractors, subcontractors, or their employees, make any warranty, express or implied, or assume any legal liability or responsibility for the accuracy, completeness, or usefulness of any information, apparatus, product, or process disclosed, or represent that its use would not infringe privately owned rights. Reference herein to any specific commercial product, process, or service by trade name, trademark, manufacturer, or otherwise, does not necessarily constitute or imply its endorsement, recommendation, or favoring by the United States Government, any agency thereof, or any of their contractors or subcontractors. The views and opinions expressed herein do not necessarily state or reflect those of the United States Government, any agency thereof, or any of their contractors.

Printed in the United States of America. This report has been reproduced directly from the best available copy.

Available to DOE and DOE contractors from
U.S. Department of Energy
Office of Scientific and Technical Information
P.O. Box 62
Oak Ridge, TN 37831

Telephone: (865) 576-8401
Facsimile: (865) 576-5728
E-Mail: reports@adonis.osti.gov
Online ordering: <http://www.osti.gov/bridge>

Available to the public from
U.S. Department of Commerce
National Technical Information Service
5285 Port Royal Rd
Springfield, VA 22161

Telephone: (800) 553-6847
Facsimile: (703) 605-6900
E-Mail: orders@ntis.fedworld.gov
Online ordering: <http://www.ntis.gov/help/ordermethods.asp?loc=7-4-0#online>



Development of Advanced Continuum Models that Incorporate Nanomechanical Deformation into Engineering Analysis

Jonathan A. Zimmerman, Reese E. Jones and Jeremy A. Templeton
Sandia National Laboratories
Livermore, CA 94551
jzimmer@sandia.gov

David L. McDowell, Jason R. Mayeur and Garritt J. Tucker
Georgia Institute of Technology
Atlanta, Georgia 30332
david.mcdowell@me.gatech.edu

Douglas J. Bammann
Mississippi State University
Mississippi State, MS 39762
bammann@cavs.msstate.edu

Huajian Gao
Brown University
Providence, RI 02912
Huajian_Gao@brown.edu

Abstract

Materials with characteristic structures at nanoscale sizes exhibit significantly different mechanical responses from those predicted by conventional, macroscopic continuum theory. For example, nanocrystalline metals display an inverse Hall-Petch effect whereby the strength of the material decreases with decreasing grain size. The origin of this effect is believed to be a change in deformation mechanisms from dislocation motion across grains and pileup at grain boundaries at microscopic grain sizes to rotation of grains and deformation within grain boundary interface regions for nanostructured materials. These rotational defects are represented by the mathematical concept of disclinations. The ability to capture these effects within continuum theory, thereby connecting nanoscale materials phenomena and macroscale behavior, has eluded the research community.

The goal of our project was to develop a consistent theory to model both the evolution of disclinations and their kinetics. Additionally, we sought to develop approaches to extract continuum mechanical information from nanoscale structure to verify any developed continuum theory that includes dislocation and disclination behavior. These approaches yield engineering-scale expressions to quantify elastic and inelastic deformation in all varieties of materials, even those that possess highly directional bonding within their molecular structures such as liquid crystals, covalent ceramics, polymers and biological materials. This level of accuracy is critical for engineering design and thermo-mechanical analysis is performed in micro- and nanosystems. The research proposed here innovates on how these nanoscale deformation mechanisms should be incorporated into a continuum mechanical formulation, and provides the foundation upon which to develop a means for predicting the performance of advanced engineering materials.

Acknowledgment

The authors acknowledge helpful discussions with Farid F. Abraham, Youping Chen, Terry J. Delph, Remi Dingreville, James W. Foulk III, Robert J. Hardy, Richard Lehoucq, Alejandro Mota, Gregory J. Wagner, Edmund B. Webb III and Xiaowang Zhou. Support for this project was provided by the Enabling Predictive Simulation Investment Area of Sandia's Laboratory Directed Research and Development (LDRD) program.

Contents

1	Introduction	19
2	Deformation Gradients for Continuum Mechanical Analysis of Atomistic Simulations	23
2.1	Introduction	23
2.2	Formulation of Atomic-Scale Deformation Gradient	25
2.3	Expressions for Higher-Order Gradients	28
2.4	Compatibility of the Atomic-Scale Deformation Gradient	31
2.5	Examples	32
2.5.1	One-dimensional atomic chain	33
2.5.2	Dislocation nucleation at a crystal surface ledge	33
2.5.3	Dislocation nucleation during nanoindentation	36
2.6	Discussion	38
2.7	Conclusions	43
3	A Material Frame Approach for Evaluating Continuum Variables in Atomistic Simulations	47
3.1	Introduction	47
3.2	Formulation for Standard Continuum Mechanics	49
3.2.1	Balance Laws	49
3.2.2	Densities and Localization	50
3.2.3	Energy and Force Assumptions	52
3.2.4	Derivation of Continuum Expressions	53
3.2.4.1	Balance of Mass	53

3.2.4.2	Balance of Linear Momentum	53
3.2.4.3	Balance of Energy	57
3.3	Evaluation of Material Frame Expressions	59
3.3.1	Construction of fields	60
3.3.2	Stress for a constrained finite temperature system	60
3.3.3	Finite temperature deformation	63
3.3.4	Tensile stretching of a center-cracked body	66
3.4	Formulation for a Micromorphic Continuum	69
3.4.1	Balance Laws	71
3.4.2	Densities	72
3.4.3	Derivation of Continuum Expressions	73
3.4.3.1	Balance of Mass and Micro-Inertia	73
3.4.3.2	Balance of Linear Momentum	73
3.4.3.3	Balance of Rotational Momentum	74
3.4.3.4	Balance of Energy	76
3.5	Discussion	80
3.6	Appendix: Non-symmetric Cauchy stress due to directional bonding	82
4	Micropolar Small Strain Deformation Theory	85
4.1	Introduction	86
4.2	Background	89
4.2.1	Generalized Crystal Plasticity	89
4.2.2	Grain Boundary Treatment within Crystal Plasticity	91
4.2.2.1	Experimental Observations and Fine-Scale Modeling Results ...	91
4.2.2.2	Continuum Elastoplasticity GB Models	92
4.2.3	Micropolar Elastoplasticity	95

4.3	Model Formulation	96
4.3.1	Kinematics	96
4.3.1.1	General Micropolar Theory	96
4.3.1.2	Compatibility Analysis of Classical and Micropolar continua ...	98
4.3.2	Balance Laws and Thermodynamics.....	105
4.3.2.1	Mechanical Balance Laws and the Principle of Virtual Work ...	105
4.3.2.2	Thermodynamics	106
4.3.3	Single Crystal Constitutive Model	107
4.3.3.1	Multi-criterion Model	109
4.3.3.2	Single Criterion Model	111
4.3.4	Non-Associative Model for Slip Transfer at Grain Boundaries	112
4.3.4.1	Grain Interiors	112
4.3.4.2	Grain Boundary Regions.....	113
4.4	Numerical Implementation	115
4.4.1	Element Formulation.....	115
4.4.2	Constitutive Update	116
4.4.2.1	Rate-Tangent Modulus Scheme	117
4.4.2.2	Return Mapping Scheme	121
4.4.3	Algorithmic Moduli	123
4.4.3.1	Rate-Tangent Modulus Scheme	124
4.4.3.2	Return Mapping Scheme	126
4.5	Simulations	128
4.5.1	Simulation Set 1: Bar With Defect	129
4.5.2	Simulation Set 2: Notched Plate	130
4.5.3	Simulation Set 3: Semi-infinite Bicrystal	133
4.6	Summary	150

4.7	Appendix: ABAQUS UEL subroutine	153
5	Atomistic Simulations of Nanocrystal Deformation	169
5.1	Atomic-scale Deformation Kinematics for Bicrystal Grain Boundaries under Shear Loading	169
5.1.1	Motivation	169
5.1.2	Research Summary	170
5.1.2.1	Background	170
5.1.2.2	Computational Setup	171
5.1.2.3	Mathematical Formulation	171
5.1.2.4	Grain Boundary Structures	173
5.1.2.5	Two-Dimensional Shear Deformation	174
5.1.2.6	Three-Dimensional Shear Deformation	185
5.1.3	Conclusions	187
5.1.4	Future Work	188
5.1.4.1	L Formulation	188
5.1.4.2	Simulations	189
5.2	Large deformation of single crystal nickel	190
5.2.1	Uniaxial compression at a rate of $10^7/\text{sec}$	190
5.2.2	Uniaxial compression at a rate of $10^8/\text{sec}$	198
5.2.3	Discussion	201
6	Finite Deformation Theory	203
7	Summary	219
8	Publications and Presentations	221
	References	223

List of Figures

1.1	From [13]: Soft flux line lattice in a type-II superconductor showing a minus-60 wedge disclination.	20
1.2	Adapted from [240]: Schematic representation of material having a mean grain size of about 100 nm. Triangles of different orientations and size represent disclinations of different magnitudes and rotations.	21
1.3	From [240]: TEM micrographs of a Al-4%Cu-0.5%Zr alloy after severe plastic torsional straining (left) and after additional annealing for 160C for 1 hour (right). .	21
2.1	Cross-sectional view of a biaxially stretched film on a rigid substrate at (a) 3.77% stretch and (b) 3.78% stretch. Atoms are colored according to their value of slip vector.	34
2.2	Cross-sectional view of a biaxially stretched film on a rigid substrate at (a), (c) 3.77% stretch and (b), (d) 3.78% stretch. Atoms are colored according to their value of (a), (b) F_{11} and (c), (d) F_{22}	35
2.3	Cross-sectional view of a biaxially stretched film on a rigid substrate at 3.78% stretch. Atoms are colored according to their value of (a) F_{12} and (b) F_{21}	36
2.4	Cross-sectional view of a biaxially stretched film on a rigid substrate at (a), (c) 3.77% stretch and (b), (d) 3.78% stretch. Atoms are colored according to their value of (a), (b) ρ_{13} and (c), (d) ρ_{23}	37
2.5	Atoms with values of slip vector > 0.5 beneath a nanoindenter: (a) prior to any defects, (b) after emission of (reversible) partial dislocation loops, (c) after emission of an (irreversible) extended dislocation/hillock structure.	38
2.6	Cross-sectional view of the nanoindented atomic system at the deformation states shown in Figures 2.5(a)-2.5(c). Atoms are colored according to their value of F_{11} . .	39
2.7	Cross-sectional view of the nanoindented atomic system at the deformation states shown in Figures 2.5(a)-2.5(c). Atoms are colored according to their value of F_{33} . .	40
2.8	Cross-sectional view of the nanoindented atomic system at the deformation states shown in Figure 2.5(b). Atoms are colored according to their value of (a) F_{12} , (b) F_{13} , (c) F_{32}	40

2.9	Cross-sectional view of the nanoindented atomic system at the deformation states shown in Figures 2.5(a)-2.5(c). Atoms are colored according to their value of ρ_{12} .	41
2.10	Top view of the nanoindented atomic system at the deformation states shown in Figures 2.5(a)-2.5(c). Atoms are colored according to their value of ρ_{12} .	41
2.11	Cross-sectional view of the nanoindented atomic system at the deformation states shown in Figures 2.5(a)-2.5(c). Atoms are colored according to their value of ρ_{22} .	42
2.12	Top view of the nanoindented atomic system at the deformation states shown in Figures 2.5(a)-2.5(c). Atoms are colored according to their value of ρ_{22} .	42
2.13	Cross-sectional view of the nanoindented atomic system at the deformation states shown in Figures 2.5(a)-2.5(c). Atoms are colored according to their value of ρ_{32} .	43
2.14	Top view of the nanoindented atomic system at the deformation states shown in Figures 2.5(a)-2.5(c). Atoms are colored according to their value of ρ_{32} .	43
2.15	Cross-sectional view of a biaxially stretched film on a rigid substrate elastically unloaded from a stretch of 3.78%. Atoms are colored according to their value of (a) F_{11} and (b) ρ_{13} .	44
2.16	Cross-sectional view of the nanoindented atomic system elastically unloaded from the deformation state shown in Figure 2.5(c). Atoms are colored according to their value of (a) F_{33} and (b) ρ_{32} .	44
3.1	Variation of instantaneous pressure with time for a constrained system at 100 K.	61
3.2	Variation of time averaged pressure with time for a constrained system at 100 K.	62
3.3	(a) Time averaged pressures after 10^6 timesteps for constrained volume simulations performed at various temperatures. (b) Differences between P-K and virial measures of pressure at various temperatures.	63
3.4	Variation of instantaneous hydrostatic stress measures with time for a stretch of 1% after equilibration at 100 K and zero pressure.	64
3.5	Variation of instantaneous hydrostatic stress measures with time for a stretch of 1% after equilibration at 100 K and zero pressure.	64
3.6	(a) Variation of time averaged hydrostatic stress measures with time for a stretch of 1% after equilibration at 100 K and zero pressure. (b) Close-up of (a) for the first 250,000 timesteps.	65
3.7	Variation of time-averaged hydrostatic stress measures after 10^6 timesteps with temperature for a stretch of (a) 1%, and (b) 5 % after equilibration at that temperature.	67

3.8	Displacement field u_y for a center-cracked body vertically stretched 6.9%. Left: Atoms pictured with overlaying mesh and nodes. Right: Mesh elements showing contours of continuum displacement field; mesh is shown with gray lines to identify elements.	68
3.9	Stress fields for a center-cracked body vertically stretched 6.9%. Left: Mesh elements showing contours of continuum field P_{yy} . Right: Mesh elements showing contours of continuum field σ_{yy} as determined from the original Hardy formulation. In both pictures, the mesh is shown with gray lines to identify elements.	69
4.1	Geometric interpretation of the micropolar shear strains.	97
4.2	Planar double slip geometry. $\phi = 35.1^\circ$	129
4.3	Single crystal with defect loaded in compression (defect is in upper left-hand corner).	130
4.4	Load-deflection curves for single crystal with defect loaded in compression.	131
4.5	Finite element mesh density for the notched single crystal simulations.	132
4.6	Notched single crystal oriented for (a) single slip and (b) symmetric double slip. ...	132
4.7	Load-deflection curves for notched plate.	134
4.8	Rotation magnitude (a) single slip ($N = 0.95$) (b) symmetric double slip ($N = 0.95$) (c) single slip ($N = 0$) and (d) symmetric double slip ($N = 0$).	135
4.9	$\bar{\epsilon}_{[12]}$ (a) single slip ($N = 0.95$) (b) symmetric double slip ($N = 0.95$) (c) single slip ($N = 0$) and (d) symmetric double slip ($N = 0$).	136
4.10	$\bar{\epsilon}_{[12]}^p$ (a) single slip ($N = 0.95$) (b) symmetric double slip ($N = 0.95$) (c) single slip ($N = 0$) and (d) symmetric double slip ($N = 0$).	137
4.11	$\bar{\epsilon}_{[12]}^e$ (a) single slip ($N = 0.95$) (b) symmetric double slip ($N = 0.95$) (c) single slip ($N = 0$) and (d) symmetric double slip ($N = 0$).	138
4.12	$\bar{\kappa}_{13}^p$ (a) single slip ($N = 0.95$) (b) symmetric double slip ($N = 0.95$).	138
4.13	$\bar{\kappa}_{23}^p$ (a) single slip ($N = 0.95$) (b) symmetric double slip ($N = 0.95$).	139
4.14	Plastic strain $\bar{\epsilon}_{22}^p$ distributions across the top of the notch (a) single slip (b) double slip.	139
4.15	Plastic strain $\bar{\epsilon}_{22}^p$ distributions in the notched plate (a) single slip ($N = 0$) (b) double slip ($N = 0$) (c) single slip ($N = 0.95$) (d) double slip ($N = 0.95$) (e) single slip (classical) (f) double slip (classical).	140
4.16	Model Geometry.	141

4.17	(a) Stress-strain curves, (b) GND density distributions, and (c) rotation distributions for all simulations with $2d = 100 \mu\text{m}$.	143
4.18	(a) Stress-strain curves, (b) GND density distributions, and (c) rotation distributions for all simulations with $2d = 1\text{mm}$.	144
4.19	Case 1: (a) Stress-strain curves, (b) GND density distributions, and (c) rotation distributions.	145
4.20	Case 2: (a) Stress-strain curves and (b) rotation distributions.	145
4.21	Case 3: (a) Stress-strain curves, (b) GND density distributions, and (c) rotation distributions.	146
4.22	Case 4: (a) Stress-strain curves, (b) GND density distributions, and (c) rotation distributions.	147
4.23	Case 5: (a) Stress-strain curves, (b) GND density distributions, and (c) rotation distributions.	148
4.24	Case 6: (a) Stress-strain curves, (b) GND density distributions, and (c) rotation distributions.	149
4.25	Case 7: (a) Stress-strain curves and (b) rotation distributions.	150
5.1	Initial 2D grain boundary structure of a symmetric tilt grain boundary with $\Psi = 9.4^\circ$. Notice the small isolated defect structures composing the grain boundary that accommodate the lattice mismatch between the upper and lower grains.	174
5.2	Initial 2D grain boundary structure of a symmetric tilt grain boundary with $\Psi = 15.2^\circ$. Notice that as the disorientation angle increases, the defect structures that compose the boundary increases.	174
5.3	Initial 2D grain boundary structure of a symmetric tilt grain boundary with $\Psi = 27.8^\circ$. Notice that the entire grain boundary is composed of repeating 2D atomic structural units to accommodate the lattice mismatch.	175
5.4	Initial thin 3D structure of a $\langle 110 \rangle$ symmetric tilt grain boundary, Cu (221) $\theta=141.1^\circ$.	175
5.5	2D schematic of grain boundary structure and applied shear deformation.	176
5.6	After 5% strain, the grain boundary has migrated upward approximately 20 atomic layers away from its original location.	176
5.7	After 5% strain, small structural changes have occurred and discrete events of grain boundary sliding have been observed.	177

5.8	After 5% strain, localized dissociation events are observed and associated with boundary structural changes.	177
5.9	The F_{11} component for the grain boundary migration mechanism. Notice the difference in deformation between the migration planes and the lattice regions located between the migration planes.	178
5.10	The F_{12} component shows a relatively uniform deformation field under grain boundary migration with regard to the x_2 direction.	178
5.11	The R_{12} component for the migration mechanism displays rotation behavior for atoms located in both the migration planes and between.	179
5.12	ϕ_3 for the migration mechanism. Notice the sign difference between the atoms located around the migration plane and those atoms in the inter-regions.	179
5.13	The gradient of ϕ_3 with respect to the x_1 direction.	180
5.14	The gradient of ϕ_3 with respect to the x_2 direction.	180
5.15	ϕ_3 for the grain boundary sliding mechanism. Notice that there is little rotation extending out away from the boundary as sliding occurs.	181
5.16	The F_{11} component is shown for grain boundary dissociation. This picture highlights the localized nature of the grain boundary deformation field.	181
5.17	The F_{12} component is shown for grain boundary dissociation. The only significant pattern observed in this image is within the dissociation region.	182
5.18	ϕ_3 for the dissociation mechanism. Notice the localized rotation values occurring in regions surrounding the slipped planes. Atoms not located in the grain boundary or in these regions experience negligible microrotation.	182
5.19	The gradient of ϕ_3 with respect to the x_1 direction.	183
5.20	The gradient of ϕ_3 with respect to the x_2 direction.	183
5.21	ω_3 under grain boundary migration. There are no obvious vorticity patterns or regions of significant interest under boundary migration. Notice the existence of lattice noise in this formulation of vorticity using instantaneous atomic velocity. ...	184
5.22	ω_3 under grain boundary dissociation. Small localized vorticity fields appear in neighborhoods surrounding the dissociated planes.	184
5.23	The shear deformation of the (221) Cu boundary at about 3% strain colored with centrosymmetry. Notice the partial dislocation nucleation from the boundary into the lower lattice accompanying numerous atomic shuffling events within the boundary.	185

5.24	F_{12} shows that all atoms located within the boundary region have experienced deformation at 3% strain. However, the dependence of the deformation on the vertical direction is not uniform for these atoms. Notice that there is no deformation reaching into either lattice other than the partial dislocation.	186
5.25	R_{12} shows similar results to F_{12} . There is non-uniform dependence of the rotation component on the vertical direction, and there is little rotation extending out beyond the boundary region.	186
5.26	ϕ_3 gives information on atomic lattice curvature, and in this case the curvature is mostly constrained to the boundary region. Small localized regions of lattice curvature exist in areas directly neighboring the nucleation regions.	187
5.27	ω_3 for shear deformation of the 3D system. Notice the lack of obvious vorticity outside of the grain boundary, and the presence of noise still in the lattice.	187
5.28	Atomic structure of a columnar hexagonal nanocrystalline model colored with energy. This image shows a possible geometry that could be used to investigate the influence of numerous variables such as boundary length, triple junctions, and grain boundary character on the resulting deformation fields outlined in this work. .	189
5.29	Compression of single crystal nickel for $\dot{e} = 10^7/\text{s}^{-1}$. Atoms colored by potential energy values.	191
5.30	Compression of single crystal nickel for $\dot{e} = 10^7/\text{s}^{-1}$. Atoms colored by centrosymmetry values.	193
5.31	Compression of single crystal nickel for $e = 6\%$. (a) and (b) are colored by centrosymmetry, (c) and (d) are colored by slip vector.	194
5.32	Compression of single crystal nickel for $e = 9\%$. (a) and (b) are colored by centrosymmetry, (c) and (d) are colored by slip vector.	195
5.33	Compression of single crystal nickel for $e = 12\%$. (a) is colored by centrosymmetry, (b) and (c) are colored by slip vector.	196
5.34	Compression of single crystal nickel for $\dot{e} = 10^7/\text{s}^{-1}$. Atoms colored by $ \kappa_{12} $	197
5.35	Stress-strain curves for compression of single crystal nickel for $\dot{e} = 10^7/\text{s}^{-1}$: (a) normal stresses (b) shear stresses. Stresses (the vertical axes) are given in units of GPa.	198
5.36	Compression of single crystal nickel for $\dot{e} = 10^8/\text{s}^{-1}$. Atoms colored by potential energy values.	199
5.37	Compression of single crystal nickel for $\dot{e} = 10^8/\text{s}^{-1}$. Atoms colored by centrosymmetry values.	200

- 5.38 Stress-strain curves for compression of single crystal nickel for $\dot{\epsilon} = 10^8/\text{s}^{-1}$: (a) normal stresses (b) shear stresses. Stresses (the vertical axes) are given in units of GPa. 201

List of Tables

3.1	Time averaged pressures after 10^6 timesteps for constrained volume simulations. . .	62
3.2	Time averaged stresses after 10^6 timesteps for simulations of a heated and triaxially strained system. Here, ‘% difference’ refers to the difference between transformed P-K stress (the 6 th column) and the virial.	66
4.1	Simulation Set 1 Material Parameters.	130
4.2	Simulation Set 2 Material Parameters.	133
4.3	Simulation Set 3 Fixed Material Parameters.	134
4.4	Simulation Set 3 Variable Material Parameters.	135

Chapter 1

Introduction

Principal Authors: Jonathan A. Zimmerman and Douglas J. Bammann

Materials with nanoscale-sized characteristic structures and defects exhibit significantly different mechanical responses from those predicted by conventional, macroscopic continuum theory. For example, nanocrystalline metals display an inverse Hall-Petch effect [181, 48] whereby the strength of the material decreases with decreasing grain size. In these materials, interface regions between grains become critical as rotation of the grains becomes a dominant mode of deformation. These rotational defects are represented by the mathematical concept of partial disclinations, include low and high angle grain boundaries and twin boundaries, and affect mechanical as well as thermal and electromagnetic properties of the material they reside in. Disclinations are internal sources of high elastic stresses. As such, the ability to incorporate these effects within continuum theory, thereby connecting nanoscale materials phenomena with macroscale behavior, has become vitally important to predict the reliability of nanosystems.

This report presents the accomplishments of a Laboratory Directed Research and Development (LDRD) project focused on the construction of a consistent theory to model both the evolution and kinetics of disclinations. Kinematics, balance laws and thermodynamic restrictions are considered for a deforming crystalline material containing distributions of dislocations and disclinations. Structural information attributed to these nanoscale defects contributes to the formulation containing degrees of freedom that express deformation at the macro- and microscopic regimes. Disclinations are essential mathematical constructs for modeling grains and grain boundaries in polycrystalline materials as they represent rotational defects and sources of incompatibility in a materials deformation. An example of a disclination is shown in Figure 1.1. When grain sizes are reduced to the nanometer scale, rotation of the grains and deformation within the grain boundaries become the dominant modes of deformation[143, 207]. These relative rotations between grains result in the formation of defect structures different from those observed at macroscopic levels, affecting mechanical as well as thermal and electromagnetic properties. Non-equilibrium grain boundaries in nanocrystalline materials that were processed using large plastic deformations contain a high density of defects in their structure resulting in excess energy and long-range elastic fields. These elastic stresses are a result of large distortions and dilatations near the grain boundaries that contain dislocations with Burgers vectors both normal and tangential to the grain boundary as well as joint disclinations in triple junctions. For example, the misorientation boundary between two grains or cells can be represented either by a series of geometrically necessary dislocations or by a disclination. In particular, a triple point, the intersection of 3 grains is most appropriately modeled as a disclination. In Figure 1.2, a 100 nm grain is depicted as elastically distorted zones several nanometers thick near the grain boundaries while the center of the grains is essentially a perfect crystal. These distortion zones have been clearly observed using transmission electron

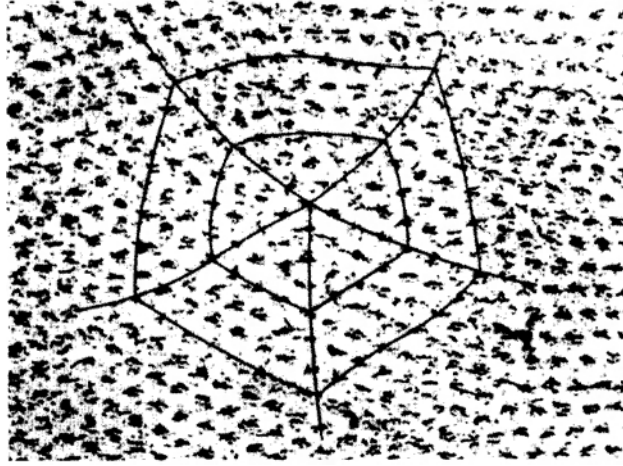


Figure 1.1. From [13]: Soft flux line lattice in a type-II superconductor showing a minus-60 wedge disclination.

microscopy (TEM) and high-resolution electron microscopy (HREM) techniques, as shown in Figure 1.3 for a nanocrystalline Al-Cu-Zr alloy. Figure 1.3 also shows how the severely deformed microstructure compares with an annealed one. While a granular type structure with high angle grain boundaries is observed for both cases, the severely deformed image shows features consistent with non-equilibrium grain boundaries.

As an effort to better understand and characterize these nanoscale mechanisms, we undertook the development of a material manifold model endowed with structure to accommodate observed additional degrees of freedom in the deformation modes. This effort addresses the need for methodologies that bridge nanoscale phenomena to macroscale behavior. A rotational component is added to the elastic-plastic decomposition of the deformation gradient in order to admit disclinations. At the micro-level, an affine connection describing spatial variations in the stretch and rotation of a triad of lattice vectors is introduced, consisting of contributions from the macroscopic lattice deformation field and micropolar degrees of freedom capturing the additional local rotations due to disclinations. State variables representing geometrically necessary dislocations and disclinations will be directly obtained from the kinematics as torsion and curvature, respectively. Thermodynamic stresses conjugate to the internal variables (defect densities) are required to satisfy mesoscopic linear and angular momentum balance laws. In addition, the thermodynamics is carefully formulated to properly account for the configurational nature of the internal stresses. Evolution equations are developed for the rates of inelastic deformations, microrotations and internal variables to complete the system. A collaboration between Sandia National Laboratories and the Georgia Institute of Technology was established to develop a small strain formulation that simplifies the system of differential equations characteristic of a finite deformation theory. This system was implemented into a finite element code.

There has been a recent resurgence of research in the area of continuum dislocation the-

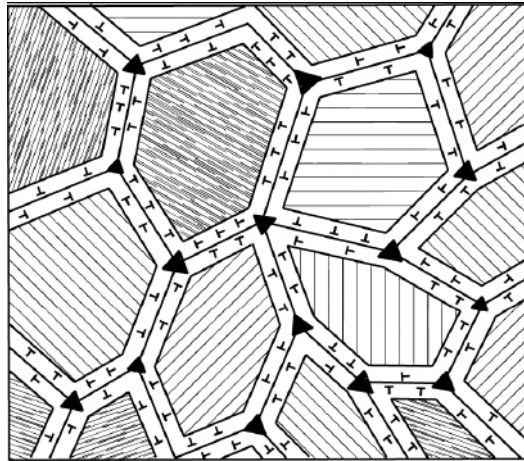


Figure 1.2. Adapted from [240]: Schematic representation of material having a mean grain size of about 100 nm. Triangles of different orientations and size represent disclinations of different magnitudes and rotations.

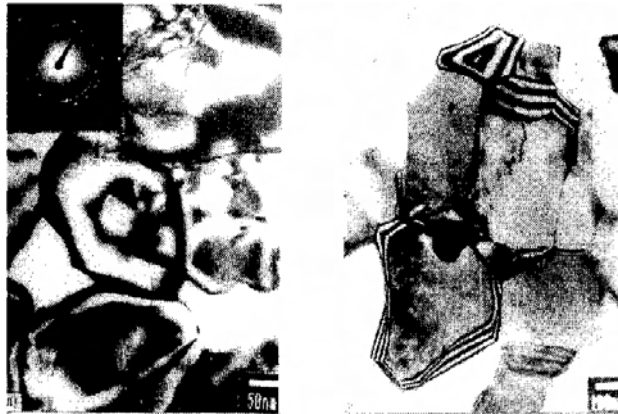


Figure 1.3. From [240]: TEM micrographs of a Al-4%Cu-0.5%Zr alloy after severe plastic torsional straining (left) and after additional annealing for 160C for 1 hour (right).

ory and strain gradient plasticity. Most of this work introduced gradients into the hardening or yield strength. Complete thermodynamic internal state variable theories incorporating the continuum representation of geometrically necessary dislocations have been proposed by Gurtin[106], Bammann[25], and Svendsen[230], among others. These theories did not address the additional kinematic degrees of freedom and balance laws required to describe rotational defects such as disclinations. It is critical to have a consistent thermodynamic theory in which these degrees of freedom correspond to the internal state variables and the associated configurational forces satisfy smaller length scale momentum balances. Our work presented here is an attempt to develop such a theory.

To aid in the development of both our finite deformation and small strain theories, we performed molecular dynamic (MD) simulations to examine the modes of deformation and microstructure evolution in single crystal and nanocrystalline metals. Connection between the atomic scale models and continuum theories is done by the derivation and use of expressions that extract continuum mechanical information from atomistic simulations. This information consists of continuum theory variables such as stress, deformation gradient, strain, rotation and lattice curvature. The latter two of these quantities can be connected to dislocation and disclination densities. These engineering-scale expressions possess validity for a variety of different materials, even those that possess highly directional inter-molecular bonding such as covalent ceramics and polymers. Expressions to quantify continuum variables in atomistic simulation have been previously developed for standard continuum theories[257] in which inter-atomic bonding is assumed pair-wise in nature. Delph has attempted the extension of these expressions to materials with more complex bonding[59], although inconsistencies in the momentum and energy balance laws exist for the derivation presented. Recent papers by Zhou and McDowell[254] and by Chen and Lee[34] have presented expressions for an elastic, micropolar continuum. However, these efforts use ill-defined functions to represent fields within a continuum, and do not admit the possibility of state variables to quantify nanoscale defects that spawn plastic behavior. The derivation of expressions that connect atomistically inspired expressions to plastic deformation state variables has never before been attempted, and our efforts contribute a worthwhile starting point for such an endeavor.

Ultimately, our goal was to develop our manifold model to a sufficient state as comparisons could be made with existing experimental data[119] on nanocrystalline materials and thin films to determine the applicability of the continuum model at these very small length scales. While this degree of development was not accomplished in this project, we have nonetheless completed a body of work that will assist model developers to achieve such a goal at some point in the future.

Chapter 2

Deformation Gradients for Continuum Mechanical Analysis of Atomistic Simulations

Principal Authors: Jonathan A. Zimmerman, Douglas J. Bammann and Huan Gao

In this chapter, we present an expression developed for calculating an atomic-scale deformation gradient within atomistic simulations. This expression is used to analyze the deformation fields for a one-dimensional atomic chain, a biaxially stretched thin film containing a surface ledge, and a FCC metal subject to indentation loading from a nanometer-scale indenter. The analyses presented show that the metric established here is consistent with the continuum mechanical concept of deformation gradient (which is known to have a zero curl for compatible deformations) in most instances. However, our metric does yield non-zero values of curl for atoms near loaded geometric inhomogeneities, such as those that form the ledges themselves and those beneath or adjacent to the indentation contact region. Also, we present expressions for higher order gradients of the deformation field and discuss the requirements for their calculation. These expressions are necessary for linking atomistic simulation results with advanced continuum mechanics theories such as strain gradient plasticity, thereby enabling fundamental, atomic-scale information to contribute to the formulation and parameterization of such theories.

2.1 Introduction

Atomistic simulation is a useful method for studying material science phenomena. Examination of the state of a simulated material and the determination of its mechanical properties is accomplished by inspecting the stress and strain (deformation) fields within the material. However, these concepts have been proven difficult to define in a physically reasonable manner at the atomic scale. While much has been done to establish expressions for stress in the framework of atomistics [41, 159, 160, 121, 238, 109, 148, 38, 49, 252, 259], far less has been done to properly define an atomic-scale deformation gradient, which is used to determine states of strain at large deformation.

Continuum mechanics [153, 156, 183] describes the finite deformation of a body from a reference, or material configuration, where a point on the body is located by a vector $\mathbf{X} = \{X_1, X_2, X_3\}$, to some current, or spatial configuration, in which the same point is now located by a new vector $\mathbf{x} =$

$\{x_1, x_2, x_3\}$ which is a function of the material coordinate and time, $\mathbf{x} = \mathbf{x}(\mathbf{X}, t) = \mathbf{x}(X_1, X_2, X_3, t)$. $\mathbf{x}(\mathbf{X}, t)$ is often referred to as a mapping from the material configuration to the spatial one. The derivative of this deformation is known as the *deformation gradient*,

$$\mathbf{F} = \frac{\partial \mathbf{x}}{\partial \mathbf{X}} \quad (2.1)$$

For the remainder of this work, we choose to work in index notation rather than the vector notation used above. Hence,

$$F_{iI} = \frac{\partial x_i}{\partial X_I}, \quad (2.2)$$

where lower case Roman letters (i) are used to refer to coordinate components of spatial quantities and upper case Roman letters (I) are used to refer to coordinate components of material quantities.

In order to determine the stretch of the differential length segment with respect to material coordinates, (2.2) is re-cast as

$$dx_i = F_{iI} dX_I. \quad (2.3)$$

From this relation, the length of the infinitesimal vectors $d\mathbf{x}$ and $d\mathbf{X}$ are $ds = \sqrt{dx_i dx_i}$ and $dS = \sqrt{dX_I dX_I}$, respectively. A measure of stretch for this differential length segment is given by $\ell \equiv \{ds\}^2 - \{dS\}^2$, equal to $2E_{IJ}dX_I dX_J$ with respect to the material configuration where E_{IJ} is known as the material or *Lagrangian* strain tensor and is

$$E_{IJ} = \frac{1}{2} (F_{iI} F_{iJ} - \delta_{IJ}). \quad (2.4)$$

Alternatively, this stretch can be expressed with respect to spatial coordinates, $\ell = 2e_{ij}dx_i dx_j$, where e_{ij} is known as the spatial or *Eulerian* strain tensor,

$$e_{ij} = \frac{1}{2} (\delta_{ij} - F_{iI}^{-1} F_{Ij}^{-1}), \quad (2.5)$$

and \mathbf{F}^{-1} is the inverse of \mathbf{F} (*i.e.* $\mathbf{F} \cdot \mathbf{F}^{-1} = \mathbf{1}$). It is realized that in the limit of small strains \mathbf{E} and \mathbf{e} are approximately equal to each other and are represented by the small strain tensor $\boldsymbol{\varepsilon}$ where

$$\varepsilon_{ij} = \frac{1}{2} \left(\frac{\partial u_i}{\partial x_j} + \frac{\partial u_j}{\partial x_i} \right) \quad (2.6)$$

and $\mathbf{u} = \mathbf{x} - \mathbf{X}$.

Some efforts have been made to quantify the deformation gradient at the atomic scale. Kruyt and Rothenburg developed a simple expression for an average displacement gradient tensor ($\frac{\partial \mathbf{u}}{\partial \mathbf{X}} = \mathbf{F} - \mathbf{1}$) for two-dimensional regions in the simulation of granular materials [134]. While their expression was both useful and easy to compute, it is not apparent how to generalize their expression to three dimensions for non-granular materials. Sengupta *et al.* [212] developed an expression based on quantifying a displacement field in the vicinity of an atom and then calculating derivatives based on finite difference schemes. However, they caution that their definition is applicable only within perfect crystals. Alternative expressions for materials with defects, or even how their

definition behaved in the presence of such defects, were not considered. An expression for displacement gradient was also developed by Inoue *et al.* [120], and later used by Jin and Yuan [122], to calculate a discrete version of the J-Integral, the energetic driving force for crack propagation. Also interested in developing a discrete form of the J-Integral expression, Nakatani *et al.* [172] used the derivative of a continuous weighting function to selectively include atomic displacement information in the determination of a displacement gradient field.

Concurrently, Horstemeyer and Baskes [115] and Zimmerman [256] developed similar expressions that perform a least squares analysis of the gradient of the deformation field local to an atom. Horstemeyer *et al.* used their expression as one of the tools to perform a multiscale analysis of fixed-end simple shear [116], while Zimmerman performed limited analysis of dislocation nucleation at crystal surface ledges [256].

While many of these prior efforts have been notable, none have investigated the issue of compatibility of the deformation field. In finite deformation theory, this can be expressed by the condition that the curl of the deformation gradient (with respect to the material frame) must equal zero: $\mathbf{F} \times \nabla = \frac{\partial F_{iK}}{\partial X_M} \epsilon_{KMJ} = \mathbf{0}$, where ϵ_{KMJ} is the permutation tensor defined as follows:

$$\epsilon_{KMJ} = \begin{cases} +1 & \text{when } K, M, J \text{ are } 1, 2, 3 \text{ or an even permutation of } 1, 2, 3, \\ -1 & \text{when } K, M, J \text{ are an odd permutation of } 1, 2, 3, \text{ e.g. } 2, 1, 3 \\ 0 & \text{when any two indices are equal.} \end{cases} \quad (2.7)$$

Recently, Steinmann *et al.* [224] have considered this issue indirectly by examining when deformations transition to non-affine, thereby violating the Cauchy-Born rule [118, 29]. While Steinmann *et al.* do not define or use a local deformation gradient, they do quantify this transition using a standard deviation for variance from deformation predicted by the Cauchy-Born rule (*i.e.* homogeneous deformation), defined for the entire atomic system. Their primary result is that this metric signifies a loss of validity of the Cauchy-Born rule for the same state of deformation as predicted by examining the determinant of the acoustic tensor.

In this chapter, we expand on the work done in [256] and present an expression for evaluating an atomic-scale deformation gradient. Further, we show analytic and simulation examples that characterize the behavior of our expression. In particular, we examine the cases of a one-dimensional atomic chain, dislocation nucleation at a crystal surface ledge due to an applied biaxial stretch, and nanoindentation. We also present expressions for higher order gradients of the deformation field and discuss the requirements for calculating them.

2.2 Formulation of Atomic-Scale Deformation Gradient

While the differential relation of equation (2.3) is exact in the limit of infinitesimal vector segments, *i.e.* $dx_i \rightarrow 0$ and $dX_I \rightarrow 0$, we note here that in the limit of finite lengths it is the first term in the

Taylor expansion

$$\Delta x_i = F_{iI} \Delta X_I + \frac{1}{2} H_{iKL} \Delta X_K \Delta X_L + \dots, \quad (2.8)$$

where H_{iKL} is the mixed second order derivative $\frac{\partial^2 x_i}{\partial X_K \partial X_L}$. Nevertheless, we use this approximation and note that the smallest length that can be measured is the distance separating neighboring atoms, *i.e.* $\Delta x \rightarrow x^{\alpha\beta} = |\mathbf{x}^{\alpha\beta}|$, where β is a nearest neighboring atom to atom α . For most crystals, a given atom has n nearest neighbors that are equidistant from the atom if the crystal is in its equilibrium structure. In this notation, $\mathbf{x}^{\alpha\beta}$ is the vector connecting atoms α and β in the current configuration. Similarly, $\mathbf{X}^{\alpha\beta}$ is this vector in the reference (undeformed) configuration. These expressions can be used within the finite length limit of (2.3) to produce

$$x_i^{\alpha\beta} = F_{iI} X_I^{\alpha\beta}. \quad (2.9)$$

Equation (2.9) can be rearranged to

$$x_i^{\alpha\beta} - F_{iI} X_I^{\alpha\beta} = 0. \quad (2.10)$$

While this relationship is exact for an atom α and one of its neighbor β , the same tensor \mathbf{F} will not satisfy this expression for all of the nearest neighbors $\beta = 1, 2, 3, \dots, n$. Hence, we assume that the components of \mathbf{F} will be based on all the nearest neighbors of atom α , and that the right hand side of equation (2.10) will no longer be zero for each individual atom-neighbor pair, but will differ from zero by some small error. It will be required that the sum (over all nearest neighbors) of the squares of these errors,

$$B_i^\alpha = \sum_{\beta=1}^n \left(x_i^{\alpha\beta} - F_{iI} X_I^{\alpha\beta} \right)^2, \quad (2.11)$$

be minimized by some choice of \mathbf{F}^α :

$$\frac{\partial B_i^\alpha}{\partial F_{iM}^\alpha} = 0, \quad \forall i \text{ and } M \quad (2.12)$$

Notice that we now use the superscript α to denote that each deformation gradient is associated with a particular atom and is determined using the inter-atomic spacings between that atom and its neighbors. Substitution of (2.11) into (2.12), and performing the differentiation, one obtains

$$\sum_{\beta=1}^n \left(x_i^{\alpha\beta} X_M^{\alpha\beta} - F_{iI}^\alpha X_I^{\alpha\beta} X_M^{\alpha\beta} \right) = 0. \quad (2.13)$$

This equation can be simplified and rearranged to produce

$$\omega_{iM}^\alpha = F_{iI}^\alpha \eta_{IM}^\alpha, \quad (2.14)$$

where

$$\omega_{iM}^\alpha \equiv \sum_{\beta=1}^n x_i^{\alpha\beta} X_M^{\alpha\beta}, \quad (2.15)$$

and

$$\eta_{IM}^\alpha \equiv \sum_{\beta=1}^n X_I^{\alpha\beta} X_M^{\alpha\beta}. \quad (2.16)$$

Equation (2.14) can be manipulated to define the atomic-scale deformation gradient as

$$F_{iI}^\alpha = \omega_{iM}^\alpha (\eta^\alpha)^{-1}_{MI} \quad (2.17)$$

This expression is a mean-value deformation gradient, which can be used in the earlier equations to estimate measures of strain.

In reflecting on this derivation, we take note of a few necessary conditions that must be satisfied in order for equations (2.15) - (2.17) to be valid. First, since the deformation gradient tensor has 9 independent components, an atom in a three-dimensional system must have, at a minimum, 3 neighbors. Second, in order for η^α to be invertible, it must be the case that these neighbors span three-dimensional space, *i.e.* the atom and its nearest neighbors are neither coplanar nor collinear. This makes sense from a physical perspective as it would be impossible to define deformation in a direction along with no neighbors exist in the reference configuration. However, it can also be proven as follows: η^α will be invertible if it can be shown that it is positive-definite, *i.e.* for any arbitrary, non-zero vector \mathbf{V} , $\mathbf{V} \cdot \eta^\alpha \cdot \mathbf{V} > 0$. Using equation (2.16),

$$\begin{aligned} \mathbf{V} \cdot \eta^\alpha \cdot \mathbf{V} &= \sum_{\beta=1}^n V_I X_I^{\alpha\beta} X_M^{\alpha\beta} V_M \\ &= \sum_{\beta=1}^n y_{\alpha\beta} y_{\alpha\beta} \\ &= \sum_{\beta=1}^n y_{\alpha\beta}^2, \end{aligned}$$

where $y_{\alpha\beta} = \mathbf{X}^{\alpha\beta} \cdot \mathbf{V}$. Since this sum is a sum of squares, then we can conclude that η^α is at least positive semi-definite, *i.e.* $\mathbf{V} \cdot \eta^\alpha \cdot \mathbf{V} \geq 0$. Clearly this quantity can only equal zero for a non-zero vector \mathbf{V} if $\mathbf{X}^{\alpha\beta} \cdot \mathbf{V} = 0$ for all neighbors β . As long as the set of neighbor vectors $\{\mathbf{X}^{\alpha\beta}\}$ spans three-dimensional space in a non-coplanar arrangement, this condition is never satisfied, proving that η^α is positive definite and hence invertible. It is also clear that the condition $\mathbf{X}^{\alpha\beta} \cdot \mathbf{V} = 0$ can be satisfied if the atom and its nearest neighbors are either collinear or coplanar. In such instances, a one or two-dimensional analog to equations (2.15) - (2.17) could be constructed, respectively.

It can be easily shown that equations (2.15) - (2.17) are exact for the case of a homogeneously applied deformation. For such a situation, $x_i^{\alpha\beta} = A_{iJ} X_J^{\alpha\beta}$, where A_{iJ} is a constant tensor. Hence, $\omega_{iM}^\alpha = A_{iJ} \sum_{\beta=1}^n X_J^{\alpha\beta} X_M^{\alpha\beta} = A_{iJ} \eta_{JM}^\alpha$. Substitution of this expression into (2.17) yields $F_{iI}^\alpha = A_{iJ} \eta_{JM}^\alpha (\eta^\alpha)^{-1}_{MI} = A_{iJ} \delta_{JI} = A_{iI}$.

An advantage of this formulation over other more simple estimates of strain is that one can take into account that atomic lattice positions in a reference (*i.e.* strain-free) state are not always straightforward. Such is the case for geometric irregularities (*e.g.* voids, corners, and ledges) and

the effect of surface relaxation. In these cases, equilibrium bond lengths are not identical for all atoms, and individual reference positions must be known for an accurate estimate of strain. This concern will be revisited in a later section.

This formulation was first presented in [256], and is similar to the one developed concurrently by Horstemeyer and Baskes [115]. In their work, Horstemeyer and Baskes included a weighting function within their expressions that are analogous to (2.15) and (2.16). Our expressions can be thought of as a specific choice of weighting function, that of the unit step defined within a region that only includes an atom's nearest neighbors, and equals zero for the neighbor shells beyond the nearest one. From these early efforts [115, 116], it was not clear that the inclusion of such a weighting function carries any benefit for other choices of functional form, nor was it known how significantly the choice of functional form affects the resulting calculated deformation gradient. Recently, Gullet *et al.* [101] have revisited this issue and performed calculations to assess how the functional form and cutoff radius of the weighting function affects the computed strains. They conclude that both of these factors affect the value of computed strain (both Lagrangian/Green and Eulerian/Almansi tensors given by (2.4) and (2.5), respectively), particularly in regions of localization where material defects such as dislocations have formed and/or propagated through. While Gullet *et al.* do examine the sensitivity of their calculated strain tensors relative to the weighting function cutoff radius and relative to the size of the localization region, they do not examine the issue of compatibility to confirm that their deformation gradient measure is consistent with continuum mechanics. This issue will be examined in detail later in this chapter.

As discussed in [256], application of this definition of deformation gradient is straight-forward for crystals of any lattice type that are describable by a primitive unit cell, *i.e.* a lattice in which the basic atomic cell that is replicated to create the full lattice structure contains a single atom. However, not all naturally occurring lattices have a primitive unit cell. For example, the diamond cubic lattice does not have a primitive unit cell, but rather is constructed from two interpenetrating face-centered cubic (FCC) cells. These sub-lattices can displace relative to each other, giving three extra degrees of freedom (representing a rigid body translation) which must be determined in order to fully describe the deformation of the lattice [127, 231]. That aside, each sub-lattice does have a deformation gradient that can be determined by applying equations (2.15) - (2.17) only to the second nearest neighbors of an atom.

2.3 Expressions for Higher-Order Gradients

Before we discuss the issue of compatibility of our atomic-scale deformation gradient, or examine numerical simulations in which this expression is used to give us insight on materials behavior, we pause to consider the possibility of expressions for higher-order gradients of the deformation field for an atomistic system. As mentioned above, the differential expansion shown in equation (2.3) is exact only in the limit of infinitesimal vector lengths, *i.e.* $dx_i \rightarrow 0$ and $dX_I \rightarrow 0$. For the finite lengths of inter-atomic spacings, we acknowledge that our formulation of an atomic deformation gradient used only the first term in a longer Taylor series expansion. We now reconsider using both

the first and second term in this expansion to describe our atomistic deformation field, *i.e.*

$$x_i^{\alpha\beta} = F_{il}X_l^{\alpha\beta} + \frac{1}{2}H_{iKL}X_K^{\alpha\beta}X_L^{\alpha\beta}. \quad (2.18)$$

where H_{iKL} represents the mixed second order derivative $\frac{\partial^2 x_i}{\partial X_K \partial X_L}$. Sunyk and Steinmann used such an expansion to describe atomic-scale deformation in an effort to examine the validity of the Cauchy-Born rule [229]. In that work, they used the symbol \mathbf{G} to represent the second order derivative. However, \mathbf{G} is commonly used to denote *displacement gradient*, defined by the quantity $\mathbf{F} - \mathbf{1}$. To avoid confusion, we therefore use the symbol \mathbf{H} .

As before, we recast (2.18) such that the right hand side equals zero:

$$x_i^{\alpha\beta} - F_{il}X_l^{\alpha\beta} - \frac{1}{2}H_{iKL}X_K^{\alpha\beta}X_L^{\alpha\beta} = 0 \quad (2.19)$$

Again, we assume that the components of \mathbf{F} and \mathbf{H} will be determined using neighbors of atom α such that the right hand side, while not equal to zero, will be minimized. Hence,

$$B_i^\alpha = \sum_{\beta=1}^n \left(x_i^{\alpha\beta} - F_{il}^\alpha X_l^{\alpha\beta} - \frac{1}{2}H_{iKL}^\alpha X_K^{\alpha\beta}X_L^{\alpha\beta} \right)^2, \quad (2.20)$$

and

$$\frac{\partial B_i^\alpha}{\partial F_{iM}^\alpha} = 0, \quad \forall i \text{ and } M \quad (2.21)$$

$$\frac{\partial B_i^\alpha}{\partial H_{iST}^\alpha} = 0, \quad \forall i, S \text{ and } T \quad (2.22)$$

Substitution of (2.20) into (2.21) yields the equation,

$$\sum_{\beta=1}^n \left(x_i^{\alpha\beta} X_M^{\alpha\beta} - F_{il}^\alpha X_l^{\alpha\beta} X_M^{\alpha\beta} - \frac{1}{2}H_{iKL}^\alpha X_K^{\alpha\beta}X_L^{\alpha\beta}X_M^{\alpha\beta} \right), \quad (2.23)$$

which can be simplified to

$$\omega_{iM}^\alpha - F_{il}^\alpha \eta_{lM}^\alpha - \frac{1}{2}H_{iKL}^\alpha \xi_{KLM}^\alpha = 0, \quad (2.24)$$

where ω^α and η^α are defined in equations (2.15) and (2.16), respectively, and ξ^α is defined by the relation

$$\xi_{KLM}^\alpha = \sum_{\beta=1}^n X_K^{\alpha\beta}X_L^{\alpha\beta}X_M^{\alpha\beta}. \quad (2.25)$$

Similarly, substitution of (2.20) into (2.22) yields the equation,

$$\sum_{\beta=1}^n \left(x_i^{\alpha\beta} X_S^{\alpha\beta}X_T^{\alpha\beta} - F_{il}^\alpha X_l^{\alpha\beta}X_S^{\alpha\beta}X_T^{\alpha\beta} - \frac{1}{2}H_{iKL}^\alpha X_K^{\alpha\beta}X_L^{\alpha\beta}X_S^{\alpha\beta}X_T^{\alpha\beta} \right) = 0, \quad (2.26)$$

which too can be simplified to the equation

$$v_{iST}^\alpha - F_{il}^\alpha \xi_{lST}^\alpha - \frac{1}{2}H_{iKL}^\alpha \phi_{KLS}^\alpha = 0, \quad (2.27)$$

where ξ^α is defined in (2.25),

$$v_{iST}^\alpha = \sum_{\beta=1}^n x_i^{\alpha\beta} X_S^{\alpha\beta} X_T^{\alpha\beta}, \quad (2.28)$$

and

$$\phi_{KLS T}^\alpha = \sum_{\beta=1}^n X_K^{\alpha\beta} X_L^{\alpha\beta} X_S^{\alpha\beta} X_T^{\alpha\beta}. \quad (2.29)$$

To solve equations (2.24) and (2.27), we first multiply (2.24) by $(\eta^\alpha)^{-1}$,

$$\omega_{iM}^\alpha (\eta^\alpha)^{-1}_{MJ} - F_{iJ}^\alpha - \frac{1}{2} H_{iKL}^\alpha \xi_{KLM}^\alpha (\eta^\alpha)^{-1}_{MJ} = 0, \quad (2.30)$$

and then isolate the expression for F_{iJ}^α ,

$$F_{iJ}^\alpha = \omega_{iM}^\alpha (\eta^\alpha)^{-1}_{MJ} - \frac{1}{2} H_{iKL}^\alpha \xi_{KLM}^\alpha (\eta^\alpha)^{-1}_{MJ}. \quad (2.31)$$

We then use this equation with equation (2.27):

$$v_{iST}^\alpha - \left[\omega_{iM}^\alpha (\eta^\alpha)^{-1}_{MI} - \frac{1}{2} H_{iKL}^\alpha \xi_{KLM}^\alpha (\eta^\alpha)^{-1}_{MI} \right] \xi_{IST}^\alpha - \frac{1}{2} H_{iKL}^\alpha \phi_{KLS T}^\alpha = 0. \quad (2.32)$$

Grouping the terms that contain \mathbf{H}^α , we obtain

$$v_{iST}^\alpha - \omega_{iM}^\alpha (\eta^\alpha)^{-1}_{MI} \xi_{IST}^\alpha + \frac{1}{2} H_{iKL}^\alpha \left[\xi_{KLM}^\alpha (\eta^\alpha)^{-1}_{MI} \xi_{IST}^\alpha - \phi_{KLS T}^\alpha \right] = 0. \quad (2.33)$$

By rearranging terms and taking the inverse of the fourth order matrix

$$\zeta_{KLS T}^\alpha \equiv \left[\phi_{KLS T}^\alpha - \xi_{KLM}^\alpha (\eta^\alpha)^{-1}_{MI} \xi_{IST}^\alpha \right], \quad (2.34)$$

we finally obtain

$$H_{iKL}^\alpha = 2 \left[v_{iST}^\alpha - \omega_{iM}^\alpha (\eta^\alpha)^{-1}_{MI} \xi_{IST}^\alpha \right] (\zeta^\alpha)^{-1}_{TSLK}. \quad (2.35)$$

Substitution of this expression into equation (2.31) yields

$$F_{iJ}^\alpha = \omega_{iM}^\alpha (\eta^\alpha)^{-1}_{MJ} - \left[v_{iST}^\alpha - \omega_{iM}^\alpha (\eta^\alpha)^{-1}_{MI} \xi_{IST}^\alpha \right] (\zeta^\alpha)^{-1}_{TSLK} \xi_{KLM}^\alpha (\eta^\alpha)^{-1}_{MJ}. \quad (2.36)$$

Clearly, this expression for \mathbf{F}^α is significantly more computationally intensive to evaluate than the earlier expression given in equation (2.17). Also, it is probably not the case that only nearest neighbors will be sufficient to determine all of the components of \mathbf{F}^α and \mathbf{H}^α . Combined, these tensors contain $9 + 27 = 36$ values to be solved for in three dimensional space. Given this, no less than 12 neighbors are needed. This extends out past the nearest neighbor shell in most lattices, and certainly includes non-nearest neighbors for atoms near geometric inhomogeneities such as surfaces, edges and corners. In contrast, only 3 neighbors are needed for the expression in equation (2.17). As before, certain arrangements of atoms may prohibit the existence of inverse transformations for tensors η^α and ζ^α in three dimensions such as neighbors that are strictly collinear or coplanar to atom α . For such cases, one and two dimensional analogs to these expressions can be derived.

While difficult to compute, the usefulness of the expressions presented in this section is profound. Calculation of higher order gradients enables atomistic simulation results to be used in the formulation and parameterization of advanced continuum theories such as strain gradient plasticity (for example, the theory by Han *et al.* [108]). In their work [229], Sunyk and Steinmann expand the hyperelastic strain energy density function to be functions of both the \mathbf{F} and \mathbf{H} , and derive balance laws that include work conjugates of both kinematic variables. While their goal is to expand the Cauchy-Born rule to include inhomogeneous deformations, a clear next step would be to use locally-calculated values of these deformation gradients to examine consistency between atomistic simulation and their higher order continuum theory, and to characterize deviations that may occur due to the creation of material defects.

Before leaving this section, we again consider the case of a homogeneously applied deformation, $x_i^{\alpha\beta} = A_{iJ}X_J^{\alpha\beta}$, where A_{iJ} is a constant tensor. In this case, $\omega_{iM}^\alpha = A_{iJ}\eta_{JM}^\alpha$ and $v_{iST}^\alpha = A_{iJ}\xi_{JST}^\alpha$. Hence,

$$H_{iKL}^\alpha = 2A_{iJ} \left[\xi_{JST}^\alpha - \eta_{JM}^\alpha (\eta^\alpha)^{-1}_{MI} \xi_{IST}^\alpha \right] (\zeta^\alpha)^{-1}_{TSLK} \quad (2.37)$$

$$= 2A_{iJ} [\xi_{JST}^\alpha - \xi_{JST}^\alpha] (\zeta^\alpha)^{-1}_{TSLK} \quad (2.38)$$

$$= 0, \quad (2.39)$$

and, as before, equation (2.36) simplifies to $F_{iJ}^\alpha = A_{iJ}$.

2.4 Compatibility of the Atomic-Scale Deformation Gradient

Given the significant cost of calculating both the deformation gradient \mathbf{F}^α and the higher order gradient \mathbf{H}^α as discussed in the previous section, we choose to return to our original expressions given in equations (2.15) - (2.17) when examining the issue of compatibility. In standard continuum mechanics theory [153], the deformation gradient \mathbf{F} is based on an underlying displacement field \mathbf{u} : $\mathbf{F} = \frac{\partial \mathbf{x}}{\partial \mathbf{X}} = \frac{\partial (\mathbf{X} + \mathbf{u})}{\partial \mathbf{X}} = \mathbf{1} + \frac{\partial \mathbf{u}}{\partial \mathbf{X}}$. As such, the nine components of \mathbf{F} are not independent, but are actually interrelated because they are derived from the 3 components of \mathbf{u} . This condition is referred to as compatibility. Mathematically, compatibility is enforced by realizing that, as a gradient, \mathbf{F} must comply with the condition that the curl of any gradient is zero, *i.e.* $\frac{\partial F_{iK}}{\partial X_M} \varepsilon_{K MJ} = \mathbf{0}$.

In order to calculate the curl of our atomic-scale deformation gradient, we need to determine the components of its gradient, $H_{iJK}^\alpha = \frac{\partial F_{iJ}^\alpha}{\partial X_K}$. As with the derivation of \mathbf{F}^α in section 2.2, we assume that we can approximate this exact differential with the first term of a Taylor series expansion. Hence,

$$F_{iJ}^{\alpha\beta} \equiv F_{iJ}^\alpha - F_{iJ}^\beta = H_{iJK}^\alpha X_K^{\alpha\beta}. \quad (2.40)$$

As before, we move all terms to the left hand side and determine \mathbf{H}^α by minimizing the square of an error function:

$$B_{iJ}^\alpha = \sum_{\beta=1}^n \left(F_{iJ}^{\alpha\beta} - H_{iJK}^\alpha X_K^{\alpha\beta} \right)^2 \quad (2.41)$$

Thus,

$$\frac{\partial B_{ij}^\alpha}{\partial H_{ijQ}^\alpha} = 0 \rightarrow \varpi_{ijQ}^\alpha = H_{ijk}^\alpha \eta_{kQ}^\alpha, \quad (2.42)$$

and

$$H_{ijk}^\alpha = \varpi_{ijQ}^\alpha (\eta^\alpha)^{-1}_{QK} \quad (2.43)$$

where

$$\varpi_{ijQ}^\alpha \equiv \sum_{\beta=1}^n F_{ij}^{\alpha\beta} X_Q^{\alpha\beta}. \quad (2.44)$$

Equation (2.43) is very similar in form to (2.17), with ϖ^α taking the place of $\boldsymbol{\omega}^\alpha$. Similar to our earlier development, we should keep in mind that the availability of neighbors, and the number used to calculate \mathbf{H}^α , will have a direct bearing on both its ability to be determined as well as its accuracy. Also, for the case of homogeneous deformation, $\mathbf{F}^\alpha = \mathbf{F}^\beta$ and hence $\mathbf{H}^\alpha = \mathbf{0}$. The components of the curl of \mathbf{F}^α can now be estimated using the expression,

$$\rho_{iM}^\alpha = H_{ijk}^\alpha \varepsilon_{JKM}^\alpha, \quad (2.45)$$

where, for a compatible deformation field $\boldsymbol{\rho}^\alpha = \mathbf{0}$.

In the framework of plasticity theory, it is common to perform a multiplicative decomposition on the deformation gradient, for example $\mathbf{F} = \mathbf{F}^e \mathbf{F}^p$ [223, 191, 55, 108]. In this decomposition, \mathbf{F}^p refers to irreversible deformations induced by the creation and motion of material defects. In metals, the defects considered are dislocations, stacking faults and disclinations and the resulting deformations are referred to as plasticity (hence, the superscript ‘p’). \mathbf{F}^e refers to the reversible deformations caused by elastic loading of the material. Separately, \mathbf{F}^e and \mathbf{F}^p are both incompatible fields, but together they produce a total deformation gradient that obeys the compatibility condition. As first done by Steinmann [223], and later clarified by Regueiro and coworkers [191, 55], non-zero expressions can be developed that relate the curls of \mathbf{F}^e and \mathbf{F}^p to dislocation density tensors that are properly defined in an intermediate configuration that lies between the material and spatial ones (*i.e.* the “space” that is defined through the mapping of \mathbf{F}^p from the material frame or the reverse mapping of $(\mathbf{F}^e)^{-1}$ from the spatial frame).

In continuum plasticity theory, these dislocation density tensors are commonly used as, or related to, internal state variables that evolve according to an assumed constitutive relation. Hence, \mathbf{F}^e and \mathbf{F}^p can be independently determined using a history dependent numerical simulation. It is not apparent that they can be clearly defined within an atomistic simulation. For that matter, it has not yet been shown that the compatibility condition itself, $\boldsymbol{\rho} = \mathbf{F} \times \nabla = \mathbf{0}$, is valid at the atomic scale. In the next section, we present example simulations that examine both the deformation gradient and its curl.

2.5 Examples

In this section, we evaluate the expressions for \mathbf{F}^α (equation (2.17)) and $\boldsymbol{\rho}^\alpha$ (equations (2.43) and (2.45)) for several atomistic simulations that give rise to inhomogeneous deformation fields.

Specifically, we first consider a one-dimensional versions of our expressions for an atomic chain. Then, we examine simulations of dislocation nucleation at a crystal surface ledge (or step) due to an applied biaxial stretch and of nanoindentation.

2.5.1 One-dimensional atomic chain

Consider an atom α that exists along a one-dimensional atomic chain in the x_1 direction and possesses only two nearest neighbors β and γ such that $x_1^\gamma > x_1^\alpha > x_1^\beta$. For this case, ω and η each contain only a single component:

$$\omega^\alpha = x_1^{\alpha\beta} X_1^{\alpha\beta} + x_1^{\alpha\gamma} X_1^{\alpha\gamma} \quad (2.46)$$

$$\eta^\alpha = (X_1^{\alpha\beta})^2 + (X_1^{\alpha\gamma})^2 \quad (2.47)$$

If we assume that our chain has a uniform atomic spacing in the reference configuration, *i.e.* $-X_1^{\alpha\beta} = X_1^{\alpha\gamma} = a_0$, then

$$\omega^\alpha = a_0 (x_1^{\alpha\gamma} - x_1^{\alpha\beta}) = a_0 x_1^{\beta\gamma}, \quad (2.48)$$

and

$$\eta^\alpha = 2a_0^2. \quad (2.49)$$

Hence,

$$F^\alpha = \frac{\omega^\alpha}{\eta^\alpha} = \frac{x_1^{\beta\gamma}}{2a_0} = \frac{x_1^\beta - x_1^\gamma}{2a_0}. \quad (2.50)$$

Equation (2.50) is recognized to be the central difference expression of the finite difference method for a one-dimensional uniform grid. If either neighbors β or γ are missing, *i.e.* atom α is at the beginning or end of the chain, then our formula for deformation gradient becomes the forward or backward difference expression, respectively. The curl is not defined for a one dimensional analysis; however, we note that the only component of H_{iJK}^α not automatically equal to zero is for $i = J = K = 1$, and that the permutation tensor in (2.45) does equal zero in this instance since $J = K$. Hence, all components of ρ^α are equal to zero.

2.5.2 Dislocation nucleation at a crystal surface ledge

The problem of dislocation nucleation from a crystal surface ledge or step was previously examined by Zimmerman [256], among others, as an explanation for the occurrence of misfit dislocations observed in thin films. Zimmerman postulated that for a sufficient amount of bi-axial strain exerted on the film due to lattice mismatch with a substrate material, dislocations would originate from the surface ledges that naturally arise due to film deposition processes. Zimmerman explored this possibility using molecular dynamics and energy minimization simulations [256]. Similar simulations using an energy minimizing conjugate gradient method are presented in this section, with emphasis placed on characterizing the deformation gradient and curl fields before and after dislocation emission.

Figure 2.1 shows an atomic system representative of a nano-scale thin film of copper, as modeled using the embedded atom method (EAM) potential by Voter [243]. The system contains a total of approximately 56,000 atoms and is constructed such that the horizontal and thickness (out of the page) directions are $\langle 110 \rangle$ crystal directions and the vertical direction is of the $\langle 100 \rangle$ type. System dimensions are roughly 179 Å in the horizontal direction, 143 Å in the vertical direction, and 26 Å in the thickness direction. Periodic boundary conditions are used on the horizontal sides and in the thickness direction. The bottom layer of atoms is constrained against movement in the vertical direction. On the top (free) surface, atoms have been removed to create a trough that is initially five atoms wide and spans the thickness dimension. The reference configuration is obtained by performing an energy minimizing molecular static calculation using the Sandia code ParaDyn [201]. Energy minimization is accomplished using a non-linear conjugate gradient algorithm [188]. The system is then stretched in increments of 0.01% in both the horizontal and thickness directions. Figure 2.1(a) shows the system just prior to dislocation emission at a stretch of 3.77%, while Figure 2.1(b) shows the system having two dislocations that have been emitted from the surface ledges at a stretch of 3.78%. Figure 2.1 has atoms colored according to their value of slip vector, as de-

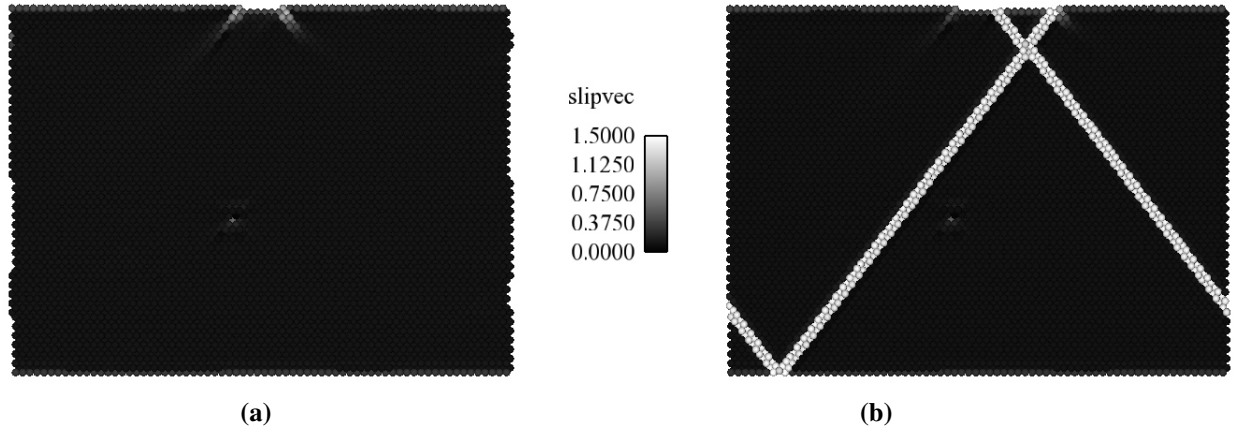


Figure 2.1. Cross-sectional view of a biaxially stretched film on a rigid substrate at (a) 3.77% stretch and (b) 3.78% stretch. Atoms are colored according to their value of slip vector.

finied in [258] by Zimmerman *et al.* We note that the emitted dislocations leave behind trails of atoms that have a slip vector magnitude near the value expected for a partial dislocation in copper, $3.615/\sqrt{6} = 1.476\text{Å}$.

Figure 2.2 shows the same system with atoms colored according to their value of F_{11} and F_{22} before and after dislocation emission. It is observed that the system contains a nearly uniform state of stretch just prior to dislocation creation ($F_{11} = F_{33} \approx 1.0377$, $F_{22} \approx 0.94$), and that this stretch is relieved in the horizontal (1) and vertical (2) directions throughout most of the crystal once the dislocations have been emitted. This is shown by the majority of atoms going to a darker shade from Figure 2.2(a) to Figure 2.2(b) (F_{11} decreases), and going from a lighter shade from Figure 2.2(c) to Figure 2.2(d) (F_{22} increases). Strain is not relieved in the thickness (3) direction

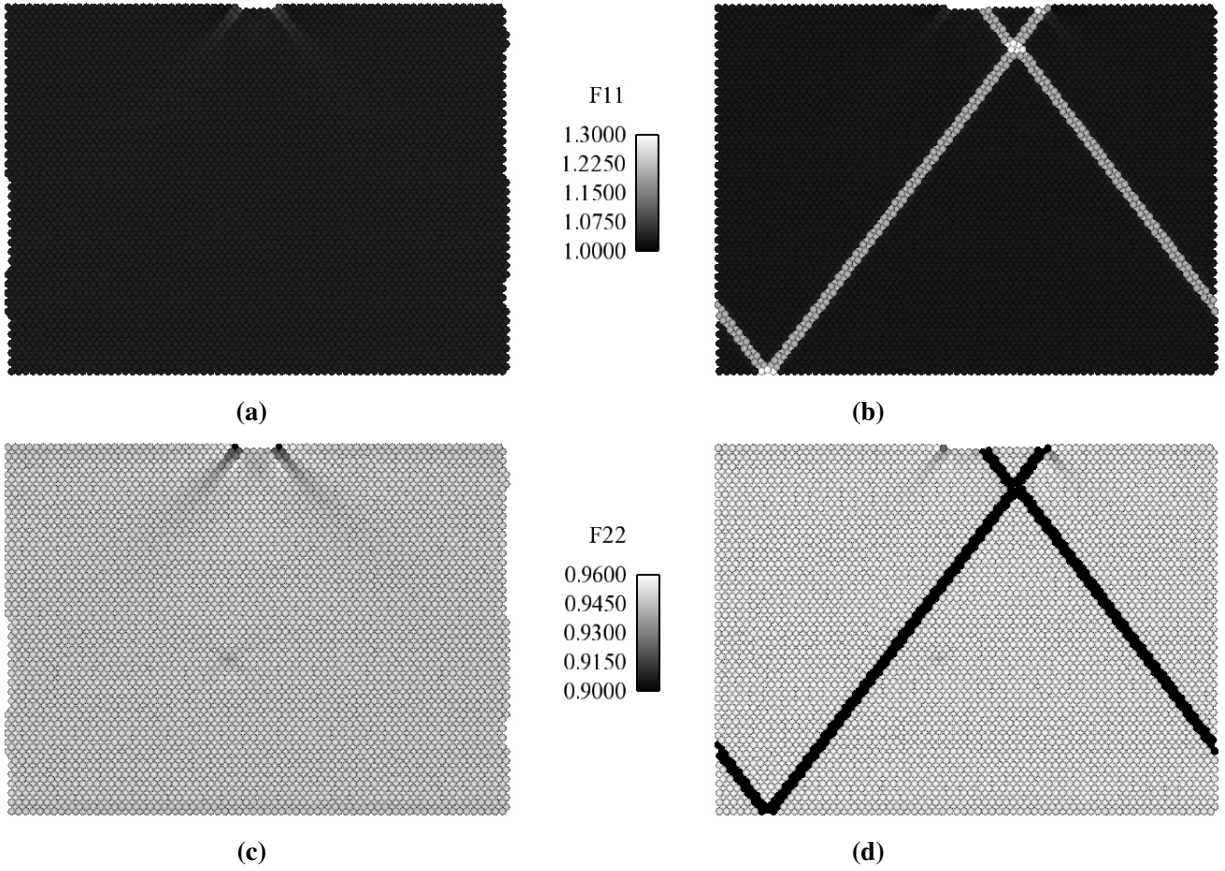


Figure 2.2. Cross-sectional view of a biaxially stretched film on a rigid substrate at (a), (c) 3.77% stretch and (b), (d) 3.78% stretch. Atoms are colored according to their value of (a), (b) F_{11} and (c), (d) F_{22} .

as the Burgers vectors of the emitted dislocations are perpendicular to that direction. It is also apparent that the stacking faults created by the emitted dislocations leave behind discontinuities in the deformation gradient field. These discontinuities also exist for the diagonal elements F_{12} and F_{21} of the deformation gradient field, as shown in Figure 2.3.

While this example shows that discontinuities exist in the atomic deformation gradient itself in the wake of created material defects, the question remains whether a compatible deformation field still exists and if the atomic scale expression we have derived reflects this. Figure 2.4 shows the 13 and 23 components of the curl tensor $\boldsymbol{\rho}$ before and after dislocation emission. These components are selected due to the two-dimensional nature of our varying deformation gradient field. While ρ_{13} and ρ_{23} are essentially zero before any material defects are created, as expected, they remain so once dislocations and stacking faults have been created. Further, it is interesting to observe that the only significantly non-zero values of these variables occurs for atoms that lie near ledges (both before and after emission), at the system's top boundary where dislocations were created, and at

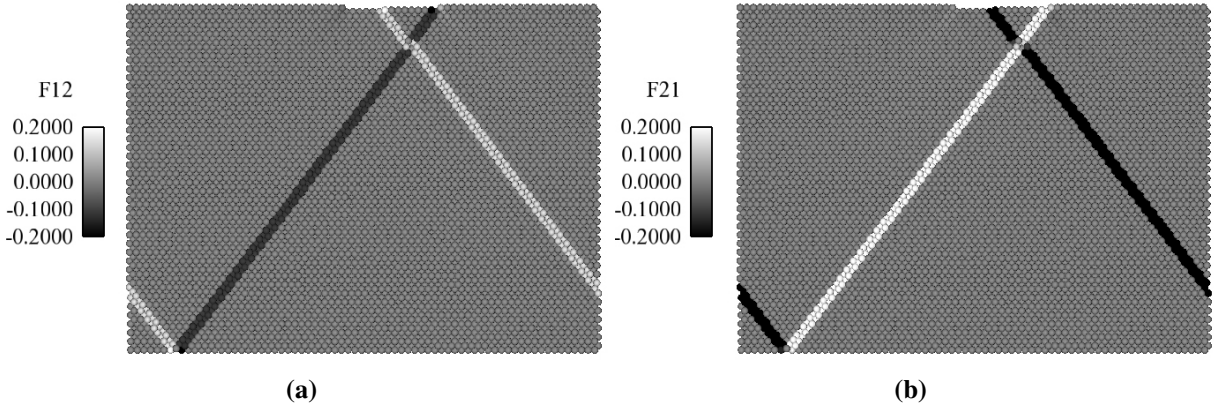


Figure 2.3. Cross-sectional view of a biaxially stretched film on a rigid substrate at 3.78% stretch. Atoms are colored according to their value of (a) F_{12} and (b) F_{21} .

the bottom boundary where dislocation cores become trapped. The stacking fault itself does not alter the zero curl of the deformation gradient.

2.5.3 Dislocation nucleation during nanoindentation

A more complex deformation field can be considered by simulating indentation by a nanometer scale indenter into a metal surface, as has been done by Kelchner *et al.* [126], Zimmerman *et al.* [258] and Rodríguez de la Fuente *et al.* [194], among others. In this section, we examine the calculated fields of \mathbf{F} and $\boldsymbol{\rho}$ for the nanoindentation simulations that appear in [194]. In that work, the authors analyzed the dislocation structures emitted during indentation of a Au(100) crystal surface by an indenter of radius equal to 40 Å. The system simulated has sides oriented along $\langle 100 \rangle$ directions and is of dimensions 204 Å x 204 Å x 122 Å. Periodic boundary conditions are used on all four side surfaces, while the bottom surface atoms are held rigidly fixed and the top surface is free. An external force field is used to emulate the nanoindenter. The indenter is lowered in displacement increments of 0.1 Å down to a total depth of 7 Å. As before in the surface ledge simulations, energy minimization is performed after each displacement increment. The EAM model for Foiles *et al.* [75] is used for the Au crystal.

Figure 2.5 shows the defect structures that form due to the indentation process. For clarity, only atoms with appreciable non-zero values of slip vector (> 0.5) are shown. Initially (Figure 2.5(a)), no discernible defect structure exists beneath the indenter; values of slip vector remain low and are appreciable only due to the highly deformed state of the material. At an indentation depth of about 4.2 Å, partial dislocations and stacking faults are created beneath the indenter, shown in Figure 2.5(b). This structure was found reversible upon elastic unloading of the material. At a larger indentation depth of 5.8 Å, an extended dislocation structure and stacking faults are created,

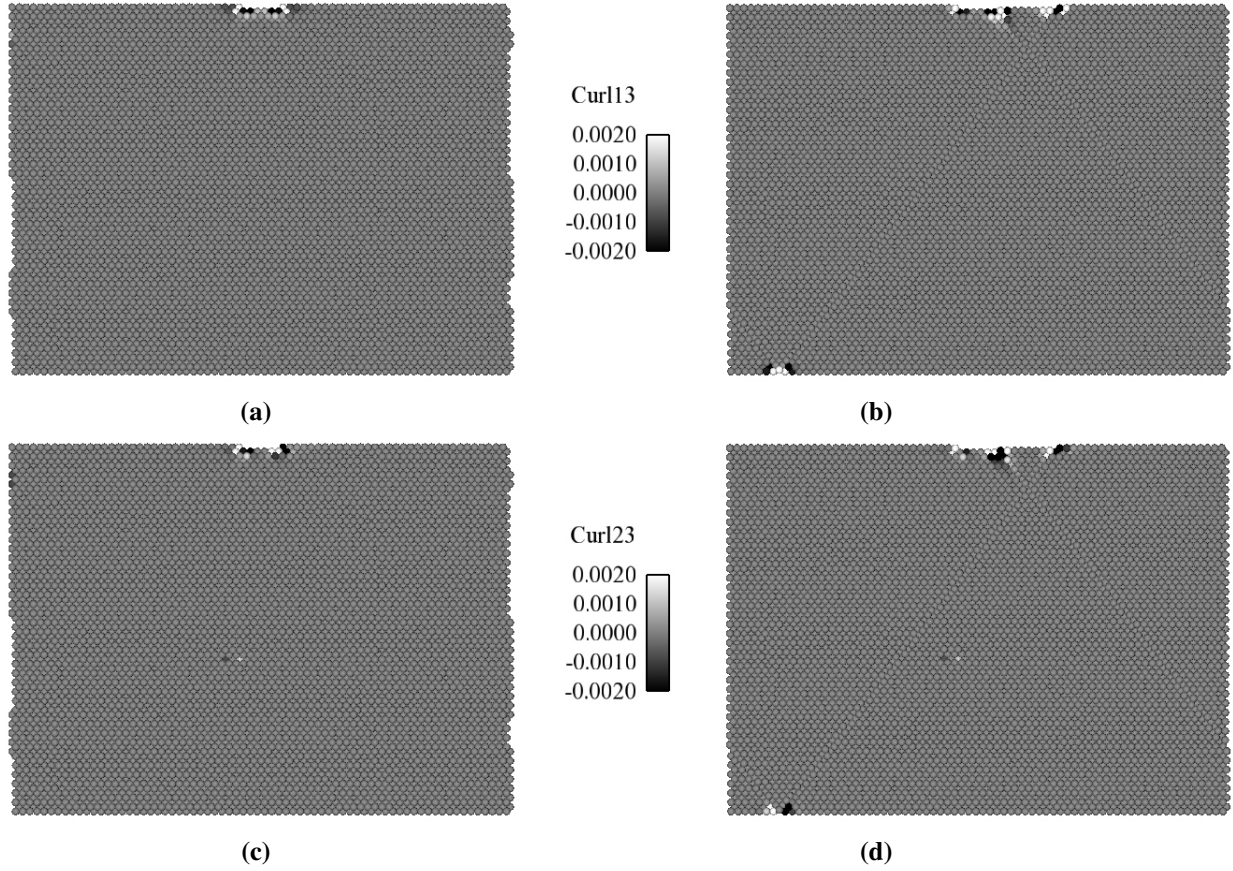


Figure 2.4. Cross-sectional view of a biaxially stretched film on a rigid substrate at (a), (c) 3.77% stretch and (b), (d) 3.78% stretch. Atoms are colored according to their value of (a), (b) ρ_{13} and (c), (d) ρ_{23} .

shown in Figure 2.5(c). This extended structure was analyzed in depth in [194], and was shown to be the origin of hillocks observed in corresponding experiments using scanning tunneling microscopy (STM). As noted in that work, this extended structure persists upon elastic unloading of the material.

Figures 2.6 and 2.7 show cross-sectional views of the crystal at the same amounts of deformation depicted in Figure 2.5, with atoms colored according to their value of F_{11} and F_{33} . For this system, indentation occurs in the $-x_3$ or $-z$ direction. As in the previous section, the deformation gradient component fields are observed to be discontinuous once material defects have been created. These discontinuities are observed within the material beneath the nanoindenter, as well as at the indentation surface. Due to the three-dimensional nature of the problem, discontinuities are also present in all components of the deformation gradient. For example, Figure 2.8 shows the system at the deformation level reached in Figure 2.5(b). In this figure, it is apparent that the defects created (partial dislocations and stacking faults) manifest as non-zero values of the off-diagonal

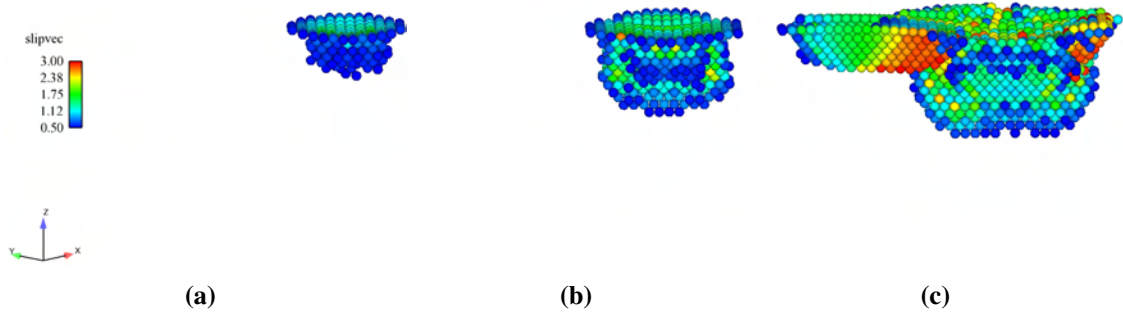


Figure 2.5. Atoms with values of slip vector > 0.5 beneath a nanoindenter: (a) prior to any defects, (b) after emission of (reversible) partial dislocation loops, (c) after emission of an (irreversible) extended dislocation/hillock structure.

components of the deformation gradient tensor.

Figures 2.9 and 2.10 show cross-sectional and top views, respectively, of the crystal at the same amounts of deformation depicted in Figure 2.5, with atoms colored according to their value of ρ_{12} .

A few features become apparent from these figures: First, non-zero values of curl are apparent at all stages of deformation for atoms that lie on the top surface both beneath, and adjacent to, the contact region with the indenter. Second, the creation of dislocation loops and stacking faults that intersect the top surface does affect the distribution of non-zero values of curl. It is particularly interesting to note that the curl fields that are visible before defects are created (Figures 2.9(a) and 2.10(a)) appear to be continuously varying in nature, whereas discontinuities in the curl fields are present once defects are present. Third, these non-zero values of curl exist only for surface atoms even once material defects have been created. In particular, the discontinuous fields of deformation gradient observed in the previous figures do not lead to non-zero values of curl; the curl remains at near zero levels for atoms in the interior of the simulation region, similar to the surface ledge simulations in the previous section. These features are consistent among the various components of $\boldsymbol{\rho}$, as shown in more detail in Figures 2.11 - 2.14.

2.6 Discussion

In section 2.4 we briefly discussed how, in the framework of plasticity theory, it is common for the deformation gradient to be multiplicatively decomposed into elastic and plastic components, \mathbf{F}^e and \mathbf{F}^p respectively. These components are individually incompatible and are used to construct a dislocation density tensor [223, 191, 55, 108]. For example, Han *et al.* [108] define the tensor

$$\tilde{\mathbf{A}} = \frac{1}{J_p} \mathbf{F}^p \text{Curl } \mathbf{F}^p = J_e (\mathbf{F}^e)^{-1} \text{curl } (\mathbf{F}^e)^{-1}, \quad (2.51)$$

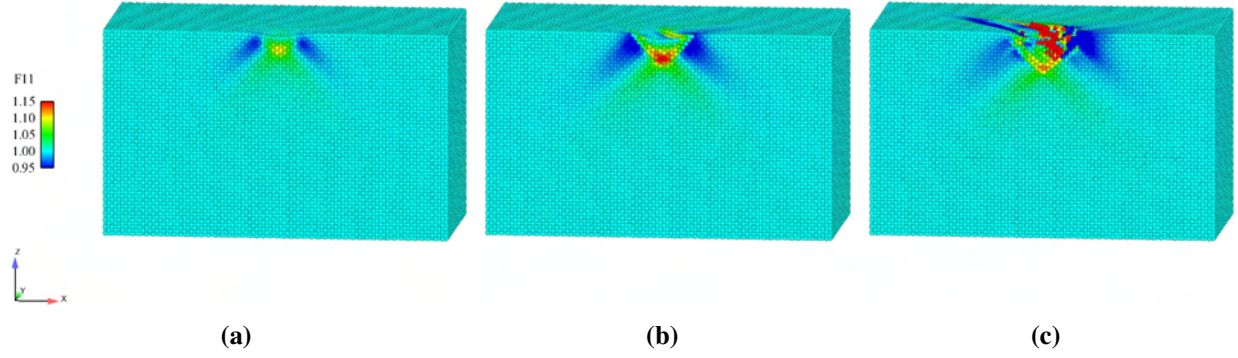


Figure 2.6. Cross-sectional view of the nanoindented atomic system at the deformation states shown in Figures 2.5(a)-2.5(c). Atoms are colored according to their value of F_{11} .

where $\text{Curl } \mathbf{F}^p = \mathbf{F}^p \times \nabla = \mathbf{F}^p \times \frac{\partial}{\partial \mathbf{x}}$ and $\text{curl}(\mathbf{F}^e)^{-1} = \frac{\partial}{\partial \mathbf{x}} \times (\mathbf{F}^e)^{-1}$. This tensor is related to the Burgers vector $\tilde{\mathbf{b}}$ and unit line tangent vector $\tilde{\boldsymbol{\xi}}$ through the relation

$$\tilde{\mathbf{A}} dv = \tilde{\boldsymbol{\xi}} \otimes \tilde{\mathbf{b}} dl, \quad (2.52)$$

where dv is an infinitesimal volume element and dl is an infinitesimal line length. In any event, it would be clearly advantageous to be able to separately quantify \mathbf{F}^e and \mathbf{F}^p in the course of analyzing an atomistic simulation.

Our earlier discussion on the meanings of \mathbf{F}^e and \mathbf{F}^p might lead one to contemplate performing an unloading simulation to atomistic systems in which defects have already formed, thereby presumably applying the inverse of the elastic deformation $(\mathbf{F}^e)^{-1}$. Figures 2.15 and 2.16 show the effect of doing this unloading to the biaxially stretched film and the nanoindented system, respectively. Both figures show that while a discontinuous deformation gradient remains within the material system once the elastic load has been removed, the resulting deformation is still compatible and produces a zero curl.

This result supports the recent work by Clayton *et al.* [47], in which these authors propose a three-term multiplicative decomposition to the deformation gradient,

$$\mathbf{F} = \mathbf{F}^e \mathbf{F}^i \mathbf{F}^p. \quad (2.53)$$

In this relation, \mathbf{F}^e now merely represents the elastic deformation due to external loading whereas the effect of the dislocations and other defects are now jointly represented by \mathbf{F}^i and \mathbf{F}^p . \mathbf{F}^p captures the deformation discontinuities introduced through dislocation cores and stacking faults and \mathbf{F}^i contains the elastic deformations created in response to the formation of these discontinuities. Individually, neither \mathbf{F}^i nor \mathbf{F}^p are compatible deformation fields, but their product is.

In addition to the issue of multiplicative decomposition of the deformation gradient, our analyses also raises a few interesting questions that merit additional discussion. First, there is some

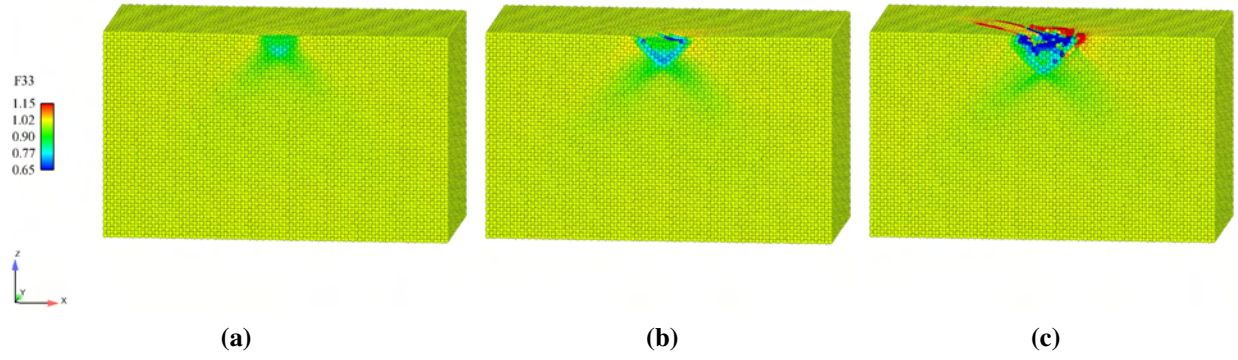


Figure 2.7. Cross-sectional view of the nanoindented atomic system at the deformation states shown in Figures 2.5(a)-2.5(c). Atoms are colored according to their value of F_{33} .

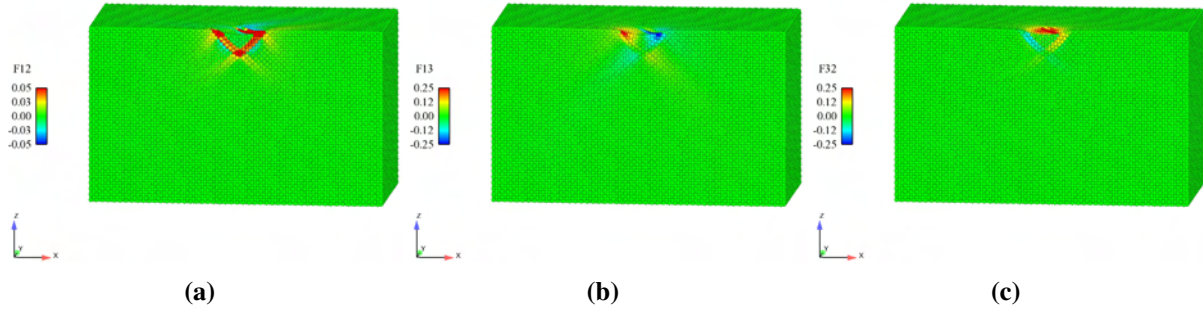


Figure 2.8. Cross-sectional view of the nanoindented atomic system at the deformation states shown in Figure 2.5(b). Atoms are colored according to their value of (a) F_{12} , (b) F_{13} , (c) F_{32} .

uncertainty with regard to the creation and propagation of full dislocations. From a materials science perspective, as full dislocations travel through a material, the material left behind possesses a perfect crystal structure. However, from a mechanics perspective, the reference configuration of this perfect crystal is unknown; there is no longer a one to one map of the deformation gradient (or any portion of it) to characteristics of the dislocations that have gone through the material. Hence, while this material would no longer have defects per se, the atomic-scale deformation gradient would still show that significant deformation has occurred. This issue also affects the slip vector calculation (as seen in Figure 2.5(c)), where it is known that atoms bordering planes on which full dislocations have slipped contain a slip vector consistent with the Burgers vectors of these dislocations.

Another question raised from our analyses pertains to the role of stacking faults. The figures in section 2.5 clearly show that although the formation of stacking faults leads to discontinuities

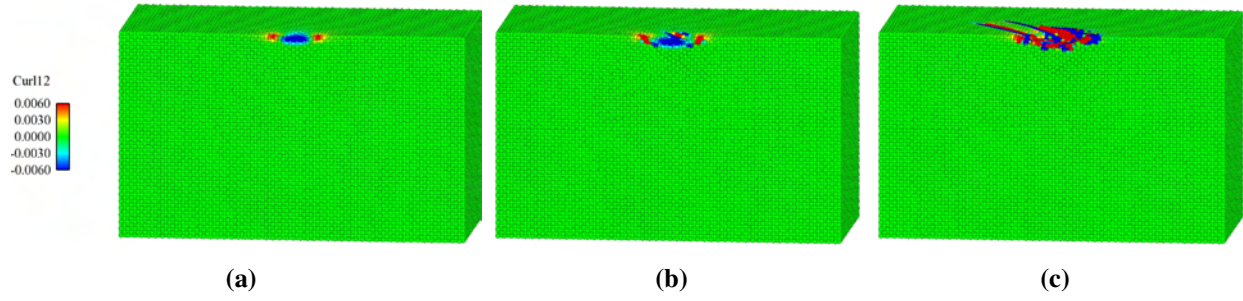


Figure 2.9. Cross-sectional view of the nanoindented atomic system at the deformation states shown in Figures 2.5(a)-2.5(c). Atoms are colored according to their value of ρ_{12} .

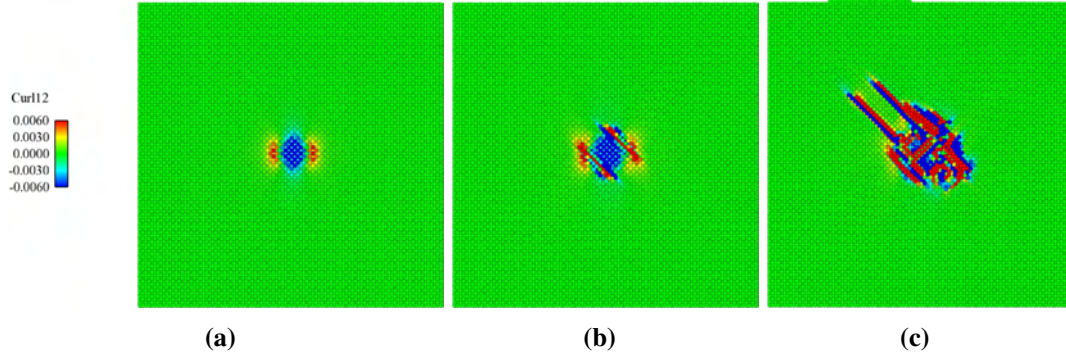


Figure 2.10. Top view of the nanoindented atomic system at the deformation states shown in Figures 2.5(a)-2.5(c). Atoms are colored according to their value of ρ_{12} .

in \mathbf{F} , these discontinuities do not produce incompatibilities that prevent the curl of \mathbf{F} from vanishing. It is assumed that, as for dislocations themselves, elastic fields are created in response to the formation of stacking faults which restore compatibility of the overall deformation. What is not clear, however, is how stacking faults contribute to dislocation density tensors (such as the one shown in equation (2.52)) as such structures no longer have a unit line tangent vector that can be identified. That stated, it may be possible to construct a meaningful tensor through a combination of the partial Burgers vector creating the stacking fault with the unit normal vector for the plane that contains the fault and the characteristic size of the fault region. Determination of these last two characteristics is not trivial and is deferred for future work.

One final concern raised by our analyses is the accuracy with which derivatives are being calculated. Our approach essentially uses a irregular grid of nearest neighbor positions to perform a variation of the finite difference method to calculate both \mathbf{F}^α , the gradient of the the deformation

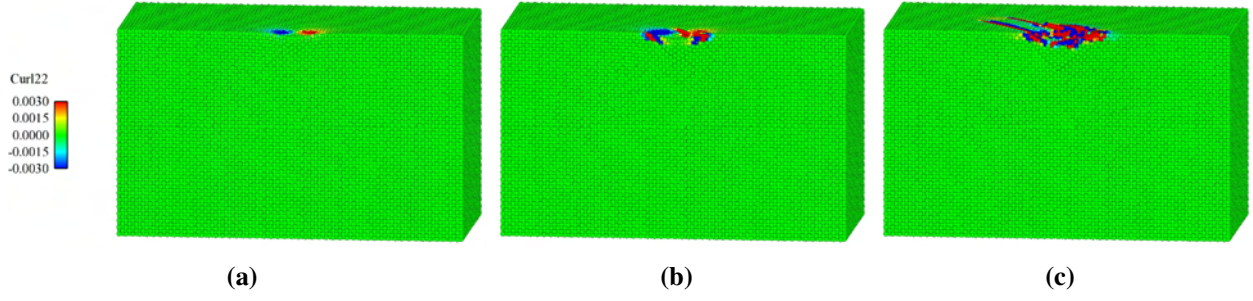


Figure 2.11. Cross-sectional view of the nanoindented atomic system at the deformation states shown in Figures 2.5(a)-2.5(c). Atoms are colored according to their value of ρ_{22} .

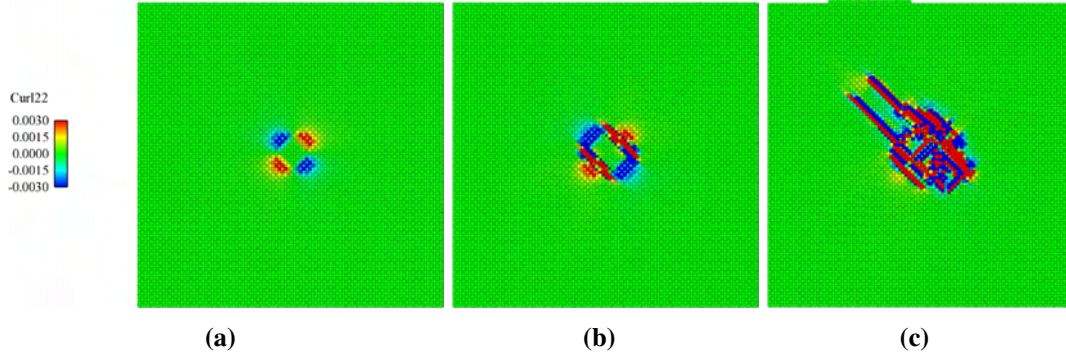


Figure 2.12. Top view of the nanoindented atomic system at the deformation states shown in Figures 2.5(a)-2.5(c). Atoms are colored according to their value of ρ_{22} .

field, and \mathbf{H}^α , the gradient of \mathbf{F}^α . It was observed that the elements of $\boldsymbol{\rho}^\alpha$, which are combinations of the components of \mathbf{H}^α , while approximately equal to zero in general were non-zero in locations where both a large amount of inhomogeneous deformation occurs and a non-bulk distribution of nearest neighbors exists. This was found to occur even for deformation states where no defects had yet been created. It is not clear whether these non-zero values of $\boldsymbol{\rho}^\alpha$ have some physical significance or a more accurate scheme for approximating derivatives needs to be used in such regions. One possible way to resolve this issue would be to apply techniques used in meshless (or mesh-free) simulation frameworks and construct continuous fields for the deformation/displacement fields. Such fields would automatically satisfy compatibility and comparison of these fields with those calculated using our expressions would quantify the accuracy of those expressions and clarify the situations under which our expressions deviate from their continuum equivalents. This exercise is deferred for future research.

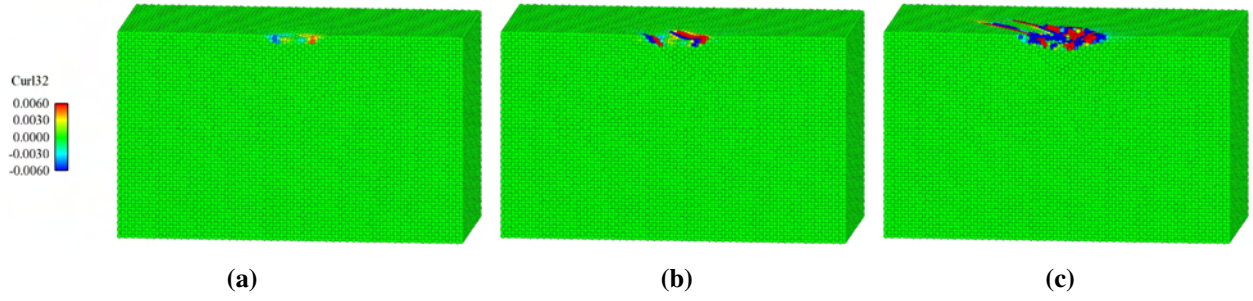


Figure 2.13. Cross-sectional view of the nanoindented atomic system at the deformation states shown in Figures 2.5(a)-2.5(c). Atoms are colored according to their value of ρ_{32} .

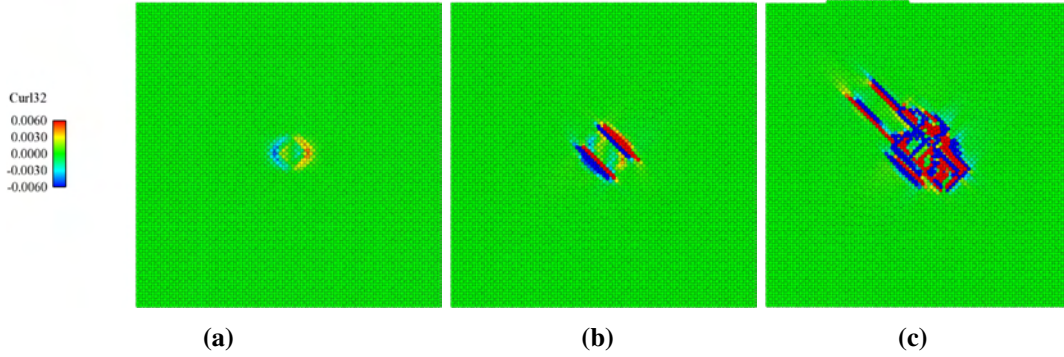


Figure 2.14. Top view of the nanoindented atomic system at the deformation states shown in Figures 2.5(a)-2.5(c). Atoms are colored according to their value of ρ_{32} .

2.7 Conclusions

In this chapter, we have developed an expression for an atomic-scale deformation gradient and have used it to analyze the deformation fields for a one-dimensional atomic chain, a biaxially stretched thin film containing a surface ledge, and a FCC metal subject to indentation loading from a nanometer-scale indenter. The analyses presented shows that the metric established here is consistent with the continuum mechanical concept of deformation gradient (which is known to have a zero curl for compatible deformations) in most instances. As would be expected, the deformation gradient expression yields discontinuities for regions of material that contain defects such as partial dislocations and stacking faults. It has been noticed that non-zero values of curl occur for atoms near loaded geometric inhomogeneities, such as those that form the ledges themselves and those beneath or adjacent to the indentation contact region. It is not yet clear whether these non-zero

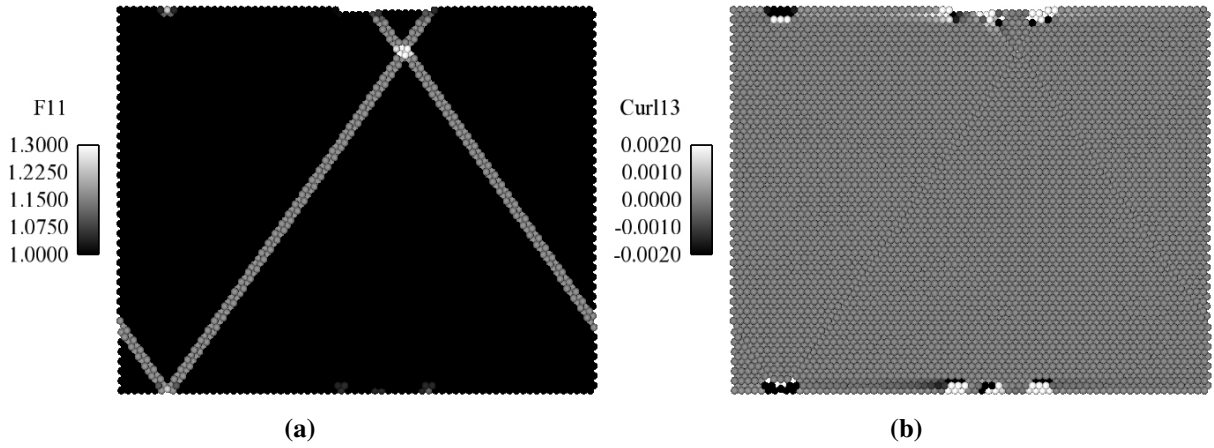


Figure 2.15. Cross-sectional view of a biaxially stretched film on a rigid substrate elastically unloaded from a stretch of 3.78%. Atoms are colored according to their value of (a) F_{11} and (b) ρ_{13} .

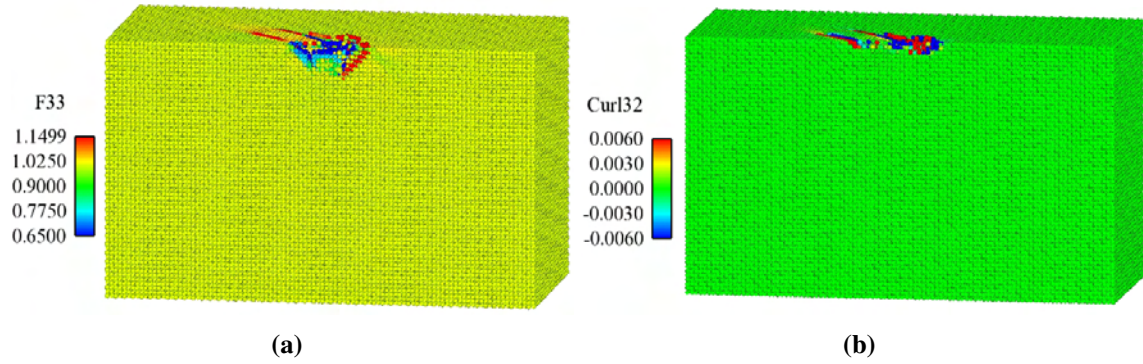


Figure 2.16. Cross-sectional view of the nanoindented atomic system elastically unloaded from the deformation state shown in Figure 2.5(c). Atoms are colored according to their value of (a) F_{33} and (b) ρ_{32} .

values can in some way be correlated to geometric information about the material defects created during deformation, and more work in this area is being pursued.

Although the concept of the multiplicative decomposition of the deformation gradient within the context of plasticity theory was discussed and considered, our simulation results show zero values of curl within material containing defects such as dislocation loops and stacking faults. As such, it appears that our atomic-scale metric captures the full, compatible deformation field that the material is subject to. As noted above, the deformation gradient expression itself produces discontinuities reflective of material that contain defects such as partial dislocations and stacking faults. These discontinuities would also exist for regions through which a full dislocation has traveled and no stacking fault or other defect remains [256]. In both instances, it may be possible to use geometric information about the material defects created (such as the Burgers vectors as quantified by the slip vector) to isolate the ‘plastic’ component of the deformation gradient \mathbf{F}^p , thereby enabling \mathbf{F}^e to also be determined. However, it is not yet apparent how to perform this decomposition and further work in this area is also warranted.

Chapter 3

A Material Frame Approach for Evaluating Continuum Variables in Atomistic Simulations

Principal Authors: Jonathan A. Zimmerman, Reese E. Jones and Jeremy A. Templeton

In this chapter, we present a material frame formulation similar to the spatial frame formulation developed by Hardy, whereby expressions for continuum mechanical variables like stress and heat flux are derived from atomic scale quantities intrinsic to molecular simulation. This formulation is ideally suited for developing an atomistic-to-continuum correspondence for solid mechanics problems. We derive expressions for the 1st Piola-Kirchhoff (P-K) stress tensor and for the material frame-based heat flux vector. Molecular dynamics simulation results for various scenarios are used to compare the stress expression with both the system virial and the Cauchy stress expression developed by Hardy. Our results show that while the P-K stress tensor appears to be missing the kinetic contribution present in the Cauchy expression, it nonetheless represents a full and consistent measure of stress. Our derivation also yields an expression for the heat flux vector, which likewise lacks the kinetic contribution appearing in its spatial frame counterpart. We also present an expanded formulation to define continuum variables from micromorphic continuum theory, which is suitable for the analysis of materials represented by directional bonding at the atomic scale.

3.1 Introduction

Continuum theory has been used for decades to analyze and predict the mechanics of materials and structures. However, as technologies shrink to the nanometer range, quantities such as stress and strain become ill defined and the application of continuum mechanics in nanomechanical frameworks becomes suspect. This brings into question whether the traditional design tools used for manufacturing can be applied to micro or nano electro-mechanical systems. And while atomic scale modeling and simulation methods, *e.g.* molecular dynamics, have provided a wealth of information for such systems, the use of such methods has not been standardized. Certainly, the use of continuum mechanics methods would be invaluable provided that clear connections between nanoscale mechanics and engineering scale analysis can be made.

The development of definitions for continuum variables that are calculable within an atomic

system has a long and rich history. In the late 19th century, Clausius [41] and Maxwell [159, 160] simultaneously developed the virial theorem (VT) to define the stress applied to the surface of a fixed volume containing interacting particles and a non-zero temperature. Since these initial efforts, there have been many subsequent works to improve on this definition [121, 238, 208, 109, 148, 197, 38, 49, 254, 252, 168, 259, 253, 169, 248], most of which have occurred in the last quarter of the 20th century and have continued into the 21st century. The articles cited here have addressed important issues such as the consistency of stress expressions with the mechanical concept of a force acting on a unit area, the validity of an atomic stress based on the VT, and the role of both spatial and time averaging. For brevity, we refer the reader to the discussions in [259] and [248] for more information.

Among these efforts is the notable work by Hardy and colleagues [109, 110, 111]. Hardy’s formalism uses a finite valued and finite ranged localization function in lieu of the Dirac delta function to establish a self-consistent manner of distributing discrete atomic contributions to thermomechanical fields. While the range and form of the localization function can be selected arbitrarily, the resulting expression for, say, the stress has a certain amount of regularity with varying sized support regions given reasonable choices for the form. Hardy’s original formulation is based on the Eulerian or spatial configuration; localization volumes are essentially control volumes fixed in space that matter occupies at a particular time. Hence, Hardy’s expressions for stress and heat flux contain both “potential” (based on derivatives of potential energy) and “kinetic” (based on the flux of momentum or energy through the localization volume) terms. The validity of kinetic contributions to stress has been an issue of some contention, and has been examined in detail by such authors as Zhou [253] and Murdoch [169].

An alternative approach that obviates the separation of potential and kinetic contributions to stress is to construct a similar formulation to Hardy’s in the Lagrangian or material frame. In the material frame, the relevant stress measure is the 1st Piola-Kirchhoff tensor \mathbf{P} , which represents the amount of current force exerted on a unit area as measured in the reference configuration. Expressions to calculate \mathbf{P} have been developed by Andia *et al.* [51, 50, 11, 12]; however, their definition is constructed as a single value representative of the average stress state for a cell with periodic boundary conditions i.e. a full system average. In addition, Andia *et al.* make the distinction between internal and external forces, separating the interactions between atoms within the cell and the interactions between atoms with “ghost” atoms located across the periodic boundaries. This distinction is not made in many of the approaches mentioned earlier, and application of this concept is not straightforward for the localization volume framework of Hardy.

Here, we present a material frame formulation similar to the one developed by Hardy for the spatial frame. This formulation is ideally suited for developing an atomistic-to-continuum correspondence for solid mechanics problems, although it does implicitly rely on a mapping from reference to current positions of what we define as material points. We derive an expression for P-K stress as well as one for heat flux. We use molecular dynamics simulations to verify our stress expression, and examine its consistency with respect to the relationship between Piola-Kirchhoff and Cauchy stresses known from continuum theory. Our results will show that while the P-K stress tensor seems to be missing the kinetic contribution that appears in the Cauchy expression, it nonetheless represents a full and consistent measure of stress. This consistency will be proven

using both mathematical arguments and a numerical example showing that the P-K and Cauchy values are nearly identical even though the kinetic portion of the Cauchy stress is a significant fraction of the total value. As a further extension of this work, we also present an expanded formulation to define continuum variables from micromorphic continuum theory. This extension relies crucially on the Lagrangian framework we develop and shows that our formulation is useful for the analysis of materials represented by directional bonding at the atomic scale.

3.2 Formulation for Standard Continuum Mechanics

3.2.1 Balance Laws

We begin by modifying Hardy's formulation for the Lagrangian or material frame. Hardy's work uses the balance equations for mass, linear momentum and energy. These are expressed in a spatial configuration as follows:

$$\frac{\partial \rho}{\partial t} + \nabla_{\mathbf{x}} \cdot (\rho \mathbf{v}) = 0 \quad (3.1)$$

$$\frac{\partial (\rho \mathbf{v})}{\partial t} = \nabla_{\mathbf{x}} \cdot (\boldsymbol{\sigma} - \rho \mathbf{v} \otimes \mathbf{v}) + \rho \mathbf{b} \quad (3.2)$$

$$\frac{\partial (\rho e)}{\partial t} = \nabla_{\mathbf{x}} \cdot (\boldsymbol{\sigma} \cdot \mathbf{v} - \rho e \mathbf{v} - \mathbf{q}) + \rho \mathbf{b} \cdot \mathbf{v} + \rho h \quad (3.3)$$

These expressions can be manipulated to use the full or material time derivative $\frac{d}{dt}$ instead of the partial time derivative $\frac{\partial}{\partial t}$:

$$\frac{d\rho}{dt} + \rho \nabla_{\mathbf{x}} \cdot \mathbf{v} = 0 \quad (3.4)$$

$$\rho \frac{d\mathbf{v}}{dt} = \nabla_{\mathbf{x}} \cdot \boldsymbol{\sigma} + \rho \mathbf{b} \quad (3.5)$$

$$\rho \frac{d\varepsilon}{dt} = \boldsymbol{\sigma} : \mathbf{L} - \nabla_{\mathbf{x}} \cdot \mathbf{q} + \rho h \quad (3.6)$$

In equations (3.1) through (3.6) the symbols ρ , \mathbf{v} , $\boldsymbol{\sigma}$, \mathbf{b} , e , ε , \mathbf{q} and h are used for mass density, velocity, Cauchy stress, body force per unit mass, total energy per unit mass, internal energy per unit mass (total energy contains contributions from both internal energy and continuum kinetic energy: $e = \varepsilon + \frac{1}{2}v^2$), heat flux and energy generation per unit mass, respectively. Also, $\nabla_{\mathbf{x}} \equiv \frac{\partial}{\partial \mathbf{x}}$

and $\mathbf{L} \equiv \nabla_{\mathbf{x}} \mathbf{v}$. Equations (3.1) - (3.3) are commonly used in fluid dynamics analyses whereas equations (3.4) - (3.6) are typically used to solve solid mechanics problems. Nevertheless, the variables used within all of these laws are defined with respect to the current/spatial configuration. These variables and equations can also be expressed with respect to the reference/material configuration:

$$\frac{d\rho_0}{dt} = 0 \quad (3.7)$$

$$\rho_0 \frac{d\mathbf{v}}{dt} = \mathbf{P} \cdot \nabla_{\mathbf{X}} + \rho_0 \mathbf{b} \quad (3.8)$$

$$\rho_0 \frac{d\varepsilon}{dt} = \mathbf{P} : \dot{\mathbf{F}} - \nabla_{\mathbf{X}} \cdot \mathbf{Q} + \rho_0 h \quad (3.9)$$

In these equations, the symbols ρ_0 , \mathbf{P} , \mathbf{b} , \mathbf{F} , \mathbf{Q} and h are used for mass density (mass per unit reference volume), 1st Piola-Kirchhoff stress (force per unit reference area), body force per unit mass, deformation gradient ($\frac{\partial \mathbf{x}}{\partial \mathbf{X}}$), reference heat flux (energy per unit reference area per unit time) and energy generation per unit mass, respectively. Also, $\dot{\mathbf{F}} \equiv \frac{d\mathbf{F}}{dt} = \mathbf{L}\mathbf{F}$. These variables are all functions of the reference configuration (\mathbf{X}) and time. The expression $\mathbf{P} \cdot \nabla_{\mathbf{X}}$ is defined to be consistent with the index notation $P_{iJ,J}$.

3.2.2 Densities and Localization

We consider a body to be a system of N atoms which are interacting with each other through some inter-atomic potential energy formulation. Each atom α is characterized by its mass m^α , its position in the reference configuration \mathbf{X}^α , its position in the current configuration \mathbf{x}^α , and its velocity $\mathbf{v}^\alpha = \frac{d\mathbf{x}^\alpha}{dt}$.

In Hardy's formulation, two views of the material system are considered. One perspective is the continuum, where quantities are point-wise functions of time and position. These quantities include mass density $\rho_0(\mathbf{X}, t)$, momentum density $\mathbf{p}_0(\mathbf{X}, t)$, and energy density $\rho_0 e(\mathbf{X}, t)$. The other perspective is that the material system contains atoms, each of which has its own mass, momentum, potential energy and kinetic energy. In order to connect the two views, Hardy uses a localization function ψ which averages the properties of the atoms, and allows many atoms to contribute to a continuum property at a specific position and time. In his original formulation, Hardy expressed ψ as a function of current position. In our derivation, we instead choose it to be a function of reference position. The three key relations analogous to Hardy's spatial forms are:

$$\rho_0(\mathbf{X}, t) = \sum_{\alpha=1}^N m^\alpha \psi(\mathbf{X}^\alpha - \mathbf{X}) \quad (3.10)$$

*In this article, a superscripted, lower-case Greek letter will denote a property associated with an atom, *e.g.* mass m^α , momentum \mathbf{p}^α , etc., whereas a subscripted, lower-case Roman letter will denote the Cartesian coordinate components of vector quantities. For example, v_i^α denotes the i -th component of the velocity vector of atom α .

$$\mathbf{p}_0(\mathbf{X}, t) = \sum_{\alpha=1}^N m^\alpha \mathbf{v}^\alpha \psi(\mathbf{X}^\alpha - \mathbf{X}) \quad (3.11)$$

$$\rho_0 e(\mathbf{X}, t) = \sum_{\alpha=1}^N \left\{ \frac{1}{2} m^\alpha (v^\alpha)^2 + \phi^\alpha \right\} \psi(\mathbf{X}^\alpha - \mathbf{X}). \quad (3.12)$$

A few important things to note:

- The localization function $\psi(\mathbf{r})$ is non-negative, *i.e.* $\psi(\mathbf{r}) \geq 0$
- $\psi(\mathbf{r})$ has dimensions of inverse volume.
- In equation (3.12), the total potential energy density of the system is expressed as the summation of individual atomic potential energies, ϕ_α .
- The velocity field \mathbf{v} is defined by the expression

$$\mathbf{v}(\mathbf{X}, t) \equiv \frac{\mathbf{p}_0(\mathbf{X}, t)}{\rho_0(\mathbf{X}, t)} = \frac{\sum_{\alpha=1}^N m^\alpha \mathbf{v}^\alpha \psi(\mathbf{X}^\alpha - \mathbf{X})}{\sum_{\alpha=1}^N m^\alpha \psi(\mathbf{X}^\alpha - \mathbf{X})}. \quad (3.13)$$

which is effectively a mass weighted average. With velocity defined in this manner, the displacement field \mathbf{u} can be defined as

$$\mathbf{u}(\mathbf{X}, t) = \frac{\sum_{\alpha=1}^N m^\alpha \mathbf{u}^\alpha \psi(\mathbf{X}^\alpha - \mathbf{X})}{\sum_{\alpha=1}^N m^\alpha \psi(\mathbf{X}^\alpha - \mathbf{X})}, \quad (3.14)$$

which is consistent, *i.e.* $\mathbf{v} = \frac{d}{dt} \mathbf{u}$, with the velocity field defined in (3.13). With a displacement field we can construct the motion of material points \mathbf{X} from reference to current configuration as a function of time. Furthermore, we can apply the differential operator $\nabla_{\mathbf{X}}$ to (3.14) to define a displacement gradient,

$$\mathbf{u} \nabla_{\mathbf{X}} = \left(\frac{\partial \mathbf{u}}{\partial \mathbf{X}} \right)^T = \frac{\sum_{\alpha=1}^N m^\alpha (\mathbf{u}^\alpha - \mathbf{u}(\mathbf{X}, t)) \otimes \nabla_{\mathbf{X}} \psi(\mathbf{X}^\alpha - \mathbf{X})}{\sum_{\alpha=1}^N m^\alpha \psi(\mathbf{X}^\alpha - \mathbf{X})}, \quad (3.15)$$

which then can be used to form a locally defined deformation gradient $\mathbf{F}(\mathbf{X}, t) = \mathbf{1} + \mathbf{u} \nabla_{\mathbf{X}}$. However, this use of Hardy localization places additional requirements on the smoothness and exact form of ψ . For example, a so-called “top hat” or radial Heaviside function that is constant and non-zero only in compact region would not produce satisfying displacement gradients.

On closing this section, we note that in his earlier works [109, 111], Hardy established two particular aspects of the localization function ψ :

1. $\psi(\mathbf{r})$ is a normalized function, thus

$$\int_{R^3} \psi(\mathbf{r}) d^3 r = 1. \quad (3.16)$$

2. $\psi(\mathbf{r})$ is regular enough to construct a bond function $B^{\alpha\beta}(\mathbf{X})$ between atoms α and β as defined by the expression

$$B^{\alpha\beta}(\mathbf{X}) \equiv \int_0^1 \psi(\lambda \mathbf{X}^{\alpha\beta} + \mathbf{X}^\beta - \mathbf{X}) d\lambda, \quad (3.17)$$

where $\mathbf{X}^{\alpha\beta} = \mathbf{X}^\alpha - \mathbf{X}^\beta$. By taking the derivative of $\psi(\lambda \mathbf{X}^{\alpha\beta} + \mathbf{X}^\beta - \mathbf{X})$ with respect to λ ,

$$\frac{\partial \psi(\lambda \mathbf{X}^{\alpha\beta} + \mathbf{X}^\beta - \mathbf{X})}{\partial \lambda} = -\mathbf{X}^{\alpha\beta} \cdot \nabla_{\mathbf{X}} \psi(\lambda \mathbf{X}^{\alpha\beta} + \mathbf{X}^\beta - \mathbf{X}), \quad (3.18)$$

and then integrating from $\lambda = 0$ to $\lambda = 1$, one obtains the identity:

$$\psi(\mathbf{X}^\alpha - \mathbf{X}) - \psi(\mathbf{X}^\beta - \mathbf{X}) = -\mathbf{X}^{\alpha\beta} \cdot \nabla_{\mathbf{X}} B^{\alpha\beta}(\mathbf{X}). \quad (3.19)$$

3.2.3 Energy and Force Assumptions

Hardy makes four key assumptions about the forms of the energies of, and forces on, the atoms in the system. The first is that the total potential energy of the system, Φ , can be considered to be the summation of individual potential energies of each atom within the system,

$$\Phi = \sum_{\alpha=1}^N \phi^\alpha. \quad (3.20)$$

Although this is not always the case, it is usually assumed true for simulations of systems governed by empirical potentials. The usual procedure for constructing ϕ^α is to partition the energies per bond to each of the constituent atoms such that the partition factors add to one.

The second assumption is that the force on any atom can be expressed by the summation

$$\mathbf{f}^\alpha \equiv -\frac{\partial \Phi}{\partial \mathbf{x}^\alpha} = \sum_{\beta \neq \alpha}^N \mathbf{f}^{\alpha\beta}. \quad (3.21)$$

This statement can always be made, although it is not always clear what the physical meaning of $\mathbf{f}^{\alpha\beta}$ is. When Φ is the summation of pair potentials, $\phi^\alpha = \frac{1}{2} \sum_{\beta \neq \alpha}^N \phi^{\alpha\beta}(x^{\alpha\beta})$ where $x^{\alpha\beta} = \|\mathbf{x}^{\alpha\beta}\|$, or for the Embedded Atom Method, $\mathbf{f}^{\alpha\beta}$ obviously means the force exerted on atom α by atom β . However, for some multi-body potentials, such as the 3-body term in the Stillinger-Weber potential [226], the meaning is not so straight-forward; nevertheless, the force partition (3.21) can be constructed. This partition is not unique; however, the selection of the specific form of $\mathbf{f}^{\alpha\beta}$ will impact the ability of our formulation to satisfy all of the continuum theory balance laws, as will be shown in subsequent sections.

The third assumption Hardy makes is that the atomic potential energies depend only on the relative inter-atomic distances, $\phi^\alpha = \phi^\alpha(x^{\alpha\beta}, x^{\alpha\gamma}, \dots, x^{\beta\gamma})$, so

$$\mathbf{f}^\alpha = - \sum_{\beta \neq \alpha}^N \sum_{\gamma=1}^N \frac{\partial \phi^\gamma}{\partial x^{\alpha\beta}} \frac{\mathbf{x}^{\alpha\beta}}{x^{\alpha\beta}}. \quad (3.22)$$

This expression includes the possibility that $\alpha = \gamma$. Again, radially-symmetric potentials such as Lennard-Jones and EAM qualify for this assumption, but it is unclear whether potential energies that depend on bond orientations do. For the 3-body term in the Stillinger-Weber potential [226], it can be shown by way of the law of cosines, which relates the bond angles to relative inter-atomic distances, that this third assumption is valid.

Finally, the fourth assumption made is that each atomic potential energy depends only on the distances between the atom under consideration and all other atoms, $\phi^\alpha = \phi^\alpha(x^{\alpha\beta}, x^{\alpha\gamma}, \dots, x^{\alpha N})$. Thus, the force between atoms α and β can be expressed as

$$\mathbf{f}^{\alpha\beta} = - \left\{ \frac{\partial \phi^\alpha}{\partial x^{\alpha\beta}} + \frac{\partial \phi^\beta}{\partial x^{\alpha\beta}} \right\} \frac{\mathbf{x}^{\alpha\beta}}{x^{\alpha\beta}} = -\mathbf{f}^{\beta\alpha}. \quad (3.23)$$

Clearly, while pair potentials and EAM qualify for this assumption, the potential of Stillinger-Weber does not since the angle between atoms α, β, γ depends on all three relative distances including $x^{\beta\gamma}$. Section 3.4 addresses this point in detail.

3.2.4 Derivation of Continuum Expressions

3.2.4.1 Balance of Mass

Inspection of equation (3.10) reveals that

$$\frac{d\rho_0}{dt} = 0$$

3.2.4.2 Balance of Linear Momentum

Starting with Hardy's expression for momentum density (3.11),

$$\begin{aligned} \rho_0 \frac{d\mathbf{v}}{dt} &= \frac{d\mathbf{p}_0}{dt} = \frac{d}{dt} \left\{ \sum_{\alpha=1}^N m^\alpha \mathbf{v}^\alpha \psi(\mathbf{X}^\alpha - \mathbf{X}) \right\} \\ &= \sum_{\alpha=1}^N m^\alpha \frac{d\mathbf{v}^\alpha}{dt} \psi(\mathbf{X}^\alpha - \mathbf{X}) \\ &= \sum_{\alpha=1}^N (\mathbf{f}^\alpha + m^\alpha \mathbf{b}^\alpha) \psi(\mathbf{X}^\alpha - \mathbf{X}), \end{aligned}$$

where we have divided the total force on atom α into the sum of total internal force \mathbf{f}^α and the body force $m^\alpha \mathbf{b}^\alpha$. The internal force term on the RHS of the above expression can be combined with Hardy's second force assumption to obtain,

$$\sum_{\alpha=1}^N \mathbf{f}^\alpha \psi(\mathbf{X}^\alpha - \mathbf{X}) = \sum_{\alpha=1}^N \sum_{\beta \neq \alpha}^N \mathbf{f}^{\alpha\beta} \psi(\mathbf{X}^\alpha - \mathbf{X}).$$

Since α and β run over all atoms in the system, they are considered dummy indices and can be switched. By doing this, and using the symmetry condition, (3.23), one obtains

$$\sum_{\alpha=1}^N \mathbf{f}^{\alpha} \psi(\mathbf{X}^{\alpha} - \mathbf{X}) = \frac{1}{2} \sum_{\alpha=1}^N \sum_{\beta \neq \alpha}^N \mathbf{f}^{\alpha\beta} \left(\psi(\mathbf{X}^{\alpha} - \mathbf{X}) - \psi(\mathbf{X}^{\beta} - \mathbf{X}) \right).$$

Using this with expression (3.19), the time derivative of the momentum density becomes

$$\rho_0 \frac{d\mathbf{v}}{dt} = \sum_{\alpha=1}^N \left(\frac{1}{2} \sum_{\beta \neq \alpha}^N \mathbf{f}^{\alpha\beta} \left(-\mathbf{X}^{\alpha\beta} \cdot \nabla_{\mathbf{X}} B^{\alpha\beta}(\mathbf{X}) \right) + m^{\alpha} \mathbf{b}^{\alpha} \psi(\mathbf{X}^{\alpha} - \mathbf{X}) \right) \quad (3.24)$$

$$= \left(-\frac{1}{2} \sum_{\alpha=1}^N \sum_{\beta \neq \alpha}^N \mathbf{f}^{\alpha\beta} \otimes \mathbf{X}^{\alpha\beta} B^{\alpha\beta}(\mathbf{X}) \right) \cdot \nabla_{\mathbf{X}} + \sum_{\alpha=1}^N m^{\alpha} \mathbf{b}^{\alpha} \psi(\mathbf{X}^{\alpha} - \mathbf{X}). \quad (3.25)$$

Comparing equation (3.25) with the continuum balance of momentum (3.8), we observe that in order for these expressions to be consistent with one another,

$$\mathbf{P} = -\frac{1}{2} \sum_{\alpha=1}^N \sum_{\beta \neq \alpha}^N \mathbf{f}^{\alpha\beta} \otimes \mathbf{X}^{\alpha\beta} B^{\alpha\beta}(\mathbf{X}), \quad (3.26)$$

and

$$\mathbf{b} = \frac{1}{\rho_0} \sum_{\alpha=1}^N m^{\alpha} \mathbf{b}^{\alpha} \psi(\mathbf{X}^{\alpha} - \mathbf{X}) = \frac{\sum_{\alpha=1}^N m^{\alpha} \mathbf{b}^{\alpha} \psi(\mathbf{X}^{\alpha} - \mathbf{X})}{\sum_{\alpha=1}^N m^{\alpha} \psi(\mathbf{X}^{\alpha} - \mathbf{X})}. \quad (3.27)$$

For pair and other central force potentials (EAM),

$$\mathbf{P} = \frac{1}{2} \sum_{\alpha=1}^N \sum_{\beta \neq \alpha}^N \left\{ \frac{\partial \phi^{\alpha}}{\partial x^{\alpha\beta}} + \frac{\partial \phi^{\beta}}{\partial x^{\alpha\beta}} \right\} \frac{\mathbf{x}^{\alpha\beta} \otimes \mathbf{X}^{\alpha\beta}}{x^{\alpha\beta}} B^{\alpha\beta}(\mathbf{X}). \quad (3.28)$$

This expression can be further simplified by splitting this expression into two terms, switching the dummy indices used in one of the terms, and using the relations $x^{\beta\alpha} = x^{\alpha\beta}$, $\mathbf{x}^{\beta\alpha} = -\mathbf{x}^{\alpha\beta}$, $\mathbf{X}^{\beta\alpha} = -\mathbf{X}^{\alpha\beta}$ and $B^{\beta\alpha} = B^{\alpha\beta}$ to obtain

$$\mathbf{P} = \sum_{\alpha=1}^N \sum_{\beta \neq \alpha}^N \frac{\partial \phi^{\beta}}{\partial x^{\alpha\beta}} \frac{\mathbf{x}^{\alpha\beta} \otimes \mathbf{X}^{\alpha\beta}}{x^{\alpha\beta}} B^{\alpha\beta}(\mathbf{X}). \quad (3.29)$$

It is interesting to note that equation (3.26) shows that \mathbf{P} is connected to the underlying atomic displacements through the inter-atomic forces $\mathbf{f}^{\alpha\beta}$. Our expression defines stress without the need to necessarily define a deformation gradient field or a hyperelastic energy function.

Also note that equation (3.26) contains only force terms on the RHS; no explicit dependence on velocity is present,[†] unlike the Cauchy stress expression

$$\boldsymbol{\sigma} = -\frac{1}{2} \sum_{\alpha=1}^N \sum_{\beta \neq \alpha}^N \mathbf{f}^{\alpha\beta} \otimes \mathbf{x}^{\alpha\beta} \tilde{B}^{\alpha\beta}(\mathbf{x}) - \sum_{\alpha=1}^N m^{\alpha} \hat{\mathbf{v}}^{\alpha} \otimes \hat{\mathbf{v}}^{\alpha} \psi(\mathbf{x}^{\alpha} - \mathbf{x}) \quad (3.30)$$

[†]The P-K expression (3.26) also differs from the Cauchy expression (3.30) in that it gives a zero value for the somewhat degenerate case of a non-interacting gas regardless of temperature.

from the Eulerian analysis done by Hardy [109, 111]. The relative velocity $\hat{\mathbf{v}}^\alpha$ is defined

$$\hat{\mathbf{v}}^\alpha \equiv \mathbf{v}^\alpha - \mathbf{v}(\mathbf{x}, t) . \quad (3.31)$$

and has the property

$$\sum_{\alpha=1}^N m^\alpha \hat{\mathbf{v}}^\alpha \psi(\mathbf{x}^\alpha - \mathbf{x}) = \mathbf{0} \quad (3.32)$$

by virtue of the Eulerian analogue of the definition (3.13). Note that \tilde{B} is the bond function expressed in units of inverse current/deformed volume rather than units of inverse reference/undeformed volume.

If we consider the continuum Piola transformation[‡] from 1st P-K stress to Cauchy stress, $\boldsymbol{\sigma} = \frac{1}{J} \mathbf{P} \cdot \mathbf{F}^T$ where $J \equiv \det \mathbf{F}$, we produce

$$\frac{1}{J} \mathbf{P} \mathbf{F}^T = -\frac{1}{J} \sum_{\alpha=1}^N \sum_{\beta \neq \alpha}^N \frac{1}{2} \mathbf{f}^{\alpha\beta} \otimes \mathbf{X}^{\alpha\beta} B^{\alpha\beta}(\mathbf{X}) \cdot \mathbf{F}^T . \quad (3.33)$$

In order to simplify this equation, the position of each atom can be decomposed into a rigid body translation and/or rotation, $\mathbf{d}(t)$, a homogeneous deformation, *i.e.* every atom experiences the same deformation gradient \mathbf{F} , plus a perturbation[§] due to thermal fluctuations and/or inhomogeneities in the deformation field,

$$\mathbf{x}^\alpha = \mathbf{d}(t) + \mathbf{F}(\mathbf{X}, t) \cdot \mathbf{X}^\alpha + \check{\mathbf{x}}^\alpha(t) \quad (3.34)$$

so that $\check{\mathbf{x}}^\alpha$ contains higher order terms in \mathbf{X}^α . We define $\boldsymbol{\Xi}^\alpha = \mathbf{X}^\alpha - \mathbf{X}$ where now \mathbf{X} satisfies

$$\mathbf{X} = \frac{1}{\rho_0} \sum_{\alpha=1}^N m^\alpha \mathbf{X}^\alpha \psi(\mathbf{X}^\alpha - \mathbf{X}) \quad (3.35)$$

without loss of generality, in order to write

$$\mathbf{v}^\alpha = \dot{\mathbf{d}} + \dot{\mathbf{F}} \cdot \mathbf{X}^\alpha + \dot{\check{\mathbf{x}}}^\alpha = \dot{\mathbf{d}} + \dot{\mathbf{F}} \cdot \mathbf{X} + \dot{\mathbf{F}} \cdot \boldsymbol{\Xi}^\alpha + \dot{\check{\mathbf{x}}}^\alpha \quad (3.36)$$

and then to identify

$$\hat{\mathbf{v}}^\alpha = \dot{\mathbf{F}} \boldsymbol{\Xi}^\alpha + \dot{\check{\mathbf{x}}}^\alpha \quad (3.37)$$

with the part of the velocity \mathbf{v}^α that satisfies (3.32). Since $\mathbf{x}^{\alpha\beta} = \mathbf{F} \cdot \mathbf{X}^{\alpha\beta} + \check{\mathbf{x}}^{\alpha\beta}$, we can recast (3.33) as

$$\begin{aligned} \frac{1}{J} \mathbf{P} \mathbf{F}^T &= -\frac{1}{2} \sum_{\alpha=1}^N \sum_{\beta \neq \alpha}^N \mathbf{f}^{\alpha\beta} \otimes (\mathbf{x}^{\alpha\beta} - \check{\mathbf{x}}^{\alpha\beta}) \tilde{B}^{\alpha\beta}(\mathbf{X}) \\ &= -\frac{1}{2} \sum_{\alpha=1}^N \sum_{\beta \neq \alpha}^N \mathbf{f}^{\alpha\beta} \otimes \mathbf{x}^{\alpha\beta} \tilde{B}^{\alpha\beta}(\mathbf{X}) + \frac{1}{2} \sum_{\alpha=1}^N \sum_{\beta \neq \alpha}^N \mathbf{f}^{\alpha\beta} \otimes \check{\mathbf{x}}^{\alpha\beta} \tilde{B}^{\alpha\beta}(\mathbf{X}) \end{aligned} \quad (3.38)$$

[‡]The Piola transform $d\mathbf{a} = \det(\mathbf{F}) \mathbf{F}^{-T} d\mathbf{A}$ relates the change in directed area elements from reference to current configuration by way of the deformation gradient.

[§]Here we are assuming that (3.34) represents a decomposition by exact mass-weighted L2 projection. Equation (3.14), on the other-hand, represents an approximate projection; Section 3.3.1 will provide a more detailed discussion of this fact.

If we now examine the special case of a full system average, such that $\Psi = B^{\alpha\beta} = 1/V$ with V the being the system volume, and more importantly the atoms in the support of Ψ do not change, the Piola transformed \mathbf{P} from (3.38) becomes

$$\frac{1}{J}\mathbf{P}\mathbf{F}^T = -\frac{1}{2V} \sum_{\alpha=1}^N \sum_{\beta \neq \alpha}^N \mathbf{f}^{\alpha\beta} \otimes \mathbf{x}^{\alpha\beta} + \frac{1}{2V} \sum_{\alpha=1}^N \sum_{\beta \neq \alpha}^N \mathbf{f}^{\alpha\beta} \otimes \dot{\mathbf{x}}^{\alpha\beta}, \quad (3.39)$$

and the Cauchy stress (3.30) becomes

$$\boldsymbol{\sigma} = -\frac{1}{2V} \sum_{\alpha=1}^N \sum_{\beta \neq \alpha}^N \mathbf{f}^{\alpha\beta} \otimes \mathbf{x}^{\alpha\beta} - \frac{1}{V} \sum_{\alpha=1}^N m^{\alpha} \hat{\mathbf{v}}^{\alpha} \otimes \hat{\mathbf{v}}^{\alpha}. \quad (3.40)$$

The difference between these two expressions, (3.39) and (3.40), is

$$\begin{aligned} \frac{1}{J}\mathbf{P}\mathbf{F}^T - \boldsymbol{\sigma} &= \frac{1}{V} \sum_{\alpha=1}^N \frac{1}{2} \sum_{\beta \neq \alpha}^N \mathbf{f}^{\alpha\beta} \otimes \dot{\mathbf{x}}^{\alpha\beta} + \sum_{\alpha=1}^N m^{\alpha} \hat{\mathbf{v}}^{\alpha} \otimes \hat{\mathbf{v}}^{\alpha} \\ &= \frac{1}{V} \sum_{\alpha=1}^N (\mathbf{f}^{\alpha} \otimes \dot{\mathbf{x}}^{\alpha} + m^{\alpha} \hat{\mathbf{v}}^{\alpha} \otimes \hat{\mathbf{v}}^{\alpha}) \end{aligned} \quad (3.41)$$

after using the identity

$$\begin{aligned} \frac{1}{2} \sum_{\alpha=1}^N \sum_{\beta \neq \alpha}^N \mathbf{f}^{\alpha\beta} \otimes \dot{\mathbf{x}}^{\alpha\beta} &= \frac{1}{2} \sum_{\alpha=1}^N \sum_{\beta \neq \alpha}^N \mathbf{f}^{\alpha\beta} \otimes (\dot{\mathbf{x}}^{\alpha} - \dot{\mathbf{x}}^{\beta}) \\ &= \frac{1}{2} \left(\sum_{\alpha=1}^N \sum_{\beta \neq \alpha}^N \mathbf{f}^{\alpha\beta} \otimes \dot{\mathbf{x}}^{\alpha} + \sum_{\alpha=1}^N \sum_{\beta \neq \alpha}^N \mathbf{f}^{\beta\alpha} \otimes \dot{\mathbf{x}}^{\beta} \right) = \sum_{\alpha=1}^N \mathbf{f}^{\alpha} \otimes \dot{\mathbf{x}}^{\alpha} \end{aligned} \quad (3.42)$$

which results simply from the manipulation of dummy indices, the definition (3.21) and the symmetry condition (3.23). In the absence of a body force ($\mathbf{f}^{\alpha} = m^{\alpha} \dot{\mathbf{v}}^{\alpha}$) then

$$\begin{aligned} \left\langle \sum_{\alpha=1}^N \mathbf{f}^{\alpha} \otimes \dot{\mathbf{x}}^{\alpha} \right\rangle &= \left\langle \frac{d}{dt} \sum_{\alpha=1}^N m^{\alpha} \mathbf{v}^{\alpha} \otimes \dot{\mathbf{x}}^{\alpha} \right\rangle - \left\langle \sum_{\alpha=1}^N m^{\alpha} \mathbf{v}^{\alpha} \otimes \ddot{\mathbf{x}}^{\alpha} \right\rangle = - \left\langle \sum_{\alpha=1}^N m^{\alpha} \mathbf{v}^{\alpha} \otimes \ddot{\mathbf{x}}^{\alpha} \right\rangle \\ &= - \left\langle \sum_{\alpha=1}^N m^{\alpha} (\mathbf{v} + \hat{\mathbf{v}}^{\alpha}) \otimes (\hat{\mathbf{v}}^{\alpha} - \dot{\mathbf{F}} \boldsymbol{\Xi}^{\alpha}) \right\rangle \\ &= - \left\langle \mathbf{v} \otimes \sum_{\alpha=1}^N m^{\alpha} \hat{\mathbf{v}}^{\alpha} \right\rangle + \left\langle \mathbf{v} \otimes \dot{\mathbf{F}} \sum_{\alpha=1}^N m^{\alpha} \boldsymbol{\Xi}^{\alpha} \right\rangle \\ &\quad - \left\langle \sum_{\alpha=1}^N m^{\alpha} \hat{\mathbf{v}}^{\alpha} \otimes \hat{\mathbf{v}}^{\alpha} \right\rangle + \left\langle \sum_{\alpha=1}^N m^{\alpha} \hat{\mathbf{v}}^{\alpha} \otimes \dot{\mathbf{F}} \boldsymbol{\Xi}^{\alpha} \right\rangle \\ &= - \left\langle \sum_{\alpha=1}^N m^{\alpha} \hat{\mathbf{v}}^{\alpha} \otimes \hat{\mathbf{v}}^{\alpha} \right\rangle + \left\langle \sum_{\alpha=1}^N m^{\alpha} \hat{\mathbf{v}}^{\alpha} \otimes \dot{\mathbf{F}} \boldsymbol{\Xi}^{\alpha} \right\rangle \end{aligned} \quad (3.43)$$

given the definition of $\boldsymbol{\Xi}^{\alpha}$, and the fact that time averages $\langle \bullet \rangle$ of exact differentials of bounded quantities are zero. The identity (3.43) is a version of the virial theorem and if we assume a steady

state, where $\dot{\mathbf{F}}$ must be zero, then we have

$$\left\langle \sum_{\alpha=1}^N \mathbf{f}^\alpha \otimes \mathbf{x}^\alpha \right\rangle + \left\langle \sum_{\alpha=1}^N m^\alpha \mathbf{v}^\alpha \otimes \mathbf{v}^\alpha \right\rangle = \mathbf{0}, \quad (3.44)$$

This does not mean that \mathbf{F} is necessarily fixed at the identity; rather, it means that (3.44) is satisfied only for truly steady systems. Now we can return to (3.41) and show that the (time-averaged) Hardy expressions for the transformed 1st Piola-Kirchhoff stress and the Cauchy stress are consistent:

$$\left\langle \frac{1}{J} \mathbf{P} \mathbf{F}^T - \boldsymbol{\sigma} \right\rangle = \frac{1}{V} \left\langle \sum_{\alpha=1}^N \mathbf{f}^\alpha \otimes \check{\mathbf{x}}^\alpha + m^\alpha \hat{\mathbf{v}}^\alpha \otimes \hat{\mathbf{v}}^\alpha \right\rangle = \mathbf{0} \quad (3.45)$$

by use of (3.44).

The main difficulty in extending this proof to the general case is that the atoms contributing to the sums in (3.30) and (3.33) may be different depending on how atoms are flowing through space. Moreover, mapping the reference frame function $B^{\alpha\beta}(\mathbf{X})$ to the spatial $\tilde{B}^{\alpha\beta}(\mathbf{x})$ is non-trivial. Rather than attempting to do this analysis, in Section 3.3 we will explore how the expression for \mathbf{P} in equation (3.26) performs for cases where the thermal fluctuations are significant, and compare our results with expectations from continuum mechanics and with the usual Hardy definition for Cauchy stress.

3.2.4.3 Balance of Energy

Starting with the Lagrangian expression for the system energy (3.12),

$$\begin{aligned} \frac{d(\rho_0 e)}{dt} &= \rho_0 \frac{de}{dt} = \frac{d}{dt} \left\{ \sum_{\alpha=1}^N \left\{ \frac{1}{2} m^\alpha (v^\alpha)^2 + \phi^\alpha \right\} \psi(\mathbf{X}^\alpha - \mathbf{X}) \right\} \\ &= \sum_{\alpha=1}^N \left\{ m^\alpha \left(\frac{d\mathbf{v}^\alpha}{dt} \cdot \mathbf{v}^\alpha \right) + \frac{d\phi^\alpha}{dt} \right\} \psi(\mathbf{X}^\alpha - \mathbf{X}) \\ &= \sum_{\alpha=1}^N \left\{ (\mathbf{f}^\alpha + m^\alpha \mathbf{b}^\alpha) \cdot \mathbf{v}^\alpha + \frac{d\phi^\alpha}{dt} \right\} \psi(\mathbf{X}^\alpha - \mathbf{X}). \end{aligned}$$

By imposing the second and third force assumptions, this simplifies to

$$\rho_0 \frac{de}{dt} = \nabla_{\mathbf{X}} \cdot \left(\sum_{\alpha=1}^N \sum_{\beta \neq \alpha}^N \sum_{\gamma \neq \alpha}^N \left(\frac{\partial \phi^\gamma}{\partial x^{\alpha\beta}} \frac{\mathbf{x}^{\alpha\beta}}{x^{\alpha\beta}} \cdot \mathbf{v}^\alpha \right) \mathbf{X}^{\alpha\gamma} B^{\alpha\gamma}(\mathbf{X}) \right) + \sum_{\alpha=1}^N m^\alpha \mathbf{b}^\alpha \cdot \mathbf{v}^\alpha \psi(\mathbf{X}^\alpha - \mathbf{X}). \quad (3.46)$$

Equation (3.46) can be further simplified by using the fourth force assumption:

$$\rho_0 \frac{de}{dt} = \nabla_{\mathbf{X}} \cdot \left(\sum_{\alpha=1}^N \sum_{\beta \neq \alpha}^N \sum_{\gamma \neq \alpha}^N \left(\frac{\partial \phi^\gamma}{\partial x^{\alpha\beta}} (\delta_{\alpha\gamma} + \delta_{\beta\gamma}) \frac{\mathbf{x}^{\alpha\beta}}{x^{\alpha\beta}} \cdot \mathbf{v}^\alpha \right) \mathbf{X}^{\alpha\gamma} B^{\alpha\gamma}(\mathbf{X}) \right) + \sum_{\alpha=1}^N m^\alpha \mathbf{b}^\alpha \cdot \mathbf{v}^\alpha \psi(\mathbf{X}^\alpha - \mathbf{X}) \quad (3.47)$$

$$= \nabla_{\mathbf{X}} \cdot \left(\sum_{\alpha=1}^N \sum_{\beta \neq \alpha}^N \left(\frac{\partial \phi^\beta}{\partial x^{\alpha\beta}} \frac{\mathbf{x}^{\alpha\beta}}{x^{\alpha\beta}} \cdot \mathbf{v}^\alpha \right) \mathbf{X}^{\alpha\beta} B^{\alpha\beta}(\mathbf{X}) \right) + \sum_{\alpha=1}^N m^\alpha \mathbf{b}^\alpha \cdot \mathbf{v}^\alpha \psi(\mathbf{X}^\alpha - \mathbf{X}) \quad (3.48)$$

To proceed further, we separate atomic motion from continuum motion in two ways. First, we split the atomic velocities \mathbf{v}^α into the continuum velocity $\mathbf{v}(\mathbf{X}, t)$ and a relative velocity $\hat{\mathbf{v}}^\alpha(\mathbf{X}, t)$ as in (3.31). Next we recall that earlier we recognized that the total energy, e contains contributions from both internal energy and continuum-scale kinetic energy. We separate this using the expression $e = \varepsilon + \frac{1}{2}v^2$:

$$\rho_0 \frac{de}{dt} = \rho_0 \frac{d\varepsilon}{dt} + \rho_0 \frac{d\mathbf{v}}{dt} \cdot \mathbf{v} \quad (3.49)$$

Application of (3.49) to the LHS of (3.48) and (3.31) to the RHS of (3.48) produces:

$$\begin{aligned} \rho_0 \frac{d\varepsilon}{dt} + \rho_0 \frac{d\mathbf{v}}{dt} \cdot \mathbf{v} &= \nabla_{\mathbf{X}} \cdot \left(\sum_{\alpha=1}^N \sum_{\beta \neq \alpha}^N \left(\frac{\partial \phi^\beta}{\partial x^{\alpha\beta}} \frac{\mathbf{x}^{\alpha\beta}}{x^{\alpha\beta}} \cdot (\mathbf{v} + \hat{\mathbf{v}}^\alpha) \right) \mathbf{X}^{\alpha\beta} B^{\alpha\beta}(\mathbf{X}) \right) \\ &\quad + \sum_{\alpha=1}^N m^\alpha \mathbf{b}^\alpha \cdot (\mathbf{v} + \hat{\mathbf{v}}^\alpha) \psi(\mathbf{X}^\alpha - \mathbf{X}) \\ &= \nabla_{\mathbf{X}} \cdot (\mathbf{v} \cdot \mathbf{P}) + \nabla_{\mathbf{X}} \cdot \left(\sum_{\alpha=1}^N \sum_{\beta \neq \alpha}^N \left(\frac{\partial \phi^\beta}{\partial x^{\alpha\beta}} \frac{\mathbf{x}^{\alpha\beta}}{x^{\alpha\beta}} \cdot \hat{\mathbf{v}}^\alpha \right) \mathbf{X}^{\alpha\beta} B^{\alpha\beta}(\mathbf{X}) \right) \\ &\quad + \rho_0 \mathbf{b} \cdot \mathbf{v} + \sum_{\alpha=1}^N m^\alpha \mathbf{b}^\alpha \cdot \hat{\mathbf{v}}^\alpha \psi(\mathbf{X}^\alpha - \mathbf{X}) \\ &= (\nabla_{\mathbf{X}} \mathbf{v}) : \mathbf{P} + \mathbf{v} \cdot (\mathbf{P} \cdot \nabla_{\mathbf{X}} + \rho_0 \mathbf{b}) + \nabla_{\mathbf{X}} \cdot \left(\sum_{\alpha=1}^N \sum_{\beta \neq \alpha}^N \left(\frac{\partial \phi^\beta}{\partial x^{\alpha\beta}} \frac{\mathbf{x}^{\alpha\beta}}{x^{\alpha\beta}} \cdot \hat{\mathbf{v}}^\alpha \right) \mathbf{X}^{\alpha\beta} B^{\alpha\beta}(\mathbf{X}) \right) \\ &\quad + \sum_{\alpha=1}^N m^\alpha \mathbf{b}^\alpha \cdot \hat{\mathbf{v}}^\alpha \psi(\mathbf{X}^\alpha - \mathbf{X}) \end{aligned}$$

Using the balance of linear momentum equation (3.8), this simplifies to

$$\rho_0 \frac{d\varepsilon}{dt} = (\nabla_{\mathbf{X}} \mathbf{v}) : \mathbf{P} + \nabla_{\mathbf{X}} \cdot \left(\sum_{\alpha=1}^N \sum_{\beta \neq \alpha}^N \left(\frac{\partial \phi^\beta}{\partial x^{\alpha\beta}} \frac{\mathbf{x}^{\alpha\beta}}{x^{\alpha\beta}} \cdot \hat{\mathbf{v}}^\alpha \right) \mathbf{X}^{\alpha\beta} B^{\alpha\beta}(\mathbf{X}) \right) + \sum_{\alpha=1}^N m^\alpha \mathbf{b}^\alpha \cdot \hat{\mathbf{v}}^\alpha \psi(\mathbf{X}^\alpha - \mathbf{X}). \quad (3.50)$$

Since the $\nabla_{\mathbf{X}}$ and $\frac{d}{dt}$ operators are commutative, $\nabla_{\mathbf{X}} \mathbf{v} = \dot{\mathbf{F}}$. Hence,

$$\rho_0 \frac{d\varepsilon}{dt} = \mathbf{P} : \dot{\mathbf{F}} - \nabla_{\mathbf{X}} \cdot \mathbf{Q} + \rho_0 h, \quad (3.51)$$

where

$$\mathbf{Q} = - \sum_{\alpha=1}^N \sum_{\beta \neq \alpha}^N \left(\frac{\partial \phi^\beta}{\partial x^{\alpha\beta}} \frac{\mathbf{x}^{\alpha\beta}}{x^{\alpha\beta}} \cdot \hat{\mathbf{v}}^\alpha \right) \mathbf{X}^{\alpha\beta} B^{\alpha\beta}(\mathbf{X}) \quad (3.52)$$

is the heat flux as expressed in the reference configuration. We note that like the expression for stress this expression contains only a potential term and not a kinetic term, unlike the spatial frame heat flux expression derived by Hardy [196].

Comparison of (3.50) with (3.51) also produces the relation defining energy generation per unit mass:

$$h = \frac{1}{\rho_0} \sum_{\alpha=1}^N m^\alpha \mathbf{b}^\alpha \cdot \hat{\mathbf{v}}^\alpha \psi(\mathbf{X}^\alpha - \mathbf{X}) = \frac{\sum_{\alpha=1}^N m^\alpha \mathbf{b}^\alpha \cdot \hat{\mathbf{v}}^\alpha \psi(\mathbf{X}^\alpha - \mathbf{X})}{\sum_{\alpha=1}^N m^\alpha \psi(\mathbf{X}^\alpha - \mathbf{X})} \quad (3.53)$$

We note that for a uniform body force field this term simplifies to zero. This term would be also be negligible for a non-uniform body force field for which significant variations in the field are defined at larger length scales than the localization volume size associated with ψ . However, for situations where \mathbf{b} truly varies from atom to atom, it appears that the work done by the field against the relative velocity field generates energy. The term h may also be related to other energy source terms that can be introduced into the atomic energy, although none are present in the above analysis.

Hardy and colleagues also derived [196] an expression for temperature by considering the equipartition theorem and the kinetic energy associated with atomic velocities relative to the velocity of the continuum at a spatial point,

$$T(\mathbf{x}, t) = \frac{1}{3k_B} \frac{\sum_{\alpha=1}^N m^\alpha (\hat{v}^\alpha)^2 \psi(\mathbf{x}^\alpha - \mathbf{x})}{\sum_{\alpha=1}^N \psi(\mathbf{x}^\alpha - \mathbf{x})}, \quad (3.54)$$

which is a simple weighted average as opposed to the volume average in (3.10) for example. Here k_B is Boltzman's constant. Similarly, we can define a temperature field using our densities expressed in the reference configuration,

$$T(\mathbf{X}, t) = \frac{1}{3k_B} \frac{\sum_{\alpha=1}^N m^\alpha (\hat{v}^\alpha)^2 \psi(\mathbf{X}^\alpha - \mathbf{X})}{\sum_{\alpha=1}^N \psi(\mathbf{X}^\alpha - \mathbf{X})}. \quad (3.55)$$

3.3 Evaluation of Material Frame Expressions

In this section, we examine the behavior of our P-K stress expression for several molecular dynamics simulations. These simulations will confirm that our expression for P-K stress is consistent with both the virial stress and the Cauchy stress expression defined by Hardy. All of our simulations involve system of copper modeled using the EAM potential by Foiles *et al.* [75]. This potential creates an equilibrium, face-centered-cubic crystal of Cu of lattice parameter equal to 3.615 Å at zero temperature. For molecular dynamics simulations, a timestep of 0.001 ps is used.

Calculations are done using specialized routines written for ParaDyn [201] and the Large-scale Atomic/Molecular Massively Parallel Simulator (LAMMPS)[200], molecular simulation codes developed at Sandia National Laboratories. The calculations in ParaDyn are done using a single point in the center of system with a spherical localization volume of radius 15 Å and a quartic polynomial localization function. The calculations in LAMMPS are done using a single element mesh that encloses the whole system in its undeformed, zero temperature configuration. The localization function consists of the multiple of three linear shape functions, one for each orthogonal direction. Since the system is subject to periodic boundary conditions, the mesh actually contains only a

single node (the point at which continuum variables are evaluated), and both ψ and $B^{\alpha\beta}$ equal the quantity V_0^{-1} (where V_0 is the system size at zero temperature and deformation) for every atom and bond, respectively.

For the analyses presented in this section, the choice of the zero temperature, undeformed system is used as our material configuration. The rationale for this selection will be elaborated upon in the subsequent discussion section.

3.3.1 Construction of fields

The Hardy formalism has much in common with the data reduction and smoothing technique called Moving Least Squares (MLS) [136]. For instance, (3.14) can be seen as the solution to a weighted least-squares problem using a lumped version of the least squares matrix [245]. Although effective, it becomes expensive to recalculate, say (3.14) at every sample point of interest in a simulation with large spatial variations. Instead we choose to sample on a collection of points $I = 1..M$ and then use finite element shape functions $N_I(\mathbf{X})$ to construct an approximation to the field of interest, for example the displacement field

$$\mathbf{u}(\mathbf{X}, t) = \sum_{I=1}^M \mathbf{u}_I(t) N_I(\mathbf{X}) = \sum_{I=1}^M \frac{\sum_{\alpha=1}^N m^\alpha \mathbf{u}^\alpha \psi(\mathbf{X}^\alpha - \mathbf{X}_I)}{\sum_{\alpha=1}^N m^\alpha \psi(\mathbf{X}^\alpha - \mathbf{X}_I)} N_I(\mathbf{X}) \quad (3.56)$$

where we can define and store the matrices $\Psi_{I\alpha} = \Psi(\mathbf{x}_\alpha - \mathbf{x}_I)$ and $B_{I\alpha\beta} = B^{\alpha\beta}(\mathbf{x}_I)$. This also gives us a second way to estimate the displacement gradient (3.15) by taking the gradient of the interpolation $N_I(\mathbf{X})$.

3.3.2 Stress for a constrained finite temperature system

In this and the following section, we present simulations of a system containing 4,000 atoms (10 x 10 x 10 unit cells), where periodic boundary conditions are enforced on all sides of the simulation box. We first examine the situation where our system is constrained to remain at the reference volume, but heated to a finite, non-zero temperature. In this instance $\mathbf{F} = \mathbf{1}$ and $J = 1$; hence, the values of 1st P-K and Cauchy stress should coincide. Unless otherwise stated, the results presented here refer to the continuum stress measures evaluated for the single point in the Para-Dyn simulations. The results obtained in the LAMMPS simulations were similar in all cases, with stress values much closer in agreement to the system virial as one would expect since all atoms and bonds contribute uniformly in that analysis.

Figure 3.1 shows the variation of instantaneous pressure with time for a system that is heated to 100 K. ‘Pressure’ in this case refers to the negative of the hydrostatic stress for each stress measure, *i.e.* the P-K pressure equals $-\frac{1}{3}\text{Trace}(\mathbf{P}) = -\frac{1}{3}P_{kk}$, the Cauchy pressure equals $-\frac{1}{3}\text{Trace}(\boldsymbol{\sigma})$ and the same relation is used for the system virial. The distributions of P-K and Cauchy nearly perfectly overlap with one another, and both distributions are centered around the virial distribution. Also,

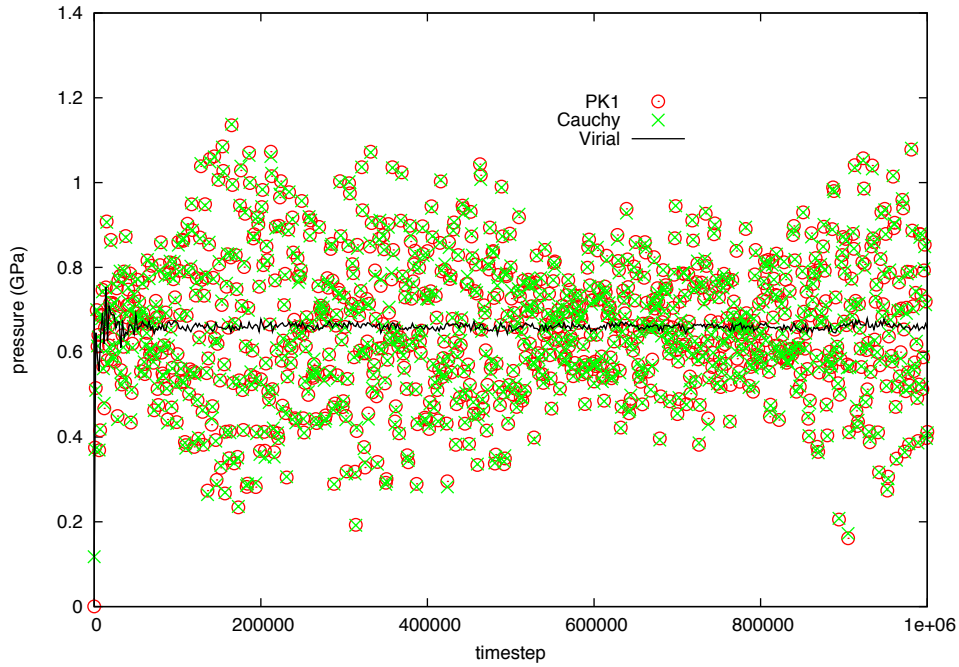


Figure 3.1. Variation of instantaneous pressure with time for a constrained system at 100 K.

since the volume of material used for evaluation is a subset of the whole system, the variations from the mean value are larger in magnitude for both P-K and Cauchy pressures as compared with the variation observed in the virial. It is interesting to note that while the mathematical analysis presented in the previous section showed that the P-K and Cauchy stress expressions agree with one another (through the $J\boldsymbol{\sigma} = \mathbf{P}\mathbf{F}^T$ transformation) only if a long time average is taken, Figure 3.1 shows that close agreement also exists for stress evaluations at specific instants in time.

The agreement between our stress measures and the virial is easier to see by using the data in Figure 3.1 to calculate cumulative time averaged pressures. Figure 3.2 shows the variation of these time averaged pressures with time for the same duration, 10^6 timesteps. This figure shows that the time averaged pressures essentially converge within 500,000 timesteps (0.5 ns), and that the converged values of P-K, Cauchy and virial pressures are very close to one another. This agreement is more clearly shown in Table 3.1, which compares the converged values of P-K pressure (after 10^6 timesteps) with the virial pressure for both the ParaDyn analysis shown in Figure 3.2 and the LAMMPS analysis. We note in Table 3.1 that the percent difference between P-K and virial pressures is much less than 1%, and that this difference is smaller for the LAMMPS analysis (which uses all atoms in the system) than for the ParaDyn analysis.

Table 3.1 also shows the converged time averaged pressures for systems heated to 300 K and 675 K, values approximately 22% and 50%, respectively, of the melting temperature of copper. It can be seen that the agreement between P-K pressure and the virial remains excellent even at

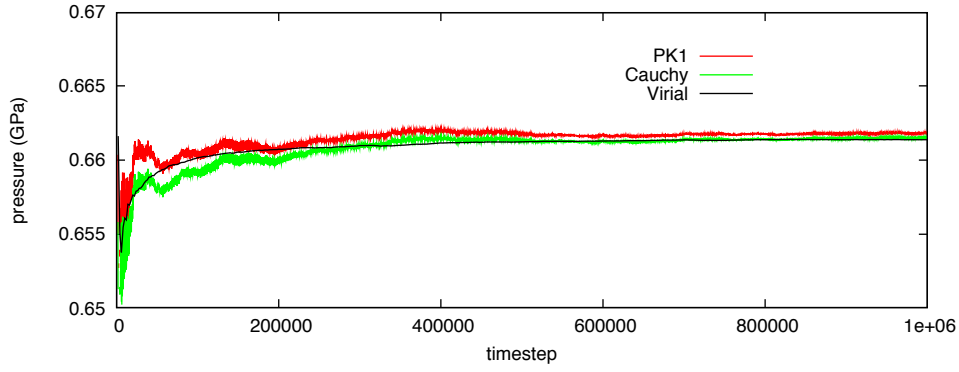


Figure 3.2. Variation of time averaged pressure with time for a constrained system at 100 K.

Table 3.1. Time averaged pressures after 10^6 timesteps for constrained volume simulations.

Temperature (K)	Point / Mesh	virial pressure (GPa)	P-K pressure (GPa)	% difference
100	Point	0.6613775	0.6618136	0.06653
100	Mesh	0.6614168	0.6613937	-0.00350
300	Point	1.944335	1.944422	0.00448
300	Mesh	1.944465	1.944413	-0.00264
675	Point	4.335872	4.334868	-0.02316
675	Mesh	4.335840	4.336577	0.01699

these high temperatures and stress levels. This close agreement is emphasized in Figure 3.3, which graphically shows the variation of pressure with increasing temperature for this constrained system. It was also observed that, at the highest temperature simulated of 675 K, agreement between the P-K pressure and the virial improved if a longer time average is taken.

The above analyses show that our derived expression for P-K stress is consistent with a thermo-mechanical measure of stress despite the fact that it contains only a potential and not a kinetic term, unlike the Cauchy stress expression derived by Hardy. The small level of error between P-K stress and the system virial noted in Table 3.1 is much smaller than the amount of stress attributed to the kinetic part of Hardy's Cauchy stress or the virial itself. That kinetic part is approximately equal to 0.1169 GPa, 0.3507 GPa and 0.7891 GPa for the temperatures considered (100 K, 300 K and 675 K, respectively). As shown in Table 3.1, these values are significant fractions of the total virial pressure listed for each temperature. Nevertheless, the P-K pressure estimate is in close agreement with the total virial pressure. This confirms our earlier mathematical argument that the expression for P-K stress (3.26) captures both the potential and the kinetic portions of the Cauchy stress.

For the situation of a constrained volume, the values of P-K and Cauchy stress were not antic-

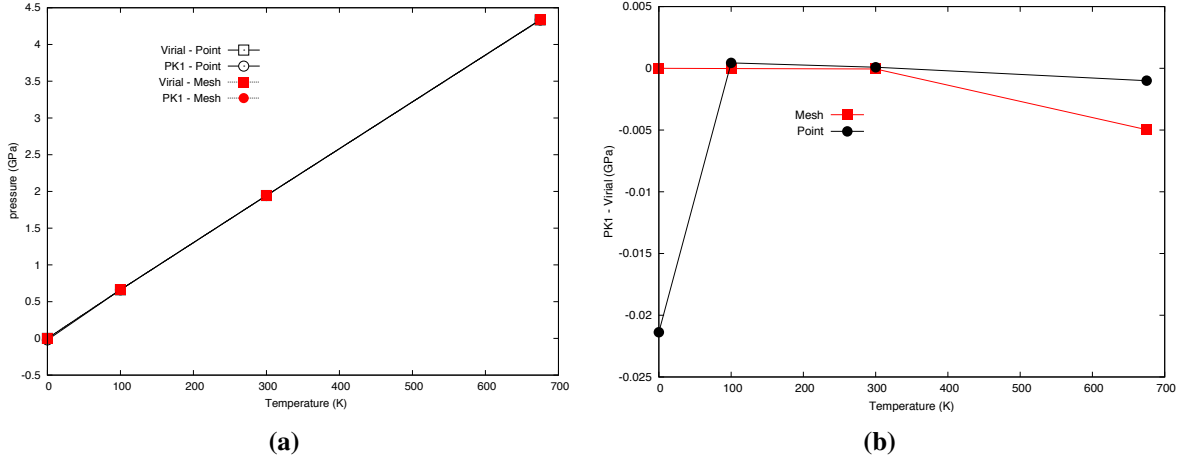


Figure 3.3. (a) Time averaged pressures after 10^6 timesteps for constrained volume simulations performed at various temperatures. (b) Differences between P-K and virial measures of pressure at various temperatures.

ipated to differ by any significant amount. This expected outcome was confirmed by our simulations. However, we have yet to consider a case for which deformation occurs and the two values should be related by the Piola transform $\boldsymbol{\sigma} = \frac{1}{J}\mathbf{P}\mathbf{F}^T$. This is done in the next section.

3.3.3 Finite temperature deformation

We now examine the scenario where our system starts out at zero temperature, is heated over the course of 10^6 timesteps (1 ns) to a finite temperature but allowed to expand in order to maintain a condition of zero pressure, is equilibrated for an additional 10^6 timesteps at that non-zero temperature and zero pressure, and is then triaxially stretched an additional 1 or 5% from this expanded state. Figure 3.4 shows the variation of the hydrostatic stresses for \mathbf{P} , $\boldsymbol{\sigma}$ (as measured using the original Hardy formulation) and the system virial for a stretch of 1% after equilibration at 100 K. In this section, we plot and discuss only values measured from the simulations performed with ParaDyn; however, values calculated with LAMMPS were virtually the same. Figure 3.4 shows large variations in the instantaneous estimates of \mathbf{P} and $\boldsymbol{\sigma}$ as compared with the system virial. It is observed that this variation stays within a limit of approximately $\pm 15\%$ of the long time average after 400,000 timesteps (0.4 ns) have elapsed. As expected, the values of \mathbf{P} are slightly higher than the values of $\boldsymbol{\sigma}$ and the virial. Figure 3.5 compares the transformed stress $\frac{1}{J}\mathbf{P}\mathbf{F}^T$ to the Cauchy stress and virial, and demonstrates that the transformed P-K stress is in close correspondence with the Cauchy measure. In this figure, we see that the distributions of transformed Piola-Kirchhoff stress and Cauchy stress nearly perfectly overlap with one another, and both distributions are centered around the virial distribution. Again, we note that although the mathematical analysis presented

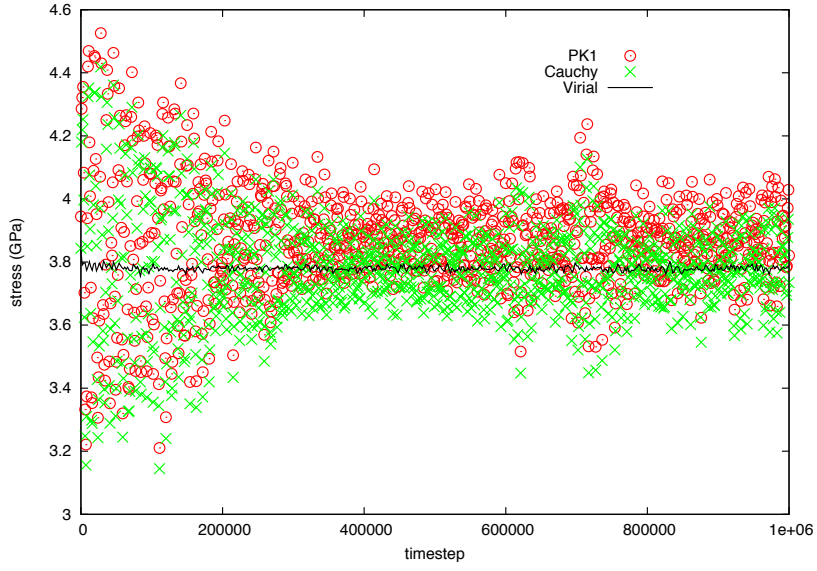


Figure 3.4. Variation of instantaneous hydrostatic stress measures with time for a stretch of 1% after equilibration at 100 K and zero pressure.

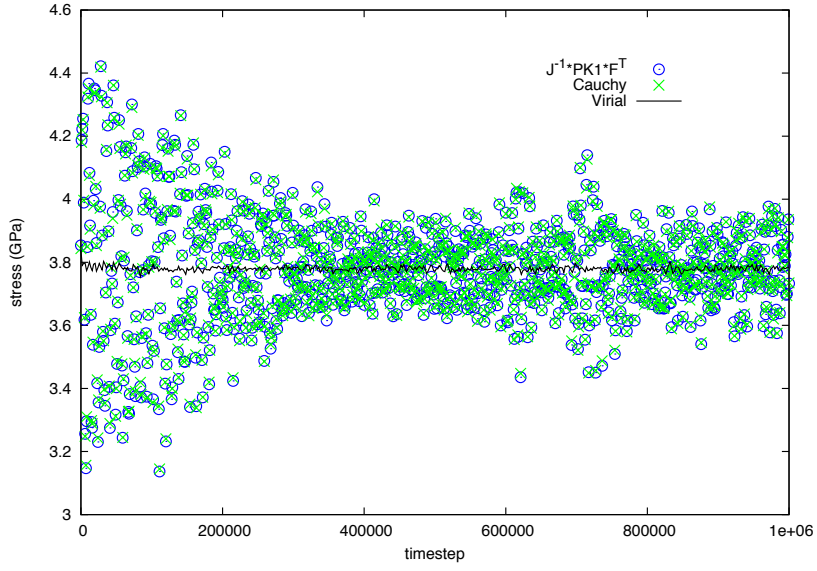


Figure 3.5. Variation of instantaneous hydrostatic stress measures with time for a stretch of 1% after equilibration at 100 K and zero pressure.

in the previous section showed that the P-K and Cauchy stress expressions agree with one another only if a long time average is taken, Figure 3.5 shows that close agreement also exists for stress evaluations at specific instants in time.

Figure 3.6 shows the cumulative time averages of the four stress values (\mathbf{P} , σ , virial and transformed \mathbf{P}). It is observed that the system virial approaches its long time average in a short amount

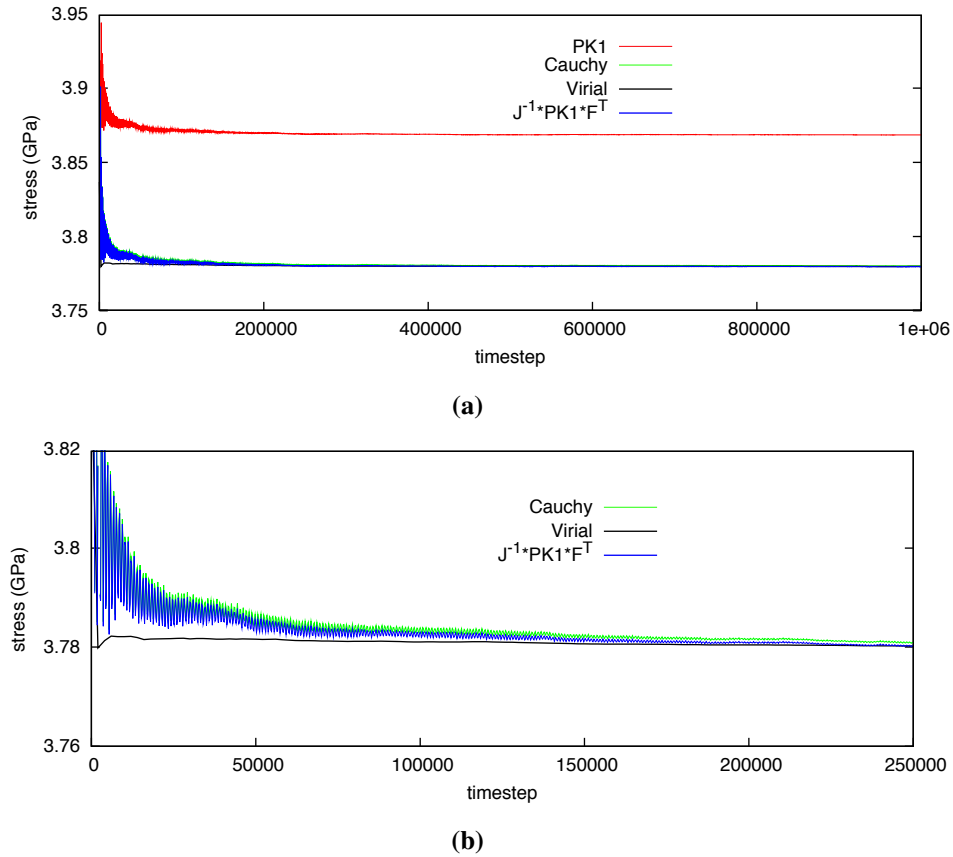


Figure 3.6. (a) Variation of time averaged hydrostatic stress measures with time for a stretch of 1% after equilibration at 100 K and zero pressure. (b) Close-up of (a) for the first 250,000 timesteps.

of time, $\sim 20,000$ timesteps (0.02 ns), and that both the Cauchy stress and transformed P-K stress approach this same value within approximately 200,000 timesteps (0.2 ns). The P-K stress also approaches its own long time average within this same amount of time, and the value is appropriately higher. Values of these long time averages are listed in Table 3.2. These results clearly show a negligible difference between the transformed P-K stress value and the virial of the system. Thus, we again conclude that our derived expression is consistent with the continuum relation between Cauchy and P-K stress despite the absence of a kinetic term.

In addition to our simulation results for the case of 1% stretch at 100 K, Table 3.2 also shows

Table 3.2. Time averaged stresses after 10^6 timesteps for simulations of a heated and triaxially strained system. Here, ‘% difference’ refers to the difference between transformed P-K stress (the 6th column) and the virial.

T (K)	Point / Mesh	total strain	virial (GPa)	P-K (GPa)	$\frac{1}{J}(\mathbf{P-K})\mathbf{F}^T$	% difference
0	Point	0.01	3.876275	3.954033	3.876123	-0.00394
0	Mesh	0.01	3.876273	3.954190	3.876277	-0.00009
0	Point	0.05	14.70036	16.20713	14.70035	-0.00009
0	Mesh	0.05	14.70036	16.20710	14.70032	-0.00026
100	Point	0.01168	3.779846	3.868452	3.779658	-0.00499
100	Mesh	0.01163	3.782552	3.871040	3.782538	-0.00038
100	Point	0.05169	14.26000	15.77334	14.26085	0.00597
300	Point	0.01495	3.581698	3.690054	3.582124	0.01190
300	Mesh	0.01495	3.579387	3.687273	3.579472	0.002386
300	Point	0.05515	13.30167	14.80901	13.30142	-0.00186
675	Point	0.02174	3.194773	3.334715	3.194304	-0.01469
675	Mesh	0.02174	3.194821	3.303813	3.164701	-0.94278
675	Point	0.06221	11.33258	12.78735	11.33345	0.00768

results for systems heated to 300 K and 675 K for stretches of both 1% and 5% following thermal equilibration at zero pressure. We observe that in all cases, the difference between the hydrostatic virial stress and the hydrostatic transformed P-K stress is very small with a difference of, at most, 1%. The results for the point evaluation of P-K hydrostatic stress (the ParaDyn simulations) are graphically shown in Figures 3.7(a) and (b), for the 1% and 5% stretches respectively. These figures reveal that at higher temperatures a lower amount of stress is produced within the system. This result can be attributed to the temperature dependence of the elastic constants that softens (decreases) their value with increasing temperature.

3.3.4 Tensile stretching of a center-cracked body

The previous two examples show that our formulation enables the calculation of 1st Piola-Kirchhoff stress that is consistent with estimates of the Cauchy stress, either using the system virial or the original Hardy formulation. However, these examples only produce a single value of stress representative of the entire system, *i.e.* systems subjected to a homogeneous deformation state. The strength of our formulation lies in its ability to produce a field of spatially varying values of stress for cases where an inhomogeneous deformation is produced. In this section, we examine a system containing a center crack and compare the inhomogeneous stress fields that arise due to tensile stretching.

Our system consists 9,840 atoms, approximately 20 x 20 x 6 unit cells, that contains a center crack 4 unit cells wide in the center. We acknowledge that this is a small and highly constrained

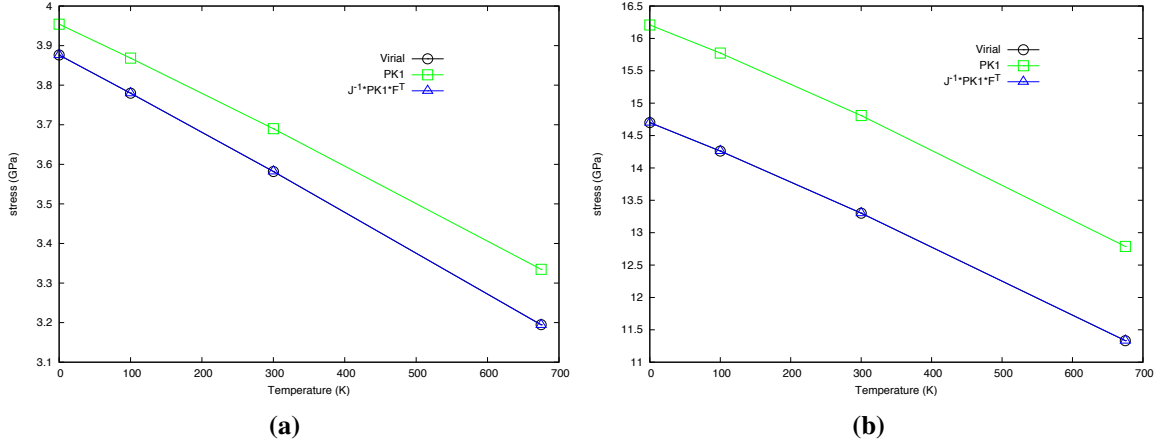


Figure 3.7. Variation of time-averaged hydrostatic stress measures after 10^6 timesteps with temperature for a stretch of (a) 1%, and (b) 5 % after equilibration at that temperature.

system, and use it only as a means to show our ability to estimate spatially varying stress fields. The crack is created by excluding interactions between atoms above the center-plane of the system (and within the 4 unit cell width) and atoms below the center-plane. Periodic boundary conditions are used in the horizontal and thickness directions, while atoms within 2 unit cells of the system's upper and lower boundaries are controlled by prescribing a fixed velocity of ± 0.1 Å/ps, respectively. Given the dimensions of our system, this produces an approximate strain rate of initial value $3.46 \times 10^{-3} \text{ ps}^{-1} = 3.46 \times 10^9 \text{ sec}^{-1}$. Before inducing the stretching, our system is relaxed using a conjugate gradient minimization algorithm in order to relax the upper, lower and crack boundaries and set the reference configuration.

To calculate stress at material points, we use LAMMPS with the previously discussed method where material points are nodes, the localization volume consists of rectangular parallelepipeds, and localization functions are again multiples of three linear shape functions, one for each orthogonal direction. For this system, our mesh consists of $10 \times 15 \times 1 = 150$ elements where our mesh extends beyond the atomic system in the vertical direction by 2.5 unit cells at both the upper and lower boundaries. In our analysis, both P-K and Cauchy stress are calculated, the latter using the original formulation by Hardy.

Figure 3.8 shows the displaced atoms, colored by the values of the component u_y of their displacement vector, as well as u_y displacement field evaluated at nodes and interpolated through elements, for the center-cracked body vertically stretched by approximately 6.9%. The left portion of Figure 3.8 clearly shows that the nodal values of displacement agree with the values of nearby atoms, while the right portion displays a displacement field consistent with expectations from fracture mechanics. It is interesting to note that the normalization present in equation (3.14) enables approximately correct values of u_y to be calculated at nodes bordering the boundaries of the atomic system, even though 1/2 of each node's localization volume is empty. This is because

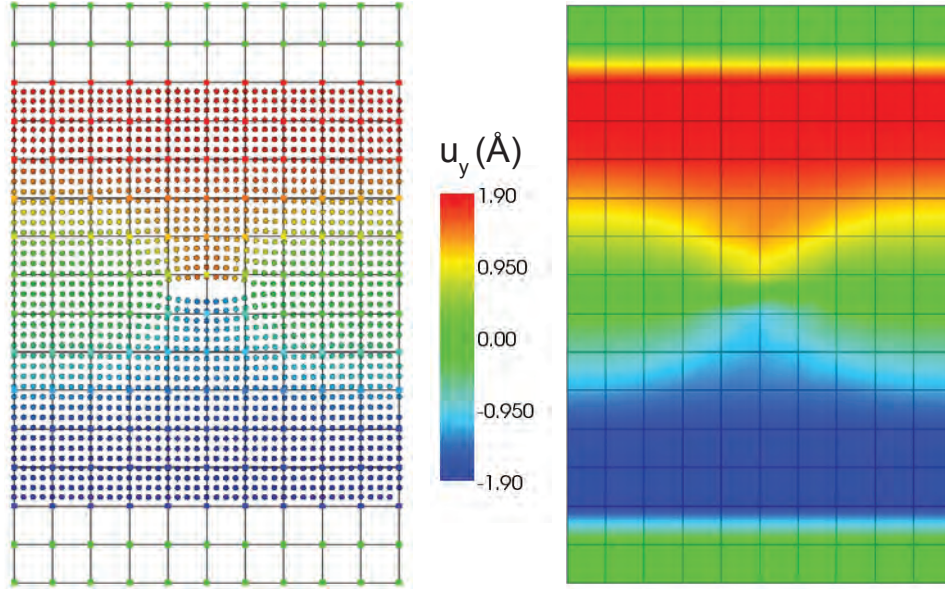


Figure 3.8. Displacement field u_y for a center-cracked body vertically stretched 6.9%. Left: Atoms pictured with overlaying mesh and nodes. Right: Mesh elements showing contours of continuum displacement field; mesh is shown with gray lines to identify elements.

the normalization produces a displacement value corresponding to the center of mass of the localization volume and assigns that value to the node. And, since each element only contains a small number of atoms, the difference between the nodal position and the center of mass position is relatively small. Obviously, special care should be taken to use small elements near the boundary of an enclosed atomistic system, or near any region for which mass is unevenly distributed within the localization volume in the reference configuration. Nodes with localization volumes that are completely empty of atoms are assigned a null value.

Figure 3.9 shows the fields of P_{yy} and σ_{yy} for the same stretch state of 6.9%. These fields are consistent with expectations from fracture mechanics, possessing features such as zero stress in the crack opening region and concentrations of tensile stress near the crack tips. Consistency between our formulation and Hardy's is shown by the qualitative similarity of the fields, with values of σ_{yy} having, in general, a slightly higher magnitude than the corresponding value of P_{yy} . Quantitative consistency can be evaluated by comparing the values at a specific material point. We choose a node near the crack tip, at a position of $\{21.69 \text{ Å}, 10.845 \text{ Å}, 10.845 \text{ Å}\}$ (6 elements down from the top of the system, and 2 elements from the right edge). At this node, the value of P_{yy} equals 9.40327 GPa, and the value of σ_{yy} is 10.0719 GPa. Using the method discussed in section 3.3.1 to estimate displacement gradient $\frac{\partial \mathbf{u}}{\partial \mathbf{X}}$, and by using the relation $\mathbf{F} = \mathbf{1} + \frac{\partial \mathbf{u}}{\partial \mathbf{X}}$, the value of transformed P-K stress is calculated to be 9.48638 GPa. This value is somewhat lower than the expected value from the Hardy expression (a difference of about -5.81%). However, our earlier

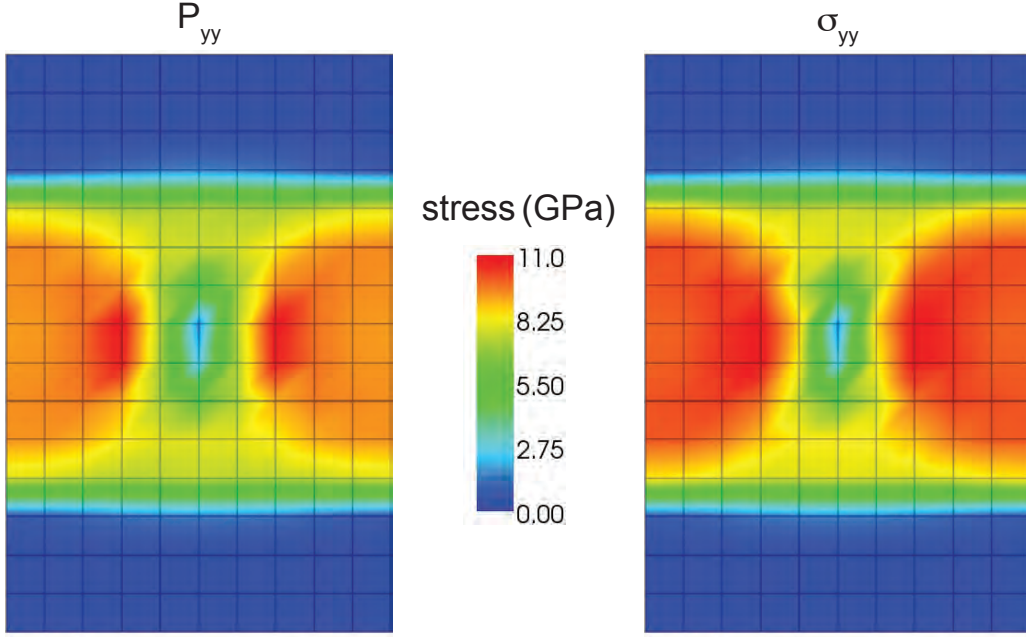


Figure 3.9. Stress fields for a center-cracked body vertically stretched 6.9%. Left: Mesh elements showing contours of continuum field P_{yy} . Right: Mesh elements showing contours of continuum field σ_{yy} as determined from the original Hardy formulation. In both pictures, the mesh is shown with gray lines to identify elements.

simulation examples indicate that this agreement may improve if the system is fixed at a given (inhomogeneous) deformation state and stress values are time averaged for periods ~ 1 ns. It may also be the case that displacement gradient values are actually higher in magnitude than estimated here due to the small size of the system and the use of (relatively) large localization volumes near the crack tip.

3.4 Formulation for a Micromorphic Continuum

In section 3.2.3, we noted that Hardy makes four assumptions about the forms of the energies of, and forces on, the atoms in the system. We also noted that arbitrary multi-body potentials do not necessarily satisfy all four assumptions. For example, the Stillinger-Weber potential for silicon [226], contains a 3-body term that violates the fourth assumption. This assumption is pivotal as it leads to a simplified form of the inter-atomic force between two atoms, which is then used to isolate the expression for stress in the balance of energy. Without this relationship, it is not straightforward to show that the stress expression derived from momentum balance also satisfies energy balance.

This issue has been examined further by both Delph [59] and Chen [35]. In his work, Delph uses the linear momentum balance to derive a generalized expression for stress that includes multi-body terms up to N^{th} order (where N is the number of atoms in the system). However, this same expression is not present within his analysis of the balance of energy. On the other hand, Chen restricts her analysis to consider only potentials with 2-body and 3-body terms, such as the aforementioned Stillinger-Weber potential and the potential by Tersoff [235, 236]. While Chen does manage to show that the stress expression defined by linear momentum appears in the energy balance, her derivation is unclear in its consistency with regard to the expression for the inter-atomic force between two atoms.

We hypothesize that the difficulties experienced by both Delph and Chen are due to the underlying assumption that potential energies that use multi-body terms representative of directional bonding constitute a standard continuum at the microscopic scale. Rather, we conjecture that an enhanced continuum theory is required in order to represent such a material. One such theory is that of a micromorphic continuum as put forth by Eringen [68, 67]. This theory is attractive as it is based on the supposition of microscopic deformations and rotations and includes the concepts of asymmetric stress and a couple stress tensor, both of which act to balance angular or rotational momentum in a body. Such concepts would seemingly be vital when defining volumes associated with continuum material points of arbitrary size and shape for a material governed by directional bonding between atoms. (This point is further addressed in the Appendix.)

In this section, we apply our material frame version of the Hardy formulation to the set of balance laws for a micromorphic continuum. The choice of a material frame analysis is not haphazard; indeed, the authors have attempted to perform a spatial frame analysis consistent with the original formulation by Hardy. However, this analysis is not trivial as an inconsistency exists between the notion of a fixed spatial point \mathbf{x} from the Hardy formulation with the material point $\bar{\mathbf{x}}$ of Eringen's theory. In micromorphic theory, $\bar{\mathbf{x}}$ represents the center of mass of a "microvolume" or "microelement" at the current state of deformation. However, Hardy's analysis requires that \mathbf{x} represent a fixed spatial point. Combining the two formulations requires the introduction of additional terms to account for the offset of the center of mass from the spatial point \mathbf{x} . We have thus far been unable to define a unambiguous set of balance laws that includes such additional variables. Eringen's original derivation for balance laws in the material frame, as shown in [68], does include such variables. For a material frame analysis (as presented in section 3.2), this inclusion is unnecessary: a set of material points \mathbf{X} can be selected that satisfy the center of mass requirement and these points remain fixed over time in the reference configuration. This statement is not true for spatial points that coincide with the material points when the system occupies the reference configuration as, at a later time, they will no longer represent mass centers.

Before proceeding, we note that Chen and Lee previously performed an analysis to connect atomistic quantities to micromorphic theory [36, 37]. In their work, they consider both instantaneous and time-averaged forms of thermomechanical variables and the consistency of these variables with the balance laws for a micromorphic continuum. However, their analysis was performed using a mixture of material and spatial frames as they use the spatial forms of the balance laws and consider current positions of microelements but define quantities relative to fixed sets of atoms associated with each microelement. In addition, they use the original form of Eringen's theory

without consideration of the mass center issue discussed above. Our work will involve manipulation of the material frame versions of the balance laws, thereby avoiding this inconsistency. It is worth noting that Zhou and McDowell considered a similar “equivalent continuum” analysis for a micropolar continuum [254] (a continuum with microelements that undergo rigid rotations only), but proceeded in an entirely different manner than we do or that Chen and Lee have. Also, Murdoch has performed an analysis in which he defined a couple stress tensor that satisfies a moment of momentum balance [168]. It will be seen that our expression for couple stress contains significant differences as compared to Murdoch’s expression, and that, unlike Murdoch, we consider the full set of micromorphic balance laws as established by Eringen.

3.4.1 Balance Laws

The material frame balance laws for a micromorphic continuum, as derived by Eringen in [68], are as follows:

$$\frac{d\rho_0}{dt} = 0 \quad (3.57)$$

$$\rho_0 \frac{d\mathbf{I}}{dt} = 0 \quad (3.58)$$

$$\rho_0 \frac{d\mathbf{v}}{dt} = \mathbf{P} \cdot \nabla_{\mathbf{X}} + \rho_0 \mathbf{b} \quad (3.59)$$

$$\rho_0 \frac{d^2 \boldsymbol{\chi}}{dt^2} \cdot \mathbf{I} = \mathbf{M} \cdot \nabla_{\mathbf{X}} + \mathbf{P} - \bar{\mathbf{P}} + \rho_0 \mathbf{c} \quad (3.60)$$

$$\rho_0 \frac{d\varepsilon}{dt} = \mathbf{P} : \dot{\mathbf{F}} + \mathbf{M} : (\dot{\boldsymbol{\chi}} \nabla_{\mathbf{X}}) + (\bar{\mathbf{P}} - \mathbf{P}) : \dot{\boldsymbol{\chi}} - \nabla_{\mathbf{X}} \cdot \mathbf{Q} + \rho_0 h \quad (3.61)$$

where \mathbf{I} is the micro-inertia tensor, $\boldsymbol{\chi}$ is the micro-deformation gradient, \mathbf{M} is the couple stress tensor, and $\dot{\boldsymbol{\chi}} \equiv \frac{d\boldsymbol{\chi}}{dt}$. The stress $\bar{\mathbf{P}}$ is a quantity related to \mathbf{P} in the sense that the latter is considered by Eringen to be a surface averaged limit of a traction while the former is a volume averaged limit of that same traction (for a more precise explanation, the reader is referred to reference [68]). We note that the total energy contains contributions from internal energy, continuum translational kinetic energy and continuum micro-rotational kinetic energy: $e = \varepsilon + \frac{1}{2}v^2 + \frac{1}{2}\mathbf{I} : (\dot{\boldsymbol{\chi}}^T \cdot \dot{\boldsymbol{\chi}})$.[¶] These equations appear in a more generalized form in [68]; however, to simplify our analysis we have made the assumption of Cartesian coordinates (instead of curvilinear coordinates) and do not separate out intrinsic surface energy density. We also assume that the material points \mathbf{X} coincide with the centers of mass of the localization volumes they are associated with, as in (3.35). Hence,

$$\mathbf{X} = \frac{1}{\rho_0} \sum_{\alpha=1}^N m^{\alpha} \mathbf{X}^{\alpha} \psi(\mathbf{X}^{\alpha} - \mathbf{X}) = \frac{\sum_{\alpha=1}^N m^{\alpha} \mathbf{X}^{\alpha} \psi(\mathbf{X}^{\alpha} - \mathbf{X})}{\sum_{\alpha=1}^N m^{\alpha} \psi(\mathbf{X}^{\alpha} - \mathbf{X})}. \quad (3.62)$$

This expression makes the selection of material points \mathbf{X} non-trivial. For an arbitrary arrangement of atoms or choice of localization volume size or shape, this selection requires iteration in order

[¶]Note that in equation (3.61), the notation $\mathbf{A} : \mathbb{B}$ represents the quantity $\sum_{i=1}^3 \sum_{j=1}^3 A_{ij} B_{ij}$ when \mathbf{A} and \mathbf{B} are second order tensors and the quantity $\sum_{i=1}^3 \sum_{j=1}^3 \sum_{k=1}^3 A_{ijk} B_{ijk}$ when \mathbf{A} and \mathbf{B} are third order tensors.

for equation (3.62) be satisfied. However, since most crystal structures possess a high degree of symmetry (especially if an undeformed, defect-free configuration is used as a reference state), immediate selection of appropriate material points in a structured grid will be possible for many problems.

3.4.2 Densities

The expressions for ρ_0 , \mathbf{p}_0 and $\rho_0 e$ defined in equations (3.10), (3.11) and (3.12), respectively, are reused for the micromorphic formulation. In addition, we define the following expression for micro-inertia tensor \mathbf{I} :

$$\rho_0 \mathbf{I}(\mathbf{X}, t) = \sum_{\alpha=1}^N m^\alpha \mathbf{\Xi}^\alpha \otimes \mathbf{\Xi}^\alpha \psi(\mathbf{X}^\alpha - \mathbf{X}) \quad (3.63)$$

In this expression, $\mathbf{\Xi}^\alpha \equiv \mathbf{X}^\alpha - \mathbf{X}$ using Eringen's notation.^{||} We also note that micro-inertia is the second moment of mass for the localization volume centered at \mathbf{X} (using relative position vectors $\mathbf{\Xi}^\alpha$), while mass density is the zeroth moment. Equation (3.62) can be used to show that the first moment of mass is, in-fact, zero:

$$\begin{aligned} \sum_{\alpha=1}^N m^\alpha \mathbf{\Xi}^\alpha \psi(\mathbf{X}^\alpha - \mathbf{X}) &= \sum_{\alpha=1}^N m^\alpha (\mathbf{X}^\alpha - \mathbf{X}) \psi(\mathbf{X}^\alpha - \mathbf{X}) \\ &= \sum_{\alpha=1}^N m^\alpha \mathbf{X}^\alpha \psi(\mathbf{X}^\alpha - \mathbf{X}) - \sum_{\alpha=1}^N m^\alpha \mathbf{X} \psi(\mathbf{X}^\alpha - \mathbf{X}) \\ &= \rho_0 \mathbf{X} - \mathbf{X} \left(\sum_{\alpha=1}^N m^\alpha \psi(\mathbf{X}^\alpha - \mathbf{X}) \right) \\ &= \rho_0 \mathbf{X} - \rho_0 \mathbf{X} = 0 \end{aligned}$$

We also define a micro-rotational momentum tensor $\mathbf{\Upsilon}$,

$$\rho_0 \mathbf{\Upsilon}(\mathbf{X}, t) = \sum_{\alpha=1}^N m^\alpha \mathbf{v}^\alpha \otimes \mathbf{\Xi}^\alpha \psi(\mathbf{X}^\alpha - \mathbf{X}). \quad (3.64)$$

As for standard continuum theory, there are several interesting aspects of this expression. Consistency between equations (3.60) and (3.64) requires that $\mathbf{\Upsilon} = \dot{\boldsymbol{\chi}} \cdot \mathbf{I}$. This makes sense; just as we earlier defined a continuum velocity field as the product of linear momentum density and the inverse of the mass density, now we define a “micro-deformational velocity tensor” ($\dot{\boldsymbol{\chi}}$) as the product of micro-rotational momentum tensor and the inverse of the micro-inertia tensor:

$$\dot{\boldsymbol{\chi}}(\mathbf{X}, t) = (\rho_0 \mathbf{\Upsilon}) \cdot (\rho_0 \mathbf{I})^{-1} = \left(\sum_{\alpha=1}^N m^\alpha \mathbf{v}^\alpha \otimes \mathbf{\Xi}^\alpha \psi(\mathbf{X}^\alpha - \mathbf{X}) \right) \cdot \left(\sum_{\alpha=1}^N m^\alpha \mathbf{\Xi}^\alpha \otimes \mathbf{\Xi}^\alpha \psi(\mathbf{X}^\alpha - \mathbf{X}) \right)^{-1}. \quad (3.65)$$

^{||}Recall that this same definition was used in (3.35).

We also note that since the only time-dependent quantities in the above expression are the individual atomic velocities, we can integrate the expression to obtain the micro-deformation gradient,

$$\boldsymbol{\chi}(\mathbf{X}, t) = \left(\sum_{\alpha=1}^N m^{\alpha} \mathbf{x}^{\alpha} \otimes \boldsymbol{\Xi}^{\alpha} \psi(\mathbf{X}^{\alpha} - \mathbf{X}) \right) \cdot \left(\sum_{\alpha=1}^N m^{\alpha} \boldsymbol{\Xi}^{\alpha} \otimes \boldsymbol{\Xi}^{\alpha} \psi(\mathbf{X}^{\alpha} - \mathbf{X}) \right)^{-1}. \quad (3.66)$$

Using the expression $\mathbf{X}^{\alpha} = \mathbf{X} + \boldsymbol{\Xi}^{\alpha}$ with equation (3.62), we notice that $\boldsymbol{\chi} \rightarrow \mathbf{1}$ in the limit of zero deformation. We can use (3.65) and (3.66) to estimate the micro-gyration tensor defined by Eringen,

$$\mathbf{v} \equiv \dot{\boldsymbol{\chi}} \cdot \boldsymbol{\chi}^{-1} = \left(\sum_{\alpha=1}^N m^{\alpha} \mathbf{v}^{\alpha} \otimes \boldsymbol{\Xi}^{\alpha} \psi(\mathbf{X}^{\alpha} - \mathbf{X}) \right) \cdot \left(\sum_{\alpha=1}^N m^{\alpha} \mathbf{x}^{\alpha} \otimes \boldsymbol{\Xi}^{\alpha} \psi(\mathbf{X}^{\alpha} - \mathbf{X}) \right)^{-1}. \quad (3.67)$$

Comparison of this expression with the expression by Chen and Lee [36] shows that our formulation, while similar, does display significant differences.

3.4.3 Derivation of Continuum Expressions

3.4.3.1 Balance of Mass and Micro-Inertia

As before, inspection of equation (3.10) reveals that $\frac{d\rho_0}{dt} = 0$. Similarly, we notice that the expression for micro-inertia given in equation (3.63) contains no atomic variables that are time-dependent. Hence,

$$\rho_0 \frac{d\mathbf{I}}{dt} = \frac{d(\rho_0 \mathbf{I})}{dt} = 0.$$

3.4.3.2 Balance of Linear Momentum

We choose not to repeat the derivation shown in section 3.2.4.2, but merely refer to our derived expressions for the 1st Piola-Kirchhoff stress tensor in equation (3.26),

$$\mathbf{P} = -\frac{1}{2} \sum_{\alpha=1}^N \sum_{\beta \neq \alpha}^N \mathbf{f}^{\alpha\beta} \otimes \mathbf{X}^{\alpha\beta} B^{\alpha\beta}(\mathbf{X}),$$

and the body force vector in equation (3.27),

$$\mathbf{b} = \frac{\sum_{\alpha=1}^N m^{\alpha} \mathbf{b}^{\alpha} \psi(\mathbf{X}^{\alpha} - \mathbf{X})}{\sum_{\alpha=1}^N m^{\alpha} \psi(\mathbf{X}^{\alpha} - \mathbf{X})}.$$

We note that in this derivation it was not necessary to define the quantity $\mathbf{f}^{\alpha\beta}$, but merely acknowledge the relations $\mathbf{f}^{\alpha} = \sum_{\beta \neq \alpha}^N \mathbf{f}^{\alpha\beta}$ and $\mathbf{f}^{\beta\alpha} = -\mathbf{f}^{\alpha\beta}$. We will address the specific form of $\mathbf{f}^{\alpha\beta}$ in a later section.

3.4.3.3 Balance of Rotational Momentum

We start with the expression for micro-rotational momentum given in (3.64) and take its time derivative:

$$\begin{aligned}
\rho_0 \frac{d^2 \boldsymbol{\chi}}{dt^2} \cdot \mathbf{I} &= \frac{d}{dt} (\rho \dot{\boldsymbol{\chi}} \cdot \mathbf{I}) \\
&= \frac{d}{dt} (\rho_0 \mathbf{R}) \\
&= \frac{d}{dt} \left(\sum_{\alpha=1}^N m^\alpha \mathbf{v}^\alpha \otimes \boldsymbol{\Xi}^\alpha \psi(\mathbf{X}^\alpha - \mathbf{X}) \right) \\
&= \sum_{\alpha=1}^N m^\alpha \frac{d\mathbf{v}^\alpha}{dt} \otimes \boldsymbol{\Xi}^\alpha \psi(\mathbf{X}^\alpha - \mathbf{X}) \\
&= \sum_{\alpha=1}^N (\mathbf{f}^\alpha + m^\alpha \mathbf{b}^\alpha) \otimes \boldsymbol{\Xi}^\alpha \psi(\mathbf{X}^\alpha - \mathbf{X})
\end{aligned}$$

By using the relation $\mathbf{f}^\alpha = \sum_{\beta \neq \alpha}^N \mathbf{f}^{\alpha\beta}$ and acknowledging that α and β are dummy indices, one obtains:

$$\rho_0 \frac{d^2 \boldsymbol{\chi}}{dt^2} \cdot \mathbf{I} = \frac{1}{2} \sum_{\alpha=1}^N \sum_{\beta \neq \alpha}^N \mathbf{f}^{\alpha\beta} \otimes \left(\boldsymbol{\Xi}^\alpha \psi(\mathbf{X}^\alpha - \mathbf{X}) - \boldsymbol{\Xi}^\beta \psi(\mathbf{X}^\beta - \mathbf{X}) \right) + \sum_{\alpha=1}^N m^\alpha \mathbf{b}^\alpha \otimes \boldsymbol{\Xi}^\alpha \psi(\mathbf{X}^\alpha - \mathbf{X}) \quad (3.68)$$

In order to use the relationship shown in equation (3.19), we rearrange the first term on the RHS of (3.68) (labeled RHS_1 for convenience) into the following expression:

$$\text{RHS}_1 = \frac{1}{2} \sum_{\alpha=1}^N \sum_{\beta \neq \alpha}^N \mathbf{f}^{\alpha\beta} \otimes \left(\mathbf{X}^\alpha \psi(\mathbf{X}^\alpha - \mathbf{X}) - \mathbf{X}^\beta \psi(\mathbf{X}^\beta - \mathbf{X}) - \mathbf{X} \left[\psi(\mathbf{X}^\alpha - \mathbf{X}) - \psi(\mathbf{X}^\beta - \mathbf{X}) \right] \right)$$

This can now be simplified to

$$\text{RHS}_1 = \sum_{\alpha=1}^N \sum_{\beta \neq \alpha}^N \mathbf{f}^{\alpha\beta} \otimes \mathbf{X}^\alpha \psi(\mathbf{X}^\alpha - \mathbf{X}) + \frac{1}{2} \sum_{\alpha=1}^N \sum_{\beta \neq \alpha}^N \mathbf{f}^{\alpha\beta} \otimes \mathbf{X} \otimes \mathbf{X}^{\alpha\beta} \cdot \nabla_{\mathbf{X}} B^{\alpha\beta}.$$

We then use the chain rule to bring the divergence operator to the outside of the second term. Hence,

$$\begin{aligned}
\rho_0 \frac{d^2 \boldsymbol{\chi}}{dt^2} \cdot \mathbf{I} &= \sum_{\alpha=1}^N \sum_{\beta \neq \alpha}^N \mathbf{f}^{\alpha\beta} \otimes \mathbf{X}^\alpha \psi(\mathbf{X}^\alpha - \mathbf{X}) \\
&\quad + \left(\frac{1}{2} \sum_{\alpha=1}^N \sum_{\beta \neq \alpha}^N \mathbf{f}^{\alpha\beta} \otimes \mathbf{X} \otimes \mathbf{X}^{\alpha\beta} B^{\alpha\beta} \right) \cdot \nabla_{\mathbf{X}} \\
&\quad - \frac{1}{2} \sum_{\alpha=1}^N \sum_{\beta \neq \alpha}^N \mathbf{f}^{\alpha\beta} \otimes \mathbf{X}^{\alpha\beta} B^{\alpha\beta} + \sum_{\alpha=1}^N m^\alpha \mathbf{b}^\alpha \otimes \boldsymbol{\Xi}^\alpha \psi(\mathbf{X}^\alpha - \mathbf{X}).
\end{aligned} \quad (3.69)$$

At this point, we note that the third term on the RHS is none other than \mathbf{P} . Also, the first two terms on the RHS of equation (3.69) appear to lack frame invariance, *i.e.* the value of these terms will depend on the material frame coordinate origin. In order to correct this, we add (to the first term) and subtract (from the second term) the quantity

$$\left(\frac{1}{2} \sum_{\alpha=1}^N \sum_{\beta \neq \alpha}^N \mathbf{f}^{\alpha\beta} \otimes \mathbf{X}^\alpha \otimes \mathbf{X}^{\alpha\beta} B^{\alpha\beta} \right) \cdot \nabla_{\mathbf{X}},$$

and again use the relation in equation (3.19). This simplifies equation (3.69) to

$$\begin{aligned} \rho_0 \frac{d^2 \boldsymbol{\chi}}{dt^2} \cdot \mathbf{I} = & \frac{1}{2} \sum_{\alpha=1}^N \sum_{\beta \neq \alpha}^N \mathbf{f}^{\alpha\beta} \otimes \mathbf{X}^\alpha \left(\psi(\mathbf{X}^\alpha - \mathbf{X}) + \psi(\mathbf{X}^\beta - \mathbf{X}) \right) \\ & + \left(-\frac{1}{2} \sum_{\alpha=1}^N \sum_{\beta \neq \alpha}^N \mathbf{f}^{\alpha\beta} \otimes \boldsymbol{\Xi}^\alpha \otimes \mathbf{X}^{\alpha\beta} B^{\alpha\beta} \right) \cdot \nabla_{\mathbf{X}} + \mathbf{P} + \sum_{\alpha=1}^N m^\alpha \mathbf{b}^\alpha \otimes \boldsymbol{\Xi}^\alpha \psi(\mathbf{X}^\alpha - \mathbf{X}). \end{aligned}$$

Finally, by separating the first term on the RHS into two separate terms, switching dummy indices α and β and using the relation $\mathbf{f}^{\beta\alpha} = -\mathbf{f}^{\alpha\beta}$, we arrive at

$$\begin{aligned} \rho_0 \frac{d^2 \boldsymbol{\chi}}{dt^2} \cdot \mathbf{I} = & \frac{1}{2} \sum_{\alpha=1}^N \sum_{\beta \neq \alpha}^N \mathbf{f}^{\alpha\beta} \otimes \mathbf{X}^{\alpha\beta} \psi(\mathbf{X}^\alpha - \mathbf{X}) \\ & + \left(-\frac{1}{2} \sum_{\alpha=1}^N \sum_{\beta \neq \alpha}^N \mathbf{f}^{\alpha\beta} \otimes \boldsymbol{\Xi}^\alpha \otimes \mathbf{X}^{\alpha\beta} B^{\alpha\beta} \right) \cdot \nabla_{\mathbf{X}} + \mathbf{P} + \sum_{\alpha=1}^N m^\alpha \mathbf{b}^\alpha \otimes \boldsymbol{\Xi}^\alpha \psi(\mathbf{X}^\alpha - \mathbf{X}). \end{aligned} \quad (3.70)$$

Comparing equation (3.70) with (3.60), we identify the expressions for couple stress,

$$\mathbf{M} = -\frac{1}{2} \sum_{\alpha=1}^N \sum_{\beta \neq \alpha}^N \mathbf{f}^{\alpha\beta} \otimes \boldsymbol{\Xi}^\alpha \otimes \mathbf{X}^{\alpha\beta} B^{\alpha\beta}, \quad (3.71)$$

for $\bar{\mathbf{P}}$,

$$\bar{\mathbf{P}} = -\frac{1}{2} \sum_{\alpha=1}^N \sum_{\beta \neq \alpha}^N \mathbf{f}^{\alpha\beta} \otimes \mathbf{X}^{\alpha\beta} \psi(\mathbf{X}^\alpha - \mathbf{X}), \quad (3.72)$$

and for the body couple,

$$\mathbf{c} = \frac{1}{\rho_0} \sum_{\alpha=1}^N m^\alpha \mathbf{b}^\alpha \otimes \boldsymbol{\Xi}^\alpha \psi(\mathbf{X}^\alpha - \mathbf{X}) = \frac{\sum_{\alpha=1}^N m^\alpha \mathbf{b}^\alpha \otimes \boldsymbol{\Xi}^\alpha \psi(\mathbf{X}^\alpha - \mathbf{X})}{\sum_{\alpha=1}^N m^\alpha \psi(\mathbf{X}^\alpha - \mathbf{X})} \quad (3.73)$$

Before proceeding to the next section, we again point out that, with regard to the inter-atomic forces, we have only used the relations $\mathbf{f}^\alpha = \sum_{\beta \neq \alpha}^N \mathbf{f}^{\alpha\beta}$ and $\mathbf{f}^{\beta\alpha} = -\mathbf{f}^{\alpha\beta}$. We have not yet specified a form for the quantity $\mathbf{f}^{\alpha\beta}$.

3.4.3.4 Balance of Energy

As before, we begin with Hardy's expression for the system energy (3.12),

$$\begin{aligned}
\rho_0 \frac{de}{dt} &= \frac{d(\rho_0 e)}{dt} = \frac{d}{dt} \left\{ \sum_{\alpha=1}^N \left\{ \frac{1}{2} m^\alpha (v^\alpha)^2 + \phi^\alpha \right\} \psi(\mathbf{X}^\alpha - \mathbf{X}) \right\} \\
&= \sum_{\alpha=1}^N \left\{ m^\alpha \left(\frac{d\mathbf{v}^\alpha}{dt} \cdot \mathbf{v}^\alpha \right) + \frac{d\phi^\alpha}{dt} \right\} \psi(\mathbf{X}^\alpha - \mathbf{X}) \\
&= \sum_{\alpha=1}^N \left\{ (\mathbf{f}^\alpha + m^\alpha \mathbf{b}^\alpha) \cdot \mathbf{v}^\alpha + \frac{d\phi^\alpha}{dt} \right\} \psi(\mathbf{X}^\alpha - \mathbf{X}) \\
&= \sum_{\alpha=1}^N \left\{ \mathbf{f}^\alpha \cdot \mathbf{v}^\alpha + \frac{d\phi^\alpha}{dt} \right\} \psi(\mathbf{X}^\alpha - \mathbf{X}) + \sum_{\alpha=1}^N m^\alpha \mathbf{b}^\alpha \cdot \mathbf{v}^\alpha \psi(\mathbf{X}^\alpha - \mathbf{X}).
\end{aligned}$$

Using Hardy's second assumption, $\mathbf{f}^\alpha = \sum_{\eta=1}^N \mathbf{f}^{\alpha\eta}$, this can be also written as

$$\rho_0 \frac{de}{dt} = \sum_{\alpha=1}^N \left\{ \sum_{\eta \neq \alpha}^N \mathbf{f}^{\alpha\eta} \cdot \mathbf{v}^\alpha + \frac{d\phi^\alpha}{dt} \right\} \psi(\mathbf{X}^\alpha - \mathbf{X}) + \sum_{\alpha=1}^N m^\alpha \mathbf{b}^\alpha \cdot \mathbf{v}^\alpha \psi(\mathbf{X}^\alpha - \mathbf{X}). \quad (3.74)$$

In order to simplify the expression above, we must (as did Hardy) provide a relationship between the inter-atomic force $\mathbf{f}^{\alpha\eta}$ and the atomic potential energies ϕ^α and ϕ^η . Earlier, we noted that Hardy's third and fourth assumptions combined are only valid for pair and central force (*e.g.* EAM) potentials and not for potentials representative of directional bonding such as the Stillinger-Weber potential. Here, we substitute a new third assumption: each atom's potential energy depends only on the vectors that connect the atom under consideration to all other atoms. Hence, $\phi^\alpha = \phi^\alpha(\mathbf{x}^{\alpha\beta}, \mathbf{x}^{\alpha\gamma}, \dots, \mathbf{x}^{\alpha N})$. While this seemingly limits the form of ϕ^α , one realizes that this is not the case as any inter-atomic bond vector in the system can be represented by combinations of vectors between atom α and the atoms belonging to the bond of interest. Using this new relation, the force between atoms α and η can be defined as

$$\mathbf{f}^{\alpha\eta} = - \left\{ \frac{\partial \phi^\alpha}{\partial \mathbf{x}^{\alpha\eta}} + \frac{\partial \phi^\eta}{\partial \mathbf{x}^{\alpha\eta}} \right\}, \quad (3.75)$$

our new fourth assumption. Regarding this assumed form for $\mathbf{f}^{\alpha\eta}$, it should be noted that ϕ^α and ϕ^η cannot depend arbitrarily on the vector $\mathbf{x}^{\alpha\eta}$. In the Appendix of reference [259], it was discussed that the system potential energy depends on its configuration through invariant quantities in order to satisfy frame invariance (In this case, 'frame' refers to the location and orientation of the coordinate system origin). Such invariant quantities include bond lengths, angles between bonds involving common atoms, areas and volumes. Nevertheless, equation (3.75) provides a simple form that is well-suited to our formulation, as will be shown.

Inserting equation (3.75) into the first term on the RHS of (3.74), this term (RHS_1) becomes

the following:

$$\begin{aligned}
\text{RHS}_1 &= \sum_{\alpha=1}^N \left\{ - \sum_{\eta \neq \alpha}^N \left\{ \frac{\partial \phi^\alpha}{\partial \mathbf{x}^{\alpha\eta}} + \frac{\partial \phi^\eta}{\partial \mathbf{x}^{\alpha\eta}} \right\} \cdot \mathbf{v}^\alpha + \frac{d\phi^\alpha}{dt} \right\} \psi(\mathbf{X}^\alpha - \mathbf{X}) \\
&= \sum_{\alpha=1}^N \left\{ - \sum_{\eta \neq \alpha}^N \left\{ \frac{\partial \phi^\alpha}{\partial \mathbf{x}^{\alpha\eta}} + \frac{\partial \phi^\eta}{\partial \mathbf{x}^{\alpha\eta}} \right\} \cdot \mathbf{v}^\alpha + \sum_{\eta \neq \alpha}^N \frac{\partial \phi^\alpha}{\partial \mathbf{x}^{\alpha\eta}} \cdot \mathbf{v}^{\alpha\eta} \right\} \psi(\mathbf{X}^\alpha - \mathbf{X}) \\
&= \sum_{\alpha=1}^N \sum_{\eta \neq \alpha}^N \left\{ - \frac{\partial \phi^\alpha}{\partial \mathbf{x}^{\alpha\eta}} \cdot \mathbf{v}^\alpha - \frac{\partial \phi^\eta}{\partial \mathbf{x}^{\alpha\eta}} \cdot \mathbf{v}^\alpha + \frac{\partial \phi^\alpha}{\partial \mathbf{x}^{\alpha\eta}} \cdot \mathbf{v}^\alpha - \frac{\partial \phi^\alpha}{\partial \mathbf{x}^{\alpha\eta}} \cdot \mathbf{v}^\eta \right\} \psi(\mathbf{X}^\alpha - \mathbf{X}) \\
&= \sum_{\alpha=1}^N \sum_{\eta \neq \alpha}^N \left\{ - \frac{\partial \phi^\eta}{\partial \mathbf{x}^{\alpha\eta}} \cdot \mathbf{v}^\alpha - \frac{\partial \phi^\alpha}{\partial \mathbf{x}^{\alpha\eta}} \cdot \mathbf{v}^\eta \right\} \psi(\mathbf{X}^\alpha - \mathbf{X}) \\
&= - \sum_{\alpha=1}^N \sum_{\eta \neq \alpha}^N \frac{\partial \phi^\eta}{\partial \mathbf{x}^{\alpha\eta}} \cdot \mathbf{v}^\alpha \psi(\mathbf{X}^\alpha - \mathbf{X}) - \sum_{\alpha=1}^N \sum_{\eta \neq \alpha}^N \frac{\partial \phi^\alpha}{\partial \mathbf{x}^{\alpha\eta}} \cdot \mathbf{v}^\eta \psi(\mathbf{X}^\alpha - \mathbf{X})
\end{aligned}$$

We now switch dummy indices on the right term of the above expression (*i.e.* $\alpha \leftrightarrow \eta$) and use the relation $\mathbf{x}^{\eta\alpha} = -\mathbf{x}^{\alpha\eta}$ to obtain

$$\text{RHS}_1 = - \sum_{\alpha=1}^N \sum_{\eta \neq \alpha}^N \frac{\partial \phi^\eta}{\partial \mathbf{x}^{\alpha\eta}} \cdot \mathbf{v}^\alpha (\psi(\mathbf{X}^\alpha - \mathbf{X}) - \psi(\mathbf{X}^\eta - \mathbf{X})). \quad (3.76)$$

Combining this result with equations (3.19) and (3.74), we arrive at

$$\rho_0 \frac{de}{dt} = \sum_{\alpha=1}^N \sum_{\eta \neq \alpha}^N \left(\frac{\partial \phi^\eta}{\partial \mathbf{x}^{\alpha\eta}} \cdot \mathbf{v}^\alpha \right) (\mathbf{X}^{\alpha\eta} \cdot \nabla_{\mathbf{X}} B^{\alpha\eta}) + \sum_{\alpha=1}^N m^\alpha \mathbf{b}^\alpha \cdot \mathbf{v}^\alpha \psi(\mathbf{X}^\alpha - \mathbf{X}). \quad (3.77)$$

As before, this can be modified to

$$\rho_0 \frac{de}{dt} = \nabla_{\mathbf{X}} \cdot \left(\sum_{\alpha=1}^N \sum_{\eta \neq \alpha}^N \left(\frac{\partial \phi^\eta}{\partial \mathbf{x}^{\alpha\eta}} \cdot \mathbf{v}^\alpha \right) \mathbf{X}^{\alpha\eta} B^{\alpha\eta} \right) + \sum_{\alpha=1}^N m^\alpha \mathbf{b}^\alpha \cdot \mathbf{v}^\alpha \psi(\mathbf{X}^\alpha - \mathbf{X}). \quad (3.78)$$

Similar to our material frame analysis of the balance of energy for standard continuum theory, we separate atomic motion from continuum motion by splitting the atomic velocities \mathbf{v}^α . However, for a micromorphic continuum, this velocity becomes the sum of three terms,

$$\mathbf{v}^\alpha = \mathbf{v}(\mathbf{X}, t) + \dot{\boldsymbol{\chi}}(\mathbf{X}, t) \cdot \boldsymbol{\Xi}^\alpha + \hat{\mathbf{v}}^\alpha(\mathbf{X}, t), \quad (3.79)$$

where $\dot{\boldsymbol{\chi}}(\mathbf{X}, t) \cdot \boldsymbol{\Xi}^\alpha$ now represents a continuum velocity associated with the microscale rotation and deformation of the microelement containing atom α . Substitution of this expression into (3.78), along with the aforementioned relation $e = \varepsilon + \frac{1}{2}v^2 + \frac{1}{2}\mathbf{I} : (\dot{\boldsymbol{\chi}}^T \cdot \dot{\boldsymbol{\chi}})$, results in the following upon

simplification:

$$\begin{aligned}
& \rho_0 \frac{d\boldsymbol{\varepsilon}}{dt} + \rho_0 \frac{d\mathbf{v}}{dt} \cdot \mathbf{v} + \left(\rho_0 \frac{d^2 \boldsymbol{\chi}}{dt^2} \cdot \mathbf{I} \right) : \dot{\boldsymbol{\chi}} = \\
& \quad \nabla_{\mathbf{X}} \cdot \left(\mathbf{v} \cdot \left\{ \sum_{\alpha=1}^N \sum_{\eta \neq \alpha}^N \frac{\partial \phi^\eta}{\partial \mathbf{x}^{\alpha\eta}} \otimes \mathbf{X}^{\alpha\eta} B^{\alpha\eta} \right\} \right) \\
& \quad + \nabla_{\mathbf{X}} \cdot \left(\dot{\boldsymbol{\chi}} : \left\{ \sum_{\alpha=1}^N \sum_{\eta \neq \alpha}^N \frac{\partial \phi^\eta}{\partial \mathbf{x}^{\alpha\eta}} \otimes \boldsymbol{\Xi}^\alpha \otimes \mathbf{X}^{\alpha\eta} B^{\alpha\eta} \right\} \right) \\
& \quad + \nabla_{\mathbf{X}} \cdot \left(\sum_{\alpha=1}^N \sum_{\eta \neq \alpha}^N \left(\frac{\partial \phi^\eta}{\partial \mathbf{x}^{\alpha\eta}} \cdot \hat{\mathbf{v}}^\alpha \right) \mathbf{X}^{\alpha\eta} B^{\alpha\eta} \right) \\
& \quad + \rho_0 \mathbf{b} \cdot \mathbf{v} + \dot{\boldsymbol{\chi}} : \left(\sum_{\alpha=1}^N m^\alpha \mathbf{b}^\alpha \otimes \boldsymbol{\Xi}^\alpha \psi(\mathbf{X}^\alpha - \mathbf{X}) \right) + \sum_{\alpha=1}^N m^\alpha \mathbf{b}^\alpha \cdot \hat{\mathbf{v}}^\alpha \psi(\mathbf{X}^\alpha - \mathbf{X})
\end{aligned} \tag{3.80}$$

Equation (3.80) can be further simplified in two ways. On the LHS, the expressions $\rho_0 \frac{d\mathbf{v}}{dt}$ and $\rho_0 \frac{d^2 \boldsymbol{\chi}}{dt^2} \cdot \mathbf{I}$ are replaced using the balance of linear and rotational momentum equations shown in equations (3.59) and (3.60), respectively. On the RHS, we can relate each divergence term to a corresponding continuum quantity. By using our new expression for inter-atomic forces defined in equation (3.75), we notice that the 1st Piola-Kirchhoff stress \mathbf{P} is

$$\begin{aligned}
\mathbf{P} &= -\frac{1}{2} \sum_{\alpha=1}^N \sum_{\eta \neq \alpha}^N \mathbf{f}^{\alpha\eta} \otimes \mathbf{X}^{\alpha\eta} B^{\alpha\eta} \\
&= \frac{1}{2} \sum_{\alpha=1}^N \sum_{\eta \neq \alpha}^N \left\{ \frac{\partial \phi^\alpha}{\partial \mathbf{x}^{\alpha\eta}} + \frac{\partial \phi^\eta}{\partial \mathbf{x}^{\alpha\eta}} \right\} \otimes \mathbf{X}^{\alpha\eta} B^{\alpha\eta} \\
&= \frac{1}{2} \left\{ \sum_{\alpha=1}^N \sum_{\eta \neq \alpha}^N \frac{\partial \phi^\alpha}{\partial \mathbf{x}^{\alpha\eta}} \otimes \mathbf{X}^{\alpha\eta} B^{\alpha\eta} + \sum_{\alpha=1}^N \sum_{\eta \neq \alpha}^N \frac{\partial \phi^\eta}{\partial \mathbf{x}^{\alpha\eta}} \otimes \mathbf{X}^{\alpha\eta} B^{\alpha\eta} \right\} \\
&= \frac{1}{2} \left\{ \sum_{\eta=1}^N \sum_{\alpha \neq \eta}^N \frac{\partial \phi^\eta}{\partial \mathbf{x}^{\eta\alpha}} \otimes \mathbf{X}^{\eta\alpha} B^{\eta\alpha} + \sum_{\alpha=1}^N \sum_{\eta \neq \alpha}^N \frac{\partial \phi^\eta}{\partial \mathbf{x}^{\alpha\eta}} \otimes \mathbf{X}^{\alpha\eta} B^{\alpha\eta} \right\} \\
&= \frac{1}{2} \left\{ \sum_{\alpha=1}^N \sum_{\eta \neq \alpha}^N \frac{\partial \phi^\eta}{\partial \mathbf{x}^{\alpha\eta}} \otimes \mathbf{X}^{\alpha\eta} B^{\alpha\eta} + \sum_{\alpha=1}^N \sum_{\eta \neq \alpha}^N \frac{\partial \phi^\eta}{\partial \mathbf{x}^{\alpha\eta}} \otimes \mathbf{X}^{\alpha\eta} B^{\alpha\eta} \right\} \\
&= \sum_{\alpha=1}^N \sum_{\eta \neq \alpha}^N \frac{\partial \phi^\eta}{\partial \mathbf{x}^{\alpha\eta}} \otimes \mathbf{X}^{\alpha\eta} B^{\alpha\eta}.
\end{aligned}$$

Hence,

$$\nabla_{\mathbf{X}} \cdot \left(\mathbf{v} \cdot \left\{ \sum_{\alpha=1}^N \sum_{\eta \neq \alpha}^N \frac{\partial \phi^\eta}{\partial \mathbf{x}^{\alpha\eta}} \otimes \mathbf{X}^{\alpha\eta} B^{\alpha\eta} \right\} \right) \rightarrow \nabla_{\mathbf{X}} \cdot (\mathbf{v} \cdot \mathbf{P}) = \mathbf{P} : \dot{\mathbf{F}} + \mathbf{v} \cdot (\mathbf{P} \cdot \nabla_{\mathbf{X}}). \tag{3.81}$$

Regarding the second divergence term in (3.80), we notice that the couple stress tensor (equation (3.71)) now has the form

$$\mathbf{M} = \frac{1}{2} \sum_{\alpha=1}^N \sum_{\eta \neq \alpha}^N \left\{ \frac{\partial \phi^\alpha}{\partial \mathbf{x}^{\alpha\eta}} + \frac{\partial \phi^\eta}{\partial \mathbf{x}^{\alpha\eta}} \right\} \otimes \mathbf{\Xi}^\alpha \otimes \mathbf{X}^{\alpha\eta} B^{\alpha\eta}.$$

Admittedly, it is not as easy to simplify this expression as it was to simplify the expression for \mathbf{P} . However, we note here that Delph asserted that any potential energy expression dependent on M atoms within the N -atom system is equally divided among the M atoms [59]. For example, the contribution for a 3-body energy term between atoms α , β and γ is divided equally into thirds for ϕ^α , ϕ^β and ϕ^γ respectively. Hence, this assertion results in the conclusion that while, in general, $\phi^\alpha \neq \phi^\eta$, it is the case that $\frac{\partial \phi^\alpha}{\partial \mathbf{x}^{\alpha\eta}} = \frac{\partial \phi^\eta}{\partial \mathbf{x}^{\alpha\eta}}$ since the portion of potential energy that provides non-zero values of this derivative is the same for both atoms α and η . Hence,

$$\mathbf{M} = \sum_{\alpha=1}^N \sum_{\eta \neq \alpha}^N \frac{\partial \phi^\eta}{\partial \mathbf{x}^{\alpha\eta}} \otimes \mathbf{\Xi}^\alpha \otimes \mathbf{X}^{\alpha\eta} B^{\alpha\eta},$$

and,

$$\nabla_{\mathbf{X}} \cdot \left(\dot{\boldsymbol{\chi}} : \left\{ \sum_{\alpha=1}^N \sum_{\eta \neq \alpha}^N \frac{\partial \phi^\eta}{\partial \mathbf{x}^{\alpha\eta}} \otimes \mathbf{\Xi}^\alpha \otimes \mathbf{X}^{\alpha\eta} B^{\alpha\eta} \right\} \right) \rightarrow \nabla_{\mathbf{X}} \cdot (\dot{\boldsymbol{\chi}} : \mathbf{M}) = \mathbf{M} : (\dot{\boldsymbol{\chi}} \nabla_{\mathbf{X}}) + \dot{\boldsymbol{\chi}} : (\mathbf{M} \cdot \nabla_{\mathbf{X}}) \quad (3.82)$$

The third divergence term provides us with the definition for heat flux vector for a micromorphic system:

$$\mathbf{Q}(\mathbf{X}, t) = - \sum_{\alpha=1}^N \sum_{\eta \neq \alpha}^N \left(\frac{\partial \phi^\eta}{\partial \mathbf{x}^{\alpha\eta}} \cdot \hat{\mathbf{v}}^\alpha \right) \mathbf{X}^{\alpha\eta} B^{\alpha\eta} \quad (3.83)$$

Combining (3.81), (3.82) and (3.83) into equation (3.80), along with the earlier definitions for energy generation per unit mass (3.53) and body couple (3.73), we obtain:

$$\begin{aligned} \rho_0 \frac{d\varepsilon}{dt} + (\mathbf{P} \cdot \nabla_{\mathbf{X}} + \rho_0 \mathbf{b}) \cdot \mathbf{v} + (\mathbf{M} \cdot \nabla_{\mathbf{X}} + \mathbf{P} - \bar{\mathbf{P}} + \rho_0 \mathbf{c}) : \dot{\boldsymbol{\chi}} = \\ \mathbf{P} : \dot{\mathbf{F}} + \mathbf{v} \cdot (\mathbf{P} \cdot \nabla_{\mathbf{X}}) + \mathbf{M} : (\dot{\boldsymbol{\chi}} \nabla_{\mathbf{X}}) + \dot{\boldsymbol{\chi}} : (\mathbf{M} \cdot \nabla_{\mathbf{X}}) \\ - \nabla_{\mathbf{X}} \cdot \mathbf{Q} + \rho_0 \mathbf{b} \cdot \mathbf{v} + \dot{\boldsymbol{\chi}} : \rho_0 \mathbf{c} + \rho_0 h \end{aligned} \quad (3.84)$$

Upon simplifying this equation, we obtain

$$\rho_0 \frac{d\varepsilon}{dt} = \mathbf{P} : \dot{\mathbf{F}} + \mathbf{M} : (\dot{\boldsymbol{\chi}} \nabla_{\mathbf{X}}) + (\bar{\mathbf{P}} - \mathbf{P}) : \dot{\boldsymbol{\chi}} - \nabla_{\mathbf{X}} \cdot \mathbf{Q} + \rho_0 h, \quad (3.85)$$

which exactly matches the balance of energy equation derived by Eringen [68] and given earlier in equation (3.61).

3.5 Discussion

By constructing a material frame-based formalism similar to the spatial frame-based formalism developed by Hardy, we have derived expressions for continuum theory variables based on atomic-scale quantities. For an atomistic system governed by central force potentials, these expressions are based on conventional continuum theory and include the 1st Piola-Kirchhoff stress tensor, a body force field, a heat flux vector field, and an energy generation rate. For an atomistic system where the inter-atomic potential is multi-body and directional in nature, these expressions are based on micromorphic continuum theory and also include a couple stress tensor and a body couple tensor field.

These expressions are distinct from both Hardy’s original formulation, as well as the many other works discussed in the Introduction section, as they are for material frame-based continuum variables. Exceptions to this are found in the text by Weiner [249, Chapter 4 and Appendix I in Chapter 6] and the articles by Andia and colleagues [51, 50, 11, 12]. As mentioned earlier, Andia *et al.* define an expression for P-K stress as a cell averaged quantity. Our expression is defined at a single material point and depends only on the size of the volume associated with that point in the sense that a minimum volume must be used to show consistency with expected continuum behavior. Additionally, both Andia *et al.* and Weiner make the distinction between internal and external forces, separating the interactions between atoms within the cell and the interactions between atoms with “ghost” atoms located across the periodic boundaries. This distinction is not needed for our approach.

Our formulations are suitable for the analysis of solid mechanics problems. For simulations involving fluid and gaseous states of matter, the concepts of a reference configuration and deformation gradient are not clear, and transformation from P-K stress to Cauchy stress would be difficult. This would also occur for situations of dramatic molecular rearrangement, such as mixing (as happens in granular materials) or extended plastic deformation. In such cases, it would be advisable to use the original spatial frame formulation developed by Hardy. The difficulty inherent to developing a spatial frame formulation for a micromorphic continuum was discussed earlier, and more work is warranted to overcome this challenge.

The analyses presented in the Evaluation section clearly show that our derived expression for P-K stress is consistent with a thermo-mechanical measure of stress despite the fact that it contains only a potential and not a kinetic term, unlike the Cauchy stress expression derived by Hardy. Our analysis also shows that our expression for \mathbf{P} satisfies the Piola transformation $\boldsymbol{\sigma} = \frac{1}{J}\mathbf{P}\mathbf{F}^T$. By comparison, Weiner refers to his P-K stress expression as ‘non-thermodynamic’ and shows that its transformation to the spatial frame results in only the potential portion of the virial stress expression.

In order to show the consistency of our expression with continuum thermodynamics, we chose our material configuration to be the zero temperature, undeformed state of the system simulated. Unlike conventional continuum mechanics where the choice of zero stress reference configuration and temperature are arbitrary, the selection of a zero temperature state as the reference configuration is mandatory for our formulation. This requirement was discussed by Weiner [249, Chapter

4], who noted that for the case of anharmonic pair potentials, a zero value of P-K stress is achieved only at zero temperature. This can be more easily understood by examining our expression for P-K stress,

$$\mathbf{P} = -\frac{1}{2} \sum_{\alpha=1}^N \sum_{\beta \neq \alpha}^N \mathbf{f}^{\alpha\beta} \otimes \mathbf{X}^{\alpha\beta} B^{\alpha\beta}(\mathbf{X}),$$

and comparing it with the expression derived by Hardy for Cauchy stress,

$$\boldsymbol{\sigma} = -\frac{1}{2} \sum_{\alpha=1}^N \sum_{\beta \neq \alpha}^N \mathbf{f}^{\alpha\beta} \otimes \mathbf{x}^{\alpha\beta} B^{\alpha\beta}(\mathbf{x}) - \sum_{\alpha=1}^N m^{\alpha} \hat{\mathbf{v}}^{\alpha} \otimes \hat{\mathbf{v}}^{\alpha} \psi(\mathbf{x}^{\alpha} - \mathbf{x}).$$

Here, we see that if we arbitrarily select a given configuration to represent our material frame, the first term on the RHS of the Cauchy expression will exactly equal the full value of the P-K expression. However, this term will not equal zero for any system that has been equilibrated to a non-zero temperature. For that case, it is apparent that the second term on the RHS will be equal to a non zero value, and thus the first term must be equal in magnitude and opposite in sign in order to produce zero Cauchy stress. Ergo, such a configuration will produce a non zero value of P-K stress, and the relationship between P-K and Cauchy stresses will no longer hold.

Although our continuum formulations are distinctly different from the works by Delph and Chen due to their material frame basis, it is interesting to notice that our formulations offers two advantages. First, unlike in Delph's derivation, our stress expression appears in both the linear momentum and energy balance laws with no modification. Second, unlike the work by Chen, the balance laws our expressions satisfy are the same as from micromorphic continuum theory; no separate "microscale balance laws" are needed. While it is certainly the case that time-averaging will improve the consistency of our expressions with continuum theory (such as was shown for stress expressions in this chapter and for Hardy's heat flux expression in [248]), this averaging is not a prerequisite towards connecting molecular simulation results with continuum formulations.

Finally, in order to relate the material frame variables defined here to their spatial frame counterparts, it is necessary to define kinematic deformation variables such as the deformation gradient. It is interesting to note that few of the aforementioned articles establish such field variables. However, in equation (3.14) we define a displacement field \mathbf{u} consistent with the same localization function and volumes used to define the thermodynamic variables. This field could easily be used to construct a locally-varying deformation gradient expression. Also, in equations (3.66) and (3.67) we derived expressions for the micro-deformation gradient $\boldsymbol{\chi}$ and micro-gyration tensor \mathbf{v} , respectively, the kinematic variables inherent to micromorphic continuum theory. It is interesting to note that if the relationship $\mathbf{x}^{\alpha} = \mathbf{x} + \boldsymbol{\xi}^{\alpha}$ is applied to equation (3.66), where $\boldsymbol{\xi}^{\alpha}$ is the spatial frame counterpart to $\boldsymbol{\Xi}^{\alpha}$, then it can also be shown that

$$\boldsymbol{\chi}(\mathbf{X}, t) = \left(\sum_{\alpha=1}^N m^{\alpha} \boldsymbol{\xi}^{\alpha} \otimes \boldsymbol{\Xi}^{\alpha} \psi(\mathbf{X}^{\alpha} - \mathbf{X}) \right) \cdot \left(\sum_{\alpha=1}^N m^{\alpha} \boldsymbol{\Xi}^{\alpha} \otimes \boldsymbol{\Xi}^{\alpha} \psi(\mathbf{X}^{\alpha} - \mathbf{X}) \right)^{-1}. \quad (3.86)$$

This expression for micro-deformation gradient bears a strong resemblance to the expressions developed by both Horstemeyer *et al.* [115, 116, 101] and Zimmerman [256] (including the relations defined in Chapter 2) to define an atomic-scale deformation gradient. In their expressions, relative

distances between an atom and its neighbors in both the reference and current configurations are used to estimate a deformation gradient. Our expression more closely resembles the one derived by Horstemeyer *et al.*, who also considered interactions with multiple shells of neighbors and used an analytic function (similar to ψ) to weight how the neighbors affect the local estimate of deformation gradient. The expression given by equation (2.17) considers the specific case of ψ being a Heaviside function defined over a volume that only encompasses the nearest neighbors to the center point. Detailed comparisons between our micro-deformation gradient and the atomic-scale equivalent defined in these works is deferred for future work.

3.6 Appendix: Non-symmetric Cauchy stress due to directional bonding

It can be shown that inter-atomic potentials representative of directional bonding will result in a non-symmetric Cauchy stress. To accomplish this, we use the “potential” portion of the Hardy expression, $\boldsymbol{\sigma} = -\frac{1}{2} \sum_{\alpha=1}^N \sum_{\beta \neq \alpha}^N \mathbf{f}^{\alpha\beta} \otimes \mathbf{x}^{\alpha\beta} \tilde{B}^{\alpha\beta}(\mathbf{x})$, combined with our new expression for $\mathbf{f}^{\alpha\beta} = -\left\{ \frac{\partial \phi^\alpha}{\partial \mathbf{x}^{\alpha\beta}} + \frac{\partial \phi^\beta}{\partial \mathbf{x}^{\alpha\beta}} \right\}$. As a simple case, we consider the interaction of only 3 atoms (α , β and δ) through a single 3-body potential energy term Φ ,

$$\Phi = \Phi(\mathbf{x}^{\alpha\beta}, \mathbf{x}^{\alpha\delta}). \quad (3.87)$$

This form fits the case of the 3-body term in the Stillinger-Weber potential [226] where α is the center atom of the β - α - δ triplet and

$$\Phi(\mathbf{x}^{\alpha\beta}, \mathbf{x}^{\alpha\delta}) = \varepsilon \lambda \exp\left(\frac{\gamma}{\frac{x^{\alpha\beta}}{\sigma} - a}\right) \exp\left(\frac{\gamma}{\frac{x^{\alpha\delta}}{\sigma} - a}\right) \left\{ \cos(\theta) + \frac{1}{3} \right\}^2, \quad (3.88)$$

where ε , λ , γ , σ and a are fitted material parameters and

$$\theta \equiv \arccos\left(\frac{\mathbf{x}^{\alpha\beta} \cdot \mathbf{x}^{\alpha\delta}}{x^{\alpha\beta} x^{\alpha\delta}}\right). \quad (3.89)$$

Using the relation $\phi^\alpha = \phi^\alpha(\mathbf{x}^{\alpha\beta}, \mathbf{x}^{\alpha\gamma}, \dots, \mathbf{x}^{\alpha N})$, the full energy Φ is partitioned equally among the 3 atoms, $\phi^\alpha = \phi^\beta = \phi^\delta = \frac{1}{3}\Phi$. However, in order to correctly take partial derivatives of these individual energies, we must express the functional dependency for each energy correctly. For atom α , the expression is trivial,

$$\phi^\alpha = \frac{1}{3}\Phi(\mathbf{x}^{\alpha\beta}, \mathbf{x}^{\alpha\delta}), \quad (3.90)$$

but for atoms β and δ , the expressions are

$$\phi^\beta = \phi^\beta(\mathbf{x}^{\beta\alpha}, \mathbf{x}^{\beta\delta}) = \frac{1}{3}\Phi(\mathbf{x}^{\alpha\beta}, \mathbf{x}^{\alpha\delta} + \mathbf{x}^{\beta\delta}) \quad (3.91)$$

$$\phi^\delta = \phi^\delta(\mathbf{x}^{\delta\alpha}, \mathbf{x}^{\delta\beta}) = \frac{1}{3}\Phi(\mathbf{x}^{\alpha\delta} + \mathbf{x}^{\delta\beta}, \mathbf{x}^{\alpha\delta}) \quad (3.92)$$

In these relations, we have substituted $\mathbf{x}^{\alpha\beta} + \mathbf{x}^{\beta\delta}$ for $\mathbf{x}^{\alpha\delta}$ in the expression for ϕ^β since it cannot depend directly on $\mathbf{x}^{\alpha\delta}$. Likewise for the ϕ^δ term, we have substituted $\mathbf{x}^{\alpha\delta} + \mathbf{x}^{\delta\beta}$ for $\mathbf{x}^{\alpha\beta}$. Obviously, clarity requires that any expression that uses Φ in a simple way must refer to its original form shown in (3.87). So, when partial derivatives are taken, they must include terms that may indirectly depend on certain variables. For example,

$$\frac{\partial \phi^\beta}{\partial \mathbf{x}^{\alpha\beta}} = \frac{1}{3} \left(\frac{\partial \Phi}{\partial \mathbf{x}^{\alpha\beta}} + \frac{\partial \Phi}{\partial \mathbf{x}^{\alpha\delta}} \frac{\partial \mathbf{x}^{\alpha\delta}}{\partial \mathbf{x}^{\alpha\beta}} \right) = \frac{1}{3} \left(\frac{\partial \Phi}{\partial \mathbf{x}^{\alpha\beta}} + \frac{\partial \Phi}{\partial \mathbf{x}^{\alpha\delta}} \right). \quad (3.93)$$

Equation (3.93) is easily understood. The first term inside the parentheses results from the derivative of Φ with respect to $\mathbf{x}^{\alpha\beta}$ as it appears explicitly within the normal functional form of Φ , but the second term is present because Φ also depends on $\mathbf{x}^{\alpha\delta}$, which itself depends on $\mathbf{x}^{\alpha\beta}$ through the relation $\mathbf{x}^{\alpha\delta} = \mathbf{x}^{\alpha\beta} + \mathbf{x}^{\beta\delta}$. Since

$$\frac{\partial \phi^\alpha}{\partial \mathbf{x}^{\alpha\beta}} = \frac{1}{3} \left(\frac{\partial \Phi}{\partial \mathbf{x}^{\alpha\beta}} \right), \quad (3.94)$$

we can now calculate $\mathbf{f}^{\alpha\beta}$ to be

$$\begin{aligned} \mathbf{f}^{\alpha\beta} &= - \left\{ \frac{\partial \phi^\alpha}{\partial \mathbf{x}^{\alpha\beta}} + \frac{\partial \phi^\beta}{\partial \mathbf{x}^{\alpha\beta}} \right\} \\ &= - \left\{ \frac{1}{3} \left(\frac{\partial \Phi}{\partial \mathbf{x}^{\alpha\beta}} \right) + \frac{1}{3} \left(\frac{\partial \Phi}{\partial \mathbf{x}^{\alpha\beta}} + \frac{\partial \Phi}{\partial \mathbf{x}^{\alpha\delta}} \right) \right\} \\ &= - \left\{ \frac{2}{3} \frac{\partial \Phi}{\partial \mathbf{x}^{\alpha\beta}} + \frac{1}{3} \frac{\partial \Phi}{\partial \mathbf{x}^{\alpha\delta}} \right\}. \end{aligned} \quad (3.95)$$

Similarly, for this example

$$\mathbf{f}^{\alpha\delta} = - \left\{ \frac{2}{3} \frac{\partial \Phi}{\partial \mathbf{x}^{\alpha\delta}} + \frac{1}{3} \frac{\partial \Phi}{\partial \mathbf{x}^{\alpha\beta}} \right\}, \quad (3.96)$$

It is interesting to note that the expression for $\mathbf{f}^{\alpha\beta}$ in (3.95) involves derivatives with respect to inter-atomic vectors other than just $\mathbf{x}^{\alpha\beta}$, and that it is not necessarily collinear with $\mathbf{x}^{\alpha\beta}$.

Combining the expressions in equations (3.95) and (3.96) with a similarly derived expression for $\mathbf{f}^{\beta\delta}$, the expression for Cauchy stress becomes:

$$\begin{aligned} \boldsymbol{\sigma}(\mathbf{x}, t) &= -\frac{1}{2} \sum_{\alpha=1}^N \sum_{\beta \neq \alpha}^N \mathbf{x}^{\alpha\beta} \otimes \mathbf{f}^{\alpha\beta} \tilde{B}^{\alpha\beta}(\mathbf{x}) \\ &= -\mathbf{x}^{\alpha\beta} \otimes \mathbf{f}^{\alpha\beta} \tilde{B}^{\alpha\beta}(\mathbf{x}) - \mathbf{x}^{\alpha\delta} \otimes \mathbf{f}^{\alpha\delta} \tilde{B}^{\alpha\delta}(\mathbf{x}) - \mathbf{x}^{\beta\delta} \otimes \mathbf{f}^{\beta\delta} \tilde{B}^{\beta\delta}(\mathbf{x}) \\ &= \mathbf{x}^{\alpha\beta} \otimes \left\{ \frac{2}{3} \frac{\partial \Phi}{\partial \mathbf{x}^{\alpha\beta}} + \frac{1}{3} \frac{\partial \Phi}{\partial \mathbf{x}^{\alpha\delta}} \right\} \tilde{B}^{\alpha\beta}(\mathbf{x}) + \mathbf{x}^{\alpha\delta} \otimes \left\{ \frac{1}{3} \frac{\partial \Phi}{\partial \mathbf{x}^{\alpha\beta}} + \frac{2}{3} \frac{\partial \Phi}{\partial \mathbf{x}^{\alpha\delta}} \right\} \tilde{B}^{\alpha\delta}(\mathbf{x}) \\ &\quad + \mathbf{x}^{\beta\delta} \otimes \left\{ -\frac{1}{3} \frac{\partial \Phi}{\partial \mathbf{x}^{\alpha\beta}} + \frac{1}{3} \frac{\partial \Phi}{\partial \mathbf{x}^{\alpha\delta}} \right\} \tilde{B}^{\beta\delta}(\mathbf{x}), \end{aligned} \quad (3.97)$$

which can be simplified to

$$\begin{aligned}\boldsymbol{\sigma}(\mathbf{x}, t) = & \mathbf{x}^{\alpha\beta} \otimes \left\{ \frac{2}{3} \frac{\partial \Phi}{\partial \mathbf{x}^{\alpha\beta}} + \frac{1}{3} \frac{\partial \Phi}{\partial \mathbf{x}^{\alpha\delta}} \right\} \tilde{B}^{\alpha\beta}(\mathbf{x}) + \mathbf{x}^{\alpha\delta} \otimes \left\{ \frac{1}{3} \frac{\partial \Phi}{\partial \mathbf{x}^{\alpha\beta}} + \frac{2}{3} \frac{\partial \Phi}{\partial \mathbf{x}^{\alpha\delta}} \right\} \tilde{B}^{\alpha\delta}(\mathbf{x}) \\ & + \left\{ \mathbf{x}^{\alpha\delta} - \mathbf{x}^{\alpha\beta} \right\} \otimes \left\{ -\frac{1}{3} \frac{\partial \Phi}{\partial \mathbf{x}^{\alpha\beta}} + \frac{1}{3} \frac{\partial \Phi}{\partial \mathbf{x}^{\alpha\delta}} \right\} \tilde{B}^{\beta\delta}(\mathbf{x}).\end{aligned}\quad (3.98)$$

To proceed further, we assume that the potential function Φ can be expressed as an alternative function $\hat{\Phi}$ that depends only on the invariants $x^{\alpha\beta}$, $x^{\alpha\delta}$ and θ (as defined in equation (3.89)):

$$\Phi = \Phi(\mathbf{x}^{\alpha\beta}, \mathbf{x}^{\alpha\delta}) = \hat{\Phi}(x^{\alpha\beta}, x^{\alpha\delta}, \cos \theta). \quad (3.99)$$

This assumption is certainly true for the Stillinger-Weber 3-body term (3.88) and can be generalized for other potentials representative of directional bonding. Using (3.99), we obtain the relations

$$\begin{aligned}\frac{\partial \Phi}{\partial \mathbf{x}^{\alpha\beta}} &= \frac{\partial \hat{\Phi}}{\partial x^{\alpha\beta}} \frac{\mathbf{x}^{\alpha\beta}}{x^{\alpha\beta}} + \frac{\partial \hat{\Phi}}{\partial c_\theta} \left[\frac{\mathbf{x}^{\alpha\delta}}{x^{\alpha\beta} x^{\alpha\delta}} - \frac{c_\theta}{x^{\alpha\beta} x^{\alpha\beta}} \right] \\ \frac{\partial \Phi}{\partial \mathbf{x}^{\alpha\delta}} &= \frac{\partial \hat{\Phi}}{\partial x^{\alpha\delta}} \frac{\mathbf{x}^{\alpha\delta}}{x^{\alpha\delta}} + \frac{\partial \hat{\Phi}}{\partial c_\theta} \left[\frac{\mathbf{x}^{\alpha\beta}}{x^{\alpha\beta} x^{\alpha\delta}} - \frac{c_\theta}{x^{\alpha\delta} x^{\alpha\delta}} \right],\end{aligned}\quad (3.100)$$

where c_θ represents $\cos \theta$. Substituting the above relations into equation (3.98), we clearly see that the expression for $\boldsymbol{\sigma}(\mathbf{x}, t)$ will contain many terms that are non-symmetric. Specifically, the quantities $\mathbf{x}^{\alpha\beta} \otimes \mathbf{x}^{\alpha\delta}$ and $\mathbf{x}^{\alpha\delta} \otimes \mathbf{x}^{\alpha\beta}$ will both be present but will not have the same scalar coefficient, a requirement for a symmetric tensor.

One result we can obtain is the expression for the average stress, $\bar{\boldsymbol{\sigma}}(t)$, for the entire volume V of the system. Integrating both sides of equation (3.98), we obtain

$$\begin{aligned}\bar{\boldsymbol{\sigma}}(t) &= \frac{1}{V} \left(\mathbf{x}^{\alpha\beta} \otimes \left\{ \frac{2}{3} \frac{\partial \Phi}{\partial \mathbf{x}^{\alpha\beta}} + \frac{1}{3} \frac{\partial \Phi}{\partial \mathbf{x}^{\alpha\delta}} \right\} + \mathbf{x}^{\alpha\delta} \otimes \left\{ \frac{1}{3} \frac{\partial \Phi}{\partial \mathbf{x}^{\alpha\beta}} + \frac{2}{3} \frac{\partial \Phi}{\partial \mathbf{x}^{\alpha\delta}} \right\} \right. \\ &\quad \left. + \left\{ \mathbf{x}^{\alpha\delta} - \mathbf{x}^{\alpha\beta} \right\} \otimes \left\{ -\frac{1}{3} \frac{\partial \Phi}{\partial \mathbf{x}^{\alpha\beta}} + \frac{1}{3} \frac{\partial \Phi}{\partial \mathbf{x}^{\alpha\delta}} \right\} \right) \\ &= \frac{1}{V} \left(\mathbf{x}^{\alpha\beta} \otimes \frac{\partial \Phi}{\partial \mathbf{x}^{\alpha\beta}} + \mathbf{x}^{\alpha\delta} \otimes \frac{\partial \Phi}{\partial \mathbf{x}^{\alpha\delta}} \right)\end{aligned}\quad (3.101)$$

Substitution of (3.100) into (3.101), along with simplification of terms, results in the expression

$$\begin{aligned}\bar{\boldsymbol{\sigma}}(t) &= \frac{1}{V} \left(\left[\frac{\partial \hat{\Phi}}{\partial x^{\alpha\beta}} - \frac{\partial \hat{\Phi}}{\partial c_\theta} \frac{c_\theta}{x^{\alpha\beta}} \right] \frac{\mathbf{x}^{\alpha\beta} \otimes \mathbf{x}^{\alpha\beta}}{x^{\alpha\beta}} + \left[\frac{\partial \hat{\Phi}}{\partial x^{\alpha\delta}} - \frac{\partial \hat{\Phi}}{\partial c_\theta} \frac{c_\theta}{x^{\alpha\delta}} \right] \frac{\mathbf{x}^{\alpha\delta} \otimes \mathbf{x}^{\alpha\delta}}{x^{\alpha\delta}} \right. \\ &\quad \left. + \frac{\partial \hat{\Phi}}{\partial c_\theta} \frac{\left\{ \mathbf{x}^{\alpha\beta} \otimes \mathbf{x}^{\alpha\delta} + \mathbf{x}^{\alpha\delta} \otimes \mathbf{x}^{\alpha\beta} \right\}}{x^{\alpha\beta} x^{\alpha\delta}} \right).\end{aligned}\quad (3.102)$$

Clearly, the average stress for the system is a symmetric quantity. This explains why standard continuum theory adequately describes the deformation of directional bonded materials such as silicon. At the macroscopic scale, asymmetries in stress are probably minor and unnoticeable. However, at the microscopic scale, these asymmetries may be significant and indicative of the need for a microcontinuum theory.

Chapter 4

Micropolar Small Strain Deformation Theory

Principal Authors: Jason R. Mayeur, David L. McDowell and Douglas J. Bammann

The initial stated objective of this project was to develop micro-continuum theories of crystal plasticity that are more advanced than what is currently used in the existing literature by appealing to the disclination concept. The genesis of this objective grew out of a series of previous works by Clayton, Bammann, and McDowell [44, 45, 42, 46, 43, 47], and was motivated by at least two related observations: i) as metallic single crystals undergo extreme deformation, they begin to fragment and separate into subgrain and blocky structures which are characterized by different characteristic length scales and ii) these structures are distinct in terms of their relative misorientation of neighboring regions, including evolution of high-angle boundaries. It was posited that the introduction of the (geometrically necessary, GN) disclinations, which is a rotational defect, in addition to the commonly used GN dislocations within the framework of a continuum crystal plasticity theory could be a valuable tool to describe such phenomena, particularly in relation to high-angle boundaries. Their rationale being that the characteristic length introduced by GN dislocations is related to the subgrain size, while the characteristic length associated with the GN disclinations is related to the cell block size, and that subgrain boundaries (low angles of misorientation) are composed of GN dislocations while cell blocks (high angles of misorientation) GN disclinations. Serving as further motivation for incorporation of the disclination concept within a continuum crystal plasticity model are several discrete models of grain boundaries (GBs), which use groups of disclination dipoles or disclination structural units to characterize the structure of high angle GBs because the description of such boundaries in terms of discrete dislocations is no longer possible due to overlapping of the dislocation cores.

As the work progressed, however, it was realized that while the rationale for including disclinations is solid, the finite deformation micropolar crystal plasticity theory presented in Clayton *et al.* [47] is still incomplete as a starting point. As a result, the objectives of the work were modified to focus more on the problem of enhanced GB descriptions within the framework of geometrically linear micropolar crystal plasticity theory building upon the previous efforts of Forest and collaborators [76, 77, 78, 79, 217]. In pursuit of these objectives several interesting discoveries have been made, which have led us down a path that is somewhat different than what was originally proposed.

In what follows, a generalized continuum crystal plasticity model is developed to account for size-dependent mechanical response, and additionally contributes a novel approach for the enhanced treatment of grain boundaries (GBs); specifically the role they play in slip obstruction,

absorption, and transmission. The model development will be couched within the context of a micropolar continuum. Borrowing from previous work on micropolar single crystal plasticity [77], we will explore alternate formulations which have formal analogies to non-crystallographically-based micropolar plasticity theories (cf. [81] and references therein). It has been suggested by Sievert *et al.* [217], that the micropolar approach can be used as a substitute to the more commonly found extended crystal plasticity theories which include constitutive dependence on Nye's [182] dislocation density tensor in terms gradients of slip (or slip rates) [16, 72, 149]. Therefore, a main contribution of this work will be to ascertain the predictive capabilities of micropolar single crystal plasticity, and determining whether or not it is fruitful to advance its development instead of pursuing the more traditional generalized crystal plasticity approaches.

Due to the uncertainty surrounding which type of micropolar plasticity framework will prove to be the most advantageous, an enhanced GB treatment will be developed, as much as is possible, such that it can be embedded into any general crystal plasticity theory. The proposed model will account for the geometry of the incoming/outgoing slip planes, the GB orientation and structure, and the evolution of the boundary's resistance to slip through an appropriate choice of internal state variables (ISVs). In contrast to current state-of-the-art approaches for modeling GBs, which tend to describe the increased slip resistance solely in terms of the presence of excess geometrically necessary dislocations or jump discontinuity in the plastic distortion, we are motivated by experimental observations to propose a non-associative plasticity model to describe the slip transmission process. In this work, the GB model will be embedded within a modified version of the micropolar single crystal treatment, and finite element (FE) simulations will be performed and compared to related experiments and finer scale simulations. The framework will require guidance from models at lower length scales in the selection of the appropriate ISVs, specification of their evolution equations, and stress-state dependence (yield function) for a given type of boundary.

The work represents advancements in both the development and understanding of a class of generalized (micropolar) crystal plasticity models. This undertaking will provide guidance on which type of micropolar formulation may be worth further pursuing as an alternative to the more common types of slip-gradient based approaches to crystal plasticity. Moreover, a novel methodology describing the effectiveness of GBs against initial slip transfer as well as boundary strength evolution is presented in terms of slip system geometry and GB structure. The model will be developed such that it is amenable for inclusion within arbitrary crystal plasticity models, and can accept information from more detailed simulations or observations of dislocation/GB interactions.

4.1 Introduction

The emergence of engineering components with specimen and microstructural features with dimensions reaching into the submicron and nanometer regimes has driven the need to develop advanced material models capable of describing their often unique and size-dependent behavior as compared to more conventional engineering components and materials. Classical continuum models, being devoid of any type of model-dependent length-scale lack the ability to adequately capture such responses. An alternate motivation for incorporating length-scale parameters in continuum-

level models arises out of the study of strain-localization and/or strain-softening problems. Within the context of FE simulations, these types of boundary value problems exhibit pathological mesh dependence of results with respect to the thickness and spacing of the localization bands. This is due to the loss of Hadamard ellipticity of the governing equations for the classical continua. To counter these types of issues, the notion of the generalized continuum was developed on several different competing conceptual fronts. Some typical classes of generalized continua are those based on: non-local integral formulations, gradients of internal state variables (ISVs), higher-order gradients of fundamental kinematic quantities (*i.e.* , displacements), and independent micro-deformations. There are also innumerable models which consist of different combinations of the aforementioned frameworks. Non-local integral formulations are based on the selection of a particular kinematic or ISV quantity in which the non-local dependence is achieved by defining the quantity of interest at a given location in terms of an influence integral over a finite spatial domain about the point. Non-local gradient of ISV theories, as the name suggests, include additional constitutive dependence on the gradient of the ISV at the material point. Theories incorporating higher-order gradients of the fundamental kinematic quantities (often referred to as Grade- n theories) rely on enriched definitions of deformation power, resulting in the appearance of hyper-stresses in generalized balances of linear and angular momentum. Finally, the class of continua with independent micro-deformations, sometimes referred to as continua with latent microstructure or micromorphic continua, are theories in which variables associated with additional microstructure (scalar, vectorial, or tensorial) are endowed to each continuum point. In such models, the micro-deformation is assumed to operate independently of the macro-motion; as a consequence these theories have non-classical expressions of deformation power and require the specification of additional boundary conditions. In summary, generalized continuum models have been developed to address both the mathematical and physical limitations of their classical continuum counterparts.

In polycrystalline metals, the grain size has long been considered as a critical microstructural dimension related to the strength of the material dating back to the works of Hall [107] and Petch [186]. In their studies an empirical relationship between the mean grain size and the initial yield strength was determined, and then subsequently extended by Armstrong *et al.* [14] to address the entire plastic regime. The respective Hall-Petch (HP) and extended HP relationships, describe in an average macroscopic way the effective resistance to dislocation transmission through GBs. While the HP relationship is essentially universally accepted within the scope of conventional grain-sized polycrystals, there is less agreement upon the physical origins of the observed effect. As outlined in Evers *et al.* [73], there are three basic schools of thought describing the smaller is stronger phenomenon in conventional micron grain-sized materials. The originally proposed explanation was centered around the idea that dislocations, because they are obstructed at GBs, form pile-ups which then activate dislocation sources in neighboring grains as a result of the stress concentration at the tip of the pile-up [107, 186, 52]. However, as Evers *et al.* [73] point out, a major flaw of this argument is that in BCC-structured materials, where no pile-ups have been observed, the HP relation still holds. A second school of thought attributes the origin of the HP effect to an increased amount of strain-hardening resulting from the accumulation of geometrically necessary dislocations (GNDs) near the GBs [19]. As the grain size decreases, there is inherently an increased degree of inhomogeneous plastic flow (*i.e.* , strain-gradients) which is directly related to the GND density. It is argued in turn, that the increased dislocation density in the presence of deformation heterogeneity leads to a reduction in the mean free path for mobile dislocation

segments and produces an enhanced strengthening effect. The main drawback of this type of model is that, as it stands, it can only predict the grain-size dependence in the strain-hardening regime and not on the initial yield strength, although more recent works have addressed this issue by calculating initial GB GND densities between neighboring grains based on lattice misorientation [71]. A third possible explanation originally presented by Li and Chou [144] appeals to the role of GBs acting as dislocation sources, which do not necessarily require the stress-concentration due to a pile-up to be activated. Other sources of stress-concentration, such as those induced by GB ledges or GB lattice mismatches aided by the elastic anisotropy of the neighboring crystals and/or the presence of initial misfit dislocations, may serve as the initiators of plastic flow in this case. One shortcoming of this explanation for the behavior of conventional grain-sized materials is that it is commonly accepted that the initial stages of plastic deformation in these materials is due to the motion of pre-existing mobile dislocation density within the grain interiors. In actuality, the manifestation of the HP effect is probably the result of a combination of all the aforementioned phenomenon.

The preceding discussion of the HP effect was presented within the context of the so-called conventional grain-size polycrystals. With the emergence of ultra-fine grained (ufg) and nanocrystalline (nc) materials, a new chapter is opened in the discussion of the HP effect and some have reported of its breakdown or in some cases the “inverse” HP effect (cf. [30] and references therein). The breakdown of HP behavior is debated within the research community, with detractors attributing the anomalous response to poor processing techniques used in some of the earlier studies on nc materials [32, 48, 130, 193]. Regardless of whether or not the HP slope for such materials becomes negative or is merely reduced is somewhat irrelevant in terms of the big picture, but what is most important is the fact that the same type of dislocation processes which dominate in conventional grain-sized materials do not dictate the mechanical response in nc materials. For example, in nc materials there is very little, if any, pre-existing mobile dislocation density within grain interiors and a much higher volume ratio of grain boundaries to grain interiors. Accordingly, for this class of materials, a number of diverse models have been developed to explain the observed size-dependent deformation behavior. Carlton and Ferreira [30] have classified these models into four generic classes: dislocation-based, diffusion-based, GB shearing, and composite. The dislocation-based models focus on the potency of GBs as dislocation sources/sinks in which a “dislocation event” [247] is proposed to consist of a simultaneous nucleation/absorption process in which the nucleated dislocation completely transverses the grain in a single “jump” and is absorbed by the boundary on the opposite side. This is thought to be possible due to the lack of dislocation obstacles within grain interiors. The diffusion-based and GB shearing models are quite diverse and rest on the assumption that these alternate deformation mechanisms either replace or compete with traditional dislocation-based inelastic deformation mechanisms. Finally, the composite-type models [165] usually consider the nc material as made up of either two (grain interior and boundary) or three (grain interior, boundary, and triple point) distinct phases which may have different types of constitutive laws and/or different material properties for each respective constituent. Again, as with the traditional grain-sized materials, the mechanical behavior of nc materials is probably the result of a combination of the above described micro-deformation mechanisms which depends on the material, the manufacturing process, loading conditions, etc. In other words, there probably is not a “universal” method of modeling all such materials in terms of one physical mechanism. What can be said for these materials is that the increased number of GBs (especially high-angle GBs)

and low initial mobile dislocation density within the grain interiors results in the accommodation of plastic deformation by GBs playing an even more critical role in nc materials than they do in their conventional grain-sized counterparts.

It is with these considerations in mind that we give our plan of proposed research centered about the development of micropolar crystal plasticity models accounting for the influence of GBs. In Section 4.2, relevant background and the current state of the art related to all aspects of the research are reviewed and discussed. Section 4.3 presents a detailed description of the model formulation, Section 4.4 covers the numerical implementation, and Section 4.5 discusses some early numerical results. In conclusion, Section 4.6 summarizes the scope of what has been accomplished to date and maps a path for the future progression of the work

4.2 Background

4.2.1 Generalized Crystal Plasticity

Traditional models of crystalline inelasticity (cf. [18]), as previously mentioned, are incapable of predicting size-dependent mechanical behavior as the constitutive formulation does not include an inherent length scale. The single crystal strength in this case is governed by strain-like ISVs whose evolution is related to the rate of plastic shearing on active slip systems and the cumulative amount of slip. Such ISVs, whether isotropic or kinematic in nature, are typically assumed to be reflective of the scalar statistically stored dislocation density. The most common approach to extending crystal plasticity to account for size effects is to appeal to the notion of GNDs. As argued by Ashby [19], GNDs are a measure of the inhomogeneity of plastic flow in the material which leads to additional strain-hardening. Because the heterogeneity of deformation within a volume of material is directly related to the size of the microstructural constituents, size-dependent mechanical behavior is a natural outcome. The origins of the connection between heterogeneous states of strain, deformation incompatibility, and geometrically necessary defects can be traced back to the early works of Kondo [129], Bilby *et al.* [28] and Kroner [133] amongst others, whereas the connection between GNDs and lattice curvature is traced back to work of Nye [182].

As evidenced by the diversity of crystal plasticity models incorporating the effects of GNDs, there are a number of ways to construct such a theory. Generally speaking, there are three main ingredients to developing an elastoplasticity theory: kinematics, thermodynamics, and kinetics. In the realm of kinematics one must define the continuum degrees-of-freedom (displacements, rotations, micro-deformations, etc.), invariant strain or deformation measures (strain, torsion-curvature, etc.), and introduce appropriate elastic-plastic decompositions of the deformation measures separating reversible and irreversible parts of the process. The thermodynamic portion of the model involves defining the deformation power (energy principle), a free energy potential functional which is separated into recoverable (elastic constitutive equations) and irreversible (specification of ISVs and their evolution equations) parts, and the determination of mechanical balance laws which is usually done employing the principle of virtual power [90, 157]. Additionally, an en-

trophy inequality is usually specified and combined with the energy principle to deduce restrictions on the constitutive equations (including kinetic relations) and determine the state laws.

When it comes to selecting the appropriate set of ISVs and specifying their evolution equations, some authors prefer a consistent continuum thermodynamic approach [215, 230], while others opt for more classical heuristic approaches [149, 73, 2]. Probably the most important model consideration is whether or not to enhance the expression for deformation power to include a contribution from either rate of the GND tensor or equivalently the slip rates. Inclusion of such terms leads to theories with ancillary balance laws concerning the micro-forces which are work conjugate to these newly added microstructural degrees-of-freedom (DOF). These micro-force balances which augment the usual Newtonian force balances of linear and angular momentum are equivalent to the so-called material or configurational force balances, which have been discussed in the monographs of Gurtin [102] and Maugin [158]. Central to these theories, as stated by Gurtin [106] “is the belief that theories of mechanics should account for the working associated with each independent kinematical process”. Within Gurtin’s theory [106] this results in the introduction of a system of micro-forces work conjugate to the slip rates and their gradients. The slip system level micro-force balance coupled with the constitutive restrictions placed on the micro-forces derived from a purely mechanical form of the entropy inequality results in what can be interpreted as the viscoplastic yield conditions for each slip system. The notion of fictitious configurational forces acting on microstructural singularities dates back to the works of Peach and Koehler [184] and Eshelby [69]. The idea that these forces should be required to satisfy their own balance laws, however, is much more recent, and in the case of dissipative material behavior (*i.e.*, plasticity, damage, etc.), these advanced theories are still the subject of intense research and debate. One of the major concerns regarding these formalisms is the question of specifying appropriate boundary conditions for the non-standard kinematic quantities and conjugate driving forces. Additionally, due to the complex structure of the governing equations of these models, they are not yet amenable to numerical computation except under certain idealized conditions.

Counter to the approaches of enhanced deformation power are those that retain the classical structure of the mechanical balance laws. In these types of models, there are two typical ways to proceed with the model development and implementation. One method takes the GND densities or slip gradients as additional degrees-of-freedom in the sense that within a finite element implementation of the constitutive framework, they serve as additional nodal DOF subject to their own (non-working) balance equation. Some examples of models that fall under this category are Evers *et al.* [70], Arsenlis and Parks [16] and Kuroda and Tvergaard [135] and like the micro-force theories previously discussed, they require the specification of additional boundary conditions for the weak form FE implementation of the GND density balance. One apparent drawback to this type of model is that it seems to lead to two distinct types of boundary conditions; the so-called micro-clamped (no slip at the boundary) or micro-free (unimpeded slip at the boundary) conditions, whereas it would seem that more intermediate types of conditions would be needed to describe GND evolution at more general types of interfaces (*i.e.*, GBs) where partial slip transmission occurs. An alternative approach, sometimes referred to as the “low-order theories”, is that in which the specification of additional boundary conditions on slip are not required. The works of Acharya and Bassani [2], Meisssonier *et al.* [163], and Ma *et al.* [149] fall under this classification, and the presence of GNDs is reflected merely through a contribution to the material strain-hardening

without the influence of any type of slip constraints.

Regardless of the model type, another important issue is how the presence of GNDs is reflected in the description of strain-hardening. A fairly standard approach [108] is the incorporation of the GND density, ρ_{GND} , into an extended Taylor expression, *i.e.* $\tau_\alpha = \alpha\mu b\sqrt{\rho_{SSD} + \rho_{GND}}$, where the statistically stored dislocation density, ρ_{SSD} , is that which appears in classical crystal plasticity theory and is function of the current slip rates as well as the amount of cumulative shear, whereas the GND density, ρ_{GND} , captures the additional hardening due to slip gradients. While this isotropic contribution to material hardening is thought to be important, it is frequently asserted that kinematic hardening associated with the long-range stresses (back stresses) caused by GNDs is the more critical physical phenomenon. It is noted here that the common understanding is that the gradient in the GND density (*i.e.* , second gradient of slip) is proportional to the back stress, and not the GND density itself [98, 99]. This contribution appears naturally in the micro-force theories (cf. Gurtin [106]), and is incorporated in more phenomenological ways in the works of [70, 17].

4.2.2 Grain Boundary Treatment within Crystal Plasticity

4.2.2.1 Experimental Observations and Fine-Scale Modeling Results

Considering the importance of dislocation/GB interactions determining the strength, ductility, and fatigue/fracture properties of metals there have been several studies focused on determining a set of criteria that can be applied to predict the likelihood of particular slip transmission events through GBs. Early experimental efforts in this regard undertaken by Shen *et al.* [24, 40, 213, 214] and Lee *et al.* [138, 139, 140, 141, 142, 198] led to the following set of rules to rank the preference for potential reactions, which are hereafter referred to as the LRB (Lee, Robertson and Birnbaum) criteria:

1. The angle between the intersection lines of the incoming and outgoing slip planes within the GB plane should be as small as possible.
2. The magnitude of the Burgers vector of any residual dislocations left at the GB after transmission should be small.
3. The resolved shear stress acting on the outgoing dislocations should be high.

These criteria underscore the importance of both GB and slip plane geometry, the dislocation character, and the local stress state. Seeking to give the criteria a quantitative backing, de Koning *et al.* [56] developed a continuum dislocation line tension model which considered a dislocation (Frank-Read) source of a certain length and distance from the boundary within the framework of isotropic elasticity. The model does not account for the atomic structure of the GB or the internal stress field that it induces, but it does result in predictions consistent with the LRB criteria, and enables a quantitative comparison of the critical stress required for transmission between different interaction scenarios. Furthermore, they state that in terms of a crude approximation, the single

most critical parameter in determining the constraint placed on slip transmission by the GB is the ratio of the critical activation stress to the source activation stress when there is no boundary present.

More recently, Dewald and Curtin [61, 60] have used the novel multi-scale framework of coupled atomistic/discrete dislocation (CADD) to study the interaction of incoming dislocations with a few different types of GBs in Al. The multi-scale nature of their code enables them to circumvent some of the limitations imposed when studying similar processes in an entirely atomistic setting, such as the limits on the size of the computation cell and the use of long-range periodic boundary conditions. Specifically, they have studied the interaction of edge dislocation pile-ups with a $\Sigma 11$ symmetric tilt boundary in Al [60] as well as screw dislocation pile-ups interacting with $\Sigma 3$, $\Sigma 9$, and $\Sigma 11$ symmetric tilt boundaries in Al [61]. As expected, their studies underscore that the interactions of a single dislocation with a specific type of boundary is insufficient for describing the physics of the problem relevant to sustained plasticity. The interaction of the lead dislocation in a pile-up depends on the prior history of dislocations that have already reached the GB, and in particular on whether or not extrinsic GB dislocations (EGBDs) have been generated as a result of these interactions. Depending on both the structure of the GB and the temperature, these EGBDs may either be locally concentrated or distributed throughout the GB plane. As a result of the edge dislocation study, they have proposed a set of amendments to the LRB criteria that account for the resolved shear stress on multiple slip systems (not just those of nucleation/transmission), the normal stress on the GB plane, and the step height at the slip plane intersection. In the related study on screw dislocations, Dewald and Curtin find that $\Sigma 3$ and $\Sigma 11$ boundaries absorb the lattice dislocations and generate EGBDs, while no transmission is ever observed. For the $\Sigma 9$ boundary, transmission is observed, but the critical stress depends on the nature of the pile-up and the location of the slip plane intersection with the GB. It is pointed out that the site of slip transfer across the GB was never observed to be coincident with the original slip plane intersection, and in some scenarios transmission has occurred on non-Schmid planes. Emerging from this study is yet another series of modifications to the original LRB criteria, which incorporates a dependence on the shear stress resolved in the GB plane for slip transmission and on the size of the primitive vectors of the GB for the generation of EGBDs. They acknowledge that these criteria may not be suitable for more complicated types of boundaries, and that more studies are required to fully validate their extensions to the LRB criteria which can be found in their cited articles. These works are just a starting point in the studying of dislocation/GB interactions, and there is hope that continued efforts along this front will eventually aid in the construction of more realistic treatments of GBs within the frameworks of discrete dislocation and generalized continuum models.

4.2.2.2 Continuum Elastoplasticity GB Models

Motivated by the desire to include grain size and/or GB effects into continuum plasticity models, several approaches have been adopted to achieve this goal. Here we exclude discussion on the modeling of GBs with cohesive zone elements as we are primarily interested in capturing GB effects on the initial yield strength and the earlier stages of strain-hardening behavior as opposed to phenomenological damage and failure mechanisms. The earliest and simplest extensions of traditional models consider a polycrystalline metal as a composite structure consisting of GB and grain

interior phases [26, 87, 88]. By assigning different material parameters and sometimes additional modes of deformation to each of the phases, a size-dependent mechanical response is predicted. Such models do not take into account any information regarding nearest neighbor grains (misorientation, etc.) or GB plane orientation when assigning the differences in material properties, which is typically done in a uniform, phenomenological manner.

On the opposite end of the spectrum are gradient-based plasticity models in which the plastic strain, slip, or plastic distortion are taken as nodal DOF which then allows for the specification of GB boundary conditions. These types of theories and the additional types of boundary conditions they require have already been discussed in the Section 4.2.1 on generalized crystal plasticity, but with the understanding that there is the potential for imposing conditions on GBs in addition to the outer boundaries of the domain. Using this sort of approach, Evers *et al.* [71] have developed a model that accounts for an initial GB-GND density based on the misorientation of neighboring grains, providing a more physical backing to the core-mantle type of composite approach. Obviously, as the ratio of GB surface area to grain interior volume increases (*i.e.*, smaller grain size while keeping the sample size fixed), the initial yield strength increases. Additionally, their model allows for independent GND evolution in each grain by “double-meshing” GB interfaces, however in their works to date they have only considered the two extreme micro-free and micro-clamped boundary conditions. A similar theory that takes advantage of the misorientation differences between neighboring grains to assign an initial GB-GND density has been proposed by Counts *et al.* [53, 54] to investigate the HP effect in fcc metals. Both theories maintain the classical form of the deformation power.

Alternatively, there are formulations that incorporate the plastic strain and plastic strain gradients into an enhanced expression for deformation power, and by taking advantage of this theoretical structure it is possible to postulate yield conditions (in terms of micro-force balances as discussed earlier) for the GB interface [31, 3, 4, 5, 6, 7, 86, 85, 83, 84, 103, 104, 105]. In these models, GBs, or other material interfaces, are treated as surfaces of discontinuity which possess the ability to store interfacial energy in terms of plastic strains and work-conjugate couple stresses. By augmenting the expressions for the free energy of the body or equivalently the deformation power to include the energy/work associated with the material interface, the interface yield conditions (*i.e.*, micro-force balance augmented with constitutive equations) are given in terms of a jump condition on the higher-order stresses at the interface and the derivative of the interfacial energy potential function, Ξ . This approach allows one to apply intermediate types of boundary conditions at material interfaces, yet as $\Xi \rightarrow 0$ and $\Xi \rightarrow \infty$ the limiting cases of micro-free and micro-clamped, respectively, are achieved. Among these formulations Fredriksson and Gudmundson [86, 85, 83, 84], Aifantis and Willis [5], Aifantis and Ngan [3], and Abu Al-Rub [6, 7] have given treatments which do not explicitly consider crystalline kinematics, preferring to deal with phenomenological plasticity. In contrast the series of papers by Gurtin and co-workers [31, 103, 104, 105] delve into many additional issues that arise when the microstructural details of slip are specifically considered. Fredriksson and Gudmundson [86, 85, 83, 84] have examined the size-dependent behavior of thin films in which an elastic material is perfectly bonded to a plastic material with an interfacial energy potential that is quadratic in the plastic strains. Aifantis and Willis [5] and Aifantis and Ngan [3] have studied the deformation behavior of 1-D uniaxially loaded bicrystals as well as periodic polycrystals with quadratic and more general nonlinear inter-

facial energy potentials. The theory Abu Al-Rub *et al.* [8] propose contains an even more complex form of the deformation power. While this form does not affect the interfacial treatment in this case [6, 7], the authors do suggest a generalization of the interface potential to include a deformation-independent term which could theoretically represent the surface energy of a free surface or the initial free energy of a GB. Gurtin and co-workers [31, 103, 104, 105] provide the most detailed theoretical considerations of such interfacial yield and/or boundary conditions, mainly because they have couched their theory within a crystalline kinematic framework which is furthermore based on a principle of virtual power written at the individual slip system level. Gurtin [103] first introduced the concept of a micro-frictional boundary condition for free surfaces, and then later [31] derived the higher-order traction jump conditions at the slip system level for a GB. Continued evolution of these ideas is advanced in Gurtin and Needleman [105], in which the traditional micro-clamped boundary condition is replaced with a less-restrictive natural boundary condition that arises from a slightly recast principle of virtual power. Most recently Gurtin [104] has introduced the concept of slip interaction moduli which allows for a clearer interpretation of the boundary conditions and constitutive dependencies at general interfaces.

For reasons pointed out in Ma *et al.* [150], the inclusion of an enhanced description of grain boundaries in terms of an excess of local GNDs has its limitations within the setting of a continuum model. Specifically, they discuss the shortcomings of two differing approaches i) an energetic equivalence concept and ii) a misorientation equivalence concept. The energy equivalence concept is based on translating the grain boundary energy into an equivalent array of dislocations via the Read-Shockley [190] formula. The two cited drawbacks to this approach are the inability to determine the exact nature in which these grain boundary dislocations would act as obstacles to mobile dislocations within their framework, and the disregard of the “tensorial nature” of the problem. This is an abbreviated way of saying that a micromechanical model describing the resistance of slip due to the presence of a GB should account for the geometry of the incoming and outgoing slip systems in addition to the GB orientation. The misorientation concept is based on using Nye’s dislocation density tensor calculated from the orientation jump across the grain boundary, and then backing out an equivalent GND density to represent the boundary. In regard to this approach, there are several shortcomings listed as well. Nye’s tensor, being defined in terms of small rotation gradients, is incapable of describing high angle boundaries. Furthermore, detailed atomistic calculations show that for high angle boundaries, a discrete dislocation description of the boundary no longer exists, and instead the structure and energetic properties of the boundary are best described in terms of the structural unit models. Finally, as shown by Arsenlis and Parks [15], the mapping of the GND tensor into a unique distribution of discrete dislocations is impossible due to the linear dependency of the slip system vectors. Since the initial stages of plastic deformation are dependent on the details of these dislocation arrangements, this non-uniqueness is unacceptable. To counter the deficiencies of the energetic and misorientation approaches discussed above, Ma *et al.* [150] propose to handle the issue of dislocation transmission through GBs within the framework of a thermally activated event. In their work, the transmission probability for an incoming mobile dislocation is related to the size of the residual dislocation debris (misfit dislocation) left behind at the boundary upon transmission. In summary, they propose the following methodology: For each incoming slip system, all of the possible transmission events for all of the outgoing slip systems are analyzed in terms of conservation of the lattice defect, which is expressed in terms of a single discrete dislocation in tensorial form. Using this conservation equation, they calculate the size of

the residual GB dislocation for each of the outgoing slip systems which can be directly related to the energy required to create the misfit dislocation. This additional activation energy is then added to the usual activation energy for slip on a given system, thereby providing an additional resistance to slip in the GB region.

A completely novel approach to the treatment of GBs has been proposed by Zikry and collaborators [20, 22, 23, 21, 124, 125, 255] in which they specify a system of coupled first-order differential equations governing the evolution of mobile and immobile dislocation densities in an otherwise classical crystal plasticity framework. The model accounts for generation, trapping, and annihilation of dislocations, and furthermore tracks the convection of the mobile dislocation density through the mesh using a new and original FE formulation. When a sufficiently large enough mobile density enters the GB region, the likelihood of transmission is determined through a set of geometrical considerations based on the LRB criteria. Three different mobile dislocation/GB interaction scenarios are considered: i) full and partial dislocation density transmission from one grain into neighboring grains ii) full and partial dislocation density transmission into GB and blockage at neighboring grains and iii) dislocation density impedance and the formation of pile-ups. Within their framework, they also use a composite-type of approach where GB regions are identified as a separate phase with different initial densities of mobile and immobile dislocations than the grain interiors.

In light of the previous discussions concerning the role of GBs in dictating the properties of crystalline metals, and the need for developing more physically-based generalized continuum models of crystal plasticity, it is the goal of this research to make strides towards these pursuits. It is with this in mind, that we pursue the development of a micropolar crystal plasticity model with an enhanced treatment of GBs. As highlighted in the work of Dewald and Curtin, there is still much to be learned about the interactions between different dislocation arrangements and general types of GBs. Nevertheless, by taking their observations into account, it is possible to envisage a broad framework which could be used to systematically explore the different types of dependencies that slip in the GB region has on non-Schmid stresses, GB plane normal and shear stresses, etc. using the model. As more general results become available from higher resolution simulations, they can then be easily incorporated to the model.

4.2.3 Micropolar Elastoplasticity

The earliest extensions of micropolar theory describing elastoplastic materials occurred in the late 1960s and early 1970s [27, 146, 204]. These works typically dealt with relatively straight-forward extensions of phenomenological Von Mises plasticity [27, 146, 204, 58] and fall under the category of single-criterion models [81]. Upon the re-examination of the micropolar continuum in the early 1990s [58, 57, 63, 220] within computational frameworks, the main application of interest was investigating the process of localization in strain-softening materials. Of interest was the ability of the formulation to provide numerical stability to the otherwise mesh-sensitive, mathematically degenerate problem that is encountered using classical continuum plasticity formulations more so than the existence of a specific type of microstructure. As noted in the rather comprehensive review article of Forest and Sievert [81], however, Von Mises plasticity may also be developed in a

multi-criterion framework as well. Micropolar elastoplasticity has been used in a wide range of applications for very different material systems including studying shear localization in granular materials [9, 10, 64, 232, 233, 234, 244, 246], magnetic particle systems [131], thin shell formulations [175], composites [33, 147, 151, 152, 251], and of course metals [76, 77, 78, 79, 62, 95, 177]. Most of the recent work in micropolar elastoplasticity has been advanced by four main groups of collaborators: Grammenoudis and Tsakmakis [95, 92, 93, 94, 96, 97], Forest and co-workers [76, 77, 217, 81, 80], Neff and co-workers [177, 176, 178, 179, 180], and Steinmann and co-workers [63, 219, 220, 221, 222, 225]. Among the various works, there are discussions concerning finite deformation micropolar elastoplasticity [217, 177, 93, 95, 220, 221, 202], the well-posedness and uniqueness of the micropolar elastic-plastic BVP [178, 179, 180], appropriate forms of generalized hardening rules [93], variational theorems [225], and the limiting cases of micropolar elastoplasticity and how they compare to different types of classical continuum models [92, 96, 176]. The most relevant literature to this proposal are the extensions of micropolar elastoplasticity incorporating crystalline kinematic descriptions by Forest and co-workers. The finite deformation theory is proposed by Sievert *et al.* [217] and then the geometrically linear theory is used to study slip and kink band formation [76] and grain-size effects in fcc polycrystals [77]. Further elaboration on these crystalline kinematics-based works is given in Section 4.3 outlining the proposed research plan as they are the starting point of our work.

4.3 Model Formulation

4.3.1 Kinematics

4.3.1.1 General Micropolar Theory

In the case of small displacements and rotations, the kinematics of the micropolar continuum are described by the displacement vector, \mathbf{u} , and the independent micro-rotation vector, $\boldsymbol{\phi}$. Given these degrees-of-freedom, a suitable set of deformation measures are the micropolar strain and torsion-curvature which are defined as

$$\bar{\boldsymbol{\epsilon}} = \nabla_{\mathbf{x}} \mathbf{u} - \mathcal{E} \cdot \boldsymbol{\phi} \quad (4.1)$$

$$\bar{\boldsymbol{\kappa}} = \nabla_{\mathbf{x}} \boldsymbol{\phi} \quad (4.2)$$

where \mathcal{E} is the 3rd order permutation tensor defined in equation (2.7), $\bar{\boldsymbol{\epsilon}}$ is the infinitesimal micropolar strain tensor and $\bar{\boldsymbol{\kappa}}$ is the infinitesimal micropolar torsion-flexure tensor. The overbar on the strain and torsion-curvature tensors are used to denote the kinematic measures in regard to micropolar theory. The micropolar strain tensor is generally unsymmetric, but upon splitting the tensor into symmetric and skew-symmetric parts, a more insightful perspective of its physical meaning is gained. The symmetric part of the micropolar strain tensor, $\text{sym}(\bar{\boldsymbol{\epsilon}})$, is just the classical small strain tensor, *i.e.* ,

$$\text{sym}(\bar{\boldsymbol{\epsilon}}) = \frac{1}{2} (\nabla_{\mathbf{x}} \mathbf{u} + \mathbf{u} \nabla_{\mathbf{x}}) = \boldsymbol{\epsilon} \quad (4.3)$$

and can be interpreted in the usual manner, whereas the skew-symmetric part is given by the expression

$$\text{skw}(\bar{\boldsymbol{\varepsilon}}) = -\mathcal{E} \cdot \boldsymbol{\phi} - \frac{1}{2} (\nabla_{\mathbf{x}} \mathbf{u} - \mathbf{u} \nabla_{\mathbf{x}}) = \boldsymbol{\Phi} - \boldsymbol{\omega} \quad (4.4)$$

where $\boldsymbol{\Phi} = -\mathcal{E} \cdot \boldsymbol{\phi}$ is the infinitesimal micro-spin tensor and $\boldsymbol{\omega} = \frac{1}{2} (\nabla_{\mathbf{x}} \mathbf{u} - \mathbf{u} \nabla_{\mathbf{x}})$ is the infinitesimal continuum spin tensor given by the skew-symmetric part of the displacement gradient. Clearly, the skew-symmetric part of the micropolar strain tensor is a measure of the difference between the micro-rotation and continuum rotation. In the special case where the microstructural and continuum rotations coincide, the kinematic description reduces to that of the so-called constrained micropolar material (also referred to in the literature as indeterminate couple-stress theory) in which the couple-stress is work conjugate to the gradient of the continuum rotation.

The two-dimensional geometric interpretation of these deformation measures is illustrated in Figure 4.1 for a material element under pure shear. In the undeformed body, the strain at a material

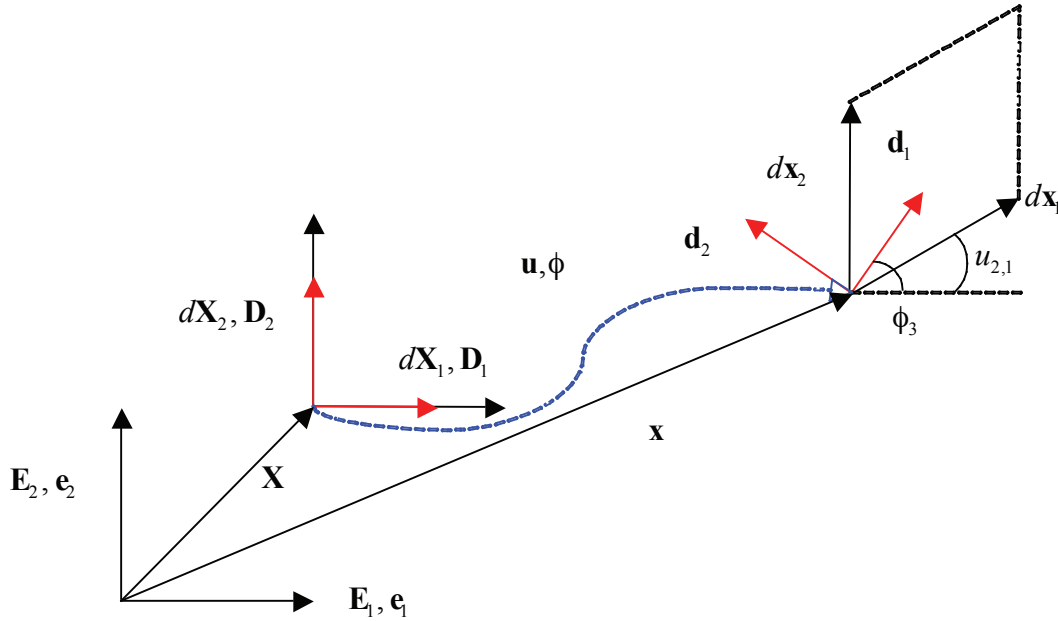


Figure 4.1. Geometric interpretation of the micropolar shear strains.

point is characterized by considering the motion of two independent sets of vectors, $d\mathbf{X}_1, d\mathbf{X}_2$ and $\mathbf{D}_1, \mathbf{D}_2$, the former being material vectors and the latter being attached to the material microstructure (drawn in red in the figure). During deformation the material and microstructural vectors are transformed into their respective counterparts, $d\mathbf{x}_1, d\mathbf{x}_2$ and $\mathbf{d}_1, \mathbf{d}_2$. The material vectors undergo both stretch and rotation, whereas the microstructural vectors undergo rigid rotation. In the figure, $u_{2,1}$ gives the magnitude of the angle of counter-clockwise rotation about the x_3 axis of the material vector $d\mathbf{X}_1$ whereas angle ϕ_3 gives the magnitude of the counter-clockwise rotation of the

microstructural vector \mathbf{D}_1 . Therefore, the relevant micropolar tensorial shear strain components $\bar{\epsilon}_{12}$ and $\bar{\epsilon}_{21}$ are the difference between the continuum and microrotations, *i.e.*, $\bar{\epsilon}_{12} = u_{2,1} - \phi_3$ and $\bar{\epsilon}_{21} = \phi_3$.

4.3.1.2 Compatibility Analysis of Classical and Micropolar continua

Note: A different convention for the micropolar deformation measures is used within this subsection in order to make direct comparisons between the classical and micropolar theories. Namely, the transposes of equations 4.1 and 4.2 are used. Both conventions appear in the literature.

Within the context of continuum plasticity models, it is obvious that the classical approach fails to describe size-dependent mechanical response due to the lack of an intrinsic length scale associated with the constitutive formulation. Numerous methodologies have been proposed to overcome this issue, including but not limited to integral formulations of the constitutive equations, constitutive dependence on higher-order displacement gradients and/or deformation measures, constitutive dependence of gradients of internal state variables, as well as models of continua with discrete microstructure or micromorphic models. In most of these models, however, the physical interpretation of the included length scale is ambiguous. Questions persist as to whether the introduced length scale is related to the size of the specimen, microstructural features, characteristic features of the deformed microstructure such as slip bands, kink bands, dislocation cell wall thickness and spacing, or some sort of combination of all of these things. Notable exceptions in this regard are the crystallographically-based plasticity models, which incorporate the notion of the GND density tensor that is related to the incompatibility of the elastic, or equivalently the plastic distortions. In the classical (non-polar) case, a one-to-one correspondence can be shown between the discrete GND density tensor [182] and the continuum representation of the GND density tensor given in terms of gradients of crystallographic slips [15]. As an alternative to the classical approach, one may consider a micropolar model of crystal plasticity [76, 77, 78, 79, 217]. Through the specification of an evolution equation for, or a compatibility-based calculation of, the plastic torsion-curvature [65], an approximate reflection of the GN dislocation density is included in a rather natural way. The purpose of this section is to outline the connection between the micropolar plastic torsion-curvature and the classical GND density tensor. To begin, the classical relationship between the discrete and continuum GND density tensors is recalled, and then a similar analysis is performed for the micropolar model of crystal plasticity.

Classical Case

Physically, the GND density is a measure of the non-redundancy (or polarity) of a general dislocation ensemble over a given reference volume. In the case of considering discrete (not necessarily straight) defect distributions over a given reference volume, Arsenlis and Parks [15] give a definition of the GND density tensor as

$$\boldsymbol{\alpha} = \sum_{\eta} \rho_{GN}^{\eta} \mathbf{b}^{\eta} \otimes \bar{\boldsymbol{\xi}}^{\eta}, \quad (4.5)$$

where \mathbf{b}^{η} is the Burger's vector and $\bar{\boldsymbol{\xi}}^{\eta}$ is the average tangent vector of the η^{th} dislocation line and

the η^{th} scalar GN dislocation density is defined as

$$\rho_{GN}^\eta = \frac{\bar{l}^\eta}{V}, \quad (4.6)$$

where \bar{l}^η is the secant length of the generally curved dislocation segment and V is the reference volume. From a simple inspection of the units in the definition of equation (4.5) it is apparent that GND density tensor has units of 1/length. In relating the above discrete definition of GND density to variables readily available within the framework of continuum crystal plasticity, an appeal is made to the analysis of the incompatibility of the elastic and/or plastic distortion fields, with the total distortion, $\boldsymbol{\beta}$, being the displacement gradient.

In the geometrically linear setting the total distortion is decomposed into elastic and plastic parts as

$$\boldsymbol{\beta} = \mathbf{u}\nabla_{\mathbf{x}} = \boldsymbol{\beta}^e + \boldsymbol{\beta}^p \quad (4.7)$$

The requirement of a single-valued displacement field within the body is manifested mathematically by requiring

$$\text{curl}(\boldsymbol{\beta}) = \mathbf{0}, \quad (4.8)$$

which is the statement of linearized compatibility. If we then associate the incompatibility of the individual elastic and plastic distortions with the GND density tensor, we arrive at the following two equivalent definitions:

$$\boldsymbol{\alpha} = \text{curl}(\boldsymbol{\beta}^e) = -\text{curl}(\boldsymbol{\beta}^p) \quad (4.9)$$

Adhering to the classical crystal plasticity assumption that the lattice remains unperturbed by the plastic distortion associated with dislocation motion, the lattice stretches and rotates according to the elastic distortion. Following the pioneering analysis of Nye [182], equation (4.9) can be used to relate the GND density to the gradient of lattice strain and lattice curvature, *i.e.* ,

$$\boldsymbol{\alpha} = \text{curl}(\boldsymbol{\beta}^e) = \text{curl}(\boldsymbol{\epsilon}^e) + \text{curl}(\boldsymbol{\omega}^e) \quad (4.10)$$

$$\boldsymbol{\epsilon}^e = \text{sym}(\boldsymbol{\beta}^e) \text{ , } \boldsymbol{\omega}^e = \text{skw}(\boldsymbol{\beta}^e) = -\boldsymbol{\mathcal{C}} \cdot \boldsymbol{\vartheta}^e, \quad (4.11)$$

The second-rank lattice curvature, $\boldsymbol{\kappa}$, is introduced as the right operating gradient of the axial vector $\boldsymbol{\vartheta}^e$ associated with the skew symmetric part of the elastic distortion $\boldsymbol{\omega}^e$, *i.e.*

$$\boldsymbol{\kappa} = \boldsymbol{\vartheta}^e \nabla_{\mathbf{x}}. \quad (4.12)$$

Given these definitions, it can be shown that

$$\text{curl}(\boldsymbol{\omega}^e) = \boldsymbol{\kappa}^T - \text{tr}(\boldsymbol{\kappa})\mathbf{1}, \quad (4.13)$$

where $\mathbf{1} \equiv \delta_{ij}\mathbf{e}_i \otimes \mathbf{e}_j$ in index notation, δ_{ij} is the Kronecker delta function, and $\{\mathbf{e}_i\}$ are the basis vectors in Eulerian space. In the original work of Nye, the elastic strain term is neglected and the GND density and lattice curvature are assumed to be related by the following reciprocal relations

$$\boldsymbol{\alpha} = \boldsymbol{\kappa}^T - \text{tr}(\boldsymbol{\kappa})\mathbf{1} \quad (4.14)$$

$$\boldsymbol{\kappa} = \boldsymbol{\alpha}^T - \frac{1}{2}\text{tr}(\boldsymbol{\alpha})\mathbf{1} \quad (4.15)$$

However, if we retain the term involving the elastic strain, the analogous relations are

$$\boldsymbol{\alpha} = \text{curl}(\boldsymbol{\epsilon}^e) + \boldsymbol{\kappa}^T - \text{tr}(\boldsymbol{\kappa})\mathbf{1} \quad (4.16)$$

$$\boldsymbol{\kappa} = \boldsymbol{\alpha}^T - \frac{1}{2}\text{tr}(\boldsymbol{\alpha})\mathbf{1} - [\text{curl}(\boldsymbol{\epsilon}^e)]^T \quad (4.17)$$

These equations are often used by researchers to link experimental measurements of lattice curvature to the GND density tensor [227, 228]. Alternatively, one can express the GND density tensor in terms of the plastic distortion, *i.e.* ,

$$\boldsymbol{\alpha} = -\text{curl}(\boldsymbol{\beta}^p), \quad (4.18)$$

where the plastic distortion is given as a summation of shears on crystallographic planes as

$$\boldsymbol{\beta}^p = \sum_{\eta} \gamma^{\eta} \mathbf{s}^{\eta} \otimes \mathbf{n}^{\eta}. \quad (4.19)$$

Here γ^{η} is the amount of shear strain on the η^{th} slip plane, \mathbf{s}^{η} is the slip direction and \mathbf{n}^{η} is the slip plane normal direction. Following Arsenlis and Parks, we may write equation (4.18) in terms of slip system level quantities as

$$\boldsymbol{\alpha} = -\text{curl}(\boldsymbol{\beta}^p) = -\sum_{\eta} \mathbf{s}^{\eta} \otimes \mathbf{n}^{\eta} \times \nabla_{\mathbf{x}} \gamma^{\eta}, \quad (4.20)$$

Considering the vector $\mathbf{t}^{\eta} = \mathbf{s}^{\eta} \times \mathbf{n}^{\eta}$, we can rewrite equation (4.20) as

$$\boldsymbol{\alpha} = -\text{curl}(\boldsymbol{\beta}^p) = -\sum_{\eta} \mathbf{s}^{\eta} \otimes (\mathbf{t}^{\eta} \times \mathbf{s}^{\eta}) \times \nabla_{\mathbf{x}} \gamma^{\eta} = -\sum_{\eta} \mathbf{s}^{\eta} \otimes \nabla_{\mathbf{x}} \gamma^{\eta} \cdot (\mathbf{t}^{\eta} \otimes \mathbf{s}^{\eta} - \mathbf{s}^{\eta} \otimes \mathbf{t}^{\eta}). \quad (4.21)$$

Using the relationships between the slip gradients and the scalar edge and screw GND densities, the expression can be rewritten as

$$\rho_{GN(e)}^{\eta} b = -\nabla_{\mathbf{x}} \gamma^{\eta} \cdot \mathbf{s}^{\eta} \quad , \quad \rho_{GN(s)}^{\eta} b = -\nabla_{\mathbf{x}} \gamma^{\eta} \cdot \mathbf{t}^{\eta} \quad (4.22)$$

$$\boldsymbol{\alpha} = -\sum_{\eta} \rho_{GN(s)}^{\eta} b \mathbf{s}^{\eta} \otimes \mathbf{s}^{\eta} + \rho_{GN(e)}^{\eta} b \mathbf{s}^{\eta} \otimes \mathbf{t}^{\eta}. \quad (4.23)$$

This expression is identical up to a sign with the expression given in equation (4.5), where the following notations have been used:

$$\boldsymbol{\alpha} = -\sum_{\eta} \rho_{GN}^{\eta} \mathbf{b}^{\eta} \otimes \bar{\boldsymbol{\xi}}^{\eta}, \quad (4.24)$$

$$\rho_{GN}^{\eta} = \sqrt{\left(\rho_{GN(e)}^{\eta}\right)^2 + \left(\rho_{GN(s)}^{\eta}\right)^2} \quad (4.25)$$

$$\bar{\boldsymbol{\xi}}^{\eta} = \frac{\rho_{GN(s)}^{\eta} \mathbf{s}^{\eta} + \rho_{GN(e)}^{\eta} \mathbf{t}^{\eta}}{\rho_{GN}^{\eta}} \quad (4.26)$$

$$\mathbf{b}^{\eta} = b \mathbf{s}^{\eta} \quad (4.27)$$

From the definition of the edge and screw components of the GND density it is clear that the gradient of slip in the direction of the dislocation line motion is the source of GND density, within the context of the linearized compatibility treatment.

Micropolar Case

A micropolar or Cosserat material [67] is a special type of generalized continuum in which each continuum point is assigned a rigid vectorial microstructure that is allowed to rotate independently with respect to the continuum rotation defined by the skew-symmetric part of the total distortion. Even considering the case of classical crystal plasticity outlined in the above section, one may be thinking “The continuum and microstructure (lattice) rotate independently in that case too.” This statement is true, but in the classical case the lattice rotation follows the portion of the continuum rotation defined by the skew-symmetric part of the elastic distortion, and is not a degree of freedom that contributes to the deformation power. Another way of viewing the difference between classical and micropolar crystal plasticity is within a numerical setting. In the classical model only the displacement vector components are nodal degrees-of-freedom, whereas in the micropolar model the displacement components are supplemented (in the geometrically linear case) by the components of the lattice rotation vector. There are additional subtle differences between the two classes of crystal plasticity theories that arise based upon the partitioning of the deformation process into elastic and plastic parts, as well as more obvious differences that arise due to the necessity of specifying additional constitutive assumptions related to the enhanced kinematic description.

As a point of departure and to highlight some of the differences between classical and micropolar crystal plasticity, a discussion of micropolar kinematics similar to that in the previous section is elaborated. A deformation process in a micropolar material is specified by the continuum and micro-motions. The discussion below follows closely the work of Forest *et al.* [77]. The continuum motion, as in the classical case is defined in terms of the distortion, $\boldsymbol{\beta}$, and the micro-motion is defined in terms of the lattice spin tensor, $\boldsymbol{\Phi}$. The relevant micropolar deformation measures are the micropolar strain tensor, $\bar{\boldsymbol{\epsilon}}$, and the micropolar lattice torsion-curvature tensor, $\bar{\boldsymbol{\kappa}}$, where the overbar indicates quantities associated with the micropolar theory and have been introduced in Section 4.3.1.1. The micropolar strain and lattice torsion-curvature are defined as (recall the note at the start of this sub-section about the different deformation measure convention used here)

$$\bar{\boldsymbol{\epsilon}} = \mathbf{u}\nabla_{\mathbf{x}} + \mathcal{E} \cdot \boldsymbol{\phi} = \boldsymbol{\beta} - \boldsymbol{\Phi} \quad (4.28)$$

$$\bar{\boldsymbol{\kappa}} = \boldsymbol{\phi}\nabla_{\mathbf{x}} = -\frac{1}{2}\mathcal{E} : \boldsymbol{\Phi}\nabla_{\mathbf{x}} \quad (4.29)$$

We now assume that the following additive elastic-plastic decompositions hold (by assuming the limit of small deformation), and that the plastic distortion is equal to plastic strain further commentary on this kinematic assumption is shelved for the time being, and will be re-examined in the section on constitutive model development. Hence,

$$\boldsymbol{\beta} = \boldsymbol{\beta}^e + \boldsymbol{\beta}^p, \quad \bar{\boldsymbol{\epsilon}} = \bar{\boldsymbol{\epsilon}}^e + \bar{\boldsymbol{\epsilon}}^p, \quad \boldsymbol{\beta}^p = \bar{\boldsymbol{\epsilon}}^p \quad (4.30)$$

$$\bar{\boldsymbol{\kappa}} = \bar{\boldsymbol{\kappa}}^e + \bar{\boldsymbol{\kappa}}^p \quad (4.31)$$

This kinematic assumption, namely that $\boldsymbol{\beta}^p = \bar{\boldsymbol{\epsilon}}^p$, implies that the micro-rotation is purely elastic, albeit generally different from the elastic continuum rotation, *i.e.* $\boldsymbol{\omega}^e \neq \boldsymbol{\Phi}$

$$\bar{\boldsymbol{\epsilon}}^e = \bar{\boldsymbol{\epsilon}} - \bar{\boldsymbol{\epsilon}}^p = \boldsymbol{\beta}^e - \mathcal{E} \cdot \boldsymbol{\phi} \quad (4.32)$$

This point of view is favored by Forest and collaborators and Neff [177], but Steinmann [221] and Tsakmakis and Grammenoudis [93, 95] have presented theories in which the micro-rotation is comprised of both elastic and plastic parts, *i.e.* $\Phi = \Phi^e + \Phi^p$.

The mathematical requirements for the existence of single-valued displacement and rotation fields are expressed for the micropolar material as

$$\text{curl}(\bar{\epsilon}) + \bar{\kappa}^T - \text{tr}(\bar{\kappa})\mathbf{1} = \mathbf{0} \quad (4.33)$$

$$\text{curl}(\bar{\kappa}) = \mathbf{0} \quad (4.34)$$

Through substitution of the elastic-plastic decompositions into the above expressions, we arrive at the following micropolar GN defect densities

$$\bar{\alpha} = \text{curl}(\bar{\epsilon}^e) + (\bar{\kappa}^e)^T - \text{tr}(\bar{\kappa}^e)\mathbf{1} = -\text{curl}(\bar{\epsilon}^p) - (\bar{\kappa}^p)^T + \text{tr}(\bar{\kappa}^p)\mathbf{1} \quad (4.35)$$

$$\bar{\theta} = \text{curl}(\bar{\kappa}^e) = -\text{curl}(\bar{\kappa}^p) \quad (4.36)$$

where $\bar{\alpha}$ is the micropolar GN dislocation density and $\bar{\theta}$ is the micropolar GN disclination density. A micropolar GN disclination, as can be seen from equation (4.36), is a measure of the incompatibility of the lattice torsion-curvature. In more general terms, the disclination is a linear rotational defect originally envisioned by Volterra as a natural counterpart to the linear translational defect, dislocations. The disclination concept has been used by many researchers to describe the structure of grain boundaries [173, 174], the formation of defect substructures and the fragmentation process in crystalline materials [195, 209, 210, 211]. However, the application of the disclination concept in the continuum theory of crystal elastoplasticity has not advanced beyond the theoretical stage, and furthermore, the validity of the notion of the “continuously distributed” disclinations has been seriously called into question by Anthony [13]. For these reasons, in this section, discussion will remain centered on the treatment of GN dislocations within micropolar crystal plasticity. The use of the disclination concept will be addressed elsewhere in the report.

Considering equation (4.35), we see that the micropolar GND density has the same general functional form as the GND density tensor in the classical case. However, we point out that in the micropolar case, the elastic strain tensor, $\bar{\epsilon}^e$, is generally unsymmetric, and the micropolar GND density does not depend on the total lattice curvature as it does in the classical case. Splitting the elastic micropolar strain into symmetric and skew-symmetric parts, we are able to see further connections between the two GND density tensors, *i.e.* ,

$$\text{sym}(\bar{\epsilon}^e) = \epsilon^e, \quad \text{skw}(\bar{\epsilon}^e) = \omega^e - \Phi \quad (4.37)$$

$$\bar{\epsilon}^e = \epsilon^e + \omega^e - \Phi \quad (4.38)$$

$$\text{curl}(\bar{\epsilon}^e) = \text{curl}(\epsilon^e) + (\kappa^T - \bar{\kappa}^T) - (\text{tr}(\kappa) - \text{tr}(\bar{\kappa}))\mathbf{1} \quad (4.39)$$

$$\bar{\alpha} = \text{curl}(\epsilon^e) + (\kappa^T - \bar{\kappa}^T) - (\text{tr}(\kappa) - \text{tr}(\bar{\kappa}))\mathbf{1} + (\bar{\kappa}^e)^T - \text{tr}(\bar{\kappa}^e)\mathbf{1} \quad (4.40)$$

Substitution of the above expression (4.40) back into equation (4.35) results in the following relationship between the classical and micropolar GND density tensors:

$$\bar{\alpha} = \alpha - (\bar{\kappa}^p)^T + \text{tr}(\bar{\kappa})\mathbf{1} \quad (4.41)$$

As can be seen from equation (4.41), the micropolar GND density tensor derived from compatibility requirements of the micropolar strain tensor is not consistent with the physical definition of the discrete GND tensor in the presence of plastic curvature, *i.e.* ,

$$\bar{\alpha} \neq -\sum_{\eta} \rho_{GN}^{\eta} \mathbf{b}^{\eta} \otimes \bar{\xi}^{\eta} \quad \text{if } \bar{\kappa}^p \neq 0 \quad (4.42)$$

The physical interpretation of $\bar{\alpha}$ in terms of crystallographic quantities is rather unclear at this point.

Another interesting tangent that was pursued in terms of shedding light on the issue of finding a relation between GNDs and plastic torsion-curvature, is the work of Ehlers *et al.* [65] in which they argue that, within the geometrically linear setting, a micropolar elastoplasticity model that assumes an additively decomposed micropolar strain tensor automatically implies (through compatibility conditions) that the curvature must also be additively decomposed. In addition, they argue that the specification of an independent micropolar plastic curvature evolution equation is an impossibility. Considering that such a specification, in fact, has been pursued by many researchers (including the present work), the details of their arguments have been worked through and are summarized below. As a starting point, we form the difference between two gradients of the micropolar strain tensor as follows:

$$\bar{\epsilon} \nabla_{\mathbf{x}} = (\mathbf{u} \nabla_{\mathbf{x}}) \nabla_{\mathbf{x}} + \mathcal{E} \cdot \phi \nabla_{\mathbf{x}} \Rightarrow \bar{\epsilon}_{ij,k} \mathbf{e}_i \otimes \mathbf{e}_j \otimes \mathbf{e}_k = (u_{i,jk} + \mathcal{E}_{ijm} \phi_{m,k}) \mathbf{e}_i \otimes \mathbf{e}_j \otimes \mathbf{e}_k \quad (4.43)$$

$$\bar{\epsilon} \nabla_{\mathbf{x}}^{23/T} = (\mathbf{u} \nabla_{\mathbf{x}}) \nabla_{\mathbf{x}}^{23/T} + \mathcal{E} \cdot \phi \nabla_{\mathbf{x}}^{23/T} \Rightarrow \bar{\epsilon}_{ik,j} \mathbf{e}_i \otimes \mathbf{e}_j \otimes \mathbf{e}_k = (u_{i,kj} + \mathcal{E}_{ikm} \phi_{m,j}) \mathbf{e}_i \otimes \mathbf{e}_j \otimes \mathbf{e}_k \quad (4.44)$$

where the notation $(\cdot)^{ij/T}$ indicates transposition of the i^{th} and j^{th} basis for higher-order tensors. By subtracting equation (4.44) from (4.43) and taking advantage of the interchangeability of the order of differentiation on the displacement field, we obtain

$$\bar{\epsilon}_{ij,k} - \bar{\epsilon}_{ik,j} = \mathcal{E}_{ijm} \phi_{m,k} - \mathcal{E}_{ikm} \phi_{m,j} \quad (4.45)$$

Now by performing the double-contraction of the permutation tensor with the two left most indices of equation 4.45 we have the expression

$$\mathcal{E}_{pij} (\bar{\epsilon}_{ij,k} - \bar{\epsilon}_{ik,j}) = \mathcal{E}_{pij} (\mathcal{E}_{ijm} \phi_{m,k} - \mathcal{E}_{ikm} \phi_{m,j}) \quad (4.46)$$

Taking advantage of the $\mathcal{E} - \delta$ identities, the RHS of equation (4.46) can be simplified to

$$\begin{aligned} \mathcal{E}_{pij} (\bar{\epsilon}_{ij,k} - \bar{\epsilon}_{ik,j}) &= \mathcal{E}_{pij} \mathcal{E}_{ijm} \phi_{m,k} - \mathcal{E}_{pij} \mathcal{E}_{ikm} \phi_{m,j} \\ &= \mathcal{E}_{ijp} \mathcal{E}_{ijm} \phi_{m,k} - \mathcal{E}_{ijp} \mathcal{E}_{ikm} \phi_{m,j} \\ &= (\delta_{jj} \delta_{pm} - \delta_{jm} \delta_{pj}) \phi_{m,k} - (\delta_{jk} \delta_{pm} - \delta_{jm} \delta_{pk}) \phi_{m,j} \\ &= 2\delta_{pm} \phi_{m,k} - \phi_{p,k} + \delta_{pk} \phi_{j,j} \\ &= \phi_{p,k} + \text{tr}(\phi \nabla_{\mathbf{x}}) \delta_{pk} \\ &= \kappa_{pk} + \text{tr}(\kappa) \delta_{pk} \end{aligned} \quad (4.47)$$

Expressing equation (4.47) in direct notation,

$$\mathcal{E} : (\bar{\epsilon} \nabla_{\mathbf{x}} - \bar{\epsilon} \nabla_{\mathbf{x}}^{23/T}) = \kappa + \text{tr}(\kappa) \mathbf{1} \quad (4.48)$$

To eliminate the trace term from the previous equation we revisit equation (4.33) and write

$$\text{tr}(\bar{\mathbf{K}})\mathbf{1} = [\text{curl}(\bar{\boldsymbol{\epsilon}})]^T + \bar{\mathbf{K}} \quad (4.49)$$

The curl term can be rewritten in terms of the appropriately defined gradient operator and contraction with the alternator tensor as follows:

$$\begin{aligned} [\text{curl}(\bar{\boldsymbol{\epsilon}})]^T &= \mathcal{E}_{ijk} \bar{\epsilon}_{m,j,k} \mathbf{e}_i \otimes \mathbf{e}_m \\ &= -\mathcal{E}_{ikj} \bar{\epsilon}_{m,j,k} \mathbf{e}_i \otimes \mathbf{e}_m \\ &= -\mathcal{E} : \bar{\boldsymbol{\epsilon}} \nabla_{\mathbf{x}}^{13/T} \end{aligned} \quad (4.50)$$

Substitution of (4.50) into (4.49) and then inserting the result back into (4.48) and solving for the micropolar curvature gives the following relation between the micropolar torsion-curvature and various gradients of the micropolar strain tensor, *i.e.* ,

$$\bar{\mathbf{K}} = \frac{1}{2} \mathcal{E} : \left(\bar{\boldsymbol{\epsilon}} \nabla_{\mathbf{x}} + \bar{\boldsymbol{\epsilon}} \nabla_{\mathbf{x}}^{13/T} - \bar{\boldsymbol{\epsilon}} \nabla_{\mathbf{x}}^{23/T} \right) \quad (4.51)$$

Since the gradient is a linear operator, an additive decomposition of the micropolar strain tensor then implies an additive decomposition of the micropolar torsion-curvature tensor, such that the evolution equation for the plastic torsion-curvature is determined once the evolution equation for the micropolar plastic strain rate is given, *i.e.*

$$\dot{\bar{\mathbf{K}}}^p = \frac{1}{2} \mathcal{E} : \left(\dot{\bar{\boldsymbol{\epsilon}}}^p \nabla_{\mathbf{x}} + \dot{\bar{\boldsymbol{\epsilon}}}^p \nabla_{\mathbf{x}}^{13/T} - \dot{\bar{\boldsymbol{\epsilon}}}^p \nabla_{\mathbf{x}}^{23/T} \right) \quad (4.52)$$

However, the problem again is that the strains are not nodal variables and therefore taking spatial derivatives of them requires modification of the standard finite element practices. It would seem that this is why independent (from the plastic strain) specification of the plastic micropolar torsion-curvature flow rule without admitting redundancy within the numerical setting is possible. If we now substitute in the relationship between the plastic micropolar strain and the crystallographic shears (equation (4.19) into equation (4.51) and simplify following the procedures of equations (4.21)-(4.27), the following results are obtained:

$$\mathcal{E} : \bar{\boldsymbol{\epsilon}}^p \nabla_{\mathbf{x}} = \sum_{\eta} \{ (\mathbf{n}^{\eta} \cdot \mathbf{n}^{\eta}) \mathbf{t}^{\eta} \otimes \gamma^{\eta} \nabla_{\mathbf{x}} - (\mathbf{t}^{\eta} \cdot \mathbf{n}^{\eta}) \otimes \gamma^{\eta} \nabla_{\mathbf{x}} \} = \sum_{\eta} \mathbf{t}^{\eta} \otimes \gamma^{\eta} \nabla_{\mathbf{x}} \quad (4.53)$$

$$\mathcal{E} : \bar{\boldsymbol{\epsilon}}^p \nabla_{\mathbf{x}}^{13/T} = \sum_{\eta} \{ (\gamma^{\eta} \nabla_{\mathbf{x}} \cdot \mathbf{s}^{\eta}) \mathbf{t}^{\eta} \otimes \mathbf{s}^{\eta} - (\gamma^{\eta} \nabla_{\mathbf{x}} \cdot \mathbf{t}^{\eta}) \mathbf{s}^{\eta} \otimes \mathbf{s}^{\eta} \} = - \sum_{\eta} \rho_{GN}^{\eta} \bar{\boldsymbol{\xi}}^{\eta} \otimes \mathbf{b}^{\eta} = \boldsymbol{\alpha}^T \quad (4.54)$$

$$\mathcal{E} : \bar{\boldsymbol{\epsilon}}^p \nabla_{\mathbf{x}}^{23/T} = \sum_{\eta} \{ (\gamma^{\eta} \nabla_{\mathbf{x}} \cdot \mathbf{n}^{\eta}) \mathbf{t}^{\eta} \otimes \mathbf{n}^{\eta} - (\gamma^{\eta} \nabla_{\mathbf{x}} \cdot \mathbf{t}^{\eta}) \mathbf{n}^{\eta} \otimes \mathbf{n}^{\eta} \} \quad (4.55)$$

Quite frankly, the physical meaning of equations (4.53) and (4.55) in terms of their crystallographic significance is not clear at this point. To our knowledge, this is the first time these results have been derived, and obviously they are not related to the classical GND density tensor in a one-to-one

correspondence. Insertion of (4.53)-(4.55) into (4.52) we have the following relationship between the plastic curvature and slip gradients

$$\bar{\mathbf{K}}^p = \frac{1}{2} \left(\boldsymbol{\alpha}^T + \sum_{\eta} \{ \mathbf{t}^{\eta} \otimes \gamma^{\eta} \nabla_{\mathbf{x}} - (\gamma^{\eta} \nabla_{\mathbf{x}} \cdot \mathbf{n}^{\eta}) \mathbf{t}^{\eta} \otimes \mathbf{n}^{\eta} + (\gamma^{\eta} \nabla_{\mathbf{x}} \cdot \mathbf{t}^{\eta}) \mathbf{n}^{\eta} \otimes \mathbf{n}^{\eta} \} \right) \quad (4.56)$$

Furthermore, if we now plug this expression back into equation (4.41) we arrive at

$$\bar{\boldsymbol{\alpha}} = \frac{1}{2} \left(\boldsymbol{\alpha}^T - 2 \sum_{\eta} \{ \gamma^{\eta} \nabla_{\mathbf{x}} \otimes \mathbf{t}^{\eta} - (\gamma^{\eta} \nabla_{\mathbf{x}} \cdot \mathbf{n}^{\eta}) \mathbf{n}^{\eta} \otimes \mathbf{t}^{\eta} + (\gamma^{\eta} \nabla_{\mathbf{x}} \cdot \mathbf{t}^{\eta}) \mathbf{n}^{\eta} \otimes \mathbf{n}^{\eta} \} + 3b \sum_{\eta} \rho_{GN(s)}^{\eta} \mathbf{1} \right), \quad (4.57)$$

where

$$\text{tr}(\bar{\mathbf{K}}^p) = \frac{3b}{2} \sum_{\eta} \rho_{GN(s)}^{\eta} \mathbf{1} \quad (4.58)$$

What the above results seem to indicate is that both the micropolar GND density tensor and the micropolar plastic torsion-curvature tensor contain information concerning the defectiveness of the crystalline body in addition to the classical GND density tensor. The physical significance of these additional terms is not understood at this time. In light of this uncertainty, it is our decision moving forward to adopt the point of view of Forest *et al.* [77] that the plastic micropolar torsion-curvature is approximately related to the quantity of GNDs within the body. In addition, we will later specify an evolution equation for the plastic micropolar torsion-curvature independent of the restriction imposed by equation (4.52) as have the majority of researchers in working with the geometrically linear theory of micropolar elastoplasticity.

4.3.2 Balance Laws and Thermodynamics

4.3.2.1 Mechanical Balance Laws and the Principle of Virtual Work

In the absence of body forces and couples, the local forms of the balance of linear and angular momentum for a micropolar continuum in static equilibrium are given as

$$\text{div}(\boldsymbol{\sigma}) = \mathbf{0} \quad \text{in } V \quad (4.59)$$

$$\text{div}(\mathbf{m}) + \mathcal{E} : \boldsymbol{\sigma} = \mathbf{0} \quad \text{in } V \quad (4.60)$$

where, for a tensor \mathbf{A} , $\text{div}(\mathbf{A}) \equiv \nabla_{\mathbf{x}} \cdot \mathbf{A}$, $\boldsymbol{\sigma}$ is the Cauchy force-stress tensor and \mathbf{m} is the Cauchy couple-stress tensor. External work is performed on a volume element of the material through the application of force- and couple-traction vectors related in the standard way to the force- and couple-stress tensors, *i.e.* ,

$$\mathbf{T} = \mathbf{n} \cdot \boldsymbol{\sigma} \quad \text{on } \partial V \quad (4.61)$$

$$\mathbf{M} = \mathbf{n} \cdot \mathbf{m} \quad \text{on } \partial V \quad (4.62)$$

where \mathbf{n} is the unit vector normal to the surface of the application of the traction vector. To derive the weak form of the balance equations used in the finite element formulation presented in a later

section, the usual steps are employed. First, the equilibrium equations are multiplied by arbitrary variations in the kinematic fields; in this case the linear momentum equation by a displacement variation, $\delta \mathbf{u}$, and the angular momentum equation by a variation of the microrotation vector, $\delta \boldsymbol{\phi}$. The scalar equations are then integrated over an arbitrary volume of material. After integrating by parts and applying the divergence theorem, the two intermediate equations (4.64) and (4.66) are obtained, *i.e.* ,

$$\int_V \text{div}(\boldsymbol{\sigma}) \cdot \delta \mathbf{u} dV = 0 = \int_V [\text{div}(\boldsymbol{\sigma} \cdot \delta \mathbf{u}) - \boldsymbol{\sigma} : \nabla_{\mathbf{x}}(\delta \mathbf{u})] dV \quad (4.63)$$

$$\int_S \mathbf{n} \cdot \boldsymbol{\sigma} \cdot \delta \mathbf{u} dS = \int_V \boldsymbol{\sigma} : \nabla_{\mathbf{x}}(\delta \mathbf{u}) dV \quad (4.64)$$

$$\int_V (\text{div}(\mathbf{m}) + \mathcal{E} : \boldsymbol{\sigma}) \cdot \delta \boldsymbol{\phi} dV = 0 = \int_V [\text{div}(\mathbf{m} \cdot \delta \boldsymbol{\phi}) - \mathbf{m} : \nabla_{\mathbf{x}}(\delta \boldsymbol{\phi}) + (\mathcal{E} : \boldsymbol{\sigma}) \cdot \delta \boldsymbol{\phi}] dV \quad (4.65)$$

$$\int_S \mathbf{n} \cdot \mathbf{m} \cdot \delta \boldsymbol{\phi} dS = \int_V [\mathbf{m} : \nabla_{\mathbf{x}}(\delta \boldsymbol{\phi}) - (\mathcal{E} : \boldsymbol{\sigma}) \cdot \delta \boldsymbol{\phi}] dV \quad (4.66)$$

$$\int_S (\mathbf{T} \cdot \delta \mathbf{u} + \mathbf{M} \cdot \delta \boldsymbol{\phi}) dS = \int_V (\boldsymbol{\sigma} : \delta \bar{\boldsymbol{\epsilon}} + \mathbf{m} : \delta \bar{\boldsymbol{\kappa}}) dV \quad (4.67)$$

The final result of equation (4.67) is achieved by adding equations (4.64) and (4.66), and substituting in the kinematic relations given in equations (4.1) and (4.2) as well as the traction definitions given in equations (4.61) and (4.62). Equation (4.67) is the starting point for the derivation of the finite element equations.

4.3.2.2 Thermodynamics

In this section a general overview of the thermodynamic analysis of a geometrically linear micropolar elastoplastic material is given within the context of internal state variable theory for an isothermal deformation process. The steps leading to the deduction of the state laws and the reduced dissipation inequality mirror those in the classical case. For a micropolar continuum the local time rate of change of internal energy is given as

$$\rho \dot{U} = \boldsymbol{\sigma} : \dot{\bar{\boldsymbol{\epsilon}}} + \mathbf{m} : \dot{\bar{\boldsymbol{\kappa}}} \quad (4.68)$$

where ρ is the material density and U is the specific internal energy. Introducing the specific Helmholtz free energy potential as $\Psi = U - T\eta_s$, where T is the absolute temperature and η_s is the specific entropy, taking its time derivative, and combining equation (4.68) with the entropy inequality,

$$\rho \dot{\eta}_s \geq 0, \quad (4.69)$$

leads to the dissipation inequality for the micropolar material,

$$-\rho \dot{\Psi} + \boldsymbol{\sigma} : \dot{\bar{\boldsymbol{\epsilon}}} + \mathbf{m} : \dot{\bar{\boldsymbol{\kappa}}} \geq 0. \quad (4.70)$$

Given a specific Helmholtz free energy potential $\Psi(\bar{\boldsymbol{\epsilon}}^e, \bar{\boldsymbol{\kappa}}^e, \zeta_i^\eta)$ that depends on elastic micropolar strains, torsion-curvatures, and a set of scalar strain-like slip and/or torsion-curvature system level ISVs, ζ_i^η , where the upper index refers to the slip and/or curvature system index and the

lower index refers to the i^{th} ISV associated with the η^{th} system, the total time derivative of the potential can be expressed as

$$\dot{\Psi}(\bar{\boldsymbol{\epsilon}}^e, \bar{\boldsymbol{\kappa}}^e, \{\zeta_i^\eta\}) = \frac{\partial \Psi}{\partial \bar{\boldsymbol{\epsilon}}^e} : \dot{\bar{\boldsymbol{\epsilon}}}^e + \frac{\partial \Psi}{\partial \bar{\boldsymbol{\kappa}}^e} : \dot{\bar{\boldsymbol{\kappa}}}^e + \sum_{\eta=1}^{N_{sys}} \sum_{i=1}^{N_{ISV}} \frac{\partial \Psi}{\partial \zeta_i^\eta} \dot{\zeta}_i^\eta. \quad (4.71)$$

In equation (4.71), N_{sys} , is the total number of slip and torsion-curvature systems. Depending on whether a single or multi-criterion single crystal micropolar crystal plasticity model is used, the number of ISVs will differ. Insertion of this result back into (4.70) leads to the expression

$$\left(\boldsymbol{\sigma} - \rho \frac{\partial \Psi}{\partial \bar{\boldsymbol{\epsilon}}^e} \right) : \dot{\bar{\boldsymbol{\epsilon}}}^e + \left(\mathbf{m} - \rho \frac{\partial \Psi}{\partial \bar{\boldsymbol{\kappa}}^e} \right) : \dot{\bar{\boldsymbol{\kappa}}}^e + \boldsymbol{\sigma} : \dot{\bar{\boldsymbol{\epsilon}}}^p + \mathbf{m} : \dot{\bar{\boldsymbol{\kappa}}}^p - \sum_{\eta=1}^{N_{sys}} \sum_{i=1}^{N_{ISV}} r_i^\eta \dot{\zeta}_i^\eta \geq 0, \quad (4.72)$$

from which the following state laws can be deduced,

$$\boldsymbol{\sigma} = \rho \frac{\partial \Psi}{\partial \bar{\boldsymbol{\epsilon}}^e}, \quad \mathbf{m} = \rho \frac{\partial \Psi}{\partial \bar{\boldsymbol{\kappa}}^e}, \quad r_i^\eta = \rho \frac{\partial \Psi}{\partial \zeta_i^\eta}, \quad (4.73)$$

and where the dissipation inequality is rewritten as

$$\boldsymbol{\sigma} : \dot{\bar{\boldsymbol{\epsilon}}}^p + \mathbf{m} : \dot{\bar{\boldsymbol{\kappa}}}^p - \sum_{\eta=1}^{N_{sys}} \sum_{i=1}^{N_{ISV}} r_i^\eta \dot{\zeta}_i^\eta \geq 0. \quad (4.74)$$

In equations (4.73) and (4.74), r_i^η , the work conjugate of ISV ζ_i^η , is referred to as a threshold stress. Upon specification of evolution equations for the micropolar plastic strain, torsion-curvature, and ISVs, the thermodynamic analysis can be carried out in more detail. Both single and multi-criterion models are presented in the following section.

4.3.3 Single Crystal Constitutive Model

In the following section, micropolar crystal plasticity is discussed in terms of potential ways that the elastoplastic constitutive equations may be formulated on a crystallographic basis. To date, the series of papers by Forest and collaborators [76, 77, 78, 79, 217] are the only works that have emerged in this vein and have been implemented within the FE framework. They have developed a multi-mechanism, multi-criterion model of single crystal elastoviscoplasticity, and have used it to study the differentiation between shear and kink banding in single crystals oriented for single and double slip, grain-size strengthening effects in fcc polycrystals, and size-dependent precipitate strengthening effects in nickel-base super alloys. A viscoplastic formulation is adopted to avoid the potential difficulty of having indeterminate plastic strain and/or torsion-curvature rates. The only inelastic deformation mechanisms considered are the plastic shearing due to the motion of dislocations, and the development of plastic torsion-curvature resulting from the presence of excess dislocations of the same sign, GNDs. The flow rules for plastic strain and torsion-curvature are independently associative and therefore maintain a normality structure in their work. The present

work will explore alternative formulations which have formal analogies to some of the developments discussed in the more general micropolar plasticity literature.

For the case of small displacements and micro-rotations we assume that micropolar strain and torsion-curvature tensors can be additively decomposed into elastic and plastic parts

$$\bar{\boldsymbol{\epsilon}} = \bar{\boldsymbol{\epsilon}}^e + \bar{\boldsymbol{\epsilon}}^p \quad (4.75)$$

$$\bar{\mathbf{K}} = \bar{\mathbf{K}}^e + \bar{\mathbf{K}}^p \quad (4.76)$$

The elastic response for the linear isotropic micropolar continuum is then given by the following two equations for the force- and couple-stress tensors, $\boldsymbol{\sigma}$ and \mathbf{m} , respectively, *i.e.* ,

$$\boldsymbol{\sigma} = \mathbb{C} : \bar{\boldsymbol{\epsilon}}^e = \lambda \text{tr}(\bar{\boldsymbol{\epsilon}}^e) \mathbf{1} + (\mu^* + 2\mu_c) \bar{\boldsymbol{\epsilon}}^e + \mu^* (\bar{\boldsymbol{\epsilon}}^e)^T \quad (4.77)$$

$$\mathbf{m} = \mathbb{D} : \bar{\mathbf{K}}^e = \mathfrak{K} \text{tr}(\bar{\mathbf{K}}^e) \mathbf{1} + \beth (\bar{\mathbf{K}}^e)^T + \beth \bar{\mathbf{K}}^e \quad (4.78)$$

where the 4th rank elasticity tensors may be written as

$$\mathbb{C} = \lambda \mathbf{1} \otimes \mathbf{1} + 2\mu \text{sym}(\mathbb{I}) + 2\mu_c \text{skw}(\mathbb{I}) \quad (4.79)$$

$$\mathbb{D} = \mathfrak{K} \mathbf{1} \otimes \mathbf{1} + 2\mathfrak{K} \text{sym}(\mathbb{I}) + 2\mathfrak{K} \text{skw}(\mathbb{I}) \quad (4.80)$$

For these expressions, $\mathbb{I} \equiv \delta_{ik} \delta_{jl} \mathbf{e}_i \otimes \mathbf{e}_j \otimes \mathbf{e}_k \otimes \mathbf{e}_l$. Note that $\mathbf{1} \otimes \mathbf{1} = \delta_{ij} \delta_{kl} \mathbf{e}_i \otimes \mathbf{e}_j \otimes \mathbf{e}_k \otimes \mathbf{e}_l \neq \mathbb{I}$. In the force-stress equation, λ is the classical Lamé constant, μ_c is the micropolar couple modulus, and μ^* is the difference between classical shear modulus and the micropolar couple modulus, *i.e.* , $\mu^* = \mu - \mu_c$. Similarly, in the couple-stress equation \mathfrak{K} , \mathfrak{K} and \mathfrak{K} are constants of proportionality between the elastic portion of the torsion-curvature tensor and the couple stress. The micropolar couple modulus μ_c can be additionally related to the classical shear modulus through the coupling parameter [74], N , via the relation $\mu_c = N^2 \mu / (1 - N^2)$, where the coupling parameter is restricted such that $0 \leq N \leq 1$. Rewriting equation (4.77) in terms of symmetric and skew-symmetric parts, yields

$$\boldsymbol{\sigma} = \lambda \text{tr}(\boldsymbol{\epsilon}^e) \mathbf{1} + 2\mu \boldsymbol{\epsilon}^e + 2\mu_c (\boldsymbol{\Phi} - \boldsymbol{\omega}^e) \quad (4.81)$$

where we have used the fact that the symmetric part of the micropolar strain tensor is nothing more than the classical infinitesimal strain tensor, *i.e.* , $\text{sym}(\bar{\boldsymbol{\epsilon}}^e) = \boldsymbol{\epsilon}^e$. When written in this form, it would seem that when the skew-symmetric part of the elastic strain tensor vanishes and/or the micropolar couple modulus is zero, the material behaves in the classical sense. Although this statement seems to be reasonable at first glance, it is not entirely correct as the constitutive response of the micropolar continuum also depends on the gradient of the micro-rotation, or torsion-curvature. In other words, even if $\boldsymbol{\Phi} - \boldsymbol{\omega}^e = \mathbf{0}$, this does not necessarily imply that the gradient of micro-rotation is also zero. If the torsion-curvature is non-zero there will be couple-stresses within the body, as shown in equation (4.78), and therefore the continuum response would be non-classical in the sense that there will be additional stored energy in the material due to work-conjugate couple-stresses and torsion-curvatures. If, however, the material constants \mathfrak{K} , \mathfrak{K} and \mathfrak{K} in equation (4.78) are chosen to be suitably small, then the magnitude of the couple-stresses would be such that the asymmetry of the force-stress tensor could be considered insignificant. As can be inferred from the constitutive equations, the elastic response of an isotropic micropolar continuum depends on six elastic constants: the two classical ones, λ and μ , and the other four constants μ_c , \mathfrak{K} , \mathfrak{K} , and \mathfrak{K} .

To complete the constitutive model, we must specify the evolution equations for the micropolar plastic strain, torsion-curvature, and ISVs. We have focused on a model constructed analogously to that proposed in Forest *et al.* [77], which is a so-called multi-criterion model. This means that independent yield functions are used for the micropolar strain and torsion-curvature, and therefore there are two plastic parameters to be determined from the consistency conditions and/or given through viscoplastic relations. Any cross-coupled hardening effects in the multi-criterion model enter via explicit dependence in the ISV evolution equations. Another possibility is the so-called single criterion model, which has been used in macroscopic J_2 -type extensions of micropolar elastoplasticity. This type of formulation has not been employed in concert with micropolar crystal plasticity theory, and may possess different advantages and capabilities as compared to the multi-criterion theory. Since this aspect of the work is a relatively new development within the scope of the project, a tentative presentation of the model is discussed after the recapitulation of the multi-criterion model.

4.3.3.1 Multi-criterion Model

The multi-criterion model presented in this section is that proposed by Forest *et al.* [77], and the basis of the formulation is the introduction of distinct viscoplastic multipliers for both strain and torsion-curvature evolution. The evolution equations for the micropolar plastic strain and torsion-curvature are written as sums over the contributions from the η^{th} slip systems in the general forms, *i.e.* ,

$$\dot{\boldsymbol{\epsilon}}^p = \sum_{\eta} \dot{\gamma}^{\eta} \mathbf{N}^{\eta} \quad (4.82)$$

$$\dot{\mathbf{K}}^p = \sum_{\eta} \dot{\phi}^{\eta} \mathbf{N}_c^{\eta} \quad (4.83)$$

where $\dot{\gamma}^{\eta}$ and $\dot{\phi}^{\eta}$ are the slip system level plastic multipliers related to slip and torsion-curvature, respectively, and \mathbf{N}^{η} and \mathbf{N}_c^{η} give the directions of plastic strain and torsion-curvature, respectively in stress space. Following Forest *et al.* [77], the specific flow rules are given in terms of crystallographic directions as

$$\dot{\boldsymbol{\epsilon}}^p = \sum_{\eta} \dot{\gamma}^{\eta} \mathbf{Z}^{\eta} \quad , \quad \mathbf{Z}^{\eta} = \mathbf{n}^{\eta} \otimes \mathbf{s}^{\eta} \quad (4.84)$$

$$\dot{\mathbf{K}}^p = \sum_{\eta} \frac{\dot{\phi}^{\eta}}{\ell_p^{\eta}} \mathbf{H}^{\eta} \quad , \quad \mathbf{H}^{\eta} = \mathbf{s}^{\eta} \otimes \mathbf{t}^{\eta} \quad (4.85)$$

where ℓ_p^{η} is a characteristic length associated with the development of plastic curvature, and \mathbf{n}^{η} , \mathbf{s}^{η} , and \mathbf{t}^{η} are unit vectors in the slip system normal, slip, and transverse directions, respectively. The flow rules are completed by specifying the functional forms relating the shear and torsion-curvature rates to the appropriate driving forces, which are given by standard viscoplastic power-law forms, *i.e.* ,

$$\dot{\gamma}^{\eta} = \dot{\gamma}_0 \left(\frac{\langle |\boldsymbol{\tau}^{\eta}| - r^{\eta} \rangle}{g^{\eta}} \right)^m \text{sgn}(\boldsymbol{\tau}^{\eta}) \quad (4.86)$$

$$\dot{\phi}^\eta = \dot{\phi}_0 \left(\frac{\langle |\pi^\eta / \ell_p^\eta| - r_c^\eta \rangle}{g_c^\eta} \right)^{m_c} \text{sgn}(\pi^\eta) \quad (4.87)$$

where $\tau^\eta = \boldsymbol{\sigma} : \mathbf{Z}^\eta$ and $\pi^\eta = \mathbf{m} : \mathbf{H}^\eta$ are the respective driving forces for the shear and torsion-curvature rates, r^η and r_c^η are threshold force- and couple-stresses, g^η and g_c^η are the reference force and couple-stresses, and m and m_c are constants. By combining equations (4.84)-(4.87) and comparing them to equations (4.82) and (4.83), it is easy to see that

$$\mathbf{N}^\eta = \mathbf{Z}^\eta \text{sgn}(\tau^\eta) \quad (4.88)$$

$$\mathbf{N}_c^\eta = \frac{1}{\ell_p^\eta} \mathbf{H}^\eta \text{sgn}(\pi^\eta) \quad (4.89)$$

If we think about the above model in terms of slip system level yield functions and plastic potential functions, it becomes apparent the model is associative and displays the classical normality structure, *i.e.*

$$F^\eta := |\tau^\eta| - r^\eta \Rightarrow \mathbf{N}^\eta = \frac{\partial F^\eta}{\partial \boldsymbol{\sigma}} = \mathbf{Z}^\eta \text{sgn}(\tau^\eta) \quad (4.90)$$

$$F_c^\eta := \left| \frac{\pi^\eta}{\ell_p^\eta} \right| - r_c^\eta \Rightarrow \mathbf{N}_c^\eta = \frac{\partial F_c^\eta}{\partial \mathbf{m}} = \frac{1}{\ell_p^\eta} \mathbf{H}^\eta \text{sgn}(\pi^\eta) \quad (4.91)$$

where F^η and F_c^η are the slip system level yield functions for the plastic strain and torsion-curvature, respectively, for the η^{th} slip system. The yield function for the plastic torsion curvature is expressed in units of stress, and its derivative with respect to the couple-stress tensor yields the appropriate expression for the direction of the plastic torsion-curvature rate. It is noted that the evolution equation for the plastic torsion-curvature contains only the term associated with the curvature development due to the presence of edge dislocations [77].

The constitutive response is completed upon specification of the evolution equations for the threshold force- and couple-stresses, r^η and r_c^η , respectively. Thus far, only relatively simple forms of hardening equations have been used in interest of probing the models predictive capabilities before moving on to more physically-inspired (*i.e.*, dislocation-based) ISVs and evolution equations in future works. The threshold stress evolution equations are given as

$$\dot{r}^\eta = \sum_v (A_1 q_1^{\eta v} - B r^\eta) |\dot{\gamma}^v| + A_2 q_2^{\eta v} |\dot{\phi}^v| \quad (4.92)$$

$$\dot{r}_c^\eta = \sum_v A_3 q_3^{\eta v} |\dot{\phi}^v| \quad (4.93)$$

$$q_i^{\eta v} = q_i + (1 - q_i) \delta^{\eta v} \quad (4.94)$$

where A_1 , B , A_2 , A_3 and $\{q_i\}$ are constants to be specified. Equation (4.92) is a typical direct hardening and dynamic recovery type of formulation augmented with the additional hardening term associated with plastic torsion-curvature and the $q_i^{\eta v}$ give the ratios of self to latent hardening. The reduced dissipation inequality for the multi-criterion model is given as

$$\sum_\eta |\tau^\eta| \dot{\gamma}^\eta + \sum_v |\pi^v| \dot{\phi}^v - \left(\sum_\eta r^\eta \dot{\zeta}^\eta + \sum_v r_c^v \dot{\zeta}_c^v \right) \geq 0. \quad (4.95)$$

4.3.3.2 Single Criterion Model

The single criterion model presented below is a new development in this work, and has not been completely investigated. Therefore, a brief overview is given in this section, with the intent being to elaborate more in future publications which stem from this project. As before, the plastic strain and torsion-curvature evolution equations are given by general forms as sums over the slip system level mechanisms in terms of the plastic multiplier and the direction of flow, *i.e.* ,

$$\dot{\boldsymbol{\epsilon}}^p = \sum_{\eta} \dot{\gamma}^{\eta} \mathbf{N}^{\eta} \quad (4.96)$$

$$\dot{\mathbf{K}}^p = \sum_{\eta} \dot{\gamma}^{\eta} \mathbf{N}_c^{\eta} \quad (4.97)$$

In contrast to the multi-criterion model, a single plastic multiplier (yield function) is used to define the viscoplastic response and is given as

$$\dot{\gamma}^{\eta} = \dot{\gamma}_0 \left(\frac{\langle |\tau^{\eta} - \pi^{\eta} / \ell_p^{\eta}| - r_{sc}^{\eta} \rangle}{g_{sc}^{\eta}} \right)^{m_{sc}} \quad (4.98)$$

$$F_{sc}^{\eta} = |\tau^{\eta} - \pi^{\eta} / \ell_p^{\eta}| - r_{sc}^{\eta} \quad (4.99)$$

In the proposed yield function, the resolved couple-stress acts as a back stress-like quantity and bears a striking resemblance to the slip system level micro-force balance law (which is interpreted as a yield function) proposed by Gurtin [103]. In Gurtins model, the back stress quantity is derived by using the principle of virtual power at the slip system level which considers the slip rates and their gradients as independent kinematic degrees-of-freedom. Our yield function has been motivated by considering single criterion J_2 -type extensions of micropolar plasticity [57, 58], the previously discussed multi-criterion single crystal formulation, and Gurtins slip-gradient based approach. We intend to further pursue the connections between Gurtins theory and the single criterion model presented herein in more detail in future work.

Assuming an associative structure to the plasticity equations, we then obtain the following specific evolution equations for the plastic strain and torsion-curvature by taking the derivative of the yield function in equation (4.99) with respect to force and couple-stress tensors, respectively:

$$\mathbf{N}^{\eta} = \frac{\partial F_{sc}^{\eta}}{\partial \boldsymbol{\sigma}} = \mathbf{Z}^{\eta} \text{sgn}(\tau^{\eta} - \pi^{\eta} / \ell_p^{\eta}) \quad (4.100)$$

$$\mathbf{N}_c^{\eta} = \frac{\partial F_{sc}^{\eta}}{\partial \mathbf{m}} = \frac{1}{\ell_p^{\eta}} \mathbf{H}^{\eta} \text{sgn}(\tau^{\eta} - \pi^{\eta} / \ell_p^{\eta}) \quad (4.101)$$

$$\dot{\boldsymbol{\epsilon}}^p = \sum_{\eta} \dot{\gamma}^{\eta} \mathbf{Z}^{\eta} \text{sgn}(\tau^{\eta} - \pi^{\eta} / \ell_p^{\eta}) \quad (4.102)$$

$$\dot{\mathbf{K}}^p = \sum_{\eta} \frac{\dot{\gamma}^{\eta}}{\ell_p^{\eta}} \mathbf{H}^{\eta} \text{sgn}(\tau^{\eta} - \pi^{\eta} / \ell_p^{\eta}) \quad (4.103)$$

The single criterion model is then completed by specifying the evolution equation for the threshold stress ISV in analogous fashion to that presented for the multi-criterion model, *i.e.*

$$\dot{r}_{sc}^\eta = \sum_v (A_1 q_1^{\eta v} - B r_{sc}^\eta) |\dot{\gamma}^v| + \frac{A_2}{\ell_p^v} q_2^{\eta v} |\dot{\gamma}^v| \quad (4.104)$$

The reduced dissipation inequality for the single criterion model is given as

$$\sum_\eta |\tau^\eta - \pi^\eta / \ell_p^\eta| |\dot{\gamma}^\eta| - \sum_\eta r_{sc}^\eta \dot{\zeta}_{sc}^\eta \geq 0. \quad (4.105)$$

The methodology for determining the material constants (both elastic and plastic) for the micropolar single crystal is still an open topic in the literature and there are differing vantage points on how to best go about this [177]. The approach advocated by Forest *et al.* is that in the elastic regime the response of the Cosserat polycrystal should not deviate too far from the classical elastic response. This is interpreted as meaning that during purely elastic deformation, micro-rotations coincide with continuum rotations and that couple-stresses remain negligibly small. To achieve this behavior, the Cosserat couple modulus, μ_c , is set to a large value to penalize large differences between the continuum and micro-rotations, while simultaneously choosing a small value for the additional micropolar elastic constants, $\underline{\underline{\mathfrak{C}}} = \underline{\underline{\mathfrak{I}}}$, in the couple-stress/torsion-curvature relation, equation (4.78).

4.3.4 Non-Associative Model for Slip Transfer at Grain Boundaries

In our proposed treatment of GBs, in the spirit of core-mantle models, the polycrystal is divided into at least two regions: grain interiors and GBs, while leaving open the possibility of defining a separate triple-junction region as well. This type of approach has also been used by many researchers with several variations to explain scale-dependent yielding/strain-hardening as well as trying to predict transitions in deformation modes in polycrystals as the grain size decreases and the GB volume fraction increases (cf. [87, 88]). The motivation for the development of such composite models is two-fold and is driven by the following observations. GBs act as significant obstacles to dislocations and obviously lead to the increase in initial yield strength with decreasing grain size in conventional grain-sized polycrystals as described by the Hall-Petch effect. In addition to enhancing the initial yield strength, GBs also play a critical role in determining strain-hardening behavior as well. Increased slip multiplicity occurs in the GB regions as a result of intergranular constraints on slip in light of lattice mismatch. As a result of this increased dislocation activity, in addition to piled-up dislocations at the interface, it is believed that the GB regions strain-harden at a much higher rate than grain interiors which are typically characterized by fewer active slip systems.

4.3.4.1 Grain Interiors

Within the grain interiors, we assume that the response remains classical in the sense that Schmid's law holds, and that strain-hardening may be described in terms of a generalized Taylor relation,

which may include dependence on both the GND and the statistically immobile dislocation (SID) density. The term “statistically immobile” is preferred here over the more common usage of “statistically stored” because we find this term misleading. The distinct separation of dislocation density into geometrically necessary and statistically stored parts is unique (in the discrete case), and requires the specification of an area or volume over which the quantities are to be calculated. However, if we consider the separation of the total dislocation density into mobile and immobile portions, there is no such unique separation in terms of GNDs and SSDs. Even if it is assumed that GNDs only contribute to the immobile density, the SSD density will still have contributions to both the mobile and immobile dislocation populations, and ultimately it is the *immobile* portion of the SSD density that contributes to the slip resistance via the Taylor relation. In other words, the SID density is a subset of the total SSD density. The buildup of SID density is described by a Kocks-Mecking type of equation [128, 162] reflecting accumulation (due to statistical trapping) and annihilation (due to dynamic recovery). A summary of the relevant equations is given by

$$r^\eta = \iota \mu b \sqrt{\rho_{tot}^\eta}, \quad \rho_{tot}^\eta = \sqrt{\rho_{SID}^\eta + \rho_{GND}^\eta} \quad (4.106)$$

$$\dot{\rho}_{SID}^\eta = \sum_v h^{\eta v} \left(c_1 \sqrt{\rho_{tot}^v} - c_2 \rho_{SID}^v \right) |\dot{\gamma}^v|, \quad \rho_{GND}^\eta = |\phi^\eta| / (b \ell^\eta) \quad (4.107)$$

Here, r^η is an isotropic hardening variable, ι is a geometrical factor related to the dislocation arrangement, μ is the shear modulus, b is the magnitude of the burgers vector, ρ_{tot}^η is the total immobile dislocation density, ρ_{SID}^η is the immobile portion of the SSD density, ρ_{GND}^η is the GND density, $h^{\eta v}$ is a coupling coefficient between slip systems η and v , and c_1 and c_2 are parameters that are specified. These equations, unlike those introduced in the previous section, are the types of relations we will employ as we move towards the use of more physically-based ISVs. The kinematics remain such that the evolution of plastic strain is given by the sum of shearing rates over all active slip systems, *i.e.* ,

$$\dot{\epsilon}^p = \sum_\eta \dot{\gamma}^\eta \mathbf{N}^\eta \quad (4.108)$$

Depending on what type of formulation (single or multi-criterion) is chosen based on the findings of the single crystal study of Section 4.3.3, the plastic-torsion curvature flow rule may be determined in a number of ways and is left unspecified for the time being.

4.3.4.2 Grain Boundary Regions

Experimental observations have shown that the slip transmission process depends not only on the resolved shear stress on the incoming glide plane, but also on the resolved shear stress on the potential outgoing glide planes [138, 139, 140]. Accordingly, we propose a non-associative flow rule for each GB slip system, which can be written in the general form

$$F_{A \rightarrow B}^{\eta, v} := |\tau_A^\eta + a \tau_B^{\eta, v}| - r^{\eta, v} \quad (4.109)$$

where τ_A^η is the resolved shear stress on plane η in grain A, a is a material parameter reflecting the magnitude of the non-Schmid stress required for successful slip transfer, $\tau_B^{\eta, v}$ is the resolved shear stress on the potential outgoing plane, v , in grain B, and $r^{\eta, v}$ is resistance to slip transfer

across the boundary. In general the transmission threshold stress depends on the orientation of the incoming and outgoing slip systems, the orientation of the GB, and the relevant structural parameters of the GB (dislocations, facets, disclination structural units, nano-porosity, etc.). Ideally, the threshold transmission threshold stress and its evolution should be determined from finer scale simulations, such as molecular dynamics, discrete dislocation, or a multi-scaled method such as CADD [61, 60]. However, there is a paucity of such results for general types of boundaries, and yet it is still undecided as to the applicability of the existing results due to the high strain-rates, low numbers of dislocations considered, and appropriate specification of boundary conditions. Therefore, while we will establish a framework which will be capable of accepting results from these types of simulations, explicit incorporation of such information is beyond the scope of the research. Instead, we focus on qualitative aspects of boundary behavior through the specification of boundary strength and its evolution by borrowing from the existing dislocation and misorientation-based arguments while readily admitting that this is a first-order approximation. The increment of plastic slip would still be given in power-law form as in the previous section, and the flow potential defining the direction of plastic straining is the same as in the classical case. The normal to the viscoplastic potential and to the yield surface are therefore given as

$$\mathbf{N}^\eta = \mathbf{Z}^\eta \text{sgn}(\tau_A^\eta) , \quad \frac{\partial F_{A \rightarrow B}^{\eta,v}}{\partial \boldsymbol{\sigma}} = (\mathbf{Z}_A^\eta + a \mathbf{Z}_B^v) \text{sgn}(\tau_A^\eta + a \tau_B^{\eta,v}) \quad (4.110)$$

and the proposed model is clearly non-associative, $\mathbf{N}^\eta \neq \frac{\partial F_{A \rightarrow B}^{\eta,v}}{\partial \boldsymbol{\sigma}}$. Again, as in the case for grain interiors, the form of the plastic torsion-curvature flow rule will be selected based on the outcome of the single crystal parametric study, and is left unspecified at present.

In addition to the proposed modifications of the flow rules, it may also be desirable to modify the plastic kinematics in the GB region as well to account for the possibility of GB shearing and torsion-curvature development independent of that induced by the glide of dislocations in active slip planes. The incorporation of these deformation modes is achieved by a superposition of the GB kinematics onto the slip system based kinematics given in previous discussions, *i.e.* ,

$$\dot{\boldsymbol{\epsilon}}^p = \sum_{\eta} \dot{\gamma}^\eta \mathbf{Z}^\eta \text{sgn}(\tau^\eta) + \sum_v \dot{\gamma}_{GB}^v \mathbf{Z}_{GB}^v \text{sgn}(\tau_{GB}^v) \quad (4.111)$$

$$\dot{\mathbf{K}}^p = \sum_{\eta} \frac{\dot{\phi}^\eta}{\ell_{slip}^\eta} \mathbf{H}_{slip}^\eta \text{sgn}(\tau^\eta) + \sum_v \frac{\dot{\phi}^v}{\ell_{GB}^v} \mathbf{H}_{GB}^v \text{sgn}(\tau_{GB}^v) , \quad \mathbf{H}_{GB}^v = \boldsymbol{\zeta}^v \otimes \mathbf{t}^v \quad (4.112)$$

where the summation is over the η slip systems and v grain boundaries, and in the simple two-dimensional conceptualization the orientation tensor, \mathbf{H}_{GB}^v , is the outer product of the unit grain-boundary tangent vector, $\boldsymbol{\zeta}^v$, and the transverse (out-of-plane) direction. The further development of these concepts is left for future work.

4.4 Numerical Implementation

4.4.1 Element Formulation

The following development concerns the implementation of a 2-D plane strain micropolar finite element, in which the active degrees of freedom are the displacements in the x_1 and x_2 directions in addition to the micro-rotation about the x_3 axis: u_1 , u_2 , and ϕ_3 . Accordingly the non-zero micropolar strain and torsion-curvature measures are $\bar{\epsilon}_{11}$, $\bar{\epsilon}_{22}$, $\bar{\epsilon}_{12}$, $\bar{\epsilon}_{21}$, $\bar{\kappa}_{13}$, and $\bar{\kappa}_{23}$, which for convenience of notation can be represented compactly via the generalized micropolar strain vector $\{\bar{E}\}$ as

$$\{\bar{E}\} = \{ \bar{\epsilon}_{11} \quad \bar{\epsilon}_{22} \quad \bar{\epsilon}_{12} \quad \bar{\epsilon}_{21} \quad \bar{\kappa}_{13} \quad \bar{\kappa}_{23} \}^T \quad (4.113)$$

In the usual manner, the continuous displacement vector, $\{a\}$, for an element is approximated by the nodal displacement vector, $\{\tilde{a}\}$, through the use of the interpolation matrix, $[N]$:

$$\{a\} = [N] \{\tilde{a}\} = \{ u_1 \quad u_2 \quad \phi_3 \}^T \quad (4.114)$$

For a linear 4-noded quadrilateral element, the nodal displacement vector and interpolation matrix then take the forms

$$\{\tilde{a}\} = \{ u_1^1 \quad u_2^1 \quad \phi_3^1 \quad u_1^2 \quad u_2^2 \quad \phi_3^2 \quad u_1^3 \quad u_2^3 \quad \phi_3^3 \quad u_1^4 \quad u_2^4 \quad \phi_3^4 \}^T \quad (4.115)$$

$$[N] = \begin{bmatrix} N_1 & 0 & 0 & N_2 & 0 & 0 & N_3 & 0 & 0 & N_4 & 0 & 0 \\ 0 & N_1 & 0 & 0 & N_2 & 0 & 0 & N_3 & 0 & 0 & N_4 & 0 \\ 0 & 0 & N_1 & 0 & 0 & N_2 & 0 & 0 & N_3 & 0 & 0 & N_4 \end{bmatrix} \quad (4.116)$$

with the linear shape functions given as

$$\begin{aligned} N_1 &= 0.25(1-r)(1-s) \quad , \quad N_2 = 0.25(1+r)(1-s) \\ N_3 &= 0.25(1+r)(1+s) \quad , \quad N_4 = 0.25(1-r)(1+s) \end{aligned} \quad (4.117)$$

where r and s are the natural (isoparametric) coordinates of the element. Using equations (4.114)-(4.117) with the strain-displacement relations given in Section 4.3.1.1 yields the relationship between the strain vector and the nodal displacement vector

$$\{\bar{E}\} = [B] \{\tilde{a}\} \quad (4.118)$$

$$[B] = \begin{bmatrix} N_{1,1} & 0 & 0 & N_{2,1} & 0 & 0 & N_{3,1} & 0 & 0 & N_{4,1} & 0 & 0 \\ 0 & N_{1,2} & 0 & 0 & N_{2,2} & 0 & 0 & N_{3,2} & 0 & 0 & N_{4,2} & 0 \\ 0 & N_{1,1} & -N_1 & 0 & N_{2,1} & -N_2 & 0 & N_{3,1} & -N_3 & 0 & N_{4,1} & -N_4 \\ N_{1,2} & 0 & N_1 & N_{2,2} & 0 & N_2 & N_{3,2} & 0 & N_3 & N_{4,2} & 0 & N_4 \\ 0 & 0 & N_{1,1} & 0 & 0 & N_{2,1} & 0 & 0 & N_{3,1} & 0 & 0 & N_{4,1} \\ 0 & 0 & N_{1,2} & 0 & 0 & N_{2,2} & 0 & 0 & N_{3,2} & 0 & 0 & N_{4,2} \end{bmatrix} \quad (4.119)$$

The strain-displacement matrix, $[B]$, contains the pertinent values of the interpolation functions and their derivatives. The individual components in equation (4.119) are derived using the Jacobian matrix of the transformation between the global and isoparametric coordinates together with the

derivatives of the interpolation functions with respect to the isoparametric coordinates as given in any standard finite element text.

The next step is to obtain the finite element equations using the principle of virtual work given which is rewritten below in matrix notation

$$\int_S \{\delta a\}^T \{\bar{T}\} dS = \int_V \{\delta \bar{E}\} \{\bar{\Sigma}\} dV \quad (4.120)$$

where $\{\bar{T}\}$ is the generalized traction vector and the generalized stress vector, $\{\bar{\Sigma}\}$, follows the appropriate convention based on that of the strain vector, *i.e.*

$$\{\bar{T}\} = \{ T_1 \quad T_2 \quad M_3 \}^T \quad (4.121)$$

$$\{\bar{\Sigma}\} = \{ \sigma_{11} \quad \sigma_{22} \quad \sigma_{12} \quad \sigma_{21} \quad m_{13} \quad m_{23} \}^T \quad (4.122)$$

Finally, the finite element equations are obtained by discretizing and linearizing the principle of virtual work, and pulling the arbitrary nodal variations out of the integrals such that

$$\int_S [N]^T \{\Delta \bar{T}\} dS = \int_V [B]^T \{\Delta \bar{\Sigma}\} dV = \int_V [B]^T [\bar{\mathbb{C}}^{ep}] [B] \{\Delta \tilde{a}\} dV \quad (4.123)$$

or

$$\{\Delta f\} = [K] \{\Delta \tilde{a}\} \quad (4.124)$$

where the incremental stress-strain relations, $\{\tilde{\Sigma}\} = [\bar{\mathbb{C}}^{ep}] \{\tilde{E}\}$, have been substituted in, $[\bar{\mathbb{C}}^{ep}]$ is the constitutive tangent matrix, and $[K]$ is the finite element tangent stiffness matrix. The element has been implemented via a user element subroutine (UEL) in the commercial finite element code ABAQUS [1], as shown in the Appendix for this chapter.

4.4.2 Constitutive Update

The following section covers the algorithmic treatment for integrating the constitutive equations presented in Section 4.3 for both the single and multi-criterion micropolar crystal plasticity models. Two such algorithms are presented: i) a rate-tangent modulus scheme which is an explicit integration method and ii) an implicit return mapping method based on local Newton-Raphson (N-R) iterations. To date, only the rate-tangent method [185] has been implemented numerically within the UEL due to the simplicity of the algorithmic treatment and the uncertainty of what will be chosen as the “final” form of the set of constitutive equations. However, upon the settling on a particular set of constitutive equations it will be advantageous to use the return mapping method for stability reasons and also to reduce the computational times by allowing for the use of larger simulation time steps. Sections 4.4.2.1 and 4.4.2.2 lay out the process for calculating the slip and torsion-curvature increments at the end of the time step for the rate-tangent and return mapping schemes, respectively. The numerical implementation is completed by calculating the algorithmic moduli which are required by the UEL to provide updated predictions for the displacement field at the end of the time step. Derivations of the algorithmic moduli for the rate-tangent and return mapping schemes are given in Sections 4.4.3.1 and 4.4.3.2, respectively.

4.4.2.1 Rate-Tangent Modulus Scheme

In the rate-tangent method, all variables except for the plastic strain and torsion-curvature increments are integrated via forward Euler method, and the plastic increments are determined by solving a set of algebraic equations based on forward-gradient expansions of the flow rules.

Multi-Criterion Model

The incremental relations for the constitutive update based on the multi-criterion model are summarized below in equations (4.125)-(4.128). The slip and torsion curvature increments, $\Delta\gamma^\eta$ and $\Delta\phi^\eta$, are determined by the solution of a set of algebraic equations based on quantities at time step n and then these values are used to update the plastic strain, torsion-curvature, and ISVs at time step $n + 1$. In the following developments, all quantities without explicit subscripts are to be interpreted as being given at time $n + 1$.

$$\bar{\boldsymbol{\epsilon}}^p = \bar{\boldsymbol{\epsilon}}^p|_n + \sum_{\eta} \Delta\gamma^\eta \mathbf{Z}^\eta \quad (4.125)$$

$$\bar{\boldsymbol{\kappa}}^p = \bar{\boldsymbol{\kappa}}^p|_n + \sum_{\eta} \frac{\Delta\phi^\eta}{\ell_p^\eta} \mathbf{H}^\eta \quad (4.126)$$

$$r^\eta = r^\eta|_n + \sum_v (A_1 q_1^{\eta v} - B r_n^\eta) |\Delta\gamma^v| + A_2 q_2^{\eta v} |\Delta\phi^v| \quad (4.127)$$

$$r_c^\eta = r_c^\eta|_n + \sum_v A_3 q_3^{\eta v} |\Delta\phi^v| \quad (4.128)$$

The plastic strain and curvature increments are given by the generalized trapezoid rule, *i.e.* ,

$$\Delta\gamma^\eta = \Delta t \left[(1-a) \dot{\gamma}_n^\eta + a \dot{\gamma}_{n+1}^\eta \right] \quad (4.129)$$

$$\Delta\phi^\eta = \Delta t \left[(1-b) \dot{\phi}_n^\eta + b \dot{\phi}_{n+1}^\eta \right] \quad (4.130)$$

If a (resp. b) is equal to 1 this corresponds to fully implicit integration, whereas if a (resp. b) equal to 0 this corresponds to explicit integration. The plastic shearing and torsion-curvature rates at the end of the time step are approximated via forward-gradient expansion of the flow rules about the state at time, t_n , *i.e.* ,

$$\dot{\gamma}_{n+1}^\eta = \dot{\gamma}_n^\eta + \left. \frac{\partial \dot{\gamma}^\eta}{\partial \tau^\eta} \right|_n \Delta\tau^\eta + \left. \frac{\partial \dot{\gamma}^\eta}{\partial r^\eta} \right|_n \Delta r^\eta \quad (4.131)$$

$$\dot{\phi}_{n+1}^\eta = \dot{\phi}_n^\eta + \left. \frac{\partial \dot{\phi}^\eta}{\partial \pi^\eta} \right|_n \Delta\pi^\eta + \left. \frac{\partial \dot{\phi}^\eta}{\partial r_c^\eta} \right|_n \Delta r_c^\eta \quad (4.132)$$

Listed below are the flow rules and other explicit expressions entering the expansions given in equations (4.131) and (4.132):

$$\dot{\gamma}^\eta = \dot{\gamma}_0 \left(\frac{\langle |\tau^\eta| - r^\eta \rangle}{g^\eta} \right)^m \text{sgn}(\tau^\eta) \quad (4.133)$$

$$\frac{\partial \dot{\gamma}^\eta}{\partial \tau^\eta} = \frac{m \dot{\gamma}_0}{g^\eta} \left(\frac{\langle |\tau^\eta| - r^\eta \rangle}{g^\eta} \right)^{m-1} = \frac{m \dot{\gamma}}{|\tau^\eta| - r^\eta} \text{sgn}(\tau^\eta) \quad (4.134)$$

$$\frac{\partial \dot{\gamma}^\eta}{\partial r^\eta} = -\frac{m\dot{\gamma}_0}{g^\eta} \left(\frac{\langle |\tau^\eta| - r^\eta \rangle}{g^\eta} \right)^{m-1} \text{sgn}(\tau^\eta) = -\frac{m\dot{\gamma}}{|\tau^\eta| - r^\eta} \text{sgn}(\tau^\eta) \quad (4.135)$$

$$\Delta \tau^\eta = \mathbf{Z}^\eta : \Delta \boldsymbol{\sigma} = \mathbf{Z}^\eta : \mathbb{C} : \Delta \bar{\boldsymbol{\epsilon}} - \sum_v \mathbf{Z}^\eta : \mathbb{C} : \mathbf{Z}^v \Delta \gamma^v \quad (4.136)$$

$$\Delta r^\eta = \sum_v (A_1 q_1^{\eta v} - B r_n^\eta) |\Delta \gamma^v| + A_2 q_2^{\eta v} |\Delta \phi^v| \quad (4.137)$$

$$\phi^\eta = \phi_0 \left(\frac{\langle |\pi^\eta / \ell_p^\eta| - r_c^\eta \rangle}{g_c^\eta} \right)^{m_c} \text{sgn}(\pi^\eta) \quad (4.138)$$

$$\frac{\partial \phi^\eta}{\partial \pi^\eta} = \frac{m_c \phi_0}{\ell_p^\eta g_c^\eta} \left(\frac{\langle |\pi^\eta / \ell_p^\eta| - r_c^\eta \rangle}{g_c^\eta} \right)^{m_c-1} = \frac{m_c \phi}{|\pi^\eta| - \ell_p^\eta r_c^\eta} \text{sgn}(\pi^\eta) \quad (4.139)$$

$$\frac{\partial \phi^\eta}{\partial r_c^\eta} = -\frac{m_c \phi_0}{g_c^\eta} \left(\frac{\langle |\pi^\eta / \ell_p^\eta| - r_c^\eta \rangle}{g_c^\eta} \right)^{m_c-1} \text{sgn}(\pi^\eta) = -\frac{m_c \phi}{|\pi^\eta / \ell_p^\eta| - r_c^\eta} \quad (4.140)$$

$$\Delta \pi^\eta = \mathbf{H}^\eta : \Delta \mathbf{m} = \mathbf{H}^\eta : \mathbb{D} : \Delta \bar{\boldsymbol{\kappa}} - \sum_v \mathbf{H}^\eta : \mathbb{D} : \mathbf{H}^v \frac{\Delta \phi^v}{\ell_p^v} \quad (4.141)$$

$$\Delta r_c^\eta = \sum_v A_3 q_3^{\eta v} |\Delta \phi^v| \quad (4.142)$$

Upon substitution of the above expressions into the generalized trapezoid rule for the plastic shear and torsion-curvature increments we obtain the two equations

$$\begin{aligned} \Delta \gamma^\eta &= \dot{\gamma}_n^\eta \Delta t + a \Delta t \left[\frac{\partial \dot{\gamma}^\eta}{\partial \tau^\eta} \Big|_n \left(\mathbf{Z}^\eta : \mathbb{C} : \Delta \bar{\boldsymbol{\epsilon}} - \sum_v \mathbf{Z}^\eta : \mathbb{C} : \mathbf{Z}^v \Delta \gamma^v \right) \right. \\ &\quad \left. + \frac{\partial \dot{\gamma}^\eta}{\partial r^\eta} \Big|_n \left(\sum_v (A_1 q_1^{\eta v} - B r_n^\eta) |\Delta \gamma^v| + A_2 q_2^{\eta v} |\Delta \phi^v| \right) \right] \end{aligned} \quad (4.143)$$

$$\begin{aligned} \Delta \phi^\eta &= \dot{\phi}_n^\eta \Delta t + b \Delta t \left[\frac{\partial \dot{\phi}^\eta}{\partial \pi^\eta} \Big|_n \left(\mathbf{H}^\eta : \mathbb{D} : \Delta \bar{\boldsymbol{\kappa}} - \sum_v \mathbf{H}^\eta : \mathbb{D} : \mathbf{H}^v \frac{\Delta \phi^v}{\ell_p^v} \right) \right. \\ &\quad \left. + \frac{\partial \dot{\phi}^\eta}{\partial r_c^\eta} \Big|_n \sum_v A_3 q_3^{\eta v} |\Delta \phi^v| \right] \end{aligned} \quad (4.144)$$

Gathering terms containing $\Delta \gamma^v$ and $\Delta \phi^v$ on the LHS, the system of equations takes the form

$$\begin{aligned} \Delta \gamma^\eta + a \Delta t \frac{\partial \dot{\gamma}^\eta}{\partial \tau^\eta} \Big|_n \sum_v \mathbf{Z}^\eta : \mathbb{C} : \mathbf{Z}^v \Delta \gamma^v - a \Delta t \frac{\partial \dot{\gamma}^\eta}{\partial r^\eta} \Big|_n \left(\sum_v (A_1 q_1^{\eta v} - B r_n^\eta) |\Delta \gamma^v| + A_2 q_2^{\eta v} |\Delta \phi^v| \right) \\ = \dot{\gamma}_n^\eta \Delta t + a \Delta t \frac{\partial \dot{\gamma}^\eta}{\partial \tau^\eta} \Big|_n (\mathbf{Z}^\eta : \mathbb{C} : \Delta \bar{\boldsymbol{\epsilon}}) \end{aligned} \quad (4.145)$$

$$\begin{aligned} \Delta \phi^\eta + b \Delta t \frac{\partial \dot{\phi}^\eta}{\partial \pi^\eta} \Big|_n \sum_v \mathbf{H}^\eta : \mathbb{D} : \mathbf{H}^v \frac{\Delta \phi^v}{\ell_p^v} - b \Delta t \frac{\partial \dot{\phi}^\eta}{\partial r_c^\eta} \Big|_n \sum_v A_3 q_3^{\eta v} |\Delta \phi^v| \\ = \dot{\phi}_n^\eta \Delta t + b \Delta t \frac{\partial \dot{\phi}^\eta}{\partial \pi^\eta} \Big|_n (\mathbf{H}^\eta : \mathbb{D} : \Delta \bar{\boldsymbol{\kappa}}) \end{aligned} \quad (4.146)$$

which can be written in a more compact notation as in equations (4.147)-(4.148) where the following equivalencies have been used, $\text{sgn}(\Delta\gamma^\eta) = \text{sgn}(\tau_n^\eta)$ and $\text{sgn}(\Delta\phi^\eta) = \text{sgn}(\pi_n^\eta)$, *i.e.* ,

$$\sum_v T_1^{\eta v} \Delta\gamma^v + \sum_v T_2^{\eta v} \Delta\phi^v = \dot{\gamma}_n^\eta \Delta t + a \Delta t \left. \frac{\partial \dot{\gamma}^\eta}{\partial \tau^\eta} \right|_n (\mathbf{Z}^\eta : \mathbb{C} : \Delta \bar{\boldsymbol{\epsilon}}) \quad (4.147)$$

$$\sum_v T_3^{\eta v} \Delta\phi^v = \dot{\phi}_n^\eta \Delta t + b \Delta t \left. \frac{\partial \dot{\phi}^\eta}{\partial \pi^\eta} \right|_n (\mathbf{H}^\eta : \mathbb{D} : \Delta \bar{\boldsymbol{\kappa}}) \quad (4.148)$$

$$T_1^{\eta v} = \delta^{\eta v} + a \Delta t \left(\left. \frac{\partial \dot{\gamma}^\eta}{\partial \tau^\eta} \right|_n (\mathbf{Z}^\eta : \mathbb{C} : \mathbf{Z}^v) - \left. \frac{\partial \dot{\gamma}^\eta}{\partial r^\eta} \right|_n (A_1 q_1^{\eta v} - B r_n^\eta) \text{sgn}(\tau_n^v) \right) \quad (4.149)$$

$$T_2^{\eta v} = -a \Delta t \left. \frac{\partial \dot{\gamma}^\eta}{\partial r^\eta} \right|_n A_2 q_2^{\eta v} \text{sgn}(\pi_n^v) \quad (4.150)$$

$$T_3^{\eta v} = \delta^{\eta v} + \frac{b \Delta t}{\ell_p^v} \left(\left. \frac{\partial \dot{\phi}^\eta}{\partial \pi^\eta} \right|_n (\mathbf{H}^\eta : \mathbb{D} : \mathbf{H}^v) - \ell_p^v \left. \frac{\partial \dot{\phi}^\eta}{\partial r_c^\eta} \right|_n A_3 q_3^{\eta v} \text{sgn}(\pi_n^v) \right) \quad (4.151)$$

The above represents a system of matrix equations (4.147)-(4.148) which can be solved for the increments of plastic shear and torsion-curvature. Since the threshold couple-stress evolution equation does not depend on the rate of plastic shear on the associated slip system, the two matrix equations are not fully coupled. In other words, we can first solve for the increment of plastic torsion-curvature and immediately insert the result into the matrix equation for the plastic shear increment. If this were not the case, the system of matrix equations above would be fully coupled and would result in a slightly more involved solution procedure for the plastic slip and torsion-curvature increments. As it stands, equation (4.148) can be directly inverted to solve for the plastic curvature increments as shown in equation (4.152). The result is then directly inserted into equation (4.147) giving the plastic shear increments in equation (4.153):

$$\Delta\phi^\eta = \sum_v (T_3^{\eta v})^{-1} \left(\dot{\phi}_n^v \Delta t + b \Delta t \left. \frac{\partial \dot{\phi}^v}{\partial \pi^v} \right|_n (\mathbf{H}^v : \mathbb{D} : \Delta \bar{\boldsymbol{\kappa}}) \right) \quad (4.152)$$

$$\Delta\gamma^\eta = \sum_v (T_1^{\eta v})^{-1} \left(\dot{\gamma}_n^v \Delta t + a \Delta t \left. \frac{\partial \dot{\gamma}^v}{\partial \tau^v} \right|_n (\mathbf{Z}^v : \mathbb{C} : \Delta \bar{\boldsymbol{\epsilon}}) \right) - \sum_v \sum_\chi (T_1^{\eta v})^{-1} T_2^{v\chi} \Delta\phi^\chi \quad (4.153)$$

Single Criterion Model

An analogous procedure is performed for the single criterion model by noting that we must only calculate the plastic slip increment. In this case, the governing incremental relations are given by

$$\bar{\boldsymbol{\epsilon}}^p = \bar{\boldsymbol{\epsilon}}^p|_n + \sum_\eta \Delta\gamma^\eta \mathbf{Z}^\eta \quad (4.154)$$

$$\bar{\boldsymbol{\kappa}}^p = \bar{\boldsymbol{\kappa}}^p|_n + \sum_\eta \frac{\Delta\gamma^\eta}{\ell_p^\eta} \mathbf{H}^\eta \quad (4.155)$$

$$r_{sc}^\eta = r_{sc}^\eta|_n + \sum_v (A_1 q_1^{\eta v} - B r_{sc}^\eta) |\Delta\gamma^v| + A_2 q_2^{\eta v} |\Delta\phi^v| \quad (4.156)$$

As before the plastic slip increment is given by the generalized trapezoid rule, *i.e.*

$$\Delta\gamma^\eta = \Delta t \left[(1-a) \dot{\gamma}_n^\eta + a \dot{\gamma}_{n+1}^\eta \right] \quad (4.157)$$

and the forward-gradient approximation of the flow rule for the single criterion model has the form

$$\dot{\gamma}_{n+1}^\eta = \dot{\gamma}_n^\eta + \left. \frac{\partial \dot{\gamma}^\eta}{\partial \tau^\eta} \right|_n \Delta \tau^\eta + \left. \frac{\partial \dot{\gamma}^\eta}{\partial \pi^\eta} \right|_n \Delta \pi^\eta + \left. \frac{\partial \dot{\gamma}^\eta}{\partial r_{sc}^\eta} \right|_n \Delta r_{sc}^\eta \quad (4.158)$$

The expressions in the forward-gradient expression are then given as

$$\dot{\gamma}^\eta = \dot{\gamma}_0 \left(\frac{\langle |\tau^\eta - \pi^\eta / \ell_p^\eta| - r_{sc}^\eta \rangle}{g_{sc}^\eta} \right)^{m_{sc}} \quad (4.159)$$

$$\frac{\partial \dot{\gamma}^\eta}{\partial \tau^\eta} = \frac{m_{sc} \dot{\gamma}_0}{g_{sc}^\eta} \left(\frac{\langle |\tau^\eta - \pi^\eta / \ell_p^\eta| - r_{sc}^\eta \rangle}{g_{sc}^\eta} \right)^{m_{sc}-1} = \frac{m_{sc} \dot{\gamma}}{|\tau^\eta - \pi^\eta / \ell_p^\eta| - r_{sc}^\eta} \text{sgn}(\tau^\eta - \pi^\eta / \ell_p^\eta) \quad (4.160)$$

$$\frac{\partial \dot{\gamma}^\eta}{\partial \pi^\eta} = -\frac{m_{sc} \dot{\gamma}_0}{\ell_p^\eta g_{sc}^\eta} \left(\frac{\langle |\tau^\eta - \pi^\eta / \ell_p^\eta| - r_{sc}^\eta \rangle}{g_{sc}^\eta} \right)^{m_{sc}-1} = -\frac{m_{sc} \dot{\gamma}}{\ell_p^\eta (|\tau^\eta - \pi^\eta / \ell_p^\eta| - r_{sc}^\eta)} \text{sgn}(\tau^\eta - \pi^\eta / \ell_p^\eta) \quad (4.161)$$

$$\frac{\partial \dot{\gamma}^\eta}{\partial r_{sc}^\eta} = -\frac{m_{sc} \dot{\gamma}_0}{g_{sc}^\eta} \left(\frac{\langle |\tau^\eta - \pi^\eta / \ell_p^\eta| - r_{sc}^\eta \rangle}{g_{sc}^\eta} \right)^{m_{sc}-1} = -\frac{m_{sc} \dot{\gamma}}{|\tau^\eta - \pi^\eta / \ell_p^\eta| - r_{sc}^\eta} \quad (4.162)$$

$$\Delta \tau^\eta = \mathbf{Z}^\eta : \Delta \boldsymbol{\sigma} = \mathbf{Z}^\eta : \mathbb{C} : \Delta \bar{\boldsymbol{\epsilon}} - \sum_v \mathbf{Z}^\eta : \mathbb{C} : \mathbf{Z}^v \Delta \gamma^v \quad (4.163)$$

$$\Delta \pi^\eta = \mathbf{H}^\eta : \Delta \mathbf{m} = \mathbf{H}^\eta : \mathbb{D} : \Delta \bar{\boldsymbol{\kappa}} - \sum_v \mathbf{H}^\eta : \mathbb{D} : \mathbf{H}^v \frac{\Delta \gamma^v}{\ell_p^v} \quad (4.164)$$

$$\Delta r_{sc}^\eta = \sum_v (A_1 q_1^{\eta v} - B r_{sc}^\eta) |\Delta \gamma^v| + \frac{A_2}{\ell_p^v} q_2^{\eta v} |\Delta \gamma^v| \quad (4.165)$$

Substitution of equations (4.160)-(4.165) into equation (4.157) then leads to

$$\begin{aligned} \Delta \gamma^\eta = & \dot{\gamma}_n^\eta \Delta t + a \Delta t \left[\left. \frac{\partial \dot{\gamma}^\eta}{\partial \tau^\eta} \right|_n \left(\mathbf{Z}^\eta : \mathbb{C} : \Delta \bar{\boldsymbol{\epsilon}} - \sum_v \mathbf{Z}^\eta : \mathbb{C} : \mathbf{Z}^v \Delta \gamma^v \right) \right. \\ & + \left. \left. \frac{\partial \dot{\gamma}^\eta}{\partial \pi^\eta} \right|_n \left(\mathbf{H}^\eta : \mathbb{D} : \Delta \bar{\boldsymbol{\kappa}} - \sum_v \mathbf{H}^\eta : \mathbb{D} : \mathbf{H}^v \frac{\Delta \gamma^v}{\ell_p^v} \right) \right. \\ & + \left. \left. \frac{\partial \dot{\gamma}^\eta}{\partial r_{sc}^\eta} \right|_n \left(\sum_v (A_1 q_1^{\eta v} - B r_{sc}^\eta) |\Delta \gamma^v| + \frac{A_2}{\ell_p^v} q_2^{\eta v} |\Delta \gamma^v| \right) \right], \end{aligned} \quad (4.166)$$

which upon rearrangement of terms containing $\Delta \gamma^v$ to the LHS leads to the matrix equation to be solved for the plastic slip increments

$$\sum_v T^{\eta v} \Delta \gamma^v = \dot{\gamma}_n^\eta \Delta t + a \Delta t \left(\left. \frac{\partial \dot{\gamma}^\eta}{\partial \tau^\eta} \right|_n (\mathbf{Z}^\eta : \mathbb{C} : \Delta \bar{\boldsymbol{\epsilon}}) + \left. \frac{\partial \dot{\gamma}^\eta}{\partial \pi^\eta} \right|_n (\mathbf{H}^\eta : \mathbb{D} : \Delta \bar{\boldsymbol{\kappa}}) \right) \quad (4.167)$$

$$T^{\eta v} = \delta^{\eta v} + a\Delta t \left[\frac{\partial \dot{\gamma}^\eta}{\partial \tau^\eta} \Big|_n (\mathbf{Z}^\eta : \mathbb{C} : \mathbf{Z}^v) + \frac{1}{\ell_p^v} \frac{\partial \dot{\gamma}^\eta}{\partial \pi^\eta} \Big|_n (\mathbf{H}^\eta : \mathbb{D} : \mathbf{H}^v) - \frac{\partial \dot{\gamma}^\eta}{\partial r_{sc}^\eta} \Big|_n \left(A_1 q_1^{\eta v} - B r_{sc}^\eta + \frac{A_2}{\ell_p^v} q_2^{\eta v} \right) \text{sgn}(\tau_n^v - \pi_n^v / \ell_p^v) \right] \quad (4.168)$$

where the solution is expressed as

$$\Delta \gamma^\eta = \sum_v (T^{\eta v})^{-1} \left[\dot{\gamma}_n^v \Delta t + a\Delta t \left(\frac{\partial \dot{\gamma}^v}{\partial \tau^v} \Big|_n (\mathbf{Z}^v : \mathbb{C} : \Delta \bar{\boldsymbol{\epsilon}}) + \frac{\partial \dot{\gamma}^v}{\partial \pi^v} \Big|_n (\mathbf{H}^v : \mathbb{D} : \Delta \bar{\boldsymbol{\kappa}}) \right) \right]. \quad (4.169)$$

4.4.2.2 Return Mapping Scheme

The return mapping integration algorithms are based on the concept of satisfying the consistency (or in the case of rate-dependent models, quasi-consistency) conditions at time step t_{n+1} . The two main components of the method are an integration scheme which transforms the constitutive equations into a system on nonlinear algebraic equations, and a solution scheme for the set of nonlinear algebraic equations. The presentation below follows that given in Miehe and Schroder [166], and is based on a fully implicit backward Euler method.

Multi-Criterion Model

The algorithmic constitutive equations are the same as given in equations (4.125)-(4.128) and are omitted here for brevity. We now introduce the notion of trial elastic strains and torsion-curvatures, $\bar{\boldsymbol{\epsilon}}^{e*}$ and $\bar{\boldsymbol{\kappa}}^{e*}$, in equations (4.170) and (4.171) which are fixed for a given increment of deformation.

$$\bar{\boldsymbol{\epsilon}}^e = \bar{\boldsymbol{\epsilon}}^{e*} - \sum_\eta \Delta \gamma^\eta \mathbf{Z}^\eta, \quad \bar{\boldsymbol{\epsilon}}^{e*} = \bar{\boldsymbol{\epsilon}} - \bar{\boldsymbol{\epsilon}}^p|_n \quad (4.170)$$

$$\bar{\boldsymbol{\kappa}}^e = \bar{\boldsymbol{\kappa}}^{e*} - \sum_\eta \frac{\Delta \phi^\eta}{\ell_p^\eta} \mathbf{H}^\eta, \quad \bar{\boldsymbol{\kappa}}^{e*} = \bar{\boldsymbol{\kappa}} - \bar{\boldsymbol{\kappa}}^p|_n \quad (4.171)$$

$$\boldsymbol{\sigma} = \boldsymbol{\sigma}^* - \sum_\eta \mathbb{C} : \mathbf{Z}^\eta \Delta \gamma^\eta, \quad \boldsymbol{\sigma}^* = \mathbb{C} : \bar{\boldsymbol{\epsilon}}^{e*} \quad (4.172)$$

$$\mathbf{m} = \mathbf{m}^* - \sum_\eta \mathbb{D} : \mathbf{H}^\eta \frac{\Delta \phi^\eta}{\ell_p^\eta}, \quad \mathbf{m}^* = \mathbb{D} : \bar{\boldsymbol{\kappa}}^{e*} \quad (4.173)$$

These trial elastic strains and torsion-curvatures are used to calculate trial force and couple-stresses in equations (4.172) and (4.173) (and their slip and/or torsion-curvature resolved counterparts) which are then used to evaluate whether or not each slip and torsion-curvature system is activated for the given increment of deformation. This evaluation is performed by checking the yield conditions which are given below for slip and torsion-curvature:

$$F^{\eta*} := \left| \tau^{\eta*} \right| - r^\eta|_n \quad (4.174)$$

$$F_c^{\eta*} := \left| \frac{\pi^{\eta*}}{\ell_p^\eta} \right| - r_c^\eta|_n \quad (4.175)$$

If $F^{\eta*}, F_c^{\eta*} < 0$, then the slip and/or torsion-curvature system is inactive, and if all slip and torsion-curvature systems are inactive then the trial elastic strain and torsion-curvature is taken to be the elastic strain and torsion-curvature at step t_{n+1} , and the constitutive update proceeds to the next time step. If, however, some of the yield conditions are violated, $F^{\eta*}, F_c^{\eta*} > 0$, we seek to find the slip and torsion-curvature increments that satisfy the quasi-consistency conditions at step $n+1$. The quasi-consistency conditions are obtained by inverting the flow rules, *i.e.* ,

$$R^{\eta} := |\tau^{\eta}| - \left(r^{\eta} + g^{\eta} \left(\frac{|\Delta\gamma^{\eta}|}{\dot{\gamma}_0 \Delta t} \right)^{\frac{1}{m}} \right) = 0 \quad (4.176)$$

$$R_c^{\eta} := \left| \frac{\pi^{\eta}}{\ell_p^{\eta}} \right| - \left(r_c^{\eta} + g_c^{\eta} \left(\frac{|\Delta\phi^{\eta}|}{\dot{\phi}_0 \Delta t} \right)^{\frac{1}{m_c}} \right) = 0 \quad (4.177)$$

Since the initial guesses for the slip and torsion-curvature increments will not satisfy the above conditions, an iterative solution process is required. This is achieved by performing Taylor series expansions of R^{η} and R_c^{η} about the end of the time increment and setting them equal to zero, *i.e.* ,

$$R^{\eta}(\bar{\epsilon}^{e*}, \Delta\gamma^{v^{i+1}}, \Delta\phi^{v^{i+1}}) = R^{\eta^i} + \sum_v \frac{\partial R^{\eta}}{\partial \Delta\gamma^v} \Big|_i \delta(\Delta\gamma^v) + \sum_v \frac{\partial R^{\eta}}{\partial \Delta\phi^v} \Big|_i \delta(\Delta\phi^v) = 0 \quad (4.178)$$

$$R_c^{\eta}(\bar{\kappa}^{e*}, \Delta\gamma^{v^{i+1}}, \Delta\phi^{v^{i+1}}) = R_c^{\eta^i} + \sum_v \frac{\partial R_c^{\eta}}{\partial \Delta\gamma^v} \Big|_i \delta(\Delta\gamma^v) + \sum_v \frac{\partial R_c^{\eta}}{\partial \Delta\phi^v} \Big|_i \delta(\Delta\phi^v) = 0 \quad (4.179)$$

$$\delta(\Delta\gamma^v) = \Delta\gamma^{v^{i+1}} - \Delta\gamma^{v^i}, \quad \delta(\Delta\phi^v) = \Delta\phi^{v^{i+1}} - \Delta\phi^{v^i} \quad (4.180)$$

The notation used in equations (4.178)-(4.180) is such that the raised integer superscripts refer to the Newton-Raphson iteration number, and $\delta(\Delta\gamma^v)$ and $\delta(\Delta\phi^v)$ represent the corrections to the slip and torsion-curvature increments. The iterative solution process is repeated until acceptable solutions are found for $\Delta\gamma^v$ and $\Delta\phi^v$, such that $\delta(\Delta\gamma^v), \delta(\Delta\phi^v) \rightarrow 0$. The system of equations to be solved can be compactly expressed in matrix notation as

$$\left[\frac{\partial R}{\partial \Delta\gamma} \right] \{ \delta(\Delta\gamma) \} + \left[\frac{\partial R}{\partial \Delta\phi} \right] \{ \delta(\Delta\phi) \} = - \{ R \} \quad (4.181)$$

$$\left[\frac{\partial R_c}{\partial \Delta\gamma} \right] \{ \delta(\Delta\gamma) \} + \left[\frac{\partial R_c}{\partial \Delta\phi} \right] \{ \delta(\Delta\phi) \} = - \{ R_c \} \quad (4.182)$$

where the derivatives necessary for the N-R procedure are given as

$$\frac{\partial R^{\eta}}{\partial \Delta\gamma^v} = -\mathbf{Z}^{\eta} : \mathbb{C} : \mathbf{Z}^v \text{sgn}(\tau^{\eta}) - \left[(A_1 q_1^{\eta v} - B r_n^{\eta}) \text{sgn}(\Delta\gamma^v) + \frac{g^v}{m \dot{\gamma}_0 \Delta t} \left(\frac{|\Delta\gamma^v|}{\dot{\gamma}_0 \Delta t} \right)^{1/(m-1)} \text{sgn}(\Delta\gamma^v) \right] \quad (4.183)$$

$$\frac{\partial R^{\eta}}{\partial \Delta\phi^v} = -A_2 q_2^{\eta v} \text{sgn}(\phi^v) \quad (4.184)$$

$$\frac{\partial R_c^{\eta}}{\partial \Delta\gamma^v} = 0 \quad (4.185)$$

$$\frac{\partial R_c^\eta}{\partial \Delta \phi^v} = -\frac{1}{\ell_p^v} \mathbf{H}^\eta : \mathbb{D} : \mathbf{H}^v \text{sgn}(\pi^\eta) - \left[A_3 q_3^{\eta v} \text{sgn}(\Delta \phi^v) + \frac{g_c^v}{m_c \dot{\phi}_0 \Delta t} \left(\frac{|\Delta \phi^v|}{\dot{\phi}_0 \Delta t} \right)^{1/(m_c-1)} \text{sgn}(\Delta \phi^v) \right] \quad (4.186)$$

Single Criterion Model

The return mapping procedure for the single criterion model is analogous to the multi-criterion model, and the governing equations are summarized below. The algorithmic treatment of the constitutive equations has previously been given in equations (4.154)-(4.156) for this model. The trial yield and quasi-consistency conditions are

$$F_{sc}^{\eta*} := \left| \tau^{\eta*} - \frac{\pi^{\eta*}}{\ell_p^\eta} \right| - r_{sc}^\eta|_n \quad (4.187)$$

$$R_{sc}^\eta := \left| \tau^{\eta*} - \frac{\pi^{\eta*}}{\ell_p^\eta} \right| - \left(r_{sc}^\eta + g_{sc}^\eta \left(\frac{|\Delta \dot{\gamma}^\eta|}{\dot{\gamma}_0 \Delta t} \right)^{\frac{1}{m_{sc}}} \right) = 0 \quad (4.188)$$

and the Taylor series expansion is given as

$$R_{sc}^\eta(\bar{\boldsymbol{\epsilon}}^{e*}, \bar{\boldsymbol{\kappa}}^{e*}, \Delta \gamma^{v^{i+1}}) = R_{sc}^\eta|^i + \sum_v \frac{\partial R_{sc}^\eta}{\partial \Delta \gamma^v} \Big|_i \delta(\Delta \gamma^v) = 0 \quad (4.189)$$

where the iterative slip increment corrections are determined by the matrix equation

$$\{\delta(\Delta \gamma)\} = - \left[\frac{\partial R_{sc}}{\partial \Delta \gamma} \right]^{-1} \{R_{sc}\} \quad (4.190)$$

The derivative of the quasi-consistency conditions with respect to the slip increment needed to calculate the iterative corrections given by

$$\begin{aligned} \frac{\partial R_{sc}^\eta}{\partial \Delta \gamma^v} = & -\mathbf{Z}^\eta : \mathbb{C} : \mathbf{Z}^v \text{sgn}(\tau^\eta) + \frac{1}{\ell_p^\eta \ell_p^v} \mathbf{H}^\eta : \mathbb{D} : \mathbf{H}^v \text{sgn}\left(\tau^\eta - \frac{\pi^\eta}{\ell_p^\eta}\right) \\ & - \left[\left(A_1 q_1^{\eta v} - B r_{sc}^\eta|_n + \frac{A_2}{\ell_p^v} q_2^{\eta v} \right) \text{sgn}(\Delta \gamma^v) + \frac{g_{sc}^v}{m_{sc} \dot{\gamma}_0 \Delta t} \left(\frac{|\Delta \gamma^v|}{\dot{\gamma}_0 \Delta t} \right)^{1/(m_{sc}-1)} \text{sgn}(\Delta \gamma^v) \right] \end{aligned} \quad (4.191)$$

4.4.3 Algorithmic Moduli

Crucial to the stability of the constitutive update algorithm is the derivation of the appropriate algorithmic elastoplastic moduli which is consistent with the integration scheme. Due to the abrupt transition in material behavior at the yield point, using the continuum elastoplastic tangent modulus can cause spurious numerical solutions during loading/unloading. The development of the algorithmic moduli for the rate-tangent and return mapping schemes are covered in Sections 4.4.3.1 and 4.4.3.2, respectively, for both multi- and single criterion models.

4.4.3.1 Rate-Tangent Modulus Scheme

Multi-Criterion Model

The algorithmic elastoplastic modulus for the rate-tangent scheme is calculated in a rather straight-forward manner by substituting the solutions for the slip and torsion-curvature increments given in equations (4.152) and (4.153) into the incremental force and couple-stress equations, and is derived as

$$\begin{aligned}
\Delta \boldsymbol{\sigma} &= \mathbb{C} : \Delta \bar{\boldsymbol{\epsilon}} - \sum_{\eta} \mathbb{C} : \mathbf{Z}^{\eta} \Delta \gamma^{\eta} \\
&= \mathbb{C} : \Delta \bar{\boldsymbol{\epsilon}} - \Delta t \sum_{\eta} \sum_v \mathbb{C} : \mathbf{Z}^{\eta} (T_1^{\eta v})^{-1} \dot{\gamma}_n^v \\
&\quad - a \Delta t \sum_{\eta} \sum_v \mathbb{C} : \mathbf{Z}^{\eta} (T_1^{\eta v})^{-1} \left. \frac{\partial \dot{\gamma}^v}{\partial \tau^v} \right|_n \mathbf{Z}^v : \mathbb{C} : \Delta \bar{\boldsymbol{\epsilon}} \\
&\quad + \Delta t \sum_{\eta} \sum_v \sum_{\chi} \sum_{\lambda} \mathbb{C} : \mathbf{Z}^{\eta} (T_1^{\eta v})^{-1} T_2^{v\chi} (T_3^{\chi\lambda})^{-1} \dot{\phi}_n^{\lambda} \\
&\quad + b \Delta t \sum_{\eta} \sum_v \sum_{\chi} \sum_{\lambda} \mathbb{C} : \mathbf{Z}^{\eta} (T_1^{\eta v})^{-1} T_2^{v\chi} (T_3^{\chi\lambda})^{-1} \left. \frac{\partial \dot{\phi}^{\lambda}}{\partial \pi^{\lambda}} \right|_n \mathbf{H}^{\lambda} : \mathbb{D} : \bar{\boldsymbol{\kappa}}
\end{aligned} \tag{4.192}$$

Rewriting in the following more compact notation for the force-stress increment we have

$$\Delta \boldsymbol{\sigma} = \mathbb{C}^{ep} : \Delta \bar{\boldsymbol{\epsilon}} + \mathbb{B}^{ep} : \Delta \bar{\boldsymbol{\kappa}} + \mathbf{y} \tag{4.193}$$

$$\mathbb{C}^{ep} = \mathbb{C} - a \Delta t \sum_{\eta} \sum_v \mathbb{C} : \mathbf{Z}^{\eta} (T_1^{\eta v})^{-1} \left. \frac{\partial \dot{\gamma}^v}{\partial \tau^v} \right|_n \mathbf{Z}^v : \mathbb{C} \tag{4.194}$$

$$\mathbb{B}^{ep} = b \Delta t \sum_{\eta} \sum_v \sum_{\chi} \sum_{\lambda} \mathbb{C} : \mathbf{Z}^{\eta} (T_1^{\eta v})^{-1} T_2^{v\chi} (T_3^{\chi\lambda})^{-1} \left. \frac{\partial \dot{\phi}^{\lambda}}{\partial \pi^{\lambda}} \right|_n \mathbf{H}^{\lambda} : \mathbb{D} \tag{4.195}$$

$$\mathbf{y} = -\Delta t \sum_{\eta} \sum_v \mathbb{C} : \mathbf{Z}^{\eta} (T_1^{\eta v})^{-1} \dot{\gamma}_n^v + \Delta t \sum_{\eta} \sum_v \sum_{\chi} \sum_{\lambda} \mathbb{C} : \mathbf{Z}^{\eta} (T_1^{\eta v})^{-1} T_2^{v\chi} (T_3^{\chi\lambda})^{-1} \dot{\phi}_n^{\lambda} \tag{4.196}$$

The analogous expressions for the incremental couple-stress equation are given as

$$\begin{aligned}
\Delta \mathbf{m} &= \mathbb{D} : \Delta \bar{\boldsymbol{\kappa}} - \sum_{\eta} \mathbb{D} : \mathbf{H}^{\eta} \frac{\Delta \phi^{\eta}}{\ell_p^{\eta}} \\
&= \mathbb{D} : \Delta \bar{\boldsymbol{\epsilon}} - \Delta t \sum_{\eta} \sum_v \frac{1}{\ell_p^{\eta}} \mathbb{D} : \mathbf{H}^{\eta} (T_3^{\eta v})^{-1} \dot{\phi}_n^v \\
&\quad - b \Delta t \sum_{\eta} \sum_v \frac{1}{\ell_p^{\eta}} \mathbb{D} : \mathbf{H}^{\eta} (T_3^{\eta v})^{-1} \left. \frac{\partial \dot{\phi}^v}{\partial \pi^v} \right|_n \mathbf{H}^v : \mathbb{D} : \bar{\boldsymbol{\kappa}}
\end{aligned} \tag{4.197}$$

$$\Delta \mathbf{m} = \mathbb{D}^{ep} : \Delta \bar{\boldsymbol{\kappa}} + \mathbf{z} \tag{4.198}$$

$$\mathbb{D}^{ep} = \mathbb{D} - b \Delta t \sum_{\eta} \sum_v \frac{1}{\ell_p^{\eta}} \mathbb{D} : \mathbf{H}^{\eta} (T_3^{\eta v})^{-1} \left. \frac{\partial \dot{\phi}^v}{\partial \pi^v} \right|_n \mathbf{H}^v : \mathbb{D} \tag{4.199}$$

$$\mathbf{z} = -\Delta t \sum_{\eta} \sum_v \frac{1}{\ell_p^{\eta}} \mathbb{D} : \mathbf{H}^{\eta} (T_3^{\eta v})^{-1} \dot{\phi}_n^v \tag{4.200}$$

Single Criterion Model

Following the same procedure for the single criterion case leads to the following incremental force stress expression in terms of increments of strain and torsion-curvature:

$$\begin{aligned}\Delta \boldsymbol{\sigma} &= \mathbb{C} : \Delta \bar{\boldsymbol{\epsilon}} - \sum_{\eta} \mathbb{C} : \mathbf{Z}^{\eta} \Delta \gamma^{\eta} \\ &= \mathbb{C} : \Delta \bar{\boldsymbol{\epsilon}} - \Delta t \sum_{\eta} \sum_v \mathbb{C} : \mathbf{Z}^{\eta} (T_1^{\eta v})^{-1} \dot{\gamma}_n^v \\ &\quad - a \Delta t \sum_{\eta} \sum_v \mathbb{C} : \mathbf{Z}^{\eta} (T_1^{\eta v})^{-1} \left(\frac{\partial \dot{\gamma}^v}{\partial \tau^v} \Big|_n \mathbf{Z}^v : \mathbb{C} : \Delta \bar{\boldsymbol{\epsilon}} + \frac{\partial \dot{\gamma}^v}{\partial \pi^v} \Big|_n \mathbf{H}^v : \mathbb{D} : \Delta \bar{\boldsymbol{\kappa}} \right)\end{aligned}\quad (4.201)$$

where the tangent elastoplastic moduli are determined as

$$\Delta \boldsymbol{\sigma} = \mathbb{C}^{ep} : \Delta \bar{\boldsymbol{\epsilon}} + \mathbb{B}^{ep} : \Delta \bar{\boldsymbol{\kappa}} + \mathbf{y} \quad (4.202)$$

$$\mathbb{C}^{ep} = \mathbb{C} - a \Delta t \sum_{\eta} \sum_v \mathbb{C} : \mathbf{Z}^{\eta} (T_1^{\eta v})^{-1} \frac{\partial \dot{\gamma}^v}{\partial \tau^v} \Big|_n \mathbf{Z}^v : \mathbb{C} \quad (4.203)$$

$$\mathbb{B}^{ep} = -a \Delta t \sum_{\eta} \sum_v \mathbb{C} : \mathbf{Z}^{\eta} (T^{\eta v})^{-1} \frac{\partial \dot{\gamma}^v}{\partial \pi^v} \Big|_n \mathbf{H}^v : \mathbb{D} \quad (4.204)$$

$$\mathbf{y} = -\Delta t \sum_{\eta} \sum_v \mathbb{C} : \mathbf{Z}^{\eta} (T^{\eta v})^{-1} \dot{\gamma}_n^v \quad (4.205)$$

Similarly the incremental couple-stress relation is given by

$$\begin{aligned}\Delta \mathbf{m} &= \mathbb{D} : \Delta \bar{\boldsymbol{\kappa}} - \sum_{\eta} \mathbb{D} : \mathbf{H}^{\eta} \frac{\Delta \gamma^{\eta}}{\ell_p^{\eta}} \\ &= \mathbb{D} : \Delta \bar{\boldsymbol{\epsilon}} - \Delta t \sum_{\eta} \sum_v \frac{1}{\ell_p^{\eta}} \mathbb{D} : \mathbf{H}^{\eta} (T^{\eta v})^{-1} \dot{\gamma}_n^v \\ &\quad - a \Delta t \sum_{\eta} \sum_v \frac{1}{\ell_p^{\eta}} \mathbb{D} : \mathbf{H}^{\eta} (T^{\eta v})^{-1} \left(\frac{\partial \dot{\gamma}^v}{\partial \tau^v} \Big|_n \mathbf{Z}^v : \mathbb{C} : \bar{\boldsymbol{\epsilon}} + \frac{\partial \dot{\gamma}^v}{\partial \pi^v} \Big|_n \mathbf{H}^v : \mathbb{D} : \bar{\boldsymbol{\kappa}} \right)\end{aligned}\quad (4.206)$$

with the elastoplastic tangent moduli having the forms

$$\Delta \mathbf{m} = \mathbb{D}^{ep} : \Delta \bar{\boldsymbol{\kappa}} + \mathbb{A}^{ep} : \Delta \bar{\boldsymbol{\epsilon}} + \mathbf{z} \quad (4.207)$$

$$\mathbb{D}^{ep} = \mathbb{D} - a \Delta t \sum_{\eta} \sum_v \frac{1}{\ell_p^{\eta}} \mathbb{D} : \mathbf{H}^{\eta} (T^{\eta v})^{-1} \frac{\partial \dot{\gamma}^v}{\partial \pi^v} \Big|_n \mathbf{H}^v : \mathbb{D} \quad (4.208)$$

$$\mathbb{A}^{ep} = -a \Delta t \sum_{\eta} \sum_v \frac{1}{\ell_p^{\eta}} \mathbb{D} : \mathbf{H}^{\eta} (T^{\eta v})^{-1} \frac{\partial \dot{\gamma}^v}{\partial \tau^v} \Big|_n \mathbf{Z}^v : \mathbb{C} \quad (4.209)$$

$$\mathbf{z} = -\Delta t \sum_{\eta} \sum_v \frac{1}{\ell_p^{\eta}} \mathbb{D} : \mathbf{H}^{\eta} (T^{\eta v})^{-1} \dot{\gamma}_n^v \quad (4.210)$$

In the case of the single criterion model, the fact that the plastic strain and torsion-curvature are coupled through the use of a single viscoplastic multiplier, $\dot{\gamma}^{\eta}$, leads to a non-zero elastoplastic moduli, \mathbb{A}^{ep} , which is not the case for the multi-criterion model in which it is found that $\mathbb{A}^{ep} = \mathbf{0}$.

4.4.3.2 Return Mapping Scheme

The algorithmic elastoplastic tangent moduli appropriate for the return mapping scheme are determined in a slightly longer series of manipulations than in the rate tangent case. The first step in the process is to take the derivatives of the force and couple-stress tensors with respect to the strain and torsion-curvature, which leads to a set of four expressions for the tangent moduli, which to be completed require the determination of the derivatives of the plastic slip and torsion-curvature increments with respect to elastic trial strains and torsion-curvatures. It is shown below following the methodology outlined in Miehe and Schroder [166] that these expressions are obtained by taking appropriate derivatives of the quasi-consistency conditions and then solving a system of algebraic matrix equations.

Multi-Criterion Model

For the multi-criterion model, the general expressions for the tangent elastoplastic moduli are given by

$$\mathbb{C}^{ep} = \frac{\partial \boldsymbol{\sigma}}{\partial \boldsymbol{\varepsilon}} = \frac{\partial \boldsymbol{\sigma}}{\partial \boldsymbol{\varepsilon}^{e*}} = \mathbb{C} - \sum_{\eta} \mathbb{C} : \mathbf{Z}^{\eta} \otimes \frac{\partial \Delta \gamma^{\eta}}{\partial \boldsymbol{\varepsilon}^{e*}} \quad (4.211)$$

$$\mathbb{B}^{ep} = \frac{\partial \boldsymbol{\sigma}}{\partial \mathbf{K}^{e*}} = - \sum_{\eta} \mathbb{C} : \mathbf{Z}^{\eta} \otimes \frac{\partial \Delta \gamma^{\eta}}{\partial \mathbf{K}^{e*}} \quad (4.212)$$

$$\mathbb{A}^{ep} = \frac{\partial \mathbf{m}}{\partial \boldsymbol{\varepsilon}^{e*}} = - \sum_{\eta} \frac{1}{\ell_p^{\eta}} \mathbb{D} : \mathbf{H}^{\eta} \otimes \frac{\partial \Delta \varphi^{\eta}}{\partial \boldsymbol{\varepsilon}^{e*}} \quad (4.213)$$

$$\mathbb{D}^{ep} = \frac{\partial \mathbf{m}}{\partial \mathbf{K}} = \frac{\partial \mathbf{m}}{\partial \mathbf{K}^{e*}} = \mathbb{D} - \sum_{\eta} \frac{1}{\ell_p^{\eta}} \mathbb{D} : \mathbf{H}^{\eta} \otimes \frac{\partial \Delta \varphi^{\eta}}{\partial \mathbf{K}^{e*}} \quad (4.214)$$

To determine the derivatives of the plastic slip and torsion-curvature increments with respect to the elastic trial strains, we take derivatives of the quasi-consistency conditions with respect to the elastic trial strains which leads to the system of matrix equations (4.215) and (4.218) for the primary unknowns:

$$\frac{\partial R^{\eta}}{\partial \boldsymbol{\varepsilon}^{e*}} = 0 \Rightarrow \mathbf{Z}^{\eta} : \mathbb{C} \operatorname{sgn}(\tau^{\eta}) = \sum_v T_1^{\eta v} \frac{\partial \Delta \gamma^v}{\partial \boldsymbol{\varepsilon}^{e*}} + \sum_v T_2^{\eta v} \frac{\partial \Delta \varphi^v}{\partial \boldsymbol{\varepsilon}^{e*}} \quad (4.215)$$

$$T_1^{\eta v} = \mathbf{Z}^{\eta} : \mathbb{C} : \mathbf{Z}^v \operatorname{sgn}(\tau^{\eta}) + (A_1 q_1^{\eta v} - B r_n^{\eta}) \operatorname{sgn}(\Delta \gamma^v) + \frac{g^{\eta} \delta^{\eta v}}{m \dot{\gamma}_0 \Delta t} \left(\frac{|\Delta \gamma^{\eta}|}{\dot{\gamma}_0 \Delta t} \right)^{1/(m-1)} \operatorname{sgn}(\Delta \gamma^{\eta}) \quad (4.216)$$

$$T_2^{\eta v} = A_2 q_2^{\eta v} \operatorname{sgn}(\Delta \varphi^v) \quad (4.217)$$

$$\frac{\partial R_c^{\eta}}{\partial \boldsymbol{\varepsilon}^{e*}} = 0 = \sum_v S_1^{\eta v} \frac{\partial \Delta \gamma^v}{\partial \boldsymbol{\varepsilon}^{e*}} + \sum_v S_2^{\eta v} \frac{\partial \Delta \varphi^v}{\partial \boldsymbol{\varepsilon}^{e*}} \quad (4.218)$$

$$S_1^{\eta v} = - \frac{\partial r_c^{\eta}}{\partial \Delta \gamma^v} = 0 \quad (4.219)$$

$$S_2^{\eta v} = - \left(\frac{1}{\ell_p^v} \mathbf{H}^\eta : \mathbb{D} : \mathbf{H}^v \operatorname{sgn}(\pi^\eta) + A_3 q_3^{\eta v} \operatorname{sgn}(\Delta \phi^v) + \frac{g_c^\eta \delta^{\eta v}}{m_c \dot{\phi}_0 \Delta t} \left(\frac{|\Delta \phi^\eta|}{\dot{\phi}_0 \Delta t} \right)^{1/(m_c-1)} \operatorname{sgn}(\Delta \phi^\eta) \right) \quad (4.220)$$

Taking advantage of the fact $S_1^{\eta v} = 0$ for this particular set of ISV evolution equations, it is apparent that

$$\frac{\partial \Delta \phi^v}{\partial \boldsymbol{\varepsilon}^{e*}} = 0 \quad (4.221)$$

which leads to the results

$$\frac{\partial \Delta \gamma^\eta}{\partial \boldsymbol{\varepsilon}^{e*}} = \sum_v (T_1^{\eta v})^{-1} \mathbf{Z}^v : \mathbb{C} \operatorname{sgn}(\tau^v) \quad (4.222)$$

$$\mathbb{A}^{ep} = \mathbf{0} \quad (4.223)$$

Similarly, we set out to obtain expressions for the derivatives of the plastic slip and torsion-curvature increments with respect to the trial elastic torsion-curvatures by taking the derivatives of the quasi-consistency conditions with respect to the elastic trial torsion-curvatures leading to two matrix equations:

$$\frac{\partial R^\eta}{\partial \bar{\mathbf{K}}^{e*}} = 0 = - \sum_v T_1^{\eta v} \frac{\partial \Delta \gamma^v}{\partial \bar{\mathbf{K}}^{e*}} - \sum_v T_2^{\eta v} \frac{\partial \Delta \phi^v}{\partial \bar{\mathbf{K}}^{e*}} \quad (4.224)$$

$$\frac{\partial R_c^\eta}{\partial \bar{\mathbf{K}}^{e*}} = 0 \Rightarrow \mathbf{H}^\eta : \mathbb{D} \operatorname{sgn}(\pi^\eta) = - \sum_v S_1^{\eta v} \frac{\partial \Delta \gamma^v}{\partial \bar{\mathbf{K}}^{e*}} - \sum_v S_2^{\eta v} \frac{\partial \Delta \phi^v}{\partial \bar{\mathbf{K}}^{e*}} \quad (4.225)$$

The terms can then be solved as follows:

$$\frac{\partial \Delta \phi^v}{\partial \bar{\mathbf{K}}^{e*}} = - \sum_v (S_2^{\eta v})^{-1} \mathbf{H}^v : \mathbb{D} \operatorname{sgn}(\pi^v) \quad (4.226)$$

which leads to the following results:

$$\frac{\partial \Delta \gamma^\eta}{\partial \bar{\mathbf{K}}^{e*}} = - \sum_v \sum_\delta (T_1^{\eta v})^{-1} T_2^{v\delta} \frac{\partial \Delta \phi^\delta}{\partial \bar{\mathbf{K}}^{e*}} \quad (4.227)$$

Single Criterion Model

The expressions for the elastoplastic tangent moduli for the single criterion model are given by

$$\mathbb{C}^{ep} = \frac{\partial \boldsymbol{\sigma}}{\partial \boldsymbol{\varepsilon}} = \frac{\partial \boldsymbol{\sigma}}{\partial \boldsymbol{\varepsilon}^{e*}} = \mathbb{C} - \sum_\eta \mathbb{C} : \mathbf{Z}^\eta \otimes \frac{\partial \Delta \gamma^\eta}{\partial \boldsymbol{\varepsilon}^{e*}} \quad (4.228)$$

$$\mathbb{B}^{ep} = \frac{\partial \boldsymbol{\sigma}}{\partial \bar{\mathbf{K}}^{e*}} = - \sum_\eta \mathbb{C} : \mathbf{Z}^\eta \otimes \frac{\partial \Delta \gamma^\eta}{\partial \bar{\mathbf{K}}^{e*}} \quad (4.229)$$

$$\mathbb{A}^{ep} = \frac{\partial \mathbf{m}}{\partial \boldsymbol{\varepsilon}^{e*}} = - \sum_\eta \frac{1}{\ell_p^\eta} \mathbb{D} : \mathbf{H}^\eta \otimes \frac{\partial \Delta \gamma^\eta}{\partial \boldsymbol{\varepsilon}^{e*}} \quad (4.230)$$

$$\mathbb{D}^{ep} = \frac{\partial \mathbf{m}}{\partial \bar{\mathbf{K}}} = \frac{\partial \mathbf{m}}{\partial \bar{\mathbf{K}}^{e*}} = \mathbb{D} - \sum_\eta \frac{1}{\ell_p^\eta} \mathbb{D} : \mathbf{H}^\eta \otimes \frac{\partial \Delta \gamma^\eta}{\partial \bar{\mathbf{K}}^{e*}} \quad (4.231)$$

The derivatives of the quasi-consistency condition with respect to the trial elastic strains and torsion-curvatures in equations (4.232) and (4.235) lead to the solutions for the derivatives of the plastic slip and torsion-curvature increments with respect to the trial quantities given in equations (4.234) and (4.236) in terms of the matrix $A^{\eta v}$ in equation (4.233):

$$\frac{\partial R_{sc}^{\eta}}{\partial \bar{\boldsymbol{\epsilon}}^{e*}} = 0 \Rightarrow \mathbf{Z}^{\eta} : \mathbb{C} \operatorname{sgn}(\tau^{\eta} - \pi^{\eta}/\ell_p^{\eta}) = \sum_v A^{\eta v} \frac{\partial \Delta \gamma^v}{\partial \bar{\boldsymbol{\epsilon}}^{e*}} \quad (4.232)$$

$$\begin{aligned} A^{\eta v} = & \left(\mathbf{Z}^{\eta} : \mathbb{C} : \mathbf{Z}^v - \frac{1}{\ell_p^v} \mathbf{H}^{\eta} : \mathbb{D} : \mathbf{H}^v \right) \operatorname{sgn}(\tau^{\eta} - \pi^{\eta}/\ell_p^{\eta}) \\ & + \left(A_1 q_1^{\eta v} - B r_n^{\eta} + \frac{A_2 q_2^{\eta v}}{\ell_p^v} \right) \operatorname{sgn}(\Delta \gamma^v) + \frac{g_{sc}^{\eta} \delta^{\eta v}}{m_{sc} \dot{\gamma}_0 \Delta t} \left(\frac{|\Delta \gamma^{\eta}|}{\dot{\gamma}_0 \Delta t} \right)^{1/(m_{sc}-1)} \operatorname{sgn}(\Delta \gamma^{\eta}) \end{aligned} \quad (4.233)$$

$$\frac{\partial \Delta \gamma^{\eta}}{\partial \bar{\boldsymbol{\epsilon}}^{e*}} = \sum_v (A^{\eta v})^{-1} \mathbf{Z}^v : \mathbb{C} \operatorname{sgn}(\tau^{\eta} - \pi^{\eta}/\ell_p^{\eta}) \quad (4.234)$$

$$\frac{\partial R_{sc}^{\eta}}{\partial \bar{\mathbf{K}}^{e*}} = 0 \Rightarrow \mathbf{H}^{\eta} : \mathbb{D} \operatorname{sgn}(\tau^{\eta} - \pi^{\eta}/\ell_p^{\eta}) = - \sum_v A^{\eta v} \frac{\partial \Delta \gamma^v}{\partial \bar{\mathbf{K}}^{e*}} \quad (4.235)$$

$$\frac{\partial \Delta \gamma^{\eta}}{\partial \bar{\mathbf{K}}^{e*}} = - \sum_v (A^{\eta v})^{-1} \mathbf{H}^v : \mathbb{D} \operatorname{sgn}(\tau^{\eta} - \pi^{\eta}/\ell_p^{\eta}) \quad (4.236)$$

Again, as is expected, it is seen that the cross-coupling elastoplastic tangent moduli, \mathbb{A}^{ep} , is non-zero for the single criterion model.

4.5 Simulations

In this section, a series of preliminary simulations are performed to demonstrate the basic functionality of the micropolar element and constitutive model. Three sets of simulations are performed:

1. A bar with a defect loaded in uniaxial compression
2. A notched plate loaded in uniaxial tension
3. A semi-infinite bicrystal loaded in simple shear.

All of the simulations to date have been performed using the multi-criterion model given in Sections 4.4.2.1 and 4.4.3.1. Simulation set 1 is used to demonstrate the mesh-regularizing capability of the micropolar model as compared to the classical case for a strain-softening material, which displays mesh sensitivity of the load-deflection curve as the mesh is refined. The notched plate simulations are undertaken to investigate the ability of the micropolar model to regularize and/or confine the plastic strain localization zone emanating from the notch. Single crystals oriented for both single and double slip have been examined. For the micropolar model, we have also investigated the extreme ends of the spectrum for the couple modulus by looking at two values of the

coupling parameter, N , to see how this affects the results. For $N = 0$, the micro-rotations are “free” and with $N = 0.95$, the micro-rotations are constrained to move with the continuum rotations in the elastic regime. The final set of simulations are performed in an attempt to qualitatively compare results with other generalized crystal plasticity theories, as the semi-infinite bicrystal loaded in simple shear is a commonly studied problem by developers of higher-order plasticity theories. All of the simulations have been performed using the 2D implementation and the planar double slip idealization shown in Figure 4.2.

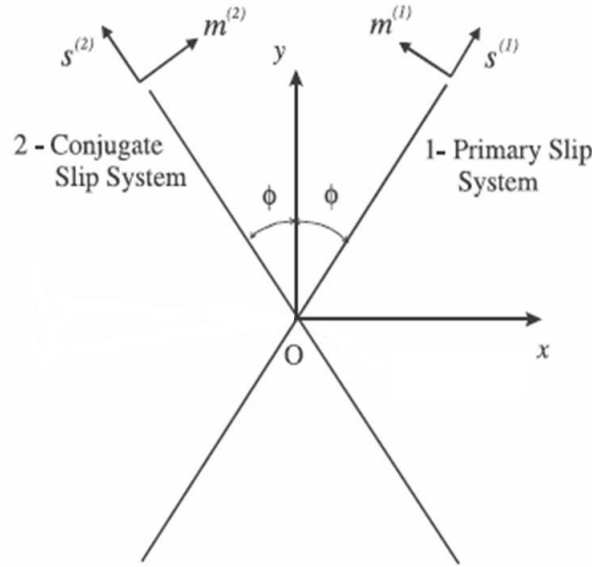


Figure 4.2. Planar double slip geometry. $\phi = 35.1^\circ$

4.5.1 Simulation Set 1: Bar With Defect

The dimensions of the plate are 120 mm x 60 mm, and four different mesh densities are examined: 16x8, 20x10, 24x12, and 40x20, respectively, and the model geometry and boundary conditions for the 20x10 mesh are shown in Figure 4.3. The left end of the plate is constrained against displacement in the x_1 -direction, with the node in the upper left hand corner being also constrained against translation in the x_2 -direction to prevent rigid body motion. The compressive load is applied via uniform displacement on the right end of the plate in the negative x_1 -direction. No constraints are placed on the micro-rotation vector, and the material parameters used in the simulation are given in Table 4.1. The material simulated is fictitious as these parameters do not correspond to any particular real material. The “defective” element is introduced in the upper left hand corner by assigning that element a yield strength a 10% lower than that of the other elements to trigger the localization event. Load-deflection curves are plotted in Figure 4.4 where the total load is given as the sum of all the nodal reaction forces at the right end of the plate. The results clearly show that

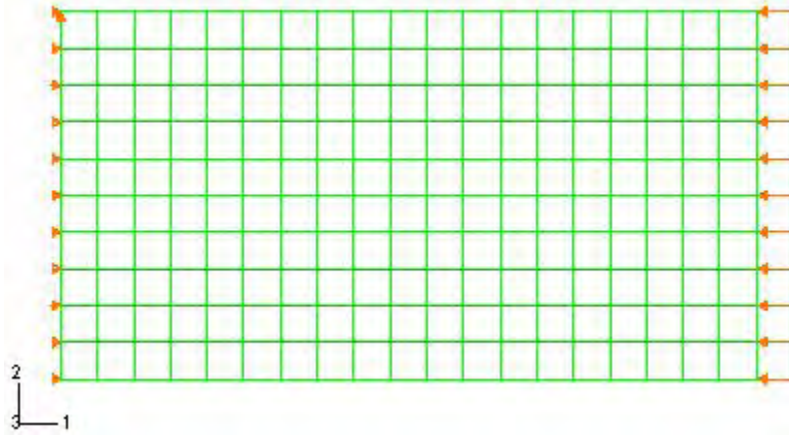


Figure 4.3. Single crystal with defect loaded in compression (defect is in upper left-hand corner).

Table 4.1. Simulation Set 1 Material Parameters.

E	11,920 MPa	ν	0.49
N	0.95	ℓ_e	1 mm
$\dot{\gamma}_0$	0.001 s^{-1}	r_0	25 MPa
A_1	-25 MPa	q_1	1
B	0	A_2	0
q_2	-	g_0	25 MPa
m	60	$\dot{\phi}_0$	0.001 s^{-1}
r_{c0}	10 MPa-mm	A_3	0
q_3	-	g_{c0}	10 MPa-mm
m_c	30	ℓ_p^η	1 mm

for the classical crystal plasticity model, as the mesh is refined, different load-deflection curves are obtained and the predicted load at the fixed end displacement of 8 mm decreases with each level of refinement. In contrast, due to the presence of the length scale in the constitutive formulation, the micropolar crystal plasticity model demonstrates a consistency of results with respect to the mesh refinement. These results are qualitatively consistent with previously reported results concerning J_2 -type extensions of micropolar plasticity [57, 58] and couple stress elastoplasticity [192].

4.5.2 Simulation Set 2: Notched Plate

The dimensions of the notched plate are 1 mm x 1 mm with a notch radius of 0.25 mm. Symmetry boundary conditions are applied on the bottom and left faces of the plate while the load is applied on the top face in terms of a uniform tensile displacement in the x_2 -direction of 0.03 mm. The

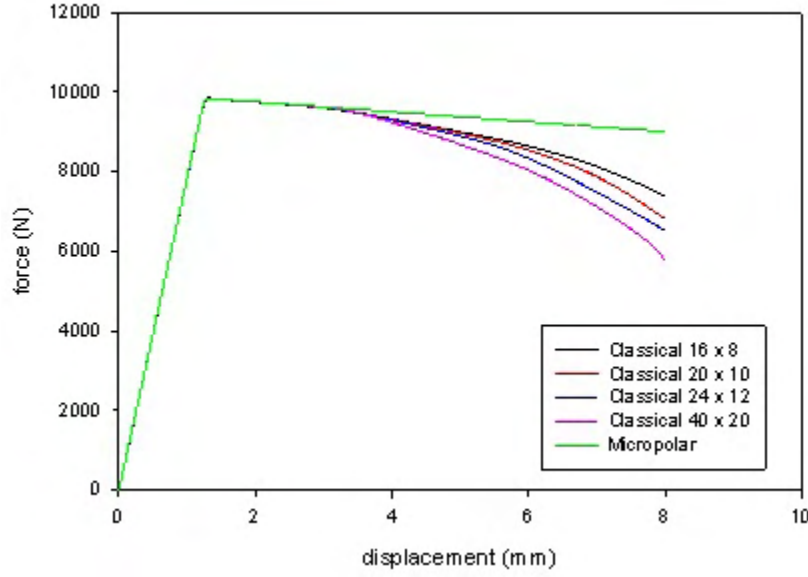


Figure 4.4. Load-deflection curves for single crystal with defect loaded in compression.

mesh consists of 880 elements and is shown along with the boundary conditions in Figure 4.5. The orientation of the slip systems for the single and double slip configurations is shown in Figure 4.6. Material parameters for this simulation set is shown in Table 4.2. As before, the material simulated is fictitious as these parameters do not correspond to any specific real material. In the single slip configuration, one of the slip systems is aligned such that one of the slip directions is perpendicular to the loading axis, while in the double slip configuration the slip systems are aligned such that the bisector axis between the two slip directions is aligned parallel to the loading direction. The load-deflection curves for each simulation are shown in Figure 4.7. In the double slip configuration, there is not much difference between the two micropolar and classical cases in terms of load-deflection response, however, in the more constrained single slip case, we see that the micropolar model gives a stiffer response which increases with the increasing value of N . Figures 4.8-4.11 show the magnitude of the micro-rotation and the skew symmetric parts of total, elastic, and plastic micropolar strain tensors, respectively. The skew part of the total strain tensor gives the difference between the continuum and micro-rotation; the skew part of the elastic strain tensor gives the difference between the elastic continuum spin (defined by the skew part of the elastic distortion) and the micro-rotation; and the skew part of the plastic micropolar strain gives the plastic continuum rotation defined by the skew part of the plastic distortion. Inspection of these plots reveals a few qualitative observations, namely that in the case of unconstrained micro-rotations ($N = 0$), no gradients in the micro-rotation field develop. It is also apparent that for the cases of $N = 0.95$ that the skew part of the total and plastic micropolar strains are nearly identical, whereas for the unconstrained cases that is not observed. Also worth mentioning is the fact that the skew part of

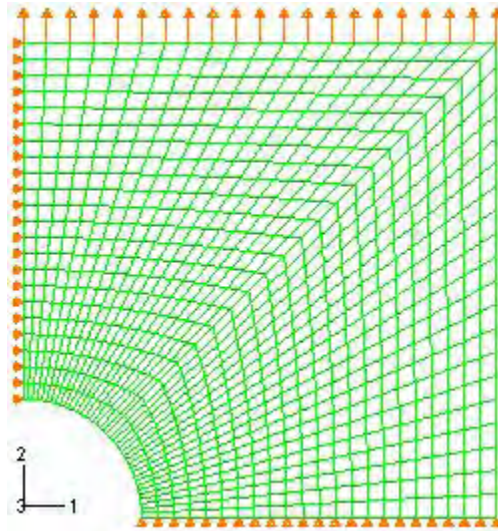


Figure 4.5. Finite element mesh density for the notched single crystal simulations.

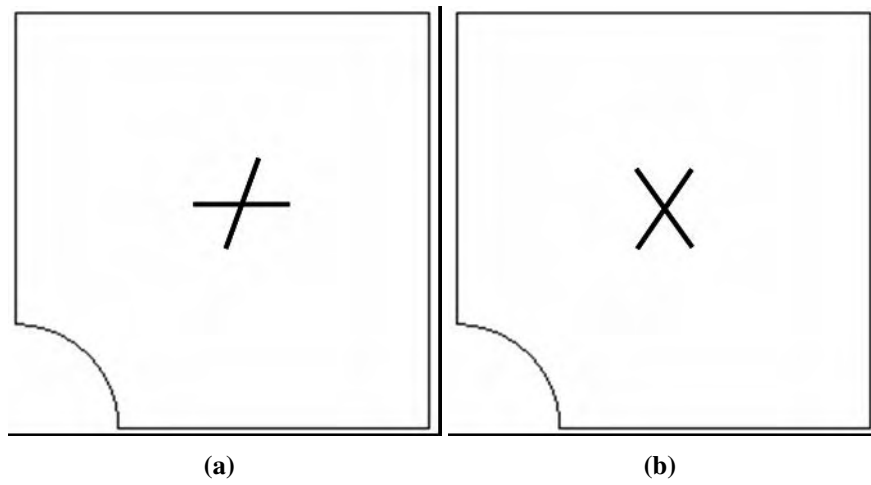


Figure 4.6. Notched single crystal oriented for (a) single slip and (b) symmetric double slip.

Table 4.2. Simulation Set 2 Material Parameters.

E	100,000 MPa	ν	0.3
N	0.95	ℓ_e	0.01 mm
$\dot{\gamma}_0$	0.001 s^{-1}	r_0	100 MPa
A_1	30 MPa	q_1	1
B	0	A_2	0
q_2	-	g_0	300 MPa
m	60	$\dot{\phi}_0$	0.001 s^{-1}
r_{c0}	5 MPa-mm	A_3	0
q_3	-	g_{c0}	10 MPa-mm
m_c	2	ℓ_p^η	1 mm

the plastic strains display qualitatively similar contours for both $N = 0$ and $N = 0.95$ as shown in Figure 4.10, while for the case $N = 0$, the skew parts of the total and elastic micropolar strains bear some similarities, especially for the single slip orientation. The plots of the plastic curvature components in Figures 4.12 and 4.13 (there is no plastic curvature for $N = 0$) show that there is a concentration of the peak values at the notch region.

A comparison of the plastic strain distributions is shown in Figures 4.14 and 4.15 for both micropolar and classical crystal plasticity models. The qualitative characteristics of the contours are similar for all cases. As expected, the classical model displays the largest peak values of plastic strain, as well as the largest regions of localization. The effect of increasing the couple modulus, *i.e.* N , seems to retard the localization of plastic strain at the notch. Figure 4.14 shows a plot of the plastic strain magnitude across the top of the notch (path shown in red), and there do not appear to be any generalizations that can be drawn from this data amongst all cases. It was expected that the classical crystal plasticity model might display higher and narrower peaks than the micropolar counterpart. This is the case for the double slip oriented crystal, but does not hold for the case of single slip.

4.5.3 Simulation Set 3: Semi-infinite Bicrystal

The finite element model geometry is shown in Figure 4.16. The bicrystal is situated such that the crystals are vertically stacked in the x_2 direction with each crystal having thickness, d . Periodic boundary conditions are applied in the x_1 direction for both displacements and lattice rotations rendering the model infinite in this direction. Each crystal is meshed with 400 elements, 40 in the x_1 direction and 10 in the x_2 direction. The bottom of crystal 1 is fixed against displacements in both the x_1 and x_2 directions, and a uniform displacement is applied to the top surface of crystal 2 in the x_1 direction, while the lattice rotations on the top and bottom surfaces are unconstrained. The general setup, as in Shu and Fleck [216], is that crystal 1 throughout all of these simulations remains fixed in a symmetric configuration, while the orientation angle (shown as θ in the figure) of crystal 2 is varied from 0-60 degrees. In addition to varying crystal orientation, a couple of the

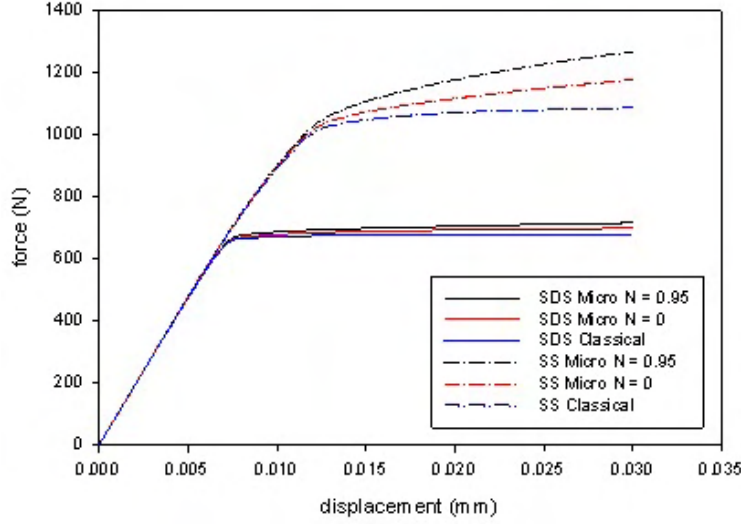


Figure 4.7. Load-deflection curves for notched plate.

other micropolar material parameters have been studied, namely the effect of curvature induced slip system hardening ($A_2 \neq 0$) as well as the plastic curvature length parameter, ℓ_p^η . A more systematic and thorough set of simulations is in the process of being setup and performed to explore in more detail the full range and interplay of material parameters available within the model. The fixed material constants are listed in Table 4.3, and those that are varied throughout the different simulations are listed in Table 4.4. For the most part, the material constant specification is in accord with what has been used in the related previous work of Forest *et al.* [77]. Simulation Case 1 is intended for comparison to Case 3 to determine the effect of curvature-induced slip hardening, Cases 2-5 examine the impact on the bicrystal misorientation for fixed plastic length parameter and strain-hardening curvature modulus, Case 6 can be compared to Case 3 to see what effect an

Table 4.3. Simulation Set 3 Fixed Material Parameters.

E	200,000 MPa	ν	0.3
N	0.75	ℓ_e	0.08 mm
$\dot{\gamma}_0$	1 s^{-1}	r_0	50 MPa
A_1	300 MPa	q_1	0
B	0	q_2	0
g_0	5 MPa	m	2
ϕ_0	1 s^{-1}	r_{c0}	0.0005 MPa-mm
A_3	0	q_3	0
g_{c0}	0.1 MPa-mm	m_c	1

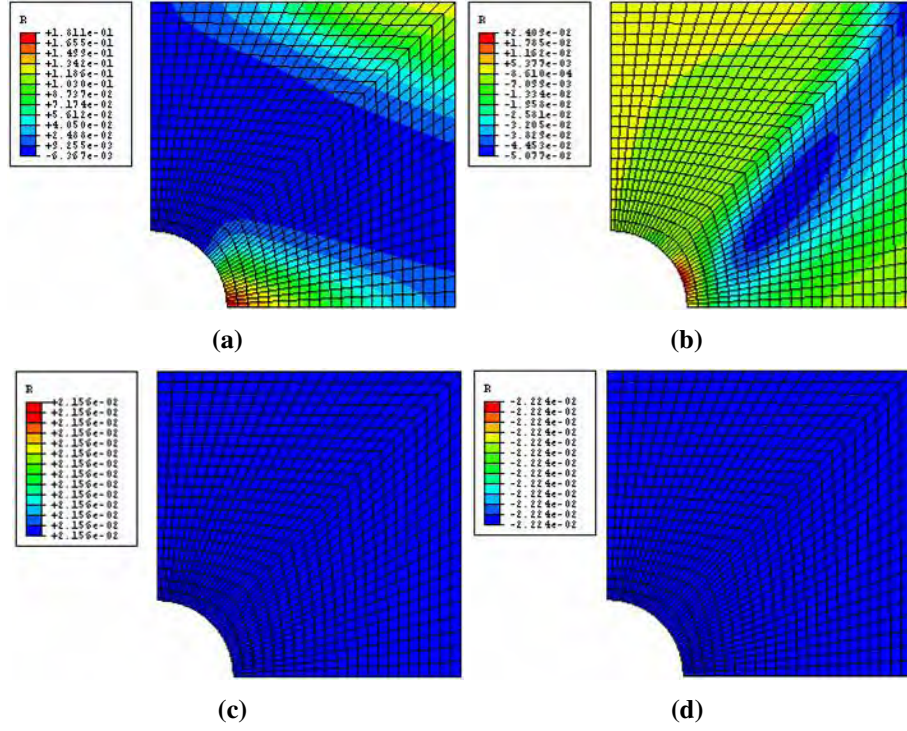


Figure 4.8. Rotation magnitude (a) single slip ($N = 0.95$) (b) symmetric double slip ($N = 0.95$) (c) single slip ($N = 0$) and (d) symmetric double slip ($N = 0$).

Table 4.4. Simulation Set 3 Variable Material Parameters.

	Case 1	Case 2	Case 3	Case 4	Case 5	Case 6	Case 7
A_2	0	500 MPa	500 MPa	500 MPa	500 MPa	500 MPa	N/A
ℓ_p^η	0.1 mm	0.1 mm	0.1 mm	0.1 mm	0.1 mm	10 mm	N/A
θ	20°	0°	20°	40°	60°	20°	20°

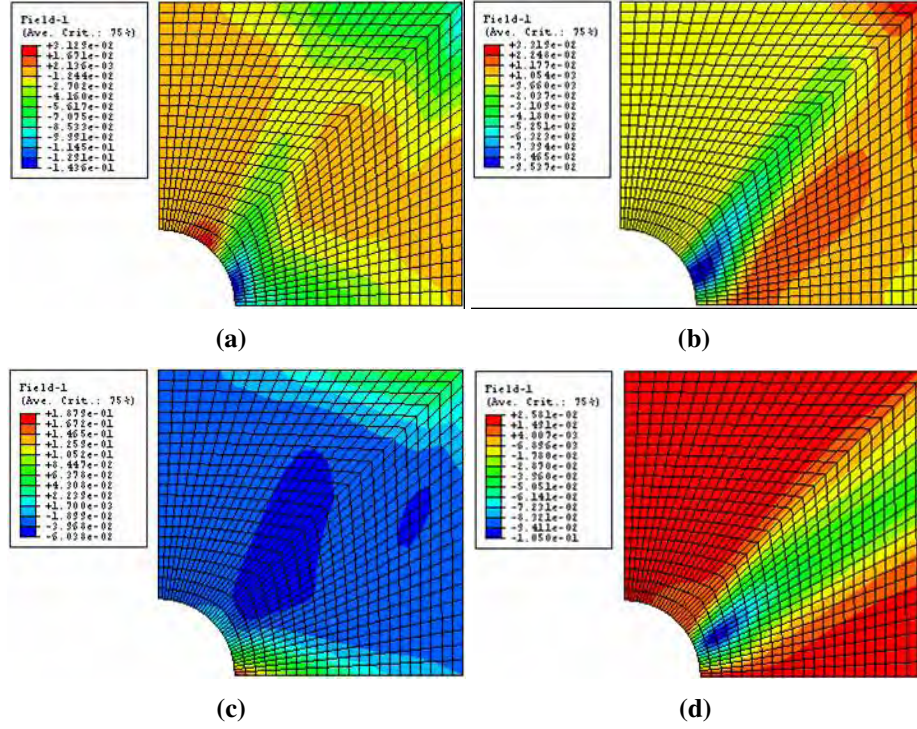


Figure 4.9. $\bar{\epsilon}_{12}$ (a) single slip ($N = 0.95$) (b) symmetric double slip ($N = 0.95$) (c) single slip ($N = 0$) and (d) symmetric double slip ($N = 0$).

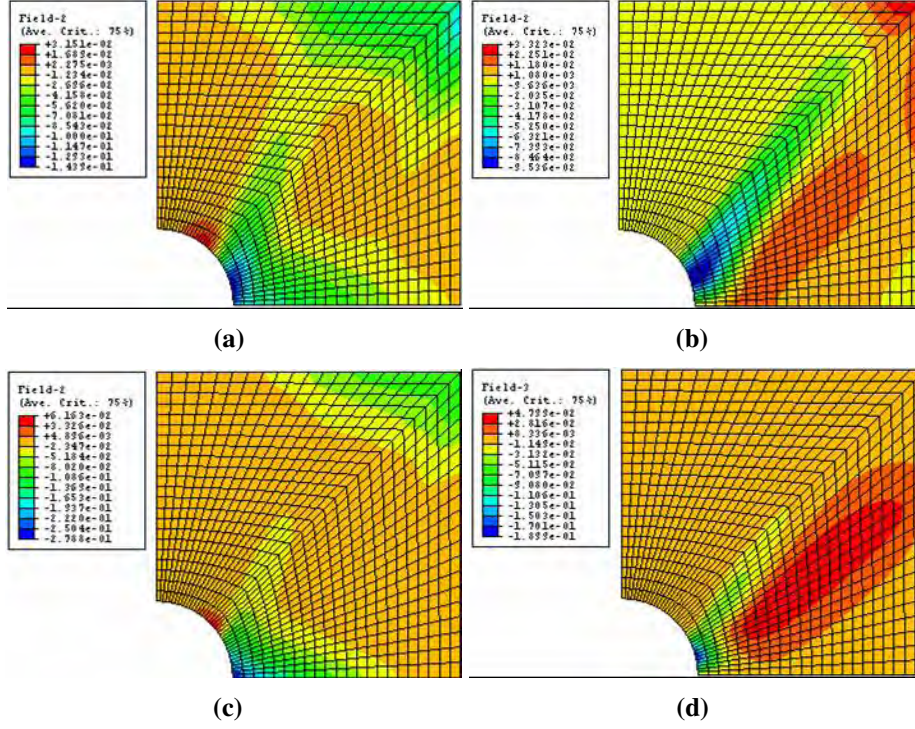


Figure 4.10. $\bar{\epsilon}_{12}^p$ (a) single slip ($N = 0.95$) (b) symmetric double slip ($N = 0.95$) (c) single slip ($N = 0$) and (d) symmetric double slip ($N = 0$).

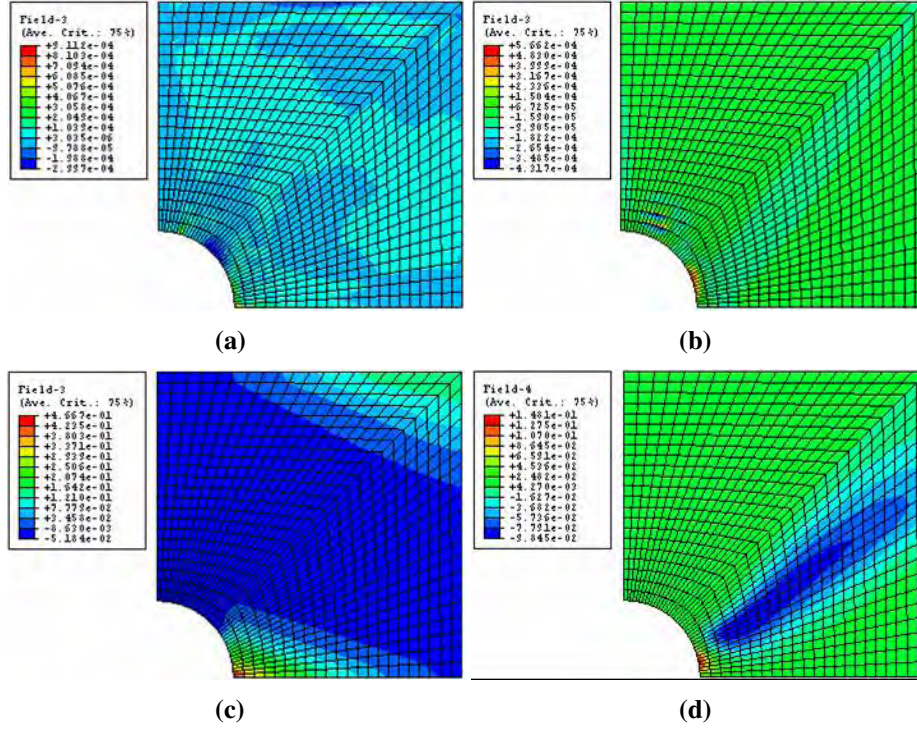


Figure 4.11. $\bar{\varepsilon}_{12}^e$ (a) single slip ($N = 0.95$) (b) symmetric double slip ($N = 0.95$) (c) single slip ($N = 0$) and (d) symmetric double slip ($N = 0$).

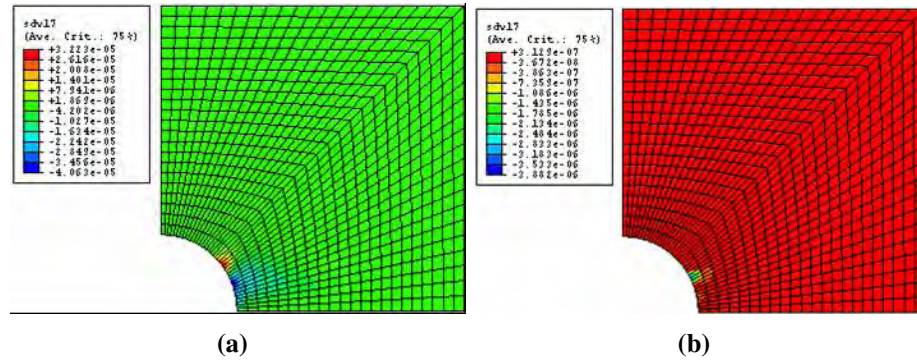


Figure 4.12. $\bar{\kappa}_{13}^p$ (a) single slip ($N = 0.95$) (b) symmetric double slip ($N = 0.95$).

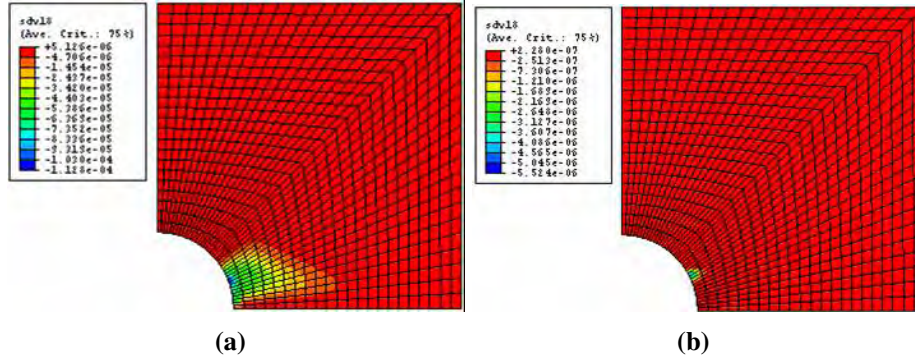


Figure 4.13. $\bar{\kappa}_{23}^p$ (a) single slip ($N = 0.95$) (b) symmetric double slip ($N = 0.95$).

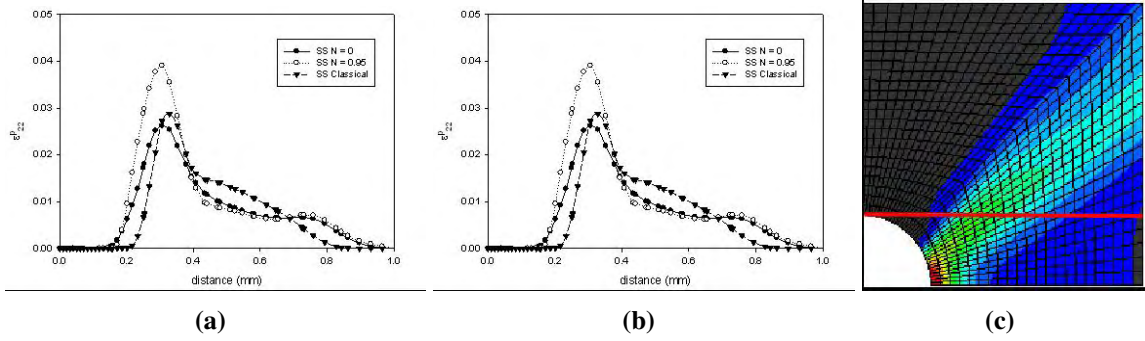


Figure 4.14. Plastic strain $\bar{\epsilon}_{22}^p$ distributions across the top of the notch (a) single slip (b) double slip.

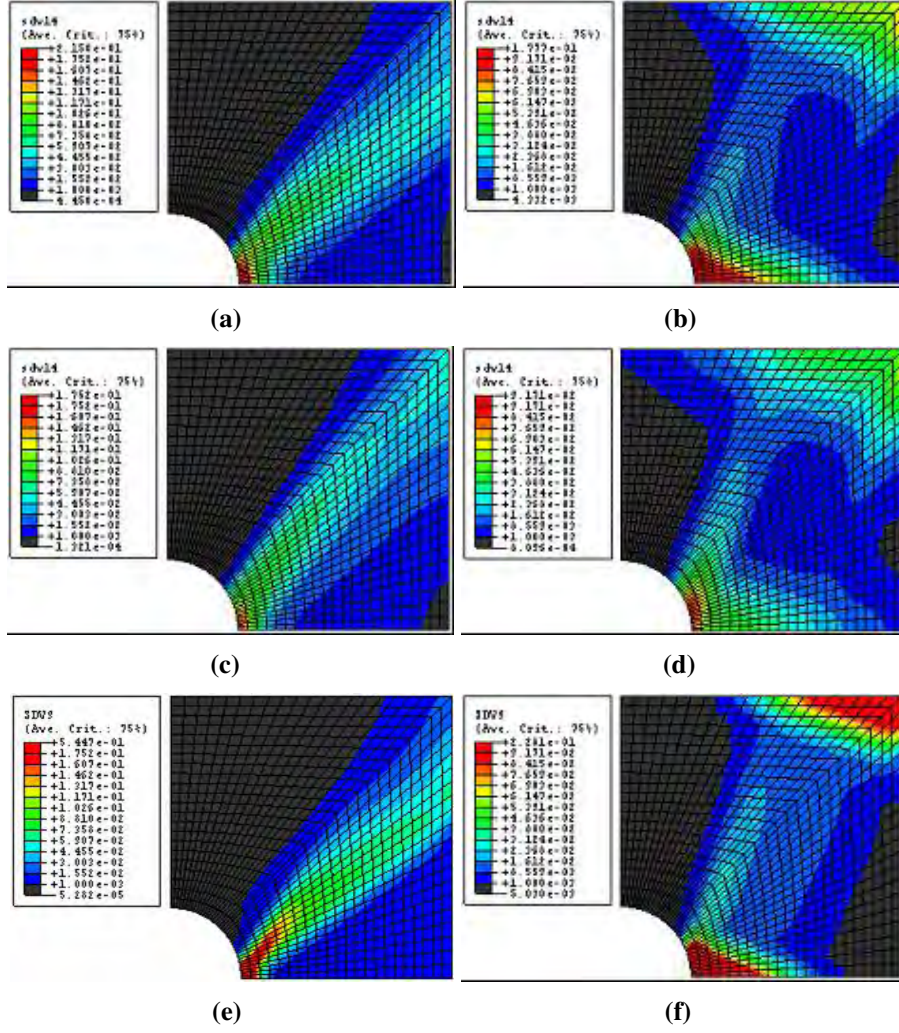


Figure 4.15. Plastic strain $\bar{\epsilon}_{22}^p$ distributions in the notched plate
(a) single slip ($N = 0$) (b) double slip ($N = 0$) (c) single slip ($N = 0.95$) (d) double slip ($N = 0.95$) (e) single slip (classical) (f) double slip (classical)

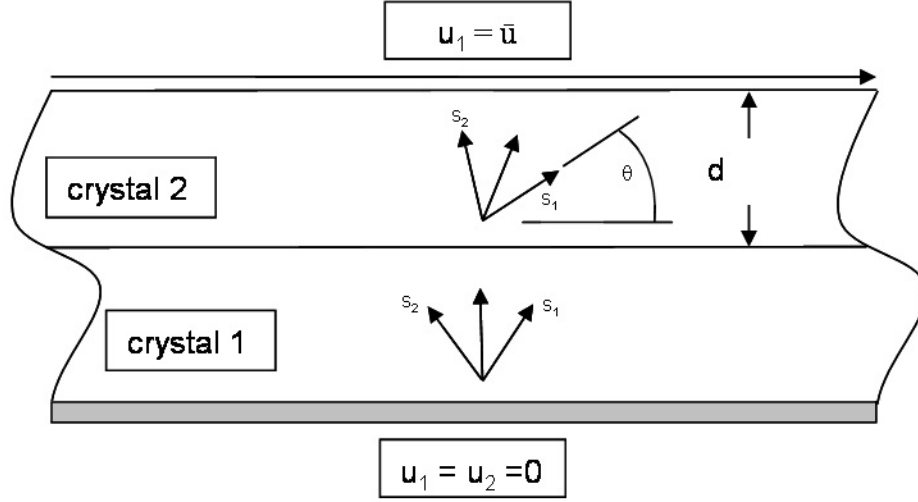


Figure 4.16. Model Geometry.

increase in the plastic curvature length parameter has, and Case 7 shows the response of a crystal in which plastic curvature has been suppressed, *i.e.* $\dot{\phi}_0 = 0$. All cases have been performed for two different bicrystal thicknesses, $d = 50 \mu\text{m}$ and $d = 0.5 \text{ mm}$ to assess the impact of the length-scale effects.

The results are summarized in Figures 4.17-4.25 with Figures 4.17 and 4.18 showing the comparison amongst all simulation cases for the two different bicrystal thicknesses and Figures 4.19-4.25 showing the comparisons of each individual simulation case for the two thicknesses considered. The stress-strain curves are generated by plotting tensorial shear strain versus the sum of the reaction forces at the displacement controlled top surface of crystal 2. The figures showing the geometrically-necessary dislocation density are, of course, not a direct measure of this quantity as it is not a directly attainable constitutive quantity. Instead we use the fact that the plastic curvature is reflective of the measure of GN dislocation density as indicated in Section 4.3.1.2 (Micropolar Case) on incompatibility mechanics and the quantity used in the plots is defined as

$$\rho_{GND} = \sqrt{(\bar{\kappa}_{13}^p/b)^2 + (\bar{\kappa}_{23}^p/b)^2} \quad (4.237)$$

The GN dislocation densities and lattice rotations reported in the figures are plotted at the midsection of the crystal where the origin of the x_2 axis has been fixed to the base of crystal 1, and the red

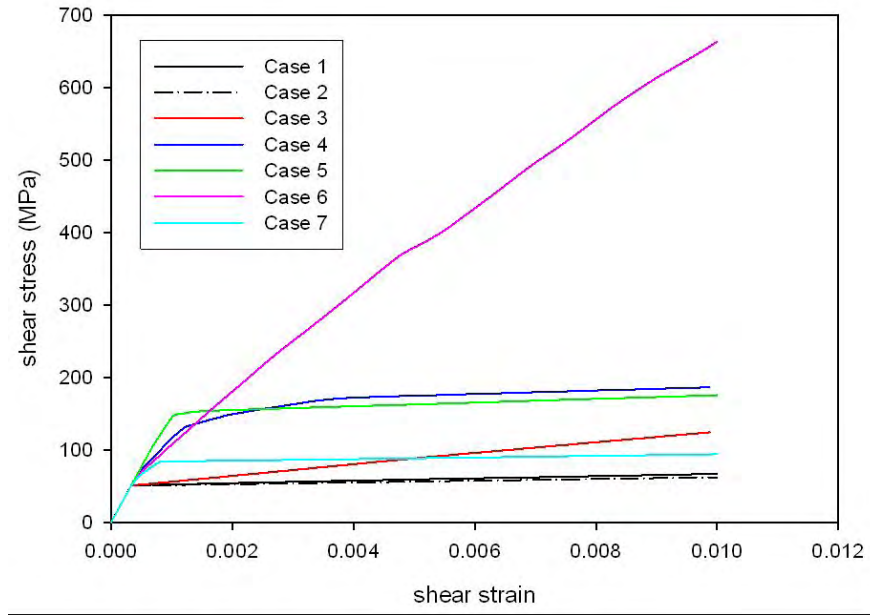
line down the center of the plots represents the grain boundary. In other words, data from crystal 1 is on the left side of the plots and data from crystal 2 is on the right.

Examining the stress-strain response of the 100 μm thick bicrystal (Figure 4.17) we see that a fairly wide range of yield strengths, from ~ 50 -200 MPa, is obtained for the various simulation cases. The effect of the plastic length scale parameter is significant and depending on its magnitude, it can affect both the initial yield strength and the strain-hardening behavior as can be seen by comparing Case 3 and 7 to Case 1. With the smaller plastic length parameter, the initial yield strength is approximately the same as when there is no rotationally-induced slip hardening, but with the larger value there is an increase in both the yield strength and strain hardening rate. With the limited number of simulations run thus far it is hard to make too many conclusions on the stress-strain response from simulation Cases 2-6 other than just observing how the misorientation affects the response. It is interesting to also note that when plastic curvature is neglected, at least for the particular orientation considered, that the bicrystal had a higher yield strength than when the plastic curvature was active for the same plastic length parameter. This indicates that plastic curvature can contribute to inelastic accommodation of deformation even at early stages of loading, and this conclusion is further supported by Case 6 in which the increased yield strength is a direct result of the increased rotationally-induced slip hardening resulting from the increase in the plastic length parameter.

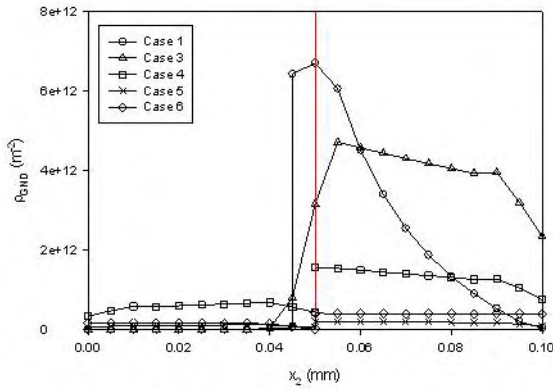
Looking at the distributions of GND density and lattice rotations in at the midsection of the bicrystal Figures 4.17 and 4.18, we see that the case without rotationally-induced slip hardening (Case 1) results in the highest peak GND density and that as one would expect that this aspect of slip system hardening would tend to temper the magnitude of the lattice rotation gradients near the boundary. This claim is further validated by Case 6 in that the increased effect of the rotationally-induced slip hardening further reduces the lattice rotation gradients near the boundary as compared to Cases 1 and 3. Notably Cases 2 and 7 have zero GND densities which in Case 7 is due to the absence of plastic curvature and the definition of GND density given in equations (4.237), but for Case 2 this is the result of the homogenous deformation of the bicrystal.

The results comparison for the 1mm thick bicrystal support all of the claims previously made about the development of the GND density and lattice rotations (Figure 4.18), however, it is apparent from investigation of the stress-strain curves that the effects of the rotationally-induced slip system hardening are much less pronounced for the thicker bicrystal as would be expected due to the less restricted nature of plastic flow for this geometry, *i.e.* smaller ratio of ℓ_p^η/d . Other than that, the most notable feature of any of the 1mm bicrystal simulations is the stress-strain curve of Case 6 where there is a plateau in the curve around 0.4% strain which then resumes hardening at approximately the initial hardening rate again around 0.8% strain. At this point in time, the reason for this behavior is not completely understood, but the data suggests that there is a transition in strain hardening behavior from that of being initially dominated by rotational plasticity to translational plasticity, which then transitions back to being dominated by the rotational modes.

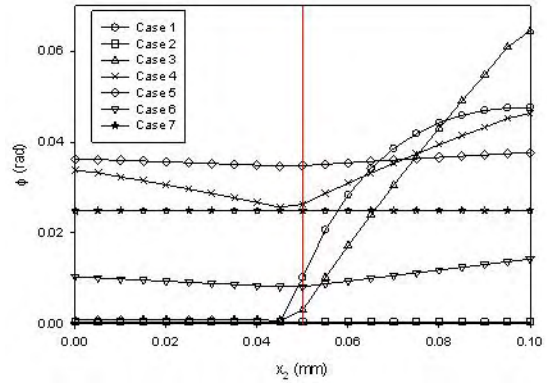
Focusing on the results that compare each simulation case at the two different bicrystal thicknesses (Figures 4.19-4.25), a few observations are enumerated. In both Cases 1 and 2, no length-scale dependent effects exist in terms of stress-strain response and lattice rotation, due in the first case to the lack of rotationally induced slip system hardening and in the latter to the state of ho-



(a)

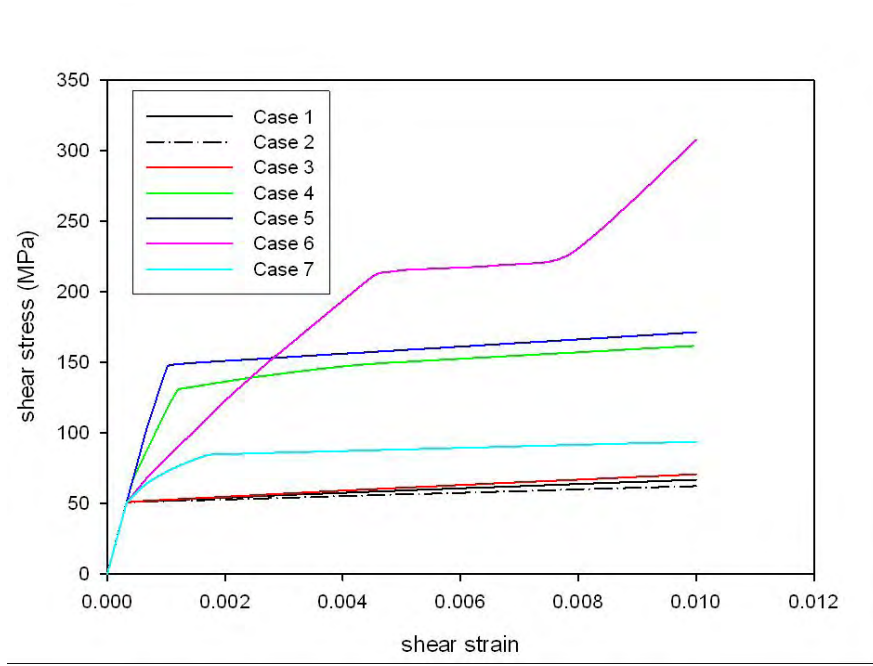


(b)

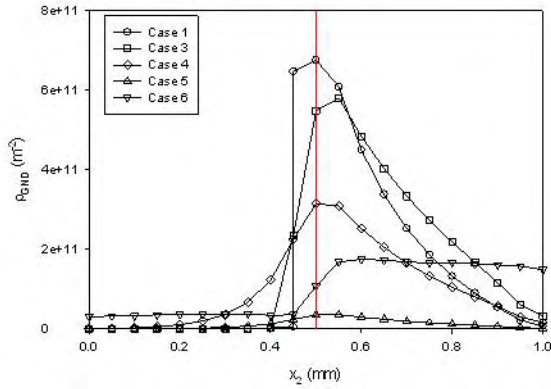


(c)

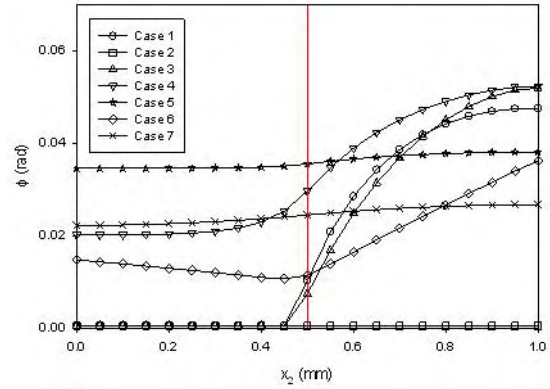
Figure 4.17. (a) Stress-strain curves, (b) GND density distributions, and (c) rotation distributions for all simulations with $2d = 100 \mu\text{m}$.



(a)



(b)



(c)

Figure 4.18. (a) Stress-strain curves, (b) GND density distributions, and (c) rotation distributions for all simulations with $2d = 1\text{mm}$.

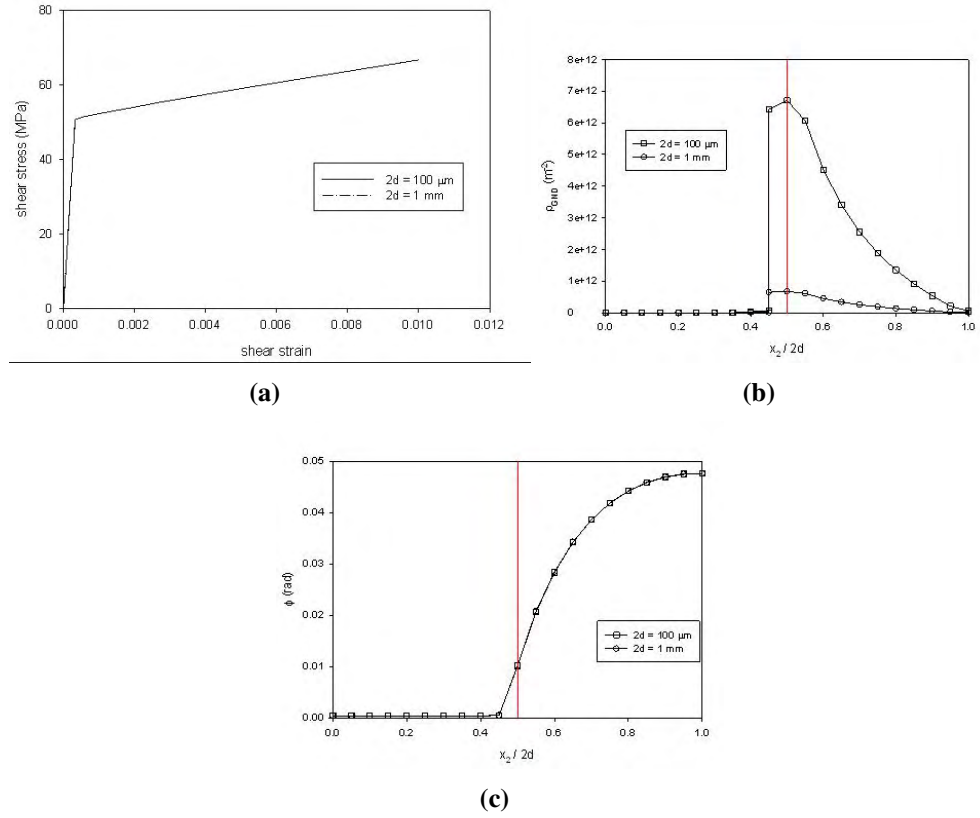


Figure 4.19. Case 1: (a) Stress-strain curves, (b) GND density distributions, and (c) rotation distributions.

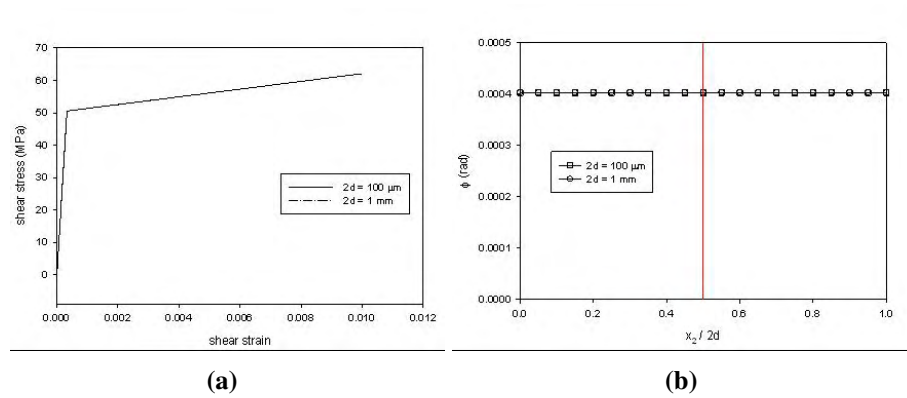


Figure 4.20. Case 2: (a) Stress-strain curves and (b) rotation distributions.

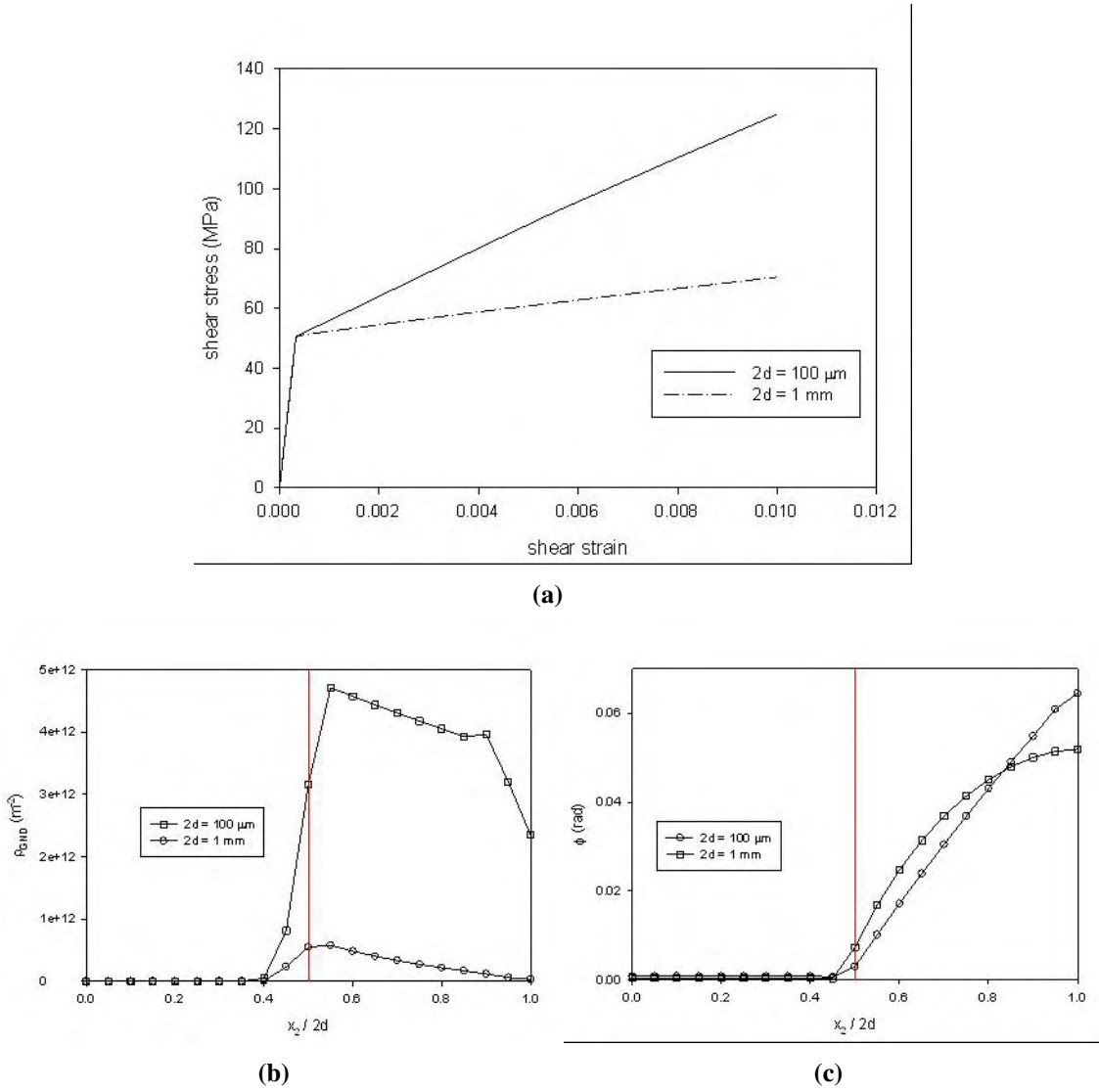


Figure 4.21. Case 3: (a) Stress-strain curves, (b) GND density distributions, and (c) rotation distributions.

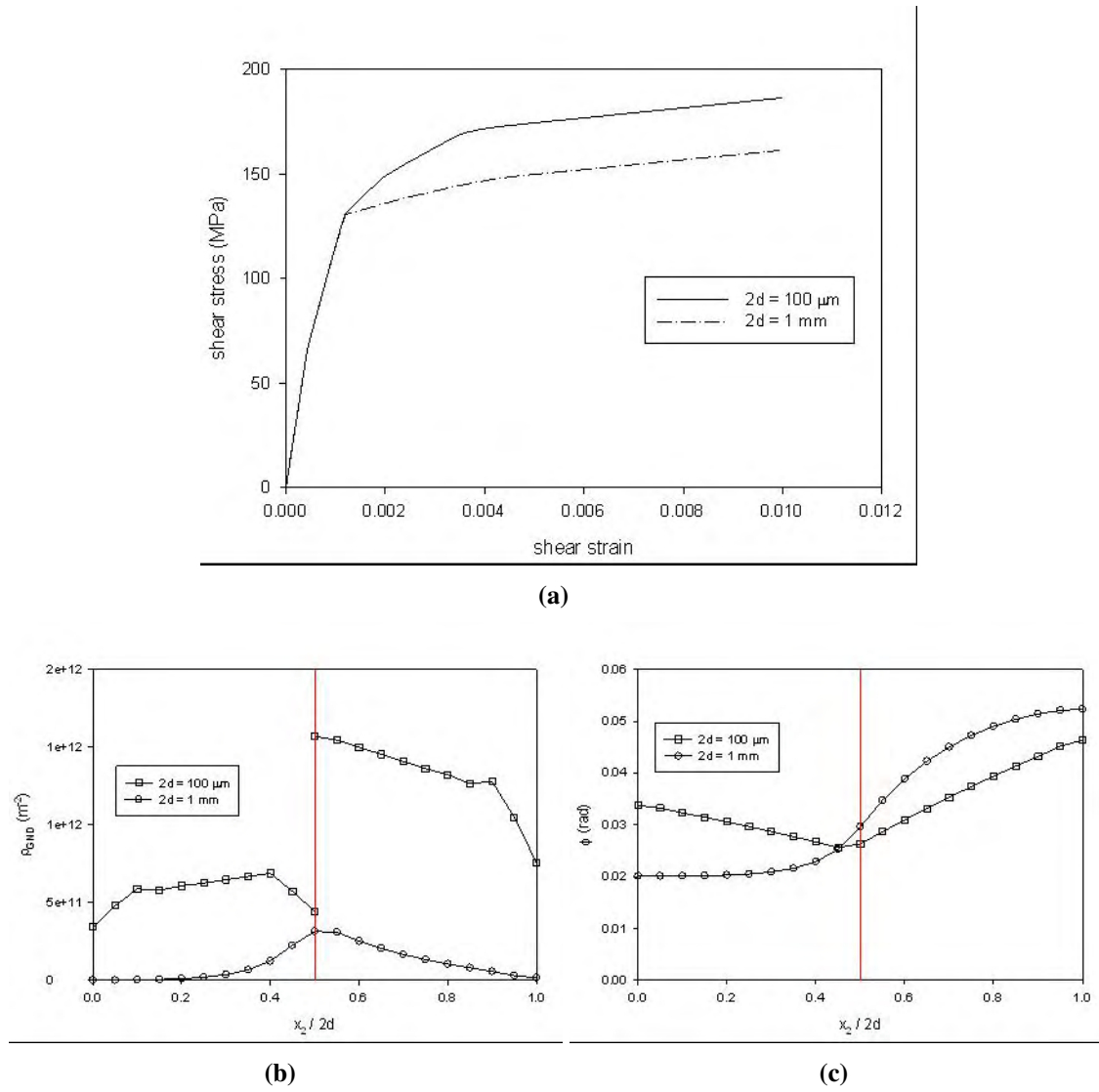


Figure 4.22. Case 4: (a) Stress-strain curves, (b) GND density distributions, and (c) rotation distributions.

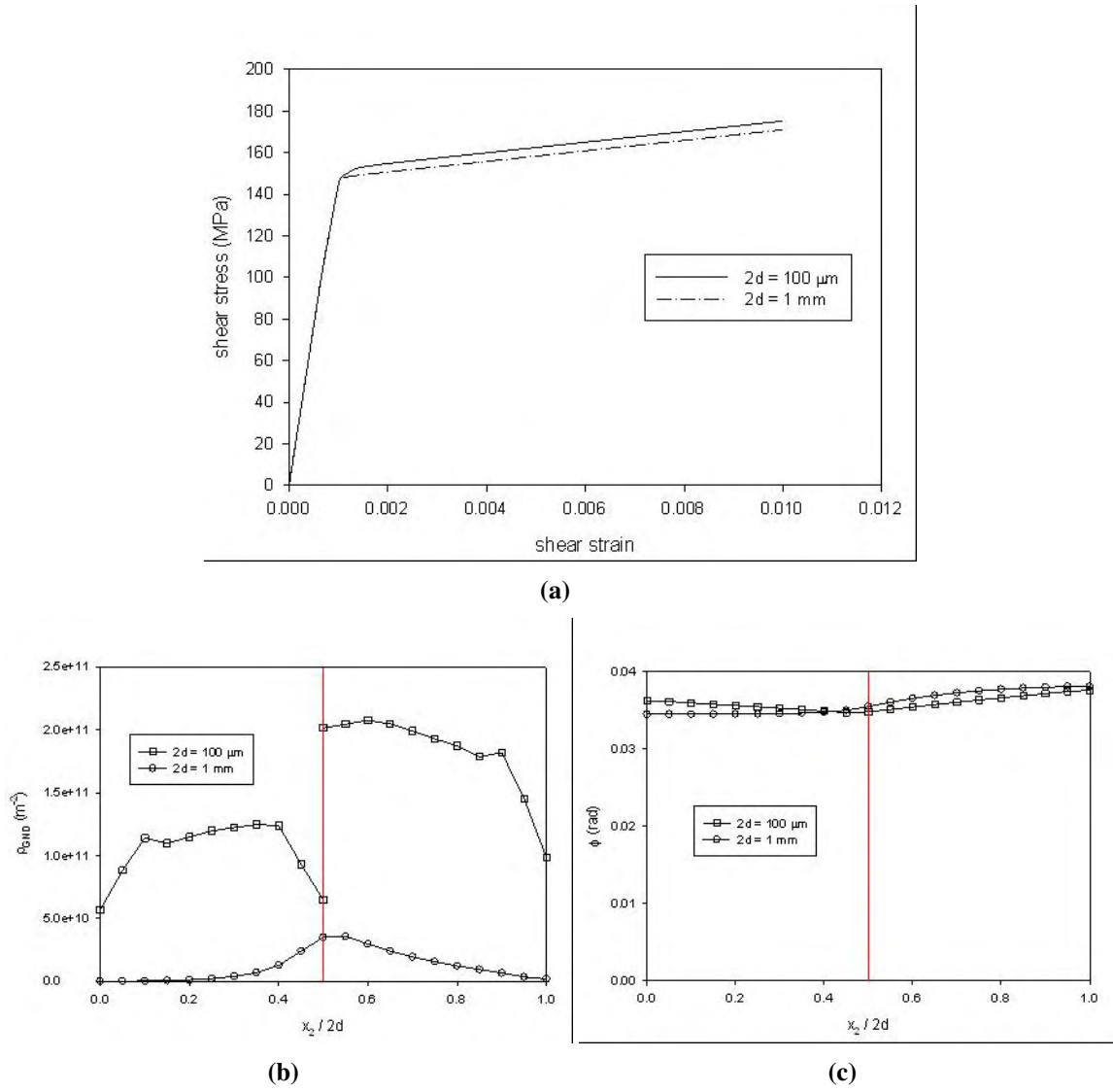
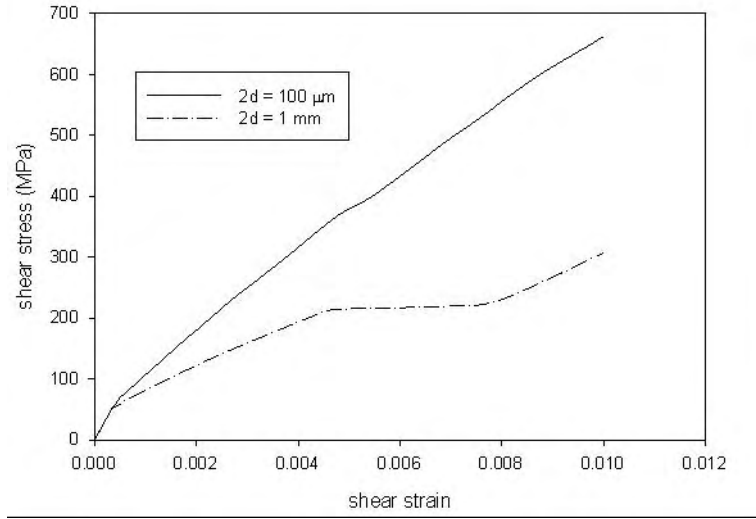
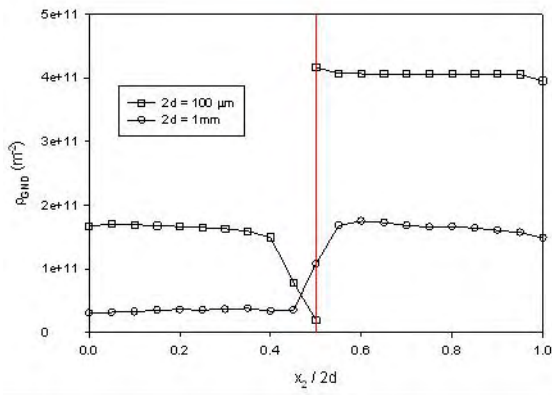


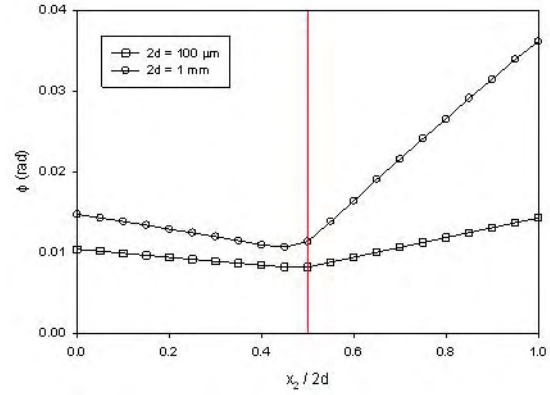
Figure 4.23. Case 5: (a) Stress-strain curves, (b) GND density distributions, and (c) rotation distributions.



(a)



(b)



(c)

Figure 4.24. Case 6: (a) Stress-strain curves, (b) GND density distributions, and (c) rotation distributions.

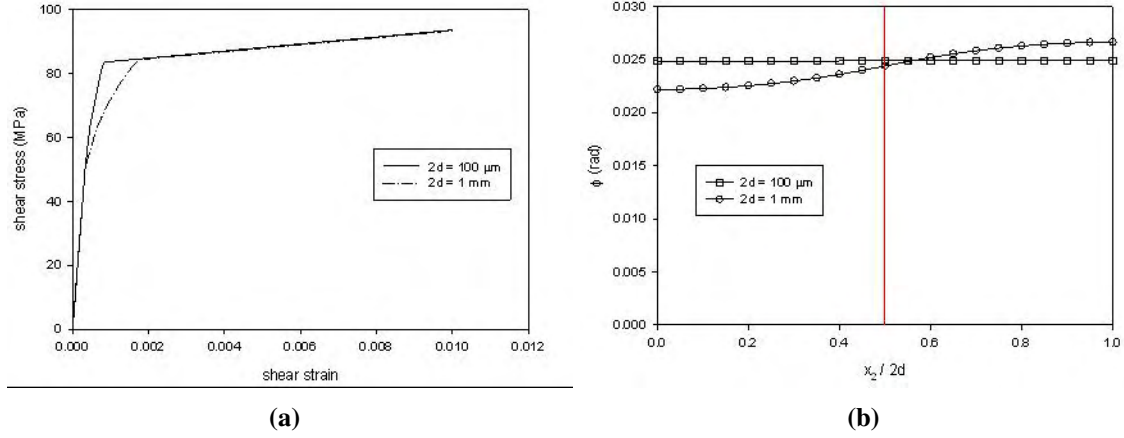


Figure 4.25. Case 7: (a) Stress-strain curves and (b) rotation distributions.

mogenous deformation of the bicrystal. In each of the simulations including rotationally-induced slip hardening with a heterogeneous deformation field the yield strength of the $100 \mu\text{m}$ bicrystal is always higher than that of the 1 mm bicrystal with the magnitude of this difference depending on the misorientation of the two crystals. One unexpected and interesting observation to emerge from these comparisons is that of simulation Case 7. Considering that plastic curvature was not active for these simulations, it was expected that stress-strain curves would be identical. However, the 1 mm thick bicrystal response deviates from the $100 \mu\text{m}$ response momentarily at the onset of yield seemingly indicating that this is some sort of elastic micropolar effect.

4.6 Summary

The objective of this work was to develop an advanced continuum crystal plasticity theory capable of accounting for more realistic treatment of GBs. Based on the theoretical developments of Clayton *et al.* [47] as a starting point, it was envisioned that this could be achieved in terms of their proposed finite deformation micropolar crystal plasticity theory that incorporates a constitutive dependence on geometrically necessary dislocations and disclinations. Upon delving into the details of their constitutive theory, a few logical inconsistencies and ambiguous propositions were discovered within their framework that we could not sort out. The nature of these issues touches all aspects of the model (kinematics, thermodynamics and balance laws, and kinetics), and depending on the intent of Clayton *et al.* [47] it could be recast in a consistent manner in a number of possible ways. Some of the inconsistencies have been pointed out in a previous progress report, and they are briefly recounted here.

The discussion of kinematics is ambiguous in terms of what is intended. On the one hand,

there is the extension of the traditional two-term multiplicative decomposition of the deformation gradient to include an additional term representing the incompatibility that develops during heterogeneous plastic flow. Similar extensions of the traditional two-term decomposition also have been proposed by Kratochvil [132], Horstemeyer and McDowell [117], Bammann [25], Regueiro *et al.* [191], Hartley [112], and Lion [145] based on several physical justifications. One thing that these models have in common is that they all maintain the classical structure of the non-polar mechanical balance equations where the local forms of linear and angular momentum balance are given by $\nabla_{\mathbf{x}} \cdot \boldsymbol{\sigma} = \mathbf{0}$ and $\boldsymbol{\sigma} = \boldsymbol{\sigma}^T$, respectively. However, when their discussion turns to the director kinematics, it is unclear whether or not they intend to use the directors in the sense of classical crystal plasticity as a way of uniquely identifying the plastic intermediate configuration [154], or if they intend to use the directors in the sense of a micropolar or micromorphic model in which the director strains lead to enhanced expressions of deformation power and therefore result in non-classical mechanical balance equations. This issue of kinematics obviously affects the eventual treatment of thermodynamics and balance laws as well as the specification of evolution equations. If the intent is to truly use a micropolar elastoplasticity theory, several modifications to the theory need to be made regarding the expressions of deformation power, rate of internal energy generation, and the mechanical balance laws. For examples of micromorphic and micropolar theories of elastoplasticity that deal with these issues the following references should be consulted [79, 93, 137, 170, 171, 177, 217, 221]. If, however, the intent is to maintain the classical form of the non-polar mechanical balance laws and introduce the GN dislocations and disclinations into the model formulation, it is recommended that the principle of virtual power [81, 89, 157] be used to derive the micro-force balance laws as in [7, 106] so that the appropriate coupling between the macro- and micro-stresses is achieved.

A second and more physically-based concern rests with the proposition of using GN disclination density as a continuum modeling quantity capable of representing various types of GBs. Unlike the notion relating discrete and continuously distributed dislocations, such a connection between discrete and continuously distributed disclinations does not exist. This is due to the fact, as pointed out by Anthony [13], that the rotational nature of a disclination defect cannot be smeared out as you transition from smaller to larger scales of observation of the continuum at hand. For example, the misorientation angle of a GB as viewed from a transmission electron microscope is the same misorientation angle that would be observed at lower scale of resolution using other imaging techniques. There is no questioning the existence of discrete disclinations in Bravais lattices, as they have been successfully used to describe the structure and misorientation-energy profiles of general high-angle boundaries in many material systems (cf. [91]). It is the transition from this discrete picture to the continuously distributed description at the continuum level and the appropriateness of the GN disclination density tensor as a physical variable that can be related to relevant crystallographic quantities that is ambiguous. As in the case for GN dislocations [15], there is no unique decomposition of the continuously distributed GN disclination into a collection of discrete defects over a given volume of material. Since the power of the disclination in describing GBs lies in its discrete nature, we feel that inclusion of the GN disclination density tensor in a continuum model with the intent of modeling GBs is on questionable physical grounds. It is our opinion that the effectiveness of GBs against slip transmission be described in alternative ways, and that disclination concepts can still be used to describe boundary strength in some manner, but not through directly assigning boundaries a GN disclination density.

In pursuit of the main objective, we set out to recast the framework of Clayton *et al.* [47] in a more consistent setting. To simplify matters to a certain degree we adopted as a starting point the geometrically-linear micropolar crystal plasticity model presented by Forest and collaborators [79, 217, 76, 77]. Their plasticity model rests on a multi-criterion formulation in which independent flow rules have been supplied for plastic strain and torsion-curvature as outlined in Section 4.3.3.1. We have also proposed a single criterion plasticity model in Section 4.3.3.2 that has formal analogies to macroscopic micropolar elastoplasticity theories, but is presented here for the first time in terms of a crystallographically-based plasticity theory. No computations have been performed with the single criterion theory, but it does seem to have potential advantages over the multi-criterion theory. For example, the formulation contains a natural back stress-like term (resolved couple-stress) and the slip system-level yield function bears a striking similarity to that proposed in Gurtin's [106] slip gradient-based single crystal plasticity theory. Since Gurtin's theory is often used to compare to other generalized crystal plasticity formulations, this would seemingly make comparing our theory to the existing literature a simpler task. Furthermore, the number of additional material constants required for the single criterion model is significantly reduced as compared to the multi-criterion model, and would therefore remove the uncertainty of specifying the non-classical constants that are required for the plastic torsion-curvature flow rule. Ultimately, which type of plasticity formulation will be deemed more physically appropriate for the modeling objectives at hand will be decided through further analytical and computational studies.

In regard to developing a GB sensitive crystal plasticity model, we have proposed a composite-type of approach in which there is a clear delineation between grain interior and GB regions. In the grain interiors, we choose to use a traditional associative Schmid Law flow rule, whereas in the GB regions we propose the novel idea of using a non-associative flow rule. This would account for the fact that the slip transmission process depends not only on the resolved shear stress on the incoming slip plane on one side of the GB, but also on the resolved shear stress on the outgoing slip plane on the other side of the GB as well. The resistance to slip transfer is envisioned to be boundary specific, and to be based upon the crystallographic structure of the GB as well as the orientation of the incoming/outgoing slip planes. It is within the determination of the transmission slip resistance that we believe the disclination concept may prove to be useful. Depending on the type of boundary and its structure in terms of GB dislocations and/or disclination structural units, the boundary strength in terms of a scalar slip system-level resistance variable would take different values.

In conclusion, we have spent the majority of the time on this project reshaping the model formulation to achieve the main objective of developing an advanced continuum crystal plasticity model sensitive to GB structure and the role they play in slip transfer, instead of merely implementing the model of Clayton *et al.* [47] and performing calculations. Nonetheless, some potentially fruitful and novel theoretical developments have emerged along the way which will be further pursued in future work. The result of these pursuits will be given in a forthcoming PhD dissertation and related journal publications.

4.7 Appendix: ABAQUS UEL subroutine

Listed here is the ABAQUS simulation code User ELement subroutine (UEL) written by Jason R. Mayeur to implement the formulation described in this chapter.

```

c      Linear (4 node) and Quadratic (8 node) User Element for 2D Micropolar Elasticity
c
c      Developed by:
c      -----
c      Rajesh S. Kumar
c      G.W.Woodruff School of Mech. Engg.
c      Georgia Tech., Atlanta, GA 30332
c      -----
c      Date: 11 Oct 2003
c      Last Modified: 30 Oct 2003
c      Checked on
c
c      -----
c      Modified by:
c      Jason Mayeur
c      Nov 3, 2007
c      The changes within this version of the UEL have been made to try
c      and address the convergence/crashing issues associated with the
c      activation of the plastic curvature evolution. Additionally, the number
c      of state variables used in this analysis has been increased so that some
c      additional field quantities are available for post-processing
c      -----
c
c      Input to be specified in the INPUT file
c      For general anisotropic micropolar media with no associated LCA
c      For 2D micropolar isotropic elastic media there are 4 material constants
c      PROPS - E, nu, N (coupling constant) and L (characteristic length)
c      lambda = E*nu/[(1+nu)*(1-2*nu)]
c      mu = E/[2*(1+nu)]
c      mu2 = mu - kappa/2
c      kappa = (2*N^2*mu)/(1-N^2)
c      gamma = 4*L^2*mu
c      STATE VARIABLES in the UEL
c      -----
c
c
c      SUBROUTINE UEL(RHS,AMATRX,SVARS,ENERGY,NDOFEL,NRHS,NSVARS,
1  PROPS,NPROPS,COORDS,MCRD,NNODE,U,DU,V,A,JTYPE,TIME,DTIME,
2  KSTEP,KINC,JELEM,PARAMS,NDLOAD,JDLTYP,ADLMAG,PREFEF,
3  NPREDF,LFLAGS,MLVARX,DDL MAG,MDLOAD,PNEWDT,JPROPS,NJPROP,
4  PERIOD)
c
c      INCLUDE 'ABA_PARAM.INC'
c
c      parameter(zero=0.d0, half=0.5d0, quart=0.25d0, one=1.d0, two=2.d0,
1  tol=0.000001)
c
c      Global Arrays
c
c      DIMENSION RHS(MLVARX,*),AMATRX(NDOFEL,NDOFEL),PROPS(*),
1  SVARS(*),ENERGY(*),COORDS(MCRD,NNODE),U(NDOFEL),
2  DU(MLVARX,*),V(NDOFEL),A(NDOFEL),TIME(2),PARAMS(*),
3  JDLTYP(MDLOAD,*),ADLMAG(MDLOAD,*),DDL MAG(MDLOAD,*),
4  PREFEF(2,NPREDF,NNODE),LFLAGS(*),JPROPS(*)
c
c      -----2D 4 Noded Element -----
c
c
c      4+-----+3
c      |      |eta |
c      |      |   |
c      |      *--xi |
c      |
c      1+-----+2
c
c
c      LOCAL VARIABLES/ARRAYS
c      dimension
c      x XGAUSS(4),
c      x YGAUSS(4),
c      x B(6,12),
c      x STIFFMAT(12,12),
c      x FORCEVEC(12),

```

```

x dU1(12),
x C_0(4,4),
x C(4,4),
x C_INV(4,4),
x C_EP(4,4),
x D_0(2,2),
x D(2,2),
x D_INV(2,2),
x D_EP(2,2),
x B_EP(4,2),
x A_EP(2,4),
x C_BAR(6,6),
x C_BAR_EP(6,6),
x E_BAR(6),
x dE_BAR(6),
x E_BAR_P_N(6),
x E_BAR_P_N1(6),
x dE_BAR_P(6),
x E_BAR_E_N1(6),
x SIG_BAR(6),
x S0(2,2),
x XN0(2,2),
x T0(3,2),
x S(2,2),
x XN(2,2),
x T(3,2),
x Q(2,2),
x P(4,2),
x H(2,2),
x P_BAR(6,4),
x DELTA2(2,2),
x Q1M(2,2),
x Q2M(2,2),
x QC1M(2,2),
x QC2M(2,2),
x R_BAR_N(4),
x G_BAR_N(4),
x R_BAR_N1(4),
x G_BAR_N1(4),
x dR_BAR(4),
x TAU_BAR(4),
x dLAMBDA_N(4),
x dLAMBDA(4),
x LAM_DOT_0(4),
x EXP_BAR(4),
x XL2V(4),
x dTHETA_N(2),
x dTHETA(2),
x dGAMMA_N(2),
x dGAMMA(2),
x dEPS(4),
x dKAP(2),
x HR_BAR(4,4),
x ddEPS_PdS(4,4),
x ddGAMdS_T(2,4),
x H1D(2,2),
x PD_T(2,4),
x ddGAMdM_T(2,2),
x ddEPS_PdM(4,2),
x ddTHETdM_T(2,2),
x ddKAP_PdM(2,2),
x H2D(2,2),
x H3D(2,2),
x HD_T(2,2),
x HP(2,2),
x TEMP1(4),
x TEMP2(2,2),
x TEMP3(2,2),
x TEMP4(4,4),
x TEMP5(2,2),
x TEMP6(2,2),

```

```

x TEMP7(2),
x TEMP8(2),
x TEMP9(4,2)

NUM_SLIP_SYS = 2
NUM_INT_P = 4
  AINTC = 1.
  BINTC = 1.
debug = 2

pi = 4.*atan(1.)

c *****
c Element Initializations: Formulation is based on Original Coordinates
c in Undeformed Configuration
c *****

c x coordinates of the 4 Gauss points
data XGAUSS /-0.577350269189626d0, 0.577350269189626d0,
x 0.577350269189626d0, -0.577350269189626d0/
c y coordinates of the 4 Gauss points
data YGAUSS /-0.577350269189626d0, -0.577350269189626d0,
x 0.577350269189626d0, 0.577350269189626d0/

x1=coords(1,1)
y1=coords(2,1)
x2=coords(1,2)
y2=coords(2,2)
x3=coords(1,3)
y3=coords(2,3)
x4=coords(1,4)
y4=coords(2,4)

RHS(1:12,1)=0.

call zero_array(12,12,AMATRX)
call zero_array(4,4,C_0)
call zero_array(2,2,D_0)
call zero_array(6,6,C_BAR)

c *****
c Define constitutive model properties
c *****
E = props(1) ! Young's Modulus
XNU = props(2) !Poisson's ratio
CN = props(3) !Elastic coupling constant
XL1 = props(4) ! Material length scale entering elastic properties
GAMMA_DOT_ZERO = props(5) !Ref shearing rate
R_ZERO = props(6) ! Initial slip threshold stress
H_DIR = props(7) ! Direct hardening constant for slip
Q1 = props(8)
H_DYN = props(9) ! Dynamic recovery constant for slip
H_KC = props(10)
Q2 = props(11)
G_ZERO = props(12) ! Reference shear strength
EXPM = props(13) ! Slip flow exponent
THETA_DOT_ZERO = props(14) !Ref curvature rate
RC_ZERO = props(15) ! Initial curvature threshold stress
HC_DIR = props(16) ! Hardening modulus for curvature
QC1 = props(17)
HC_DYN = props(18)
H_EC = props(19)
QC2 = props(20)
GC_ZERO = props(21) ! Reference curvature strength
EXPMC = props(22) ! Curvature flow exponent
XL2 = props(23) ! Material length scale entering curvature flow rule
PSI = props(24) ! Orientation angle for 2D crystal

c *****

```



```

c      Define elastic constants for a linearized isotropic micropolar material
c      *****

      XLAMBDA = (E*XNU)/((1+XNU)*(1-2.*XNU))
      XMU = E/(2.*(1+XNU))
      XKAPPA = 2.*CN*2.*XMU/(1-CN*2.)
      XMU2 = XMU - XKAPPA/2.
      XGAMMA = 4.*XL1*2.*XMU

c      *****
c      Define elastic stiffness matrix for a linearized micropolar material
c      *****

      C_0(1,1) = XLAMBDA + 2.*XMU2 + XKAPPA
      C_0(1,2) = XLAMBDA
      C_0(2,1) = XLAMBDA
      C_0(2,2) = XLAMBDA + 2.*XMU2 + XKAPPA
      C_0(3,3) = XMU2 + XKAPPA
      C_0(3,4) = XMU2
      C_0(4,3) = XMU2
      C_0(4,4) = XMU2 + XKAPPA

      D_0(1,1) = XGAMMA
      D_0(2,2) = XGAMMA

      LAM_DOT_0(1:2) = GAMMA_DOT_ZERO
      LAM_DOT_0(3:4) = THETA_DOT_ZERO
      EXP_BAR(1:2) = EXPM
      EXP_BAR(3:4) = EXPMC
      XL2V(1:2) = XL2

c      *****
c      Define slip system vectors in crystal coordinate system for planar double slip
c      s0(i,j) - jth slip system and the ith component of the slip direction
c      xn0(i,j) - jth slip system and the ith component of the slip plane normal
c      *****
c      Planar Double Slip
c      *****

      S0(1,1) = 1.
      S0(2,1) = 0.
      XN0(1,1) = 0.
      XN0(2,1) = 1.
      T0(3,1) = 1.
      T0(1:2,1) = 0.

      S0(1,2) = cos(70.2*pi/180.)
      S0(2,2) = sin(70.2*pi/180.)
      XN0(1,2) = -sin(70.2*pi/180.)
      XN0(2,2) = cos(70.2*pi/180.)
      T0(3,2) = 1.
      T0(1:2,2) = 0.

c      *****
c      Initialize arrays that appear in the threshold stress evolution equations
c      *****

      do i = 1,2
        do j = 1,2
          DELTA2(i,j) = 0.0
        end do
        DELTA2(i,i) = 1.0
      end do

      Q1M = Q1 + (1. - Q1)*DELTA2
      Q2M = Q2 + (1. - Q2)*DELTA2
      QC1M = QC1 + (1. - QC1)*DELTA2

```

```

QC2M = QC2 + (1. - QC2)*DELTA2

c *****
c Flag variable for determining whether or not this increment is the first increment in
c the simulation in order to properly initialize the state variable arrays
c *****
UMAG = 0.
do i = 1,NDOFEL
  UMAG = UMAG + (U(i)-DU(i,1))*2.
  dU1(i) = dU(i,1)
end do
UMAG = sqrt(UMAG)

c write(7,*) 'ELEMENT NUMBER =',JELEM
c write(7,*) '*****'
c write(7,*) 'Nodal Displacement Vector'
c do i = 1,4
c   write(7,1),U((i-1)*3+1),U((i-1)*3+2),U((i-1)*3+3)
c end do
c write(7,*) '*****'

c *****
c Loop over integration points to perform element level calculations
c *****
n = 0 !counter variable for reading state variable arrays
m = 0 !counter variable for storing state variable arrays

do KINTP = 1,NUM_INT_P

  if (debug.eq.1) write(7,*) 'INTEGRATION POINT',KINTP
  write(7,*) 'kinc =',kinc,'int pt = ',kintp

c -----
c Initialize state variable arrays
c -----

  if ((KINC.eq.0).or.(UMAG.lt.tol)) then

    do j = 1,6
      E_BAR(j) = 0.
      E_BAR_P_N(j) = 0.
      SIG_BAR(j) = 0.
    end do

    do j = 1,num_slip_sys
      R_BAR_N(j) = R_ZERO
      R_BAR_N(j+2) = RC_ZERO
      G_BAR_N(j) = G_ZERO
      G_BAR_N(j+2) = GC_ZERO
    end do

    else !Starting values are end values from a previous call to the subroutine

      do j=1,6
        n = n + 1
        E_BAR(j) = svars(n)
      end do

      do j=1,6
        n = n+1
        SIG_BAR(j) = svars(n)
      end do

      do j=1,6
        n = n+1
        E_BAR_P_N(j) = svars(n)
      end do

      do j=1,num_slip_sys*2

```

```

        n = n+1
        R_BAR_N(j) = svars(n)
    end do

    do j=1,num_slip_sys*2
        n = n+1
        G_BAR_N(j) = svars(n)
    end do

    end if !Initialization flow control
c -----
c End of initialization of state variable arrays
c -----

c     Initializations of various arrays

    call zero_array(12,12,STIFFMAT)
    call zero_array(6,12,B)
    call zero_vector(6,E_BAR)
    call zero_vector(6,dE_BAR)

c     xi and eta at the current gauss point - kintp

    xi=xgauss(kintp)
    eta=ygauss(kintp)

c     shape functions evaluated at the gauss point

    shape1=quart*(one-xi)*(one-eta)
    shape2=quart*(one+xi)*(one-eta)
    shape3=quart*(one+xi)*(one+eta)
    shape4=quart*(one-xi)*(one+eta)

c     derivative of shape functions wrt natural coordinates

    dN1dxi=-quart*(one-eta)
    dN1deta=-quart*(one-xi)
    dN2dxi=quart*(one-eta)
    dN2deta=-quart*(one+xi)
    dN3dxi=quart*(one+eta)
    dN3deta=quart*(one+xi)
    dN4dxi=-quart*(one+eta)
    dN4deta=quart*(one-xi)

c     derivative of physical coordinates wrt natural coords

    dxdxi=dN1dxi*x1+dN2dxi*x2+dN3dxi*x3+dN4dxi*x4
    dxdeta=dN1deta*x1+dN2deta*x2+dN3deta*x3+dN4deta*x4
    dydxi=dN1dxi*y1+dN2dxi*y2+dN3dxi*y3+dN4dxi*y4
    dydeta=dN1deta*y1+dN2deta*y2+dN3deta*y3+dN4deta*y4

c     determinant of the Jacobian transformation between physical and natural
c     coords

    detJ=dxdxi*dydeta-dxdeta*dydxi

c     derivative of shape functions wrt physical coords x and y

    dN1dx=(dN1dxi*dydeta-dN1deta*dydxi)/detJ
    dN1dy=(-dN1dxi*dxdeta+dN1deta*dxdxi)/detJ
    dN2dx=(dN2dxi*dydeta-dN2deta*dydxi)/detJ
    dN2dy=(-dN2dxi*dxdeta+dN2deta*dxdxi)/detJ
    dN3dx=(dN3dxi*dydeta-dN3deta*dydxi)/detJ
    dN3dy=(-dN3dxi*dxdeta+dN3deta*dxdxi)/detJ
    dN4dx=(dN4dxi*dydeta-dN4deta*dydxi)/detJ
    dN4dy=(-dN4dxi*dxdeta+dN4deta*dxdxi)/detJ

c     POPULATE STRAIN-DISPLACEMENT MATRIX WITH APPROPRIATE COMPONENTS
c     B(NDI+NSHR,NDOFEL)

```

```

B(1,1)=dN1dx
B(1,4)=dN2dx
B(1,7)=dN3dx
B(1,10)=dN4dx

B(2,2)=dN1dy
B(2,5)=dN2dy
B(2,8)=dN3dy
B(2,11)=dN4dy

B(3,2)=dN1dx
B(3,3)=-shape1
B(3,5)=dN2dx
B(3,6)=-shape2
B(3,8)=dN3dx
B(3,9)=-shape3
B(3,11)=dN4dx
B(3,12)=-shape4

B(4,1)=dN1dy
B(4,3)=shape1
B(4,4)=dN2dy
B(4,6)=shape2
B(4,7)=dN3dy
B(4,9)=shape3
B(4,10)=dN4dy
B(4,12)=shape4

B(5,3)=dN1dx
B(5,6)=dN2dx
B(5,9)=dN3dx
B(5,12)=dN4dx

B(6,3)=dN1dy
B(6,6)=dN2dy
B(6,9)=dN3dy
B(6,12)=dN4dy

c      CALCULATE THE STRAIN VECTOR BASED ON THE DISPLACEMENT VECTOR FED IN BY ABAQUS
C      {E}=[B]{U}

      E_BAR = matmul(B,U)
      dE_BAR = matmul(B,dU1)

1      format(6(e12.5,2x))
c-----
c-----
c-----
c      Explicit Integration of Constitutive Equations (UMAT)

c      Rotate elasticity matrix to its global orientation (for isotropy C=C_0

      C = C_0

      D = D_0

      C_BAR(1:4,1:4) = C(1:4,1:4)
      C_BAR(5:6,5:6) = D(1:2,1:2)

      if (debug.eq.1) write(7,*) 'CHECKPOINT 1'

c      Rotate slip directions from crystal basis to global coordinates

      Q(1,1) = cos(PSI*pi/180.)
      Q(1,2) = -sin(PSI*pi/180.)
      Q(2,1) = sin(PSI*pi/180.)
      Q(2,2) = cos(PSI*pi/180.)

      S = matmul(Q,S0)
      XN = matmul(Q,XN0)

```

```

T(3,1) = T0(3,1)
T(3,2) = T0(3,2)
T(1:2,1) = 0.
T(1:2,2) = 0.

c      Calculate resolved shear stress and resolved moment stress
c      Define slip tensor in vectorial form

P(1,1) = XN(1,1)*S(1,1)
P(2,1) = XN(2,1)*S(2,1)
P(3,1) = XN(1,1)*S(2,1)
P(4,1) = XN(2,1)*S(1,1)
P(1,2) = XN(1,2)*S(1,2)
P(2,2) = XN(2,2)*S(2,2)
P(3,2) = XN(1,2)*S(2,2)
P(4,2) = XN(2,2)*S(1,2)

H(1,1) = S(1,1)*T(3,1) ! Curvature system
H(2,1) = S(2,1)*T(3,1) ! Curvature system
H(1,2) = S(1,2)*T(3,2) ! Curvature system
H(2,2) = S(2,2)*T(3,2) ! Curvature system

call zero_array(6,4,P_BAR)

P_BAR(1:4,1:2) = P(1:4,1:2)
P_BAR(5:6,3:4) = H(1:2,1:2)

if (debug.eq.1) write(7,*) 'CHECKPOINT 2'
C*****
C*****
C*****

c      CALCULATE THE FIRST ESTIMATE OF THE RESOLVED STRESSES

TAU_BAR = matmul(transpose(P_BAR),SIG_BAR)

c      CALCULATE THE SHEARING/CURVATURE RATES FROM THE FLOW RULE

      do 50 i = 1,4
      dLAMBDA_N(i) = 0.
      TAUD = max((abs(TAU_BAR(i))-R_BAR_N(i)),0.)
      if (TAUD.eq.0.0) GOTO 50
      SGNTAU_BAR_I = abs(TAU_BAR(i))/TAU_BAR(i)
      dLAMBDA_N(i) = LAM_DOT_0(i)*(TAUD/G_BAR_N(i))*EXP_BAR(i)*
&      SGNTAU_BAR_I*DTIME
50    continue

C      CALCULATE THE MATRICES NECESSARY FOR DETERMINING THE PLASTIC ROTATION
C      INCREMENTS, dTHETA
call zero_array(2,2,HD_T)
call zero_array(2,2,HP)
call zero_array(2,2,H2D)
call zero_array(2,2,H3D)
call zero_vector(2,dTHETA)

do i = 1,2
  if (dLAMBDA_N(i+2).eq.0.0) GOTO 53
  do j = 1,2
    SGNTAU_BAR_I = abs(TAU_BAR(i+2))/TAU_BAR(i+2)
    SGNTAU_BAR_J = abs(TAU_BAR(j+2))/TAU_BAR(j+2)
    HP(i,j) = H(i,j) / XL2V(j)
    HD_T(i,j) = EXP_BAR(i+2)*dLAMBDA_N(i+2)/(abs(TAU_BAR(i+2))-
&      R_BAR_N(i+2))*SGNTAU_BAR_I*H(j,i)
    H2D(i,j) = -EXP_BAR(i)*dLAMBDA_N(i)/(abs(TAU_BAR(i))-R_BAR_N(i))
&      *H_KC*Q2M(i,j)*SGNTAU_BAR_J
    H3D(i,j) = -EXP_BAR(i+2)*dLAMBDA_N(i+2)/(abs(TAU_BAR(i+2))-
&      R_BAR_N(i+2))*(HC_DIR*QC1M(i,j)-HC_DYN*R_BAR_N(i+2))
&      *SGNTAU_BAR_J
  end do
end do

```

```

53     end do

        TEMP2 = matmul(matmul(HD_T,D),HP)

        TEMP3 = DELTA2 + BINTC*TEMP2 - BINTC*H3D

        dKAP(1:2) = dE_BAR(5:6)
        dTHETA_N(1:2) = dLAMBDA_N(3:4)

        TEMP6 = matmul(matmul(HD_T,D),dKAP)

        TEMP7 = dTHETA_N + BINTC*TEMP6

        call inverse(2,TEMP3,TEMP2)

        dTHETA = matmul(TEMP2,TEMP7)

C      CALCULATE THE MATRICES NECESSARY FOR DETERMINING THE PLASTIC SLIP INCREMENTS,
C      dGAMMA

        call zero_array(2,4,PD_T)
        call zero_array(2,2,H1D)
        call zero_vector(2,dGAMMA)

        do i = 1,2
            if (dLAMBDA_N(i).eq.0.0) GOTO 51
            do j = 1,2
                SGNTAU_BAR_J = abs(TAU_BAR(j))/TAU_BAR(j)
                H1D(i,j) = -EXP_BAR(i)*dLAMBDA_N(i)/(abs(TAU_BAR(i))-R_BAR_N(i))
&                *(H_DIR*Q1M(i,j) - H_DYN*R_BAR_N(i))*SGNTAU_BAR_J
            end do
51        end do

        do i = 1,2
            if (dLAMBDA_N(i).eq.0.0) GOTO 52
            do j = 1,4
                SGNTAU_BAR_I = abs(TAU_BAR(i))/TAU_BAR(i)
                PD_T(i,j) = EXP_BAR(i)*dLAMBDA_N(i)/(abs(TAU_BAR(i))-R_BAR_N(i))
&                *SGNTAU_BAR_I*P(j,i)
            end do
52        end do

        dEPS(1:4) = dE_BAR(1:4)

        TEMP3 = matmul(matmul(PD_T,C),P)

        TEMP5 = DELTA2 + AINTC*TEMP3 - AINTC*H1D

        call inverse(2,TEMP5,TEMP3)

        TEMP6 = matmul(matmul(PD_T,C),dEPS)
        TEMP7 = matmul(H2D,dTHETA)

        dGAMMA_N(1:2) = dLAMBDA_N(1:2)

        TEMP8 = dGAMMA_N + AINTC*TEMP6 + AINTC*TEMP7

        dGAMMA = matmul(TEMP3,TEMP8)

        if (debug.eq.1) write(7,*) 'CHECKPOINT 3'

c      CALCULATE THE PLASTIC STRAIN/CURVATURE INCREMENTS

        dLAMBDA(1:2) = dGAMMA(1:2)
        dLAMBDA(3:4) = dTHETA(1:2) / XL2V(1:2)

        dE_BAR_P = matmul(P_BAR,dLAMBDA)

        dLAMBDA(3:4) = dLAMBDA(3:4) * XL2V(1:2)

```

```

c      CALCULATE THE ELASTIC & PLASTIC STRAIN VECTORS AT T + DT

      E_BAR_P_N1 = E_BAR_P_N + dE_BAR_P
      E_BAR_E_N1 = E_BAR - E_BAR_P_N1

      if (debug.eq.1) write(7,*) 'CHECKPOINT 4'

c      CALCULATE THE STRESS AT N + 1

      SIG_BAR = matmul(C_BAR,E_BAR_E_N1)

116    format(6(e12.5,2x))

112    format(6(f12.5,2x))

c      CALCULATE SLIP SYSTEM VARIABLES FOR T + DT

do i = 1,2
  do j = 1,2
    HR_BAR(i,j) = H_DIR*Q1M(i,j) - H_DYN*R_BAR_N(i)
    HR_BAR(i,j+2) = H_KC*Q2M(i,j)
    HR_BAR(i+2,j) = H_EC*QC2M(i,j)
    HR_BAR(i+2,j+2) = HC_DIR*QC1M(i,j) - HC_DYN*R_BAR_N(i+2)
  end do
end do

TEMP1 = abs(dLAMBDA)

dR_BAR = matmul(HR_BAR,TEMP1)

R_BAR_N1 = R_BAR_N + dR_BAR
G_BAR_N1 = G_BAR_N

C*****
C*****
C*****
C*****
C*****
c      CALCULATE THE MATERIAL JACOBIAN
c
      call zero_array(4,4,C_EP)
      call zero_array(2,2,D_EP)
      call zero_array(4,2,B_EP)
      call zero_array(6,6,C_BAR_EP)
      call zero_array(4,4,TEMP4)
      call zero_array(4,2,TEMP9)
      call zero_array(2,2,TEMP5)

      TEMP4 = matmul(matmul(matmul(matmul(C,P),TEMP3),PD_T),C)

      C_EP = C - AINTC*TEMP4

      TEMP9 = matmul(matmul(matmul(matmul(matmul(matmul(C,P),TEMP3),H2D)
&      ,TEMP2),HD_T),D)

      B_EP = AINTC*BINTC*TEMP9

      TEMP5 = matmul(matmul(matmul(matmul(D,HP),TEMP2),HD_T),D)

      D_EP = D - BINTC*TEMP5

c      POPULATE THE GENERALIZED FINITE ELEMENT ELASTIC MATRIX

      C_BAR_EP(1:4,1:4) = C_EP(1:4,1:4)
      C_BAR_EP(1:4,5:6) = B_EP(1:4,1:2)

```

```

C_BAR_EP(5:6,5:6) = D_EP(1:2,1:2)

c      write(7,*)'CEP'
c      do i =1,6
c          write(7,990),C_BAR_EP(i,1),C_BAR_EP(i,2),C_BAR_EP(i,3),
c      &      C_BAR_EP(i,4),C_BAR_EP(i,5),C_BAR_EP(i,6)
c      end do

990 format(6(f12.2,2x))
991 format(4(f12.2,2x))
992 format(4(e12.5,2x))

c      Do matrix multiplications to get Stiffness Matrix

          STIFFMAT = matmul(matmul(transpose(B),C_BAR_EP),B)

c      Update the element Stiffness matrix AMATRX

          AMATRX = AMATRX + STIFFMAT*detJ

c      Calculate the element force vector for each integration point

          FORCEVEC = matmul(transpose(B),SIG_BAR)

c      Sum integration point contributions to the total element force vector

          RHS(1:12,1) = RHS(1:12,1) - FORCEVEC(1:12)*detJ

C-----
c      Store state variables
C-----
      if (debug.eq.1) write(7,*) 'CHECKPOINT 6'

      do j=1,6
          m = m + 1
          svars(m) = E_BAR(j)
      end do

      do j=1,6
          m = m + 1
          svars(m) = SIG_BAR(j)
      end do

      do j=1,6
          m = m+1
          svars(m) = E_BAR_P_N1(j)
      end do

      do j=1,num_slip_sys*2
          m = m+1
          svars(m) = R_BAR_N1(j)
      end do

      do j=1,num_slip_sys*2
          m = m+1
          svars(m) = G_BAR_N1(j)
      end do

C-----
      enddo !end loop over kintp (number of integration points)

c      do i = 1,12
c          write(7,'(12(f9.2,1x))') (AMATRX(I,J),J=1,12)
c      end do
c      write(7,*)'*****'
c      write(7,'(12(f10.7,1x))') -ForceVecG
c      write(7,*)'*****'

```



```

C      do i = 1,NSVARS/4
C      write(7,989) 'STV',i,svars(i),svars(i+NSVARS/4),svars(i+NSVARS/2),svars(i+NSVARS*3/4)
C      end do

989      format(A3,1x,i3,f12.5,2x,f12.5,2x,f12.5,2x,f12.5)

C-----
      return
      end

C=====
C=====
C Utility Subroutines
C=====
C=====
C=====
C=====
C
C Calculate the inverse of a matrix using
C LU decomposition (Crout's method)
C
C Reference: "Numerical Recipes" Section 2.3 p. 31
C
C-----

      subroutine inverse(n,a,b)

      include 'ABA_PARAM.INC'

      dimension a(n,n), b(n,n), c(n,n), index(n)

      do i = 1,n
        do j = 1,n
          c(i,j) = a(i,j)
        end do
      end do

      do i = 1,n
        do j = 1,n
          b(i,j) = 0.0
        end do
        b(i,i) = 1.0
      end do

      call kLU-Decomp(n,c,index)

      do j = 1,n
        call kLU-BackSub(n,c,index,b(1,j))
      end do

      return
      end

C=====
C=====
C
C This sub performs an LU Decomposition (Crout's method) on the
C matrix "a". It uses partial pivoting for stability. The index()
C vector is used for the partial pivoting. The v() vector is
C a dummy work area.
C
C Reference: "Numerical Recipes" Section 2.3 p. 31
C
C-----

      subroutine kLU-Decomp(n,a,index)

      include 'ABA_PARAM.INC'

      dimension a(n,n), index(n), v(n)

```

```

tiny = 1.0e-20

c-----
c Loop over the rows to get the implicit scaling info.
c-----

do i = 1,n
  a_max = 0.0
  do j = 1,n
    a_max = max(a_max,abs(a(i,j)))
  end do !j
  v(i) = 1.0 / a_max
end do !i

c-----
c Begin big loop over all the columns.
c-----

do j = 1,n

  do i = 1,j-1
    sum = a(i,j)
    do k = 1,i-1
      sum = sum - a(i,k) * a(k,j)
    end do
    a(i,j) = sum
  end do

  a_max = 0.0
  do i = j,n
    sum = a(i,j)
    do k = 1,j-1
      sum = sum - a(i,k) * a(k,j)
    end do
    a(i,j) = sum
    dummy = v(i) * abs(sum)
    if ( dummy .gt. a_max ) then
      imax = i
      a_max = dummy
    end if
  end do

c-----
c Pivot rows if necessary.
c-----

  if ( j .ne. imax ) then
    do k = 1,n
      dummy = a(imax,k)
      a(imax,k) = a(j,k)
      a(j,k) = dummy
    end do
    v(imax) = v(j)
  end if
  index(j) = imax

c-----
c Divide by the pivot element.
c-----

  if ( a(j,j) .eq. 0.0 ) a(j,j) = tiny
  if ( j .ne. n ) then
    dummy = 1.0 / a(j,j)
    do i = j+1,n
      a(i,j) = a(i,j) * dummy
    end do
  end if

end do !j

```

```

        return
    end

C=====
C=====
C
C Solves a set of simultaneous equations by doing back substitution.
C The answer is returned in the b() vector. The a(,) matrix
C must have already been "LU Decomposed" by the above subroutine.
C
C Reference: "Numerical Recipes" Section 2.3 p. 31
C
C-----

    subroutine kLU_BackSub(n,a,index,b)

    include 'ABA_PARAM.INC'

    dimension a(n,n), index(n), b(n)

    ii = 0

C-----
C Do the forward substitution.
C-----

    do i = 1,n
        m = index(i)
        sum = b(m)
        b(m) = b(i)
        if ( ii .ne. 0 ) then
            do j = ii,i-1
                sum = sum - a(i,j) * b(j)
            end do
        else if ( sum .ne. 0.0 ) then
            ii = i
        end if
        b(i) = sum
    end do

C-----
C Do the back substitution.
C-----

    do i = n,1,-1
        sum = b(i)
        if ( i .lt. n ) then
            do j = i+1,n
                sum = sum - a(i,j) * b(j)
            end do
        end if
        b(i) = sum / a(i,i)
    end do

    return
end

C=====
C=====
C Subroutine to initialize an arbitrary array
C=====
C=====

    subroutine zero_array(m,n,a)

    include 'ABA_PARAM.INC'

    dimension a(m,n)

    do i = 1,m
        do j = 1,n
            a(i,j) = 0.
        end do
    end do

```

```

        end do
    end do

    return
end

C=====
C=====
c Subroutine to initialize an arbitrary vector
C=====
C=====
    subroutine zero_vector(m,a)

        include 'ABA_PARAM.INC'

        dimension a(m)

        do i = 1,m
            a(i) = 0.
        end do

        return
    end

C=====
C=====
C=====
C=====

```

Chapter 5

Atomistic Simulations of Nanocrystal Deformation

Principal Authors: Garritt J. Tucker, David L. McDowell and Jonathan A. Zimmerman

5.1 Atomic-scale Deformation Kinematics for Bicrystal Grain Boundaries under Shear Loading

This research presented in this section utilizes the method for calculating an atomic-scale deformation gradient within the framework of atomistic simulations (described in detail in Chapter 2) to examine bicrystal grain boundaries subjected to shear loading. Here, we calculate the deformation gradient, its associated rotation tensor, and estimates of lattice curvature and vorticity for thin equilibrated bicrystal geometries deformed at low temperature. These simulations reveal pronounced deformation fields that exist in small regions surrounding the grain boundary, and demonstrate the influence of interfacial structure on mechanical behavior for the thin models investigated. It is shown that significant differences in deformation mechanisms exist for different grain boundary structures and these mechanisms are responsible for varying lattice curvature and vorticity values. Our results are also examined with regard to their consistency with the continuum mechanical concept of deformation gradient, which is known to have a zero curl for compatible deformations. The utility of this research is apparent through its ability to link atomistic simulation results with continuum mechanics over various volumes of interest.

5.1.1 Motivation

Nanostructured materials have shown potential improvements in numerous engineering applications; however, insight into deformation mechanisms governing their enhanced mechanical behavior and eventual failure is still limited [161, 242]. As material grain size is reduced to this scale, intercrystalline regions (e.g. grain boundaries and triple junctions) become more influential on material behavior owing to an increase in percentage of atoms located at or near these regions [189, 250]. Recently, research results have supported the idea that deformation accommodation mechanisms change as grain size is reduced, and the breakdown of the classical Hall-Petch relationship describing the connection between grain size and strength [39, 199, 206]. This research

suggests that intercrystalline atomic activities begin to control the onset of nanoscale plasticity in these materials, and that grain boundaries and triple junctions become suspect for the localization of inelastic deformation mechanisms. It is important to remember that while the origins of these events occur at atomic length scales, material behavior is ultimately realized at the macroscopic level. Accordingly, recent modeling efforts have focused on bridging both length and time scales to understand the influence of structural features on material plasticity. However, there commonly seems to be an inherent disconnect in larger-scale models from the underlying behavior of these nanoscale deformation mechanisms. Thus, it is necessary to compliment such large-scale models with nanoscale information such as insight into various inelastic deformation mechanisms from atomistic simulations. The eventual outcome of such activities could lead to improved modeling methods for understanding nanoscale feature influence on macroscale behavior, and the implementation of fracture/fatigue resistant features into current engineering materials.

In this section, we present research that concerns implementing continuum mechanical concepts within an atomistic formulation. Additionally, both 2D and 3D bicrystalline structures will be used to analyze the shear deformation response in terms of these continuum mechanical metrics and look at the production of various deformation fields in regions at or near each grain boundary. It will be shown that there is a direct correlation between atomic grain boundary structure and shear deformation mechanism in each structure, and that each mechanism leads to a unique deformation field that will then be analyzed using the continuum metrics.

5.1.2 Research Summary

5.1.2.1 Background

Continuum mechanical concepts such as the deformation gradient \mathbf{F} , rotation tensor (\mathbf{R}), velocity gradient (\mathbf{L}), and vorticity (\mathbf{W}) have been formulated within an atomistic framework and utilized for investigating the shear deformation behavior of bicrystalline structures of 2D and thin 3D nature. Chapter 2 has provided a method to compute \mathbf{F} in an atomistic framework using the interatomic spacing of an atom (α) and its nearest neighbor (β) to estimate atomic strain.

$$\mathbf{F} = \frac{\partial \mathbf{x}}{\partial \mathbf{X}} \quad (5.1)$$

$$x_i^{\alpha\beta} = F_{il} X_l^{\alpha\beta} \quad (5.2)$$

Then by minimizing the least squares summation with respect to \mathbf{F} and over all nearest neighbors, an appropriate value for \mathbf{F} is obtained for a particular atom α as shown below

$$F_{il}^{\alpha} = \omega_{iM}^{\alpha} (\eta^{\alpha})_{MI}^{-1} \quad (5.3)$$

where both ω and η are defined in Chapter 2. This formulation provides an atomistic definition of the deformation gradient defined for each atom α based on the nearest neighbor list from the reference configuration. Additional continuum mechanical concepts as previously mentioned can also be formulated within an atomistic framework based on this description and associated definitions.

5.1.2.2 Computational Setup

Both two-dimensional and thin three-dimensional bicrystals were generated containing a symmetric tilt grain boundary located at the vertical center of the simulation domain with the boundary plane normal in the vertical direction. Periodic boundary conditions were employed in directions parallel to the grain boundary, and constrained free surfaces were enforced in the vertical direction. A conjugate gradient energy minimization method in LAMMPS [187] was used to obtain the initial grain boundary structure with an energy criteria of 10^{-25} , and all grain boundaries were then equilibrated for 10 picoseconds before undergoing shear deformation at 10 K consistent with the NVE ensemble.

In the 2D simulations, an interatomic pair potential based on a lattice parameter (the nearest neighbor distance in a 2D triangular lattice) of 4.08\AA was used. The 2D potential is a shifted Lennard-Jones potential so that both the potential energy and its first derivative are zero at the cutoff radius. Thus, it is also truncated so that the energy is zero at any radius greater than the cutoff value. The key potential parameters are the cutoff radius (7.6364\AA) which includes the first and second neighbor shells only, the cohesive energy (-3.93 eV), mass (196.97 amu), σ (3.63638\AA) and ϵ (1.5726 eV). While the values of lattice parameter, cohesive energy and atomic mass are identical to those for gold, this simulated material is **not** gold as both the potential and the material are truly two-dimensional. An Embedded Atom Method (EAM) potential for copper [167] was used in the 3D simulations.

In all simulations, atoms located within a distance of at least three times the potential cutoff distance of both the top and bottom surfaces were 'frozen' and held fixed in their perfect lattice positions throughout the simulation. Shear deformation was applied to each structure by holding the bottom group completely fixed from movement in all directions, and applying a constant velocity in the shear direction to the top region. Due to inherent high strain rate conditions of molecular dynamics (MD), a ramped velocity field was also imposed on all atoms between the two rigid regions. This condition prevents possible shock wave generation in the structure from the prescribed velocity of the top atomic region. The prescribed velocity given to the top region corresponds to an approximate strain rate of 10^8s^{-1} .

5.1.2.3 Mathematical Formulation

In addition to \mathbf{F} , continuum measures of \mathbf{R} , \mathbf{L} , and \mathbf{W} were also formulated within an atomistic framework. A summary of the mathematical formulation of these measures within atomistics is provided.

Once \mathbf{F} is known based on the nearest neighbor list, its multiplicative decomposition into a rotation tensor \mathbf{R} and stretch tensor \mathbf{U} is straightforward.

$$\mathbf{F} = \mathbf{R}\mathbf{U} \quad (5.4)$$

From there, \mathbf{R} is separated into both symmetric and skew-symmetric components.

$$\mathbf{R} = \mathbf{R}_{\text{sym}} + \mathbf{R}_{\text{skew}} \quad (5.5)$$

Where R_{skew} is defined by

$$\mathbf{R}_{skew} = \frac{1}{2}(\mathbf{R} - \mathbf{R}^T) \quad (5.6)$$

As with any skew-symmetric tensor, it can be defined by a single vector. For R_{skew} this vector is the microrotation vector ϕ

$$\phi_k = -\frac{1}{2}\epsilon_{ijk}(R_{skew})_{ij} \quad (5.7)$$

where ϵ_{ijk} is the permutation symbol.

Another important continuum concept to formulate within this framework is the vorticity vector, ω , which is derived from the calculation of the velocity gradient, \mathbf{L} . In our formulation, we use the instantaneous atomic velocities output from LAMMPS to approximate \mathbf{L} .

$$\mathbf{L} = \frac{\partial \mathbf{v}}{\partial \mathbf{x}} \quad (5.8)$$

Please note that both the atomic velocities and positions to calculate \mathbf{L} are from the current configuration, while the neighbor list remains from the undeformed configuration.

From this description, an atomic definition of \mathbf{L} can be formulated in a similar manner to the formulation of \mathbf{F} for each individual atom, α . Beginning with equation (5.8), and forming a summation over the squared differences, we get

$$C_i^\alpha = \sum_{\beta=1}^n (v_i^{\alpha\beta} - L_{ik}^\alpha x_k^{\alpha\beta})^2 \quad (5.9)$$

where $v_i^{\alpha\beta}$ represents the relative atomic velocity between atom α and its neighbor β , and then minimize \mathbf{C}^α by some choice of \mathbf{L}^α .

$$\sum_{\beta=1}^n (v_i^{\alpha\beta} x_l^{\alpha\beta} - L_{ik}^\alpha x_k^{\alpha\beta} x_l^{\alpha\beta}) = 0 \quad (5.10)$$

This equation is rearranged and simplified to become

$$\rho_{il}^\alpha = L_{ik}^\alpha \tau_{kl}^\alpha \quad (5.11)$$

where

$$\rho_{il}^\alpha = \sum_{\beta=1}^n v_i^{\alpha\beta} x_l^{\alpha\beta} \quad (5.12)$$

and

$$\tau_{kl}^\alpha = \sum_{\beta=1}^n x_k^{\alpha\beta} x_l^{\alpha\beta} \quad (5.13)$$

Once these substitutions are made, equation (5.11) is rewritten as

$$L_{ik}^\alpha = \rho_{il}^\alpha (\tau_{lk}^\alpha)^{-1} \quad (5.14)$$

which is now the atomic formulation of the velocity gradient for each atom α depending on all nearest neighbors β .

The vorticity or spin tensor (\mathbf{W}) is the skew-symmetric component of \mathbf{L} and is derived from the additive decomposition of \mathbf{L} .

$$\mathbf{L} = \mathbf{D} + \mathbf{W} \quad (5.15)$$

Where \mathbf{D} defines the rate of deformation tensor and \mathbf{W} is the spin or vorticity tensor. The calculation of \mathbf{W} from \mathbf{L} is identical to the method used to determine \mathbf{R}_{skew} ,

$$\mathbf{W} = \frac{1}{2}(\mathbf{L} - \mathbf{L}^T) \quad (5.16)$$

Then the calculation of ω from \mathbf{W} is as follows

$$\omega_k = -\frac{1}{2}\epsilon_{ijk}W_{ij} \quad (5.17)$$

5.1.2.4 Grain Boundary Structures

As previously mentioned, the 2D grain boundary structures were generated with a symmetric tilt grain boundary located at the vertical center of the simulation domain. Each lattice (upper and lower) was rotated around a common tilt axis by some degree, $\frac{\theta}{2}$, from a chosen zero degree direction. Although this rotation angle was identical for both lattices, the rotation of the upper lattice was in the opposite direction of the lower lattice from the zero degree direction, thereby creating a total misorientation angle of θ between the upper and lower lattices. We take a moment to clarify the difference between misorientation and disorientation angles, because in many continuum models the disorientation angle is an input variable for grain boundary description. As mentioned, the misorientation angle, θ , is described as the total angle difference between two lattices from a common zero degree direction, or common grain boundary period direction. Disorientation angle, Ψ , is described as the lowest angle difference between the two lattices composing the grain boundary. In other words, imagine a collection of symmetric tilt grain boundaries of varying misorientation angles around a common axis, and this collection of boundaries is symmetric with respect to 180° misorientation. A grain boundary with a 170° misorientation angle in this collection with respect to some zero degree direction will be defined as having a 10° disorientation angle, $\Psi=10^\circ$.

For this research, we will be investigating the shear deformation behavior of three 2D grain boundary structures with a common tilt axis and different Ψ values, and one thin 3D copper symmetric tilt grain boundary. Each of the 2D grain boundary structures is approximately 300Å² in total area, and the 3D boundary is 300Å x 300Å x 5Å. The three different Ψ values for the 2D case are 9.4°, 15.2°, and 27.8°. These three different disorientation angle values were chosen because each boundary structure displayed a different deformation mechanism under applied shear. The three different mechanisms are grain boundary migration, sliding, and dissociation respectively. Images of the initial grain boundary structures after energy minimization are shown below in Figures 5.1-5.3 and are colored with respect to potential energy. For the 3D case, the $\Sigma 9$ (221) $\theta=141.1^\circ$ symmetric tilt grain boundary was chosen due to its high free volume content and ease of calculation. The initial grain boundary structure is shown in Figure 5.4 and is also colored with respect to potential energy. The misorientation tilt axis is $\langle 110 \rangle$ for the 3D system.

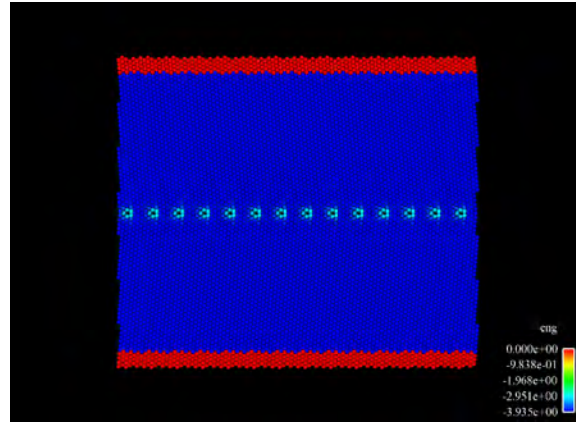


Figure 5.1. Initial 2D grain boundary structure of a symmetric tilt grain boundary with $\Psi = 9.4^\circ$. Notice the small isolated defect structures composing the grain boundary that accommodate the lattice mismatch between the upper and lower grains.

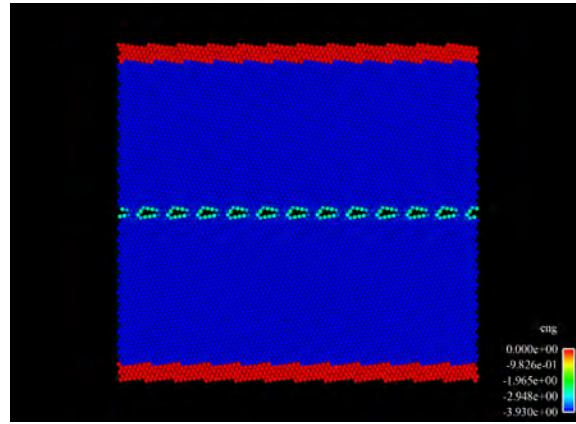


Figure 5.2. Initial 2D grain boundary structure of a symmetric tilt grain boundary with $\Psi = 15.2^\circ$. Notice that as the disorientation angle increases, the defect structures that compose the boundary increases.

5.1.2.5 Two-Dimensional Shear Deformation

After the initial grain boundary structures were obtained, two atomic regions were isolated from the remaining structure and designated as rigid blocks of atoms. These regions are composed of all atoms located within 15\AA of both the vertical (x_2) top and bottom of the structure and are fixed in their equilibrium positions. The bottom group is held fixed to movement and the top group is given a constant velocity in the horizontal (x_1) direction to cause shear in the structure. All atoms located between these two regions experience an additional ramped velocity value to the present thermal

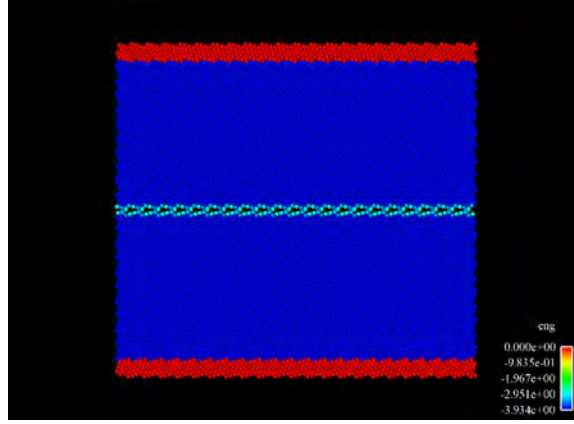


Figure 5.3. Initial 2D grain boundary structure of a symmetric tilt grain boundary with $\Psi = 27.8^\circ$. Notice that the entire grain boundary is composed of repeating 2D atomic structural units to accommodate the lattice mismatch.

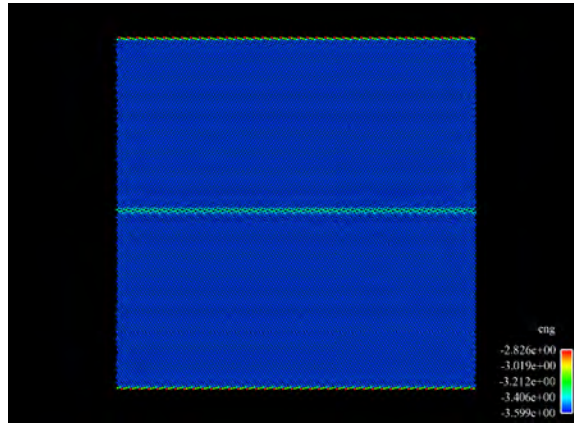


Figure 5.4. Initial thin 3D structure of a $\langle 110 \rangle$ symmetric tilt grain boundary, Cu (221) $\theta=141.1^\circ$.

vibrations. The ramped velocity value varies linearly depending on the x_2 position of each atom between the rigid regions. Since the bottom block is held fixed, atoms located in surrounding layers are given the lowest ramped velocity values and atoms near the top rigid block experience ramped velocities approximately identical to that given to the top block of atoms. A 2D representation of this setup is shown in Figure 5.5.

The applied velocity is consistent with an approximate 10^8 s^{-1} strain rate for each structure investigated. After approximately 5% strain of each boundary, the structures were analyzed with regard to the aforementioned continuum metrics. Figures 5.6-5.8 show the resulting 2D structures colored with potential energy in order of increasing disorientation angle.

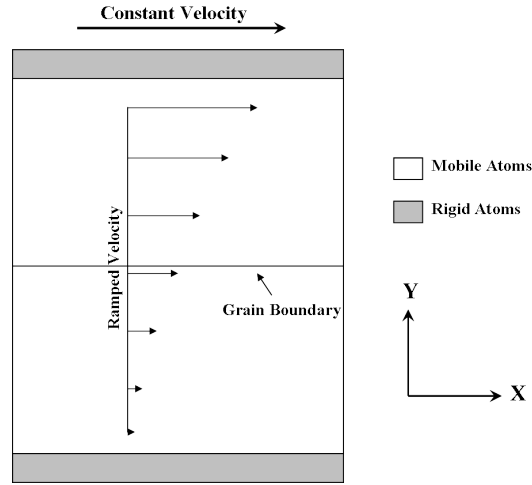


Figure 5.5. 2D schematic of grain boundary structure and applied shear deformation.

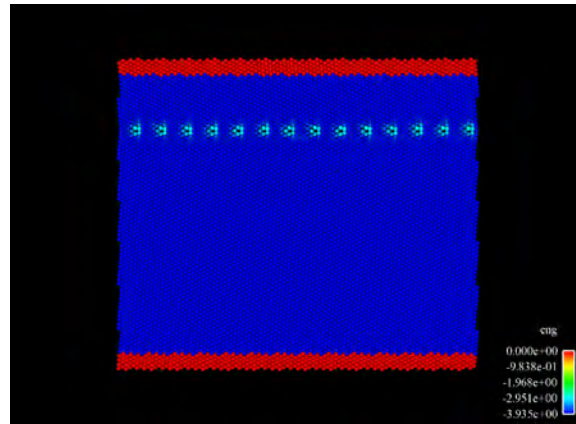


Figure 5.6. After 5% strain, the grain boundary has migrated upward approximately 20 atomic layers away from its original location.

It is obvious from Figures 5.6-5.8 that each boundary displays a different deformation mechanism. In order of increasing disorientation angle, the mechanisms displayed are grain boundary migration, sliding, and dissociation. This is important because it shows that there is an inherent connection between grain boundary structure and deformation behavior under shear. In other words, the atomic structure of each grain boundary differs, and this difference in structure leads to different observed deformation accommodation mechanisms under shear. This does not imply that each grain boundary structure within this misorientation range will display a unique deformation mechanism, but that atomic grain boundary structure influences its mechanical response. It is possible that other shear deformation mechanisms exist within this misorientation range; however,

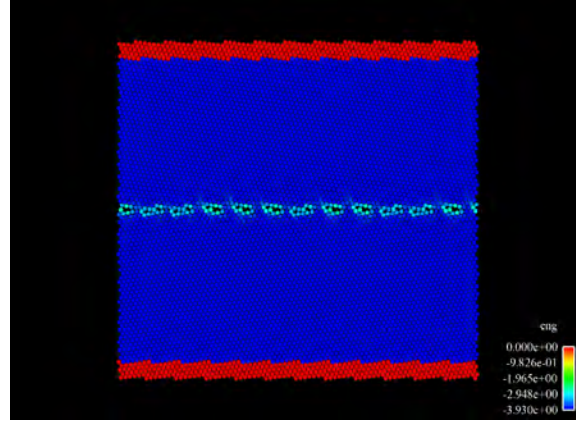


Figure 5.7. After 5% strain, small structural changes have occurred and discrete events of grain boundary sliding have been observed.

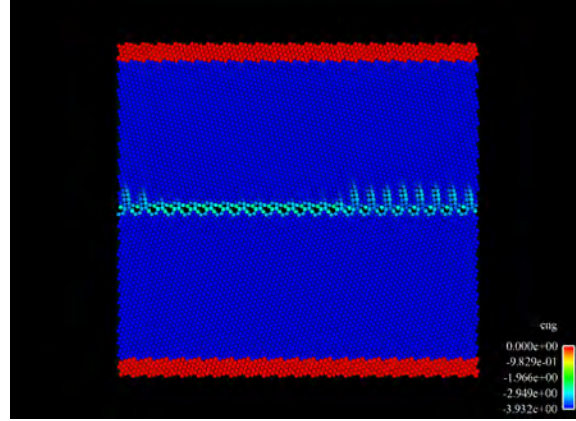


Figure 5.8. After 5% strain, localized dissociation events are observed and associated with boundary structural changes.

it is more likely that additional boundaries within this misorientation range would display some variational combination of the aforementioned mechanisms.

To further investigate the shear deformation response of these grain boundary structures, continuum mechanical concepts such as \mathbf{F} , \mathbf{R} , \mathbf{L} , and \mathbf{W} are employed. First, we will look at the grain boundary migration mechanism with regard to each metric.

The components of the deformation gradient provide information about the influence of a specific direction on atomic deformation. The migration planes are highlighted in Figure 5.9 (by their high value of F_{11}) because they undergo a different deformation than the lattice regions located between the migration planes (inter-regions) with regard to the x_1 direction. In Figure 5.10,

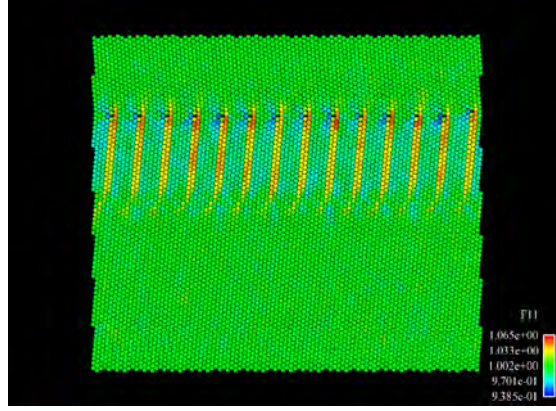


Figure 5.9. The F_{11} component for the grain boundary migration mechanism. Notice the difference in deformation between the migration planes and the lattice regions located between the migration planes.

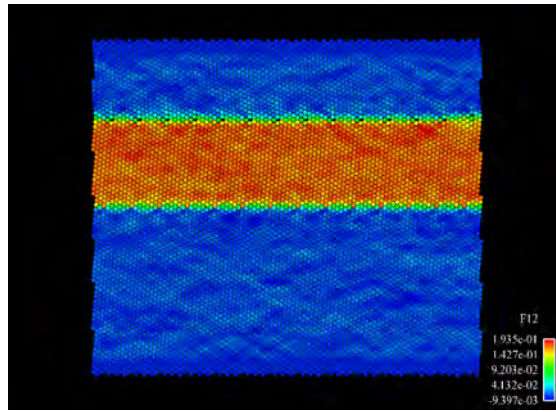


Figure 5.10. The F_{12} component shows a relatively uniform deformation field under grain boundary migration with regard to the x_2 direction.

a relatively uniform deformation field is shown that highlights the lattice region that underwent deformation as a consequence of the migration with respect to x_2 . This region is without large contrasts because there is very little difference in the dependence of the x_1 component of atomic position in the deformed configuration on the x_2 direction in the initial configuration. Figure 5.11 displays rotation information about the migration mechanism. Atoms located on the migration path experience a different rotation than inter-region atoms. One thing to note is that as the grain boundary migrates, the orientation of the upper lattice region traversed by the migrating boundary rotates to match the lower lattice orientation.

In addition to the valuable information obtained from analyzing the deformation fields with

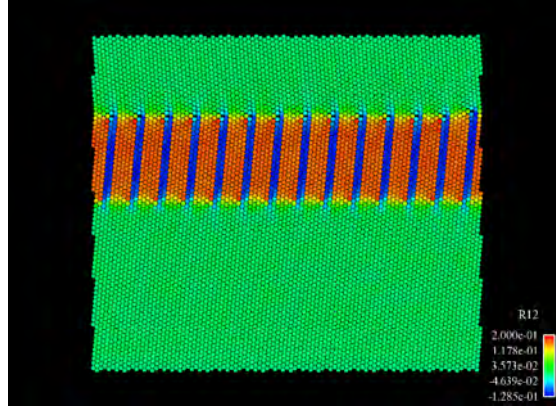


Figure 5.11. The R_{12} component for the migration mechanism displays rotation behavior for atoms located in both the migration planes and between.

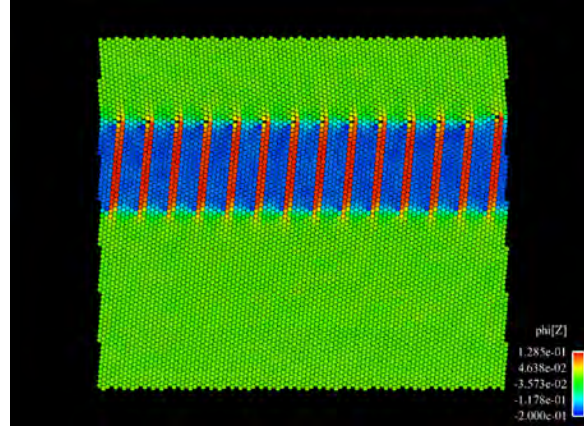


Figure 5.12. ϕ_3 for the migration mechanism. Notice the sign difference between the atoms located around the migration plane and those atoms in the inter-regions.

regard to \mathbf{F} and \mathbf{R} , further insight can be provided from specific descriptions of ϕ and ω within our atomistic framework to estimate lattice curvature and vorticity. It is this information that is useful for larger scale models.

Figures 5.12 through 5.14 show ϕ_3 , $\phi_{3,1}$ and $\phi_{3,2}$ for the migration mechanism. It can be seen that ϕ can be extremely useful for analyzing atomistic data. The implementation of \mathbf{R} and its derived parameter ϕ provide insight into the extent of atomic rotation in localized regions. For example, consider the grain boundary migration case shown in Figure 5.12. We have already discussed that atoms located around the migration planes undergo a different deformation path than those atoms located in inter-regions. ϕ further provides insight into the rotation of their

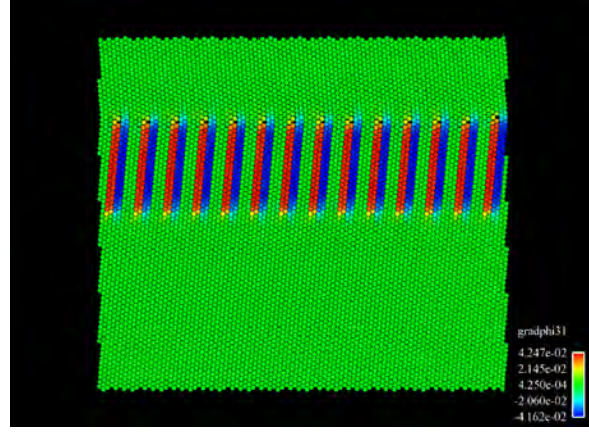


Figure 5.13. The gradient of ϕ_3 with respect to the x_1 direction.

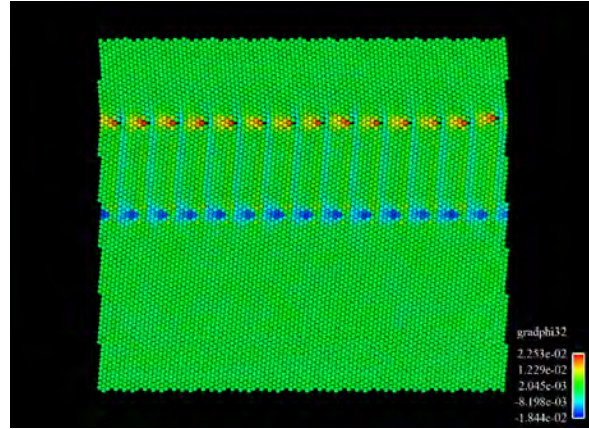


Figure 5.14. The gradient of ϕ_3 with respect to the x_2 direction.

deformation path. From this description, it is clear that the rotation of migration plane atoms is different from that of inter-region atoms not only in magnitude but also in direction. Additionally, it is clear that a large collective atomic rotation, but not small isolated rotation fields, is present. All inter-region atoms possess an almost identical value of ϕ_3 (near -0.2), as do migration plane atoms (near 0.13).

The grain boundary sliding mechanism produces negligible deformation in the surrounding lattice regions as shown in Figures 5.7 and 5.15. The observed deformation for this mechanism is highly localized to the boundary and does not generate considerable deformation fields outside of the boundary. Therefore, explicit consideration of this mechanism and its continuum mechanical treatment are ignored in this paper.

Next, the grain boundary dissociation mechanism is analyzed using the continuum metrics.

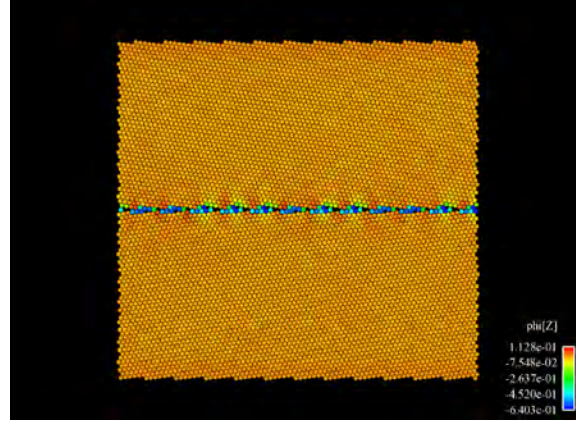


Figure 5.15. ϕ_3 for the grain boundary sliding mechanism. Notice that there is little rotation extending out away from the boundary as sliding occurs.

Similarities and differences between the results of this mechanism and the migration mechanism follow.

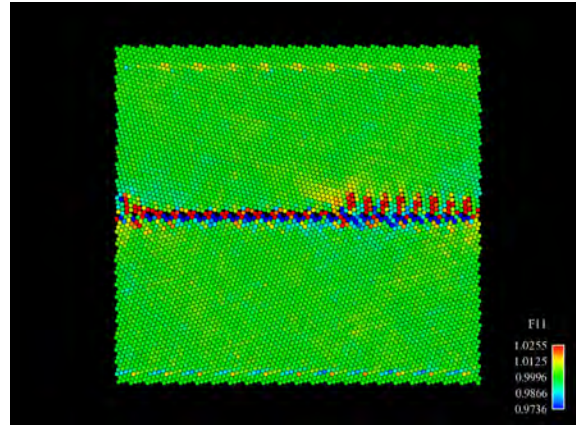


Figure 5.16. The F_{11} component is shown for grain boundary dissociation. This picture highlights the localized nature of the grain boundary deformation field.

Confined deformation is observed in the grain boundary dissociation mechanism. In Figure 5.16, the F_{11} component shows the dependence of x_1 deformation on the x_1 direction. Most of the obvious deformation in the x_1 direction occurs within the grain boundary plane as sliding. However, there is small deformation for atoms located near the dissociated planes extending out away from the boundary. In Figure 5.17, the F_{12} component shows the x_1 deformation dependence on x_2 position. Atoms located within the dissociated region experience the greatest effect.

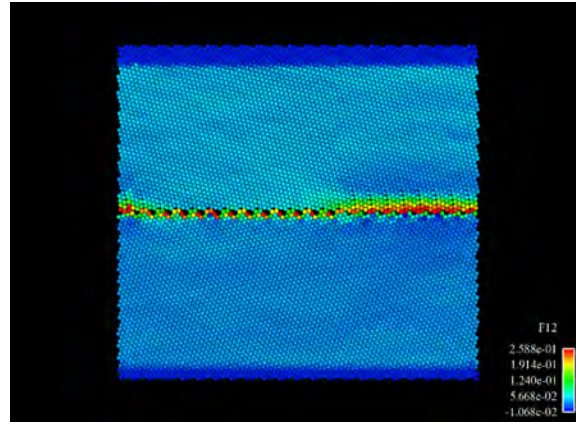


Figure 5.17. The F_{12} component is shown for grain boundary dissociation. The only significant pattern observed in this image is within the dissociation region.

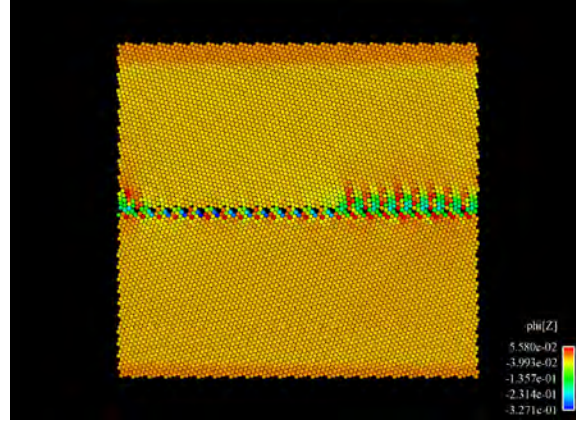


Figure 5.18. ϕ_3 for the dissociation mechanism. Notice the localized rotation values occurring in regions surrounding the slipped planes. Atoms not located in the grain boundary or in these regions experience negligible microrotation.

As the dissociation occurs, atoms located on neighboring atomic planes to the slip plane possess some small component of rotation in their neighboring atoms. It is obvious from Figure 5.18 that the direction of the microrotation component is different on either side of the slip plane, indicating that an atom's nearest neighbors undergo a small simultaneous rotation as dissociation occurs. Figures 5.19 and 5.20 display the x_1 and x_2 components of the gradient of ϕ_3 , respectively.

This mechanism is quite different from the migration mechanism because the atomic deformation accommodation is mainly due to sliding events between atoms with small atomic rotations around the slipped planes, and in the migration mechanism it is mainly due to large collective

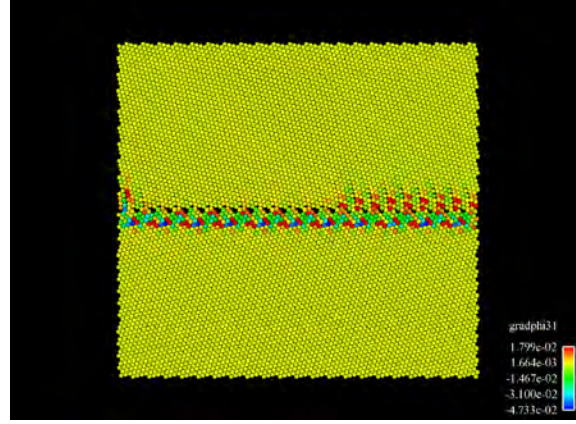


Figure 5.19. The gradient of ϕ_3 with respect to the x_1 direction.

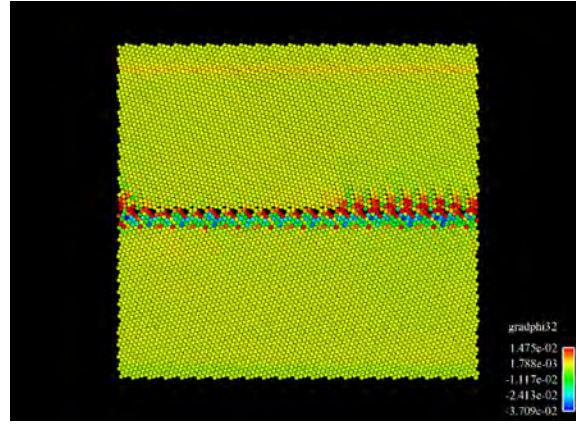


Figure 5.20. The gradient of ϕ_3 with respect to the x_2 direction.

atomic rotation. The dissociations that arise in this case are localized slipping events occurring between two planes with small rotation fields between the slip planes. This mechanism is unlike the large atomic region rotations observed in Figure 5.12 as the grain boundary migrates vertically, which accommodates the mismatch between the two grain orientations.

The calculation of \mathbf{L} from the instantaneous atomic velocities can be decomposed into symmetric and skew-symmetric components. From the skew-symmetric component an axial vector is defined to be representative of vorticity. In particular, the third component of this axial vector provides an estimate of the atomic vorticity. Figures 5.21 and 5.22 show ω_3 for both the migration and dissociation mechanisms.

One of the most obvious features of these figures is the presence of noise in the lattices. We think that this is a natural consequence of the proposed method for determining \mathbf{L} from the instantaneous atomic velocities. This point will be further elaborated on in the final section of this report

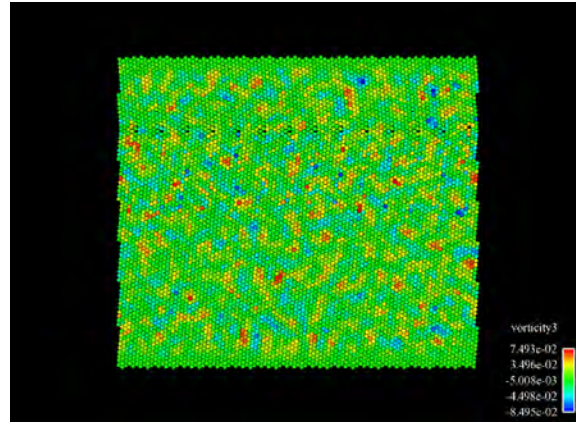


Figure 5.21. ω_3 under grain boundary migration. There are no obvious vorticity patterns or regions of significant interest under boundary migration. Notice the existence of lattice noise in this formulation of vorticity using instantaneous atomic velocity.

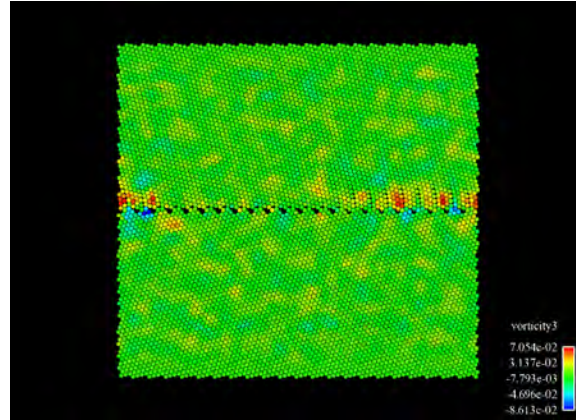


Figure 5.22. ω_3 under grain boundary dissociation. Small localized vorticity fields appear in neighborhoods surrounding the dissociated planes.

concerning future work. In the migration example (Figure 5.21), there are no defining vorticity fields at 5% strain, and the dissociation example (Figure 5.22) displays only small localized vorticity fields near the slip planes. This indicates that during grain boundary dissociation, only atoms located near dissociated planes experience some small vorticity during deformation.

5.1.2.6 Three-Dimensional Shear Deformation

A thin 3D bicrystalline structure containing a $\Sigma 9$ (221) symmetric tilt grain boundary with a misorientation angle of $\theta=109.5^\circ$ was used to investigate the 3D shear deformation. This grain boundary structure is fairly unique due to its atomic composition and presence of high free volume associated with the E structural unit [218, 239]. These qualities have previously been noted to trigger significant atomic shuffling events providing a high susceptibility for this boundary to sliding under shear [241, 203]. As revealed by the centrosymmetry parameter shown in Figure 5.23, a partial dislocation is nucleated at the boundary and emitted into the lower lattice along with atomic shuffling within the boundary at an approximate strain of 3%.

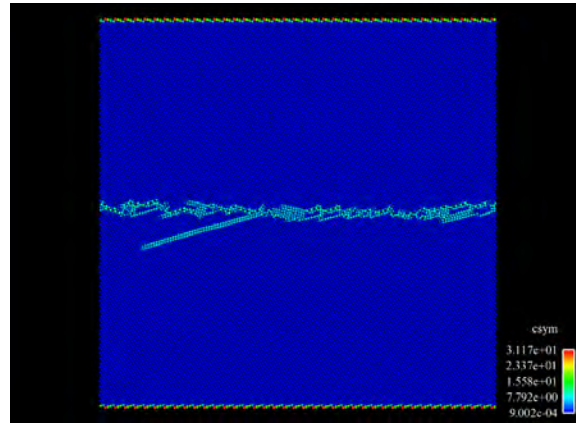


Figure 5.23. The shear deformation of the (221) Cu boundary at about 3% strain colored with centrosymmetry. Notice the partial dislocation nucleation from the boundary into the lower lattice accompanying numerous atomic shuffling events within the boundary.

As in the 2D cases, \mathbf{F} , \mathbf{R} , ϕ , and ω can provide a deeper insight into atomic phenomena during the partial dislocation nucleation process. F_{12} and R_{12} are shown in Figures 5.24 and 5.25, and ϕ_3 and ω_3 in Figures 5.26 and 5.27.

While comparing the shear deformation of this boundary to that observed in the 2D cases, there are a few points to note. Because this boundary is 3D in nature and of approximately the same area perpendicular to the tilt axis, there are many more atoms to consider in the structure. In addition, atomic interactions in all three dimensions are considered during the simulation, so there is an influence from the third dimension on deformation response. A different deformation mechanism is observed in this case, a single partial dislocation is nucleated and emitted from the grain boundary into the lower lattice. This is seen in all images for the 3D case. In particular, the stacking fault left behind the leading partial dislocation after emission is obvious in Figure 5.23. Accompanying the emission are many atomic shuffling events within the boundary. As noted previously, this occurs due to the atomic structural makeup of the boundary being composed entirely of E structural units [203].

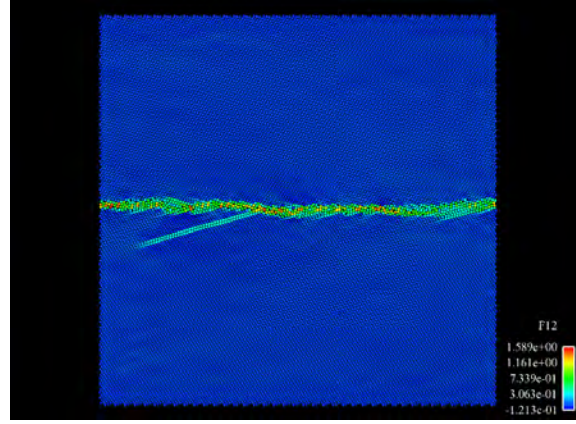


Figure 5.24. F_{12} shows that all atoms located within the boundary region have experienced deformation at 3% strain. However, the dependence of the deformation on the vertical direction is not uniform for these atoms. Notice that there is no deformation reaching into either lattice other than the partial dislocation.

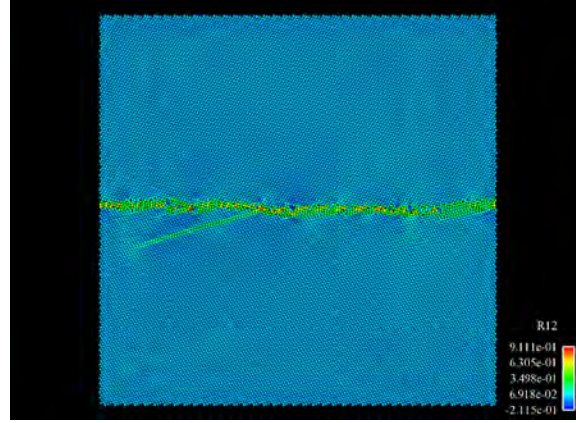


Figure 5.25. R_{12} shows similar results to F_{12} . There is non-uniform dependence of the rotation component on the vertical direction, and there is little rotation extending out beyond the boundary region.

Figures 5.24-5.27 display some of the important continuum mechanical concepts applied within our atomistic framework for this grain boundary structure. Particularly, Figures 5.24 and 5.25 show F_{12} and R_{12} respectively. These figures point out that besides the partial dislocation, all other atomic deformation is confined to the grain boundary region and tends to be non-uniform. Figures 5.26 and 5.27 are images of ϕ_3 and of ω_3 , once again showing lattice curvature and vorticity. We see that lattice curvature exists in and around the previously noted deformation regions, and that there is little atomic curvature extending out beyond these regions. The vorticity is also con-

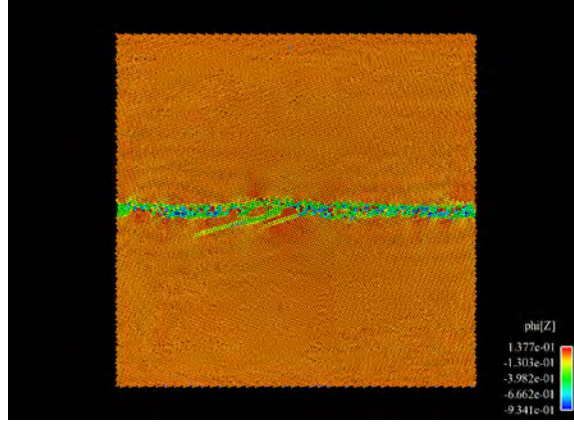


Figure 5.26. ϕ_3 gives information on atomic lattice curvature, and in this case the curvature is mostly constrained to the boundary region. Small localized regions of lattice curvature exist in areas directly neighboring the nucleation regions.

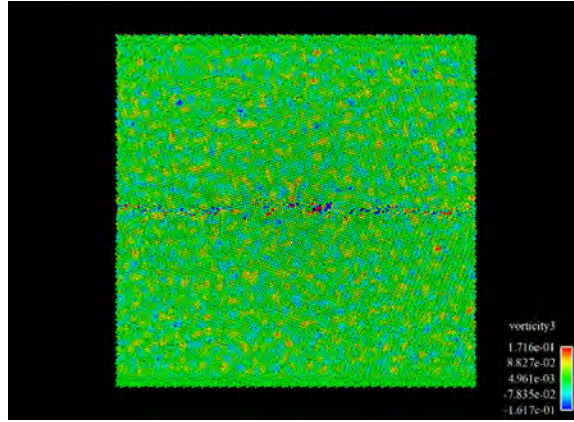


Figure 5.27. ω_3 for shear deformation of the 3D system. Notice the lack of obvious vorticity outside of the grain boundary, and the presence of noise still in the lattice.

finned to the grain boundary, indicating the lack of any significant atomic vorticity accompanying the partial emission into the lattice.

5.1.3 Conclusions

This work has shown that continuum mechanical metrics such as \mathbf{R} , \mathbf{L} , ϕ and ω can be computed using an atomistic framework based on the description of \mathbf{F} as provided in Chapter 2. Addition-

ally, the implementation of these descriptions can provide unique and fundamental insight into atomic phenomena occurring at the origins of nanoscale plasticity events under applied shear in both 2D and thin 3D bicrystalline structures. Examples of three different deformation mechanisms (grain boundary migration, sliding and dissociation) associated with three different grain boundary structures in 2D were shown and explained in the context of these continuum metrics. Each metric provided distinct information about atomic behavior during each mechanism. It was also shown that estimates of lattice curvature and vorticity can be obtained from these simulations. By applying these continuum mechanical concepts, additional insight can be obtained into these mechanisms from an atomistic point of view. Various atomic behaviors were seen in the context of each continuum metric during shear deformation, and information about the extent of deformation away from the boundary was provided.

In 3D, the shear deformation response of the $\Sigma 9$ (221) symmetric tilt grain boundary was analyzed with regard to these continuum mechanical concepts. A combination of partial dislocation emission and atomic shuffling was observed in these simulations accompanying grain boundary sliding, and useful insight of these mechanisms and subsequent deformation fields was obtained via the aforementioned metrics. It was also noted that, up to the strain investigated at the simulated strain rate, negligible deformation occurred away from the grain boundary itself. It is possible that more complex deformation behavior would be observed at different strain rates and in simulations considering higher strain levels. Therefore, we wish to explore these ideas as outlined in the following section. In addition, we feel that possible improvement in the vorticity calculations can be achieved by altering the formulation of \mathbf{L} .

5.1.4 Future Work

5.1.4.1 \mathbf{L} Formulation

It was mentioned in section 5.1.2.3 that due to the formulation of \mathbf{L} , which uses instantaneous atomic velocities directly to compute \mathbf{L} , inherent noise is observed in lattice regions surrounding the grain boundaries (Figures 5.21 and 5.22). Therefore, we present two additional methods for determining \mathbf{L} that we wish to explore. However, before these two methods are outlined, a brief overview of \mathbf{L} is required.

The present method for determining \mathbf{L} is based on instantaneous atomic velocities with regard to spatial positions according to the following equation.

$$\mathbf{L} = \frac{\partial \mathbf{v}}{\partial \mathbf{x}} \quad (5.18)$$

In this equation, \mathbf{v} represents the current atomic velocity and \mathbf{x} is the current or spatial atomic position. \mathbf{L} can also be defined by the following:

$$\mathbf{L} = \dot{\mathbf{F}}\mathbf{F}^{-1} \quad (5.19)$$

Since \mathbf{F} is determined at each timestep throughout the simulation, approximating $\dot{\mathbf{F}}$ is possible.

The second method comes from a chain-rule description of \mathbf{L} ,

$$\mathbf{L} = \frac{\partial \mathbf{v}}{\partial \mathbf{x}} = \frac{\partial \mathbf{v}}{\partial \mathbf{X}} \frac{\partial \mathbf{X}}{\partial \mathbf{x}} = \frac{\partial \mathbf{v}}{\partial \mathbf{X}} \mathbf{F}^{-1} \quad (5.20)$$

In this description, the formulation of $\frac{\partial \mathbf{v}}{\partial \mathbf{X}}$ is dependent on the reference atomic positions and \mathbf{F}^{-1} . Within this formulation of \mathbf{L} , a current neighbor list is stored and the calculated velocity gradient measures are dependent on the reference neighbor distances of this list. It is quite possible that one or both methods discussed here could improve the vorticity results shown previously, as the new \mathbf{L} formulation can minimize the effect of thermal vibration.

5.1.4.2 Simulations

An important extension of the current simulations is to implement larger simulation domains and continue the deformations to much larger strains. The effect of lattice size on both 2D and 3D shear simulations is not well understood. It is possible that different deformation phenomena or more complex mechanisms would appear within larger structures. The influence of the rigid atomic regions or periodic grain boundary length on shear deformation behavior is another point to address. Questions regarding these subjects still remain unanswered and will be addressed in our future work.

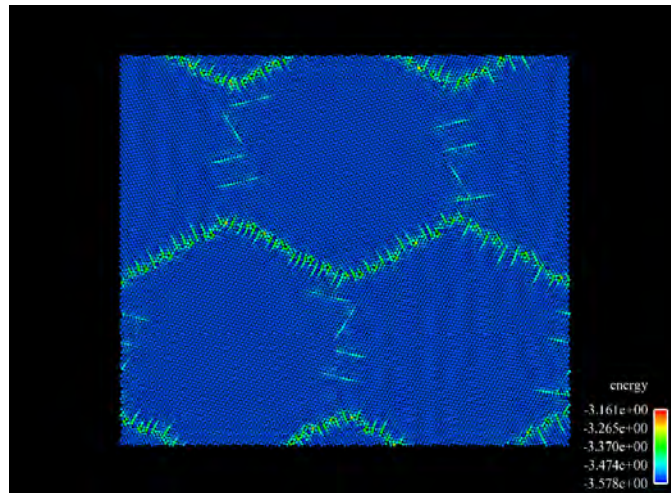


Figure 5.28. Atomic structure of a columnar hexagonal nanocrystalline model colored with energy. This image shows a possible geometry that could be used to investigate the influence of numerous variables such as boundary length, triple junctions, and grain boundary character on the resulting deformation fields outlined in this work.

We would also like to analyze deformation fields in more complex atomic structures. For example, in Figure 5.28 a nanocrystalline hexagonal grain structure is shown colored with respect

to energy. The structure is 3D periodic containing 4 separate grains with different atomic lattice orientations producing tilt boundary structures with a common $\langle 110 \rangle$ tilt axis. The goal would be to apply uniaxial tension to the structure and investigate the evolution of the aforementioned continuum metrics with deformation. Most of the grain boundaries would experience components of both tension and shear stress giving rise to more complex deformation mechanisms than those already investigated in this work. The influence of boundary length, boundary character and distribution, nearby triple junctions, and deformation mechanisms on the mentioned continuum metrics would be of primary interest. Their dependence on these variables would be characterized, and the evolution of such fields could provide valuable insight into collective atomic behavior vital to understanding the structure-property relationships observed in nanocrystalline materials.

5.2 Large deformation of single crystal nickel

We also performed 3D MD simulations of single crystal nickel (modeled with the EAM potential by Foiles *et al.* [75]) subject to uniaxial compression. The purpose of these simulations was two-fold:

- First, we wished to examine the extent of defects created during deformations up to large strains. In this case, ‘large’ denotes strains in excess of 10% and reaching values as high as 40%. It was our goal to visualize simulation results and determine if disclination structures could be identified.
- Second, we wished to use the results of such simulations to assess the usefulness of simulation metrics both developed during the course of this project, *e.g.* lattice curvature, and those developed previously, *e.g.* centrosymmetry parameter [126] and slip vector [258].

The system we analyzed was cubic in shape in its undeformed configuration of dimensions 176 Å on each side and consisted of 500,000 atoms. Compression rates of $10^7/\text{sec}$ and $10^8/\text{sec}$ were applied in one of the cubic directions, with periodic boundary conditions applied in the directions transverse to the loading direction.

5.2.1 Uniaxial compression at a rate of $10^7/\text{sec}$

Figure 5.29 shows the system subjected to a compression rate of $10^7/\text{sec}$ at various amounts of compression with atoms colored according to their value of potential energy. For clarity, only atoms with potential energy higher than a particular value are shown. The loading direction is the horizontal “x” direction shown in the sub-figures. This figure shows several interesting features: First, dislocations (shown in the sub-figures as light-blue curves) are only nucleated at strains higher than 3.7%. Above this strain, dislocation threads or ribbons are created and propagate to various positions along $\{111\}$ slip planes. As compression increases, a complex but structured pattern appears. This pattern becomes hard to discern for strains higher than 8%, but Figure 5.29

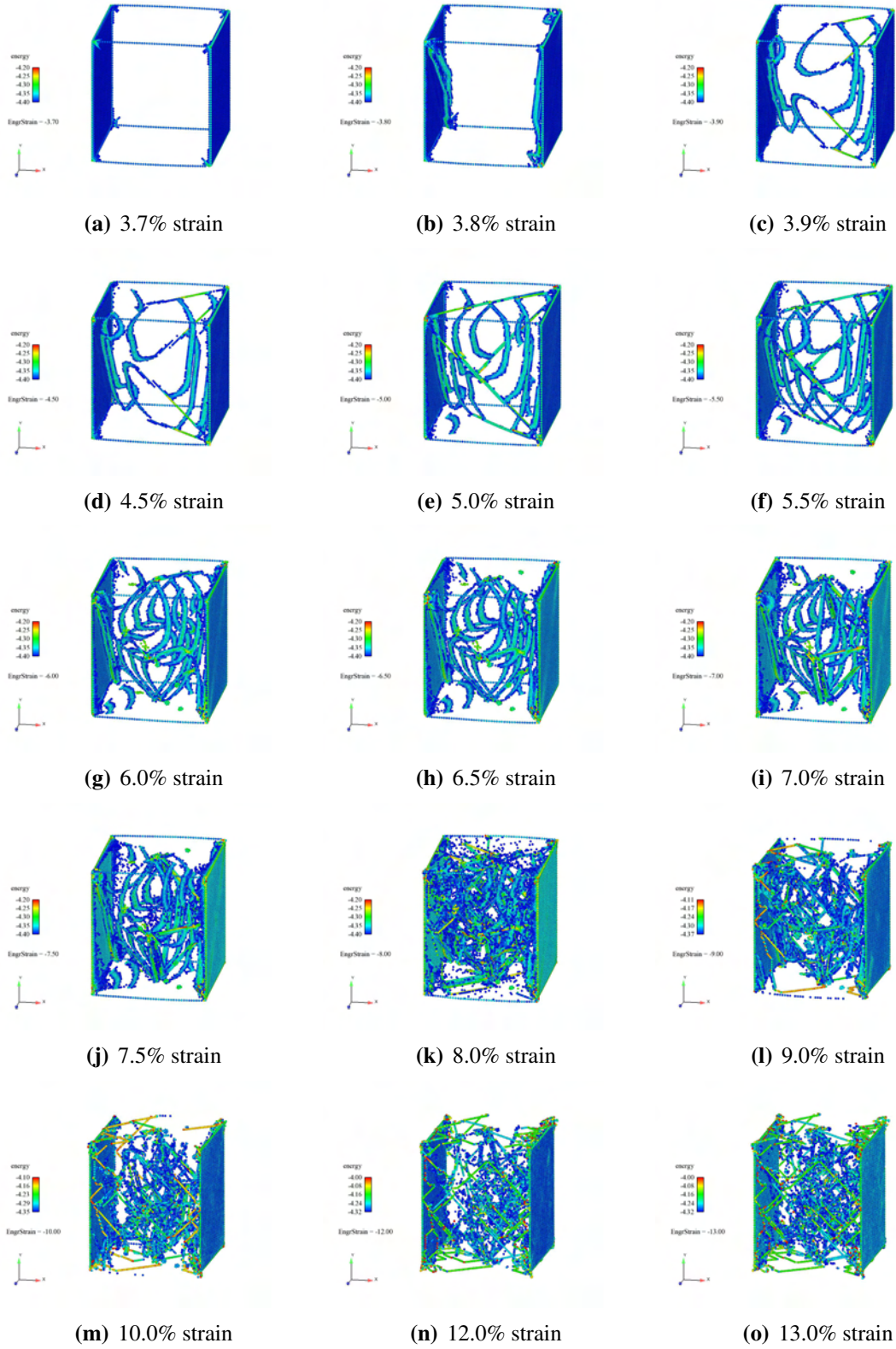


Figure 5.29. Compression of single crystal nickel for $\dot{\epsilon} = 10^7/\text{s}^{-1}$. Atoms colored by potential energy values.

clearly shows an increase in the density of dislocations present as well as an alteration in the pattern that isolates atoms of high potential energy.

Figure 5.30 shows many of the same compression states as shown in Figure 5.29, but has atoms colored according to their value of centrosymmetry parameter. As before, atoms are filtered according to a minimum value of centrosymmetry in order to eliminate many of the atoms not involved with a crystalline defect. This figure shows that the dislocations nucleated at strains higher than 3.7% consist of both partial $\langle 112 \rangle$ -type dislocations and full $\langle 110 \rangle$ -type dislocations. This is evidenced by the large number of green atoms shown on oblique $\{111\}$ planes, indicating that those planes contain stacking faults. The dislocation cores themselves can be identified as light blue and cyan curves that lie on top of the faulted planes. It is observed that as compression increases, a majority of these faults do not dissipate; rather, multiple faults on parallel $\{111\}$ planes are created and intersect one another.

More about the dislocation and defect structures created during compression can be learned by isolating specific levels of compression and examining the full and partial dislocation structures by using both centrosymmetry [126] and slip vector [258]. Both of these quantities are more sensitive to the presence of dislocations, stacking faults and similar crystalline defects than potential energy is. Figures 5.31, 5.32 and 5.33 show the system at compressions of 6%, 9% and 12%, respectively. Figures 5.31(a) and 5.31(b) both show the system with atoms colored by centrosymmetry parameter, albeit with different filtering ranges. This filtering confirms that the pattern observed in Figure 5.29 using potential energy values does indeed identify dislocation cores that lie between stacking fault regions on the same slip planes. Figures 5.31(c) and 5.31(d), which show atoms colored by slip vector, reveal that full dislocations are also present and have left behind isolated regions that should contain perfectly structured crystal (shown in red and orange-red in the two figures). Figures 5.32 and 5.33 show that these structures continue to evolve with increased compression. At 12% compression, many atoms possess very high values of slip vector (higher than the value corresponding to a single, full dislocation, *i.e.* 2.489 Å), indicating that multiple full and/or partial dislocations have been created and propagated through the crystal.

Regarding the deformation metrics that have been developed during the course of this project and have been described elsewhere in this report, Figure 5.34 shows the system at various levels of compression with atoms colored by the absolute value of one component of the lattice curvature tensor ($|\kappa_{12}|$), again with some atoms not shown due to the filter imposing a minimum value of this variable. This figure is very interesting; it shows some atoms along the side faces perpendicular to the loading direction in specific “X”-shaped patterns. Also, it reveals (at strains of 6% and above) the regions where full $\langle 110 \rangle$ -type dislocations have been nucleated and have propagated through. In contrast with other variables, it does not show any of the partial dislocation cores and stacking faults present when centrosymmetry and potential energy was used for visualization. While the “X” pattern may be caused by boundary effects due to the small size of our system, the semi-circular shapes present along with absence of partial dislocations and stacking faults indicate that the kinematic variables developed may need enhancement in order to detect and identify the latter defects.

Regarding the evolution of thermodynamic continuum variables, Figure 5.35 shows stress-strain curves (both normal and shear stresses) during compression. Figure 5.35(a) shows that

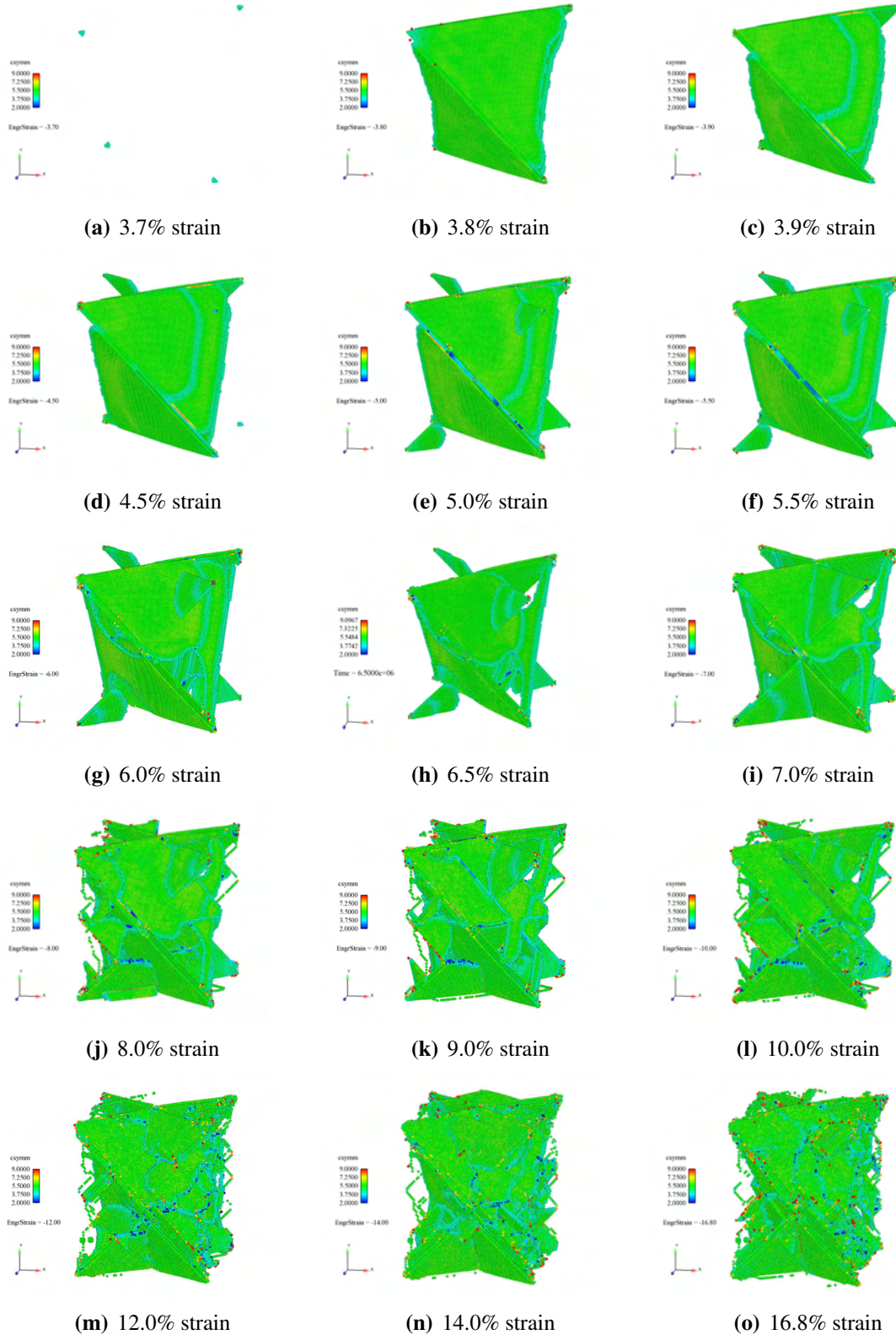


Figure 5.30. Compression of single crystal nickel for $\dot{\epsilon} = 10^7/\text{s}^{-1}$. Atoms colored by centrosymmetry values.

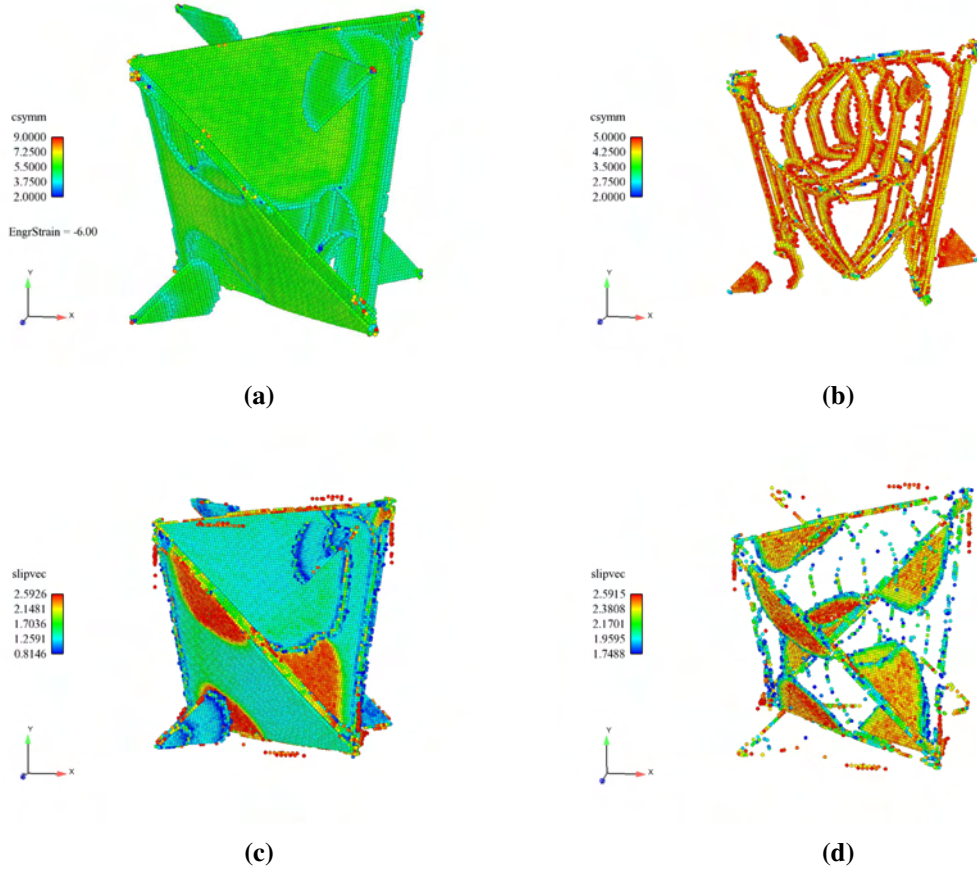


Figure 5.31. Compression of single crystal nickel for $e = 6\%$. (a) and (b) are colored by centrosymmetry, (c) and (d) are colored by slip vector.

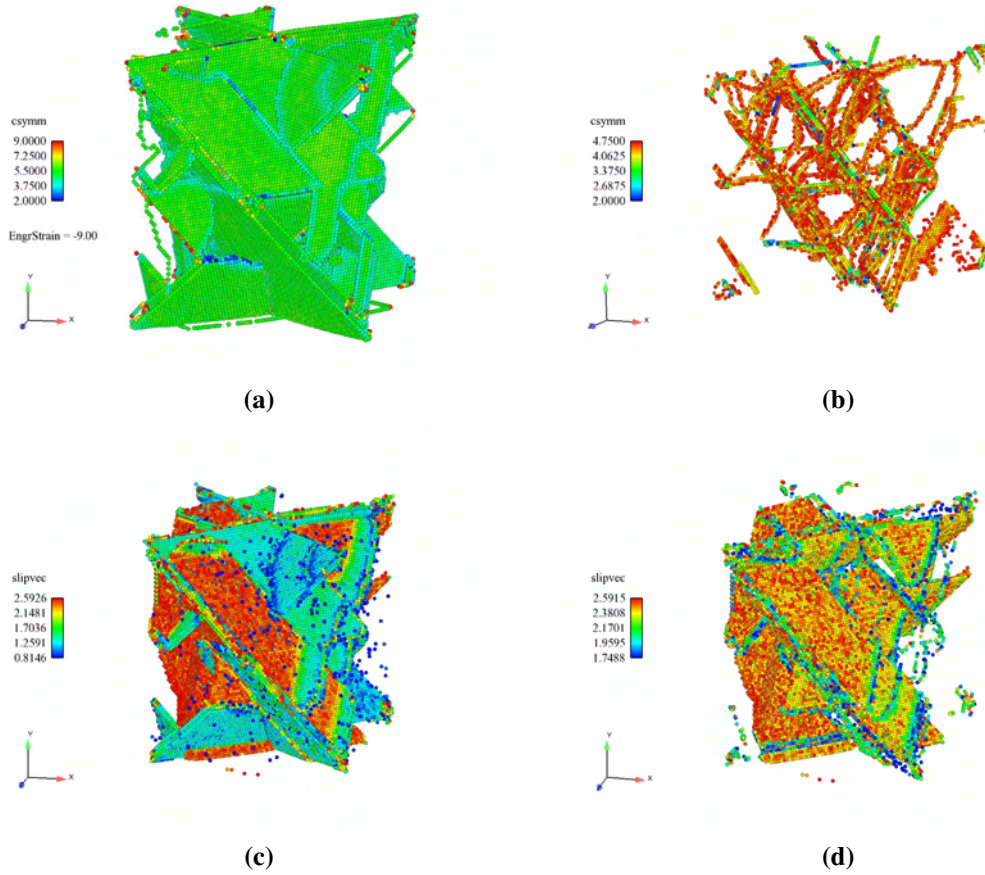


Figure 5.32. Compression of single crystal nickel for $e = 9\%$. (a) and (b) are colored by centrosymmetry, (c) and (d) are colored by slip vector.

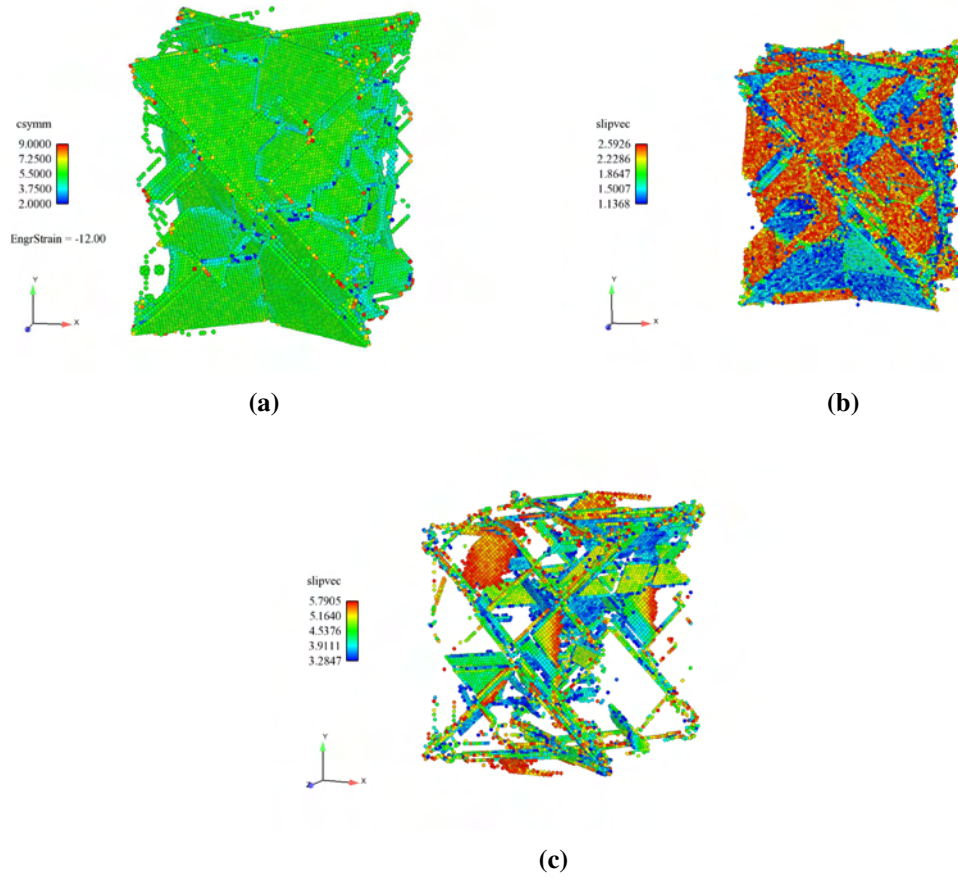


Figure 5.33. Compression of single crystal nickel for $e = 12\%$. (a) is colored by centrosymmetry, (b) and (c) are colored by slip vector.

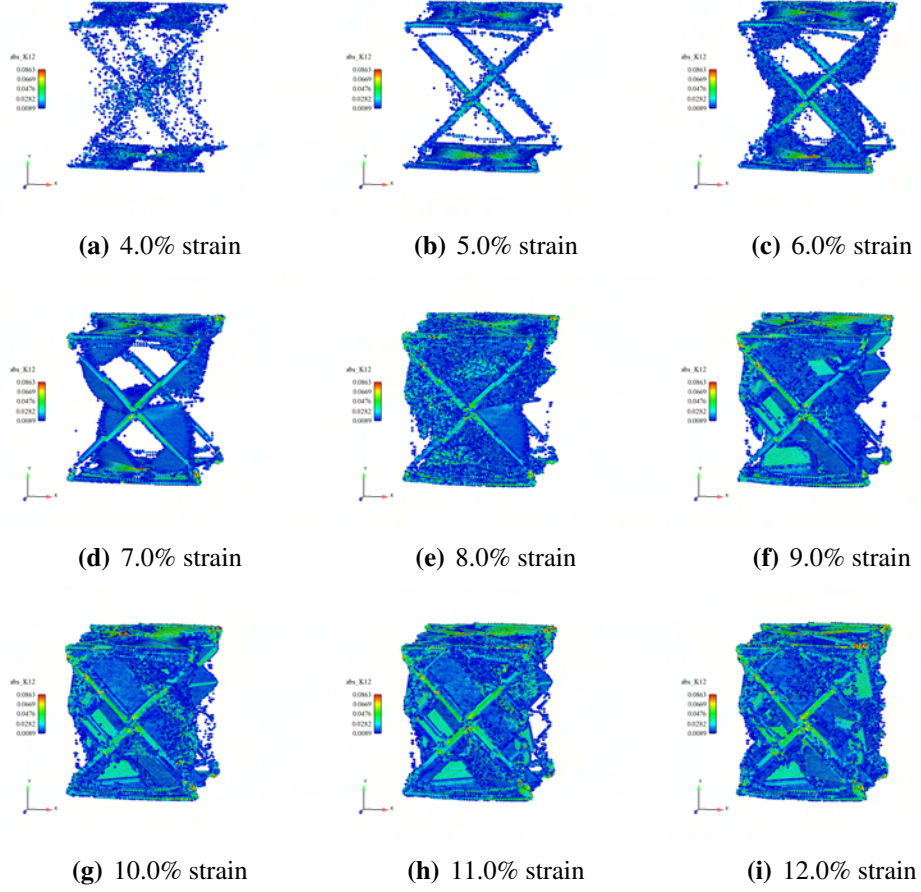


Figure 5.34. Compression of single crystal nickel for $\dot{\epsilon} = 10^7/\text{s}^{-1}$. Atoms colored by $|\kappa_{12}|$.

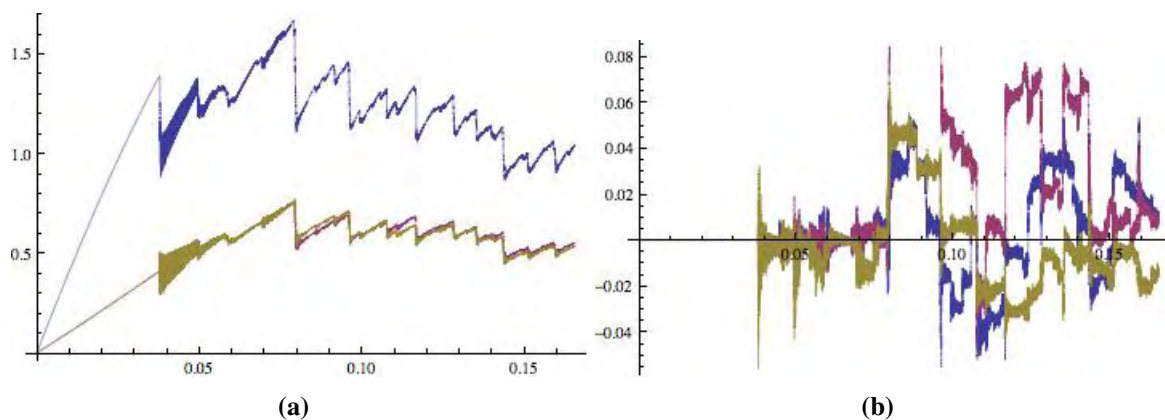


Figure 5.35. Stress-strain curves for compression of single crystal nickel for $\dot{\epsilon} = 10^7/\text{s}^{-1}$: (a) normal stresses (b) shear stresses. Stresses (the vertical axes) are given in units of GPa.

normal stresses (σ_{xx} shown in blue, σ_{yy} shown in red and σ_{zz} shown in gold) increase nonlinearly until dislocation nucleation begins (at a strain of approximately 3.8%), and then oscillate as an increasing number of dislocations and other defects are created. Figure 5.35(b), which displays shear stress evolution (σ_{xy} shown in blue, σ_{xz} shown in red and σ_{yz} shown in gold), shows that shear stresses are zero prior to dislocation nucleation, and oscillate with increasing magnitude as the amount of compression increases. An interesting observation is that hardening is not observed in the evolution of normal stresses. In fact, the normal stress in the compression direction appears to be softening at strains higher than 8%, while the other normal stresses level off in this high-strain regime.

5.2.2 Uniaxial compression at a rate of $10^8/\text{sec}$

For comparison, we performed the same simulation as in the previous section but at a higher compression rate, $10^8/\text{sec}$. Figure 5.36 shows various amounts of compression during the course of this simulation with atoms colored by their value of potential energy. Similarly, Figure 5.37 shows these levels of compression (and ones higher) with atoms colored by their value of centrosymmetry parameter. These figures display the same characteristics as did the lower compression rate. A complex, structured pattern evolves at levels of strain less than about 8%, and then becomes more complex and irregular as strain is increased to 10% and beyond. This disorder persists to strains up to 40%, as shown in Figure 5.37(o).

As we did in the previous section, we also examine the evolution of normal and shear stresses as compression occurs. This is shown in Figure 5.38. Colors in these curves denote the same quantities as in Figure 5.35. These curves also display similar characteristics to their lower rate counterparts. It is observed that as compression exceeds 20% strain, normal stress in the direction

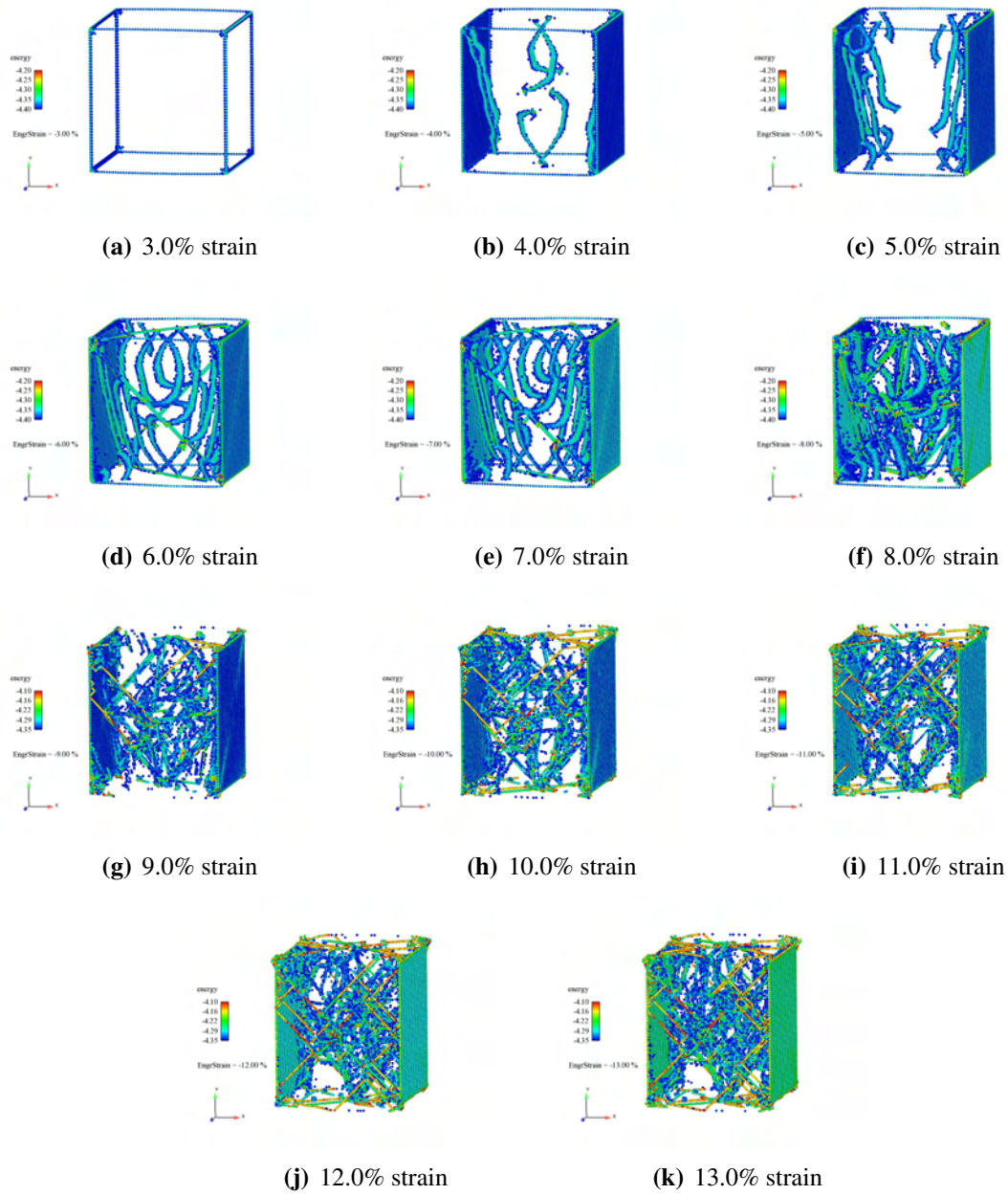


Figure 5.36. Compression of single crystal nickel for $\dot{\epsilon} = 10^8/\text{s}^{-1}$. Atoms colored by potential energy values.

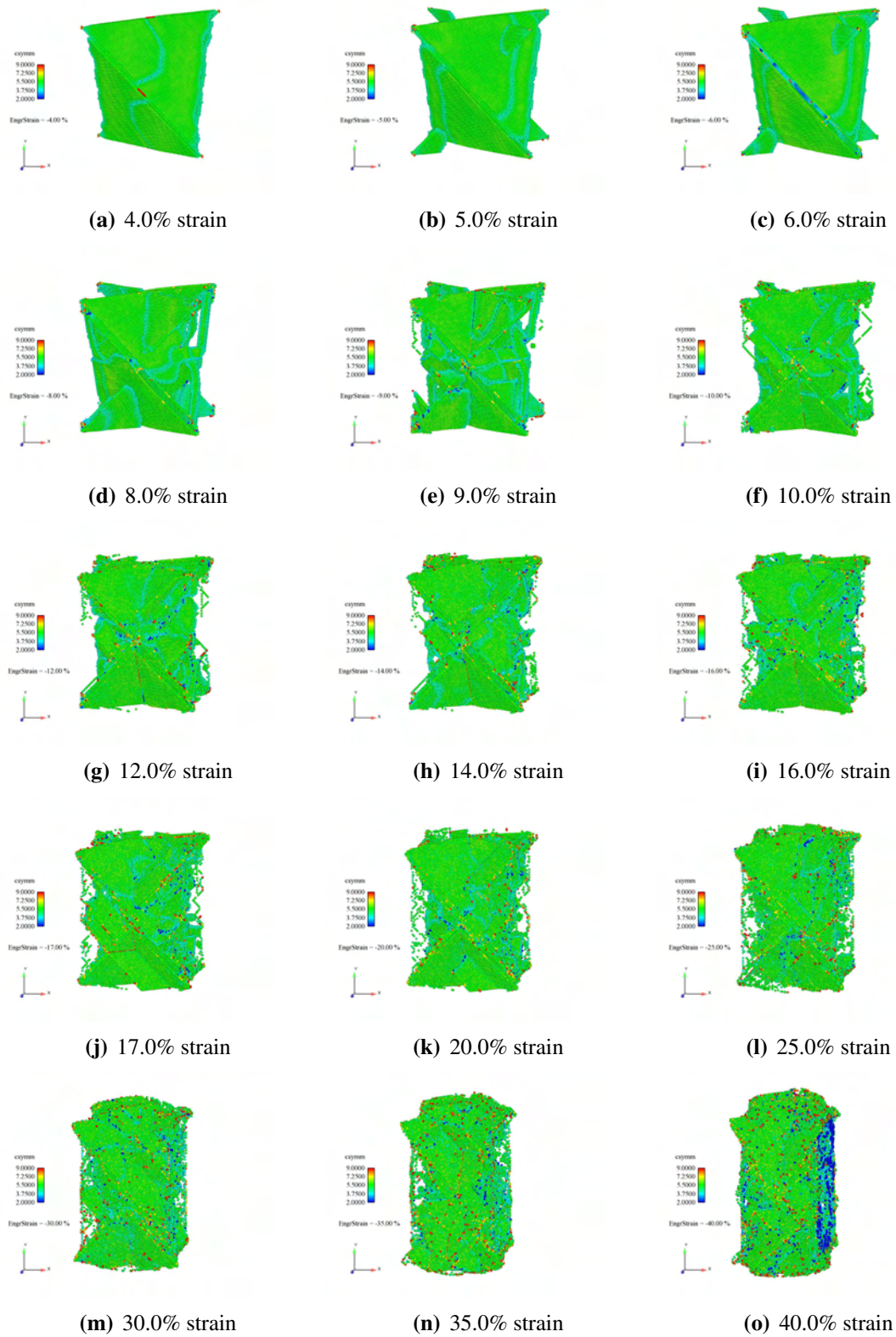


Figure 5.37. Compression of single crystal nickel for $\dot{\epsilon} = 10^8/\text{s}^{-1}$. Atoms colored by centrosymmetry values.

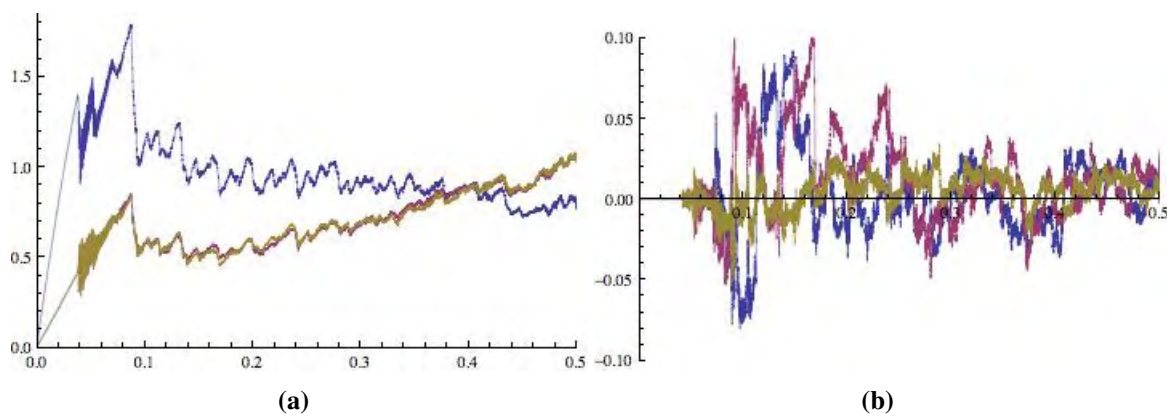


Figure 5.38. Stress-strain curves for compression of single crystal nickel for $\dot{\epsilon} = 10^8/\text{s}^{-1}$: (a) normal stresses (b) shear stresses. Stresses (the vertical axes) are given in units of GPa.

of compression decreases (or perhaps levels off) while normal stress in the transverse directions increases, indicating that hardening may be occurring. One interesting difference is that the magnitude of shear stresses that arise due to defect creation appears high at low strains and decreases with increasing compression. The same trend was not observed for the slower rate case.

5.2.3 Discussion

Clearly more analysis of the presented simulations is warranted, as are additional simulations to explore the effects of boundary conditions, loading rate and system size. It has been observed that substructure formation in metals is typically on the order of hundreds of nanometers (thousands of Å's), whereas our system here is only 176 Å on a side prior to compression. It would be desirable to simulate systems of dimension ~ 1000 nm on each side, but that would require approximately 91.7 billion atoms, a time-consuming and burdensome computation. A better strategy would be to explore a range of sizes (*i.e.* 200 Å - 500 Å) consisting of a manageable number of atoms, thereby identifying those aspects related to system size and other features that are independent of system size.

One further consideration is the use of the EAM potential by Foiles *et al.* [75]. This potential is known to exhibit an un-characteristically low value of stacking fault energy, which directly governs the size and shape of dislocations cores and stacking faults. Use of a potential with a more accurate stacking fault energy would be useful in comparison with experimental results of dislocation and disclination substructure evolution.

The figures shown in the previous sections have demonstrated that the metrics developed here and elsewhere provide unique insight on the evolution of defects in deforming crystalline materials.

Future work should focus on counting atoms with metric values in specific ranges in order to quantify dislocation and defect densities. Also, calculation of additional variables (such as rotation and vorticity) for these and other simulations may enable a stronger connection to be made to the micropolar small-strain theory developed in Chapter 4 and the finite strain theory discussed in the next chapter.

Chapter 6

Finite Deformation Theory

Principal Authors: Douglas J. Bammann and Jonathan A. Zimmerman

Our initial plan for this task was to significantly improve the finite strain, coupled dislocation-disclination theory of Clayton *et al.* [47] by expanding the multiplicative decomposition of the deformation gradient (\mathbf{F}) to include distinct components related to lattice distortions due to tilt, twist and other types of interfacial boundaries, and by developing physically reasonable forms of constitutive relations that govern the evolution of dislocations and disclinations. However, during the course of our development we discovered fundamental issues regarding physical and mathematical consistency across length scales that cloud that theory's implementation. We have discovered that the original decomposition of the deformation gradient, along with the associated lattice directors, is inconsistent with the assumption of micropolar deformation. Indeed, this theory is implicitly micromorphic in its mathematical development, although the system of equations developed is underdetermined with regard to the number of degrees of freedom now represented. We have reformulated the deformation gradient decomposition to produce a truly micropolar framework:

$$\mathbf{F} = \mathbf{V}^e \mathbf{F}^i \hat{\mathbf{R}} \mathbf{F}^p \quad (6.1)$$

In this expression, \mathbf{F}^p represents plastic deformation related to crystallographic slip, $\hat{\mathbf{R}}$ represents rotations associated with the presence of disclinations, \mathbf{F}^i represents deformations associated with geometrically necessary dislocations (GNDs), and \mathbf{F}^e represents deformation associated with elastic loading. Decoupling the deformations associated with GNDs from those associated with disclinations is an essential, innovative feature of our new theory. Restricting the deformation associated with disclinations to be rotational ensures the resulting theory will be micropolar in nature.

Another innovation developed for our nanomechanical continuum theory is the realization that the state variables used should be the elastic strain fields resulting from the GND and disclination defect densities. In previous models, the defect densities themselves were used as state variables. However, our research has shown that use of such densities as state variables leads to incorrect expressions for the thermodynamic conjugate forces, *i.e.* macro and microscale stresses.

Unfortunately, our documentation on this effort is limited due to a project team member leaving Sandia. On the following pages are a technical presentation given by D.J. Bammann at both the 2007 TMS Annual Meeting (held in Orlando, Florida) and the 1st World Symposium on Multiscale Material Mechanics and Engineering Sciences (held in Thessaloniki, Greece).

An Internal State Variable Model of Micro-polar Elasto-Viscoplasticity

Douglas Bammann

Sandia National Labs, Livermore, CA

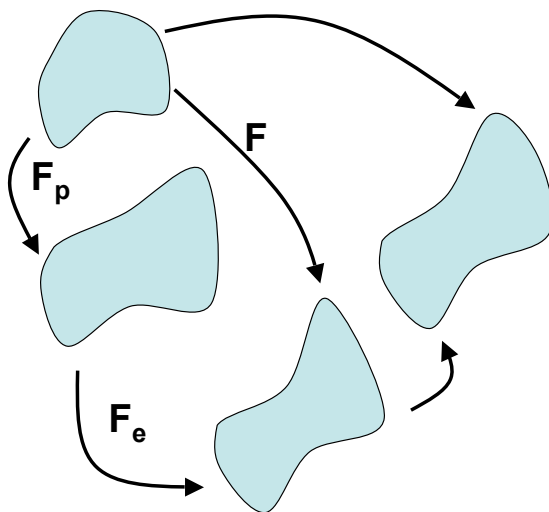
David McDowell

Jason Mayeur

Georgia Tech, Atlanta, GA

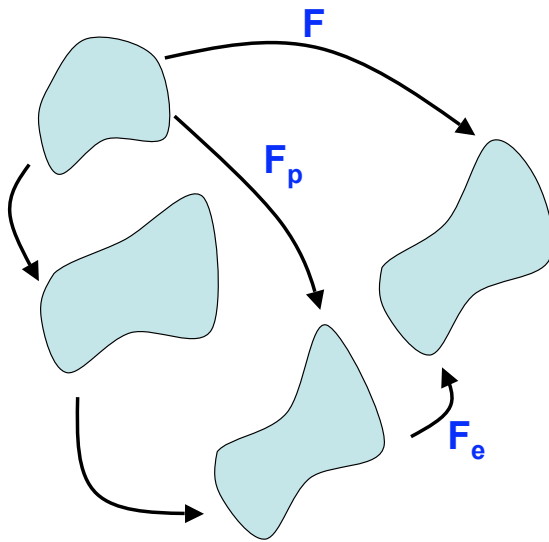
John Clayton

Army Research Lab, Aberdeen, Md



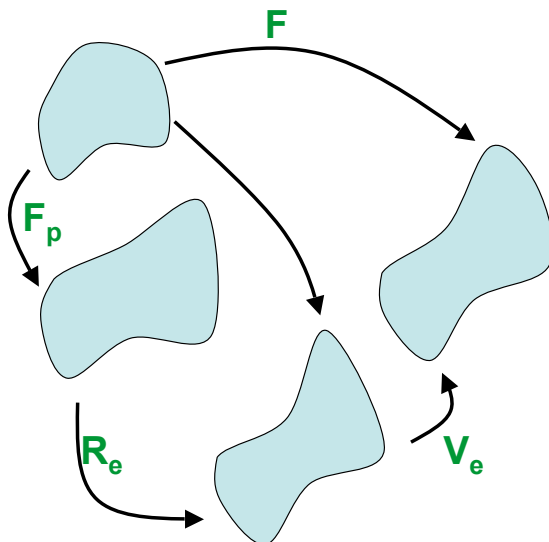
Bilby-1957, Kroner 1960

$$\mathbf{F} = \mathbf{F}_e \mathbf{F}_p$$



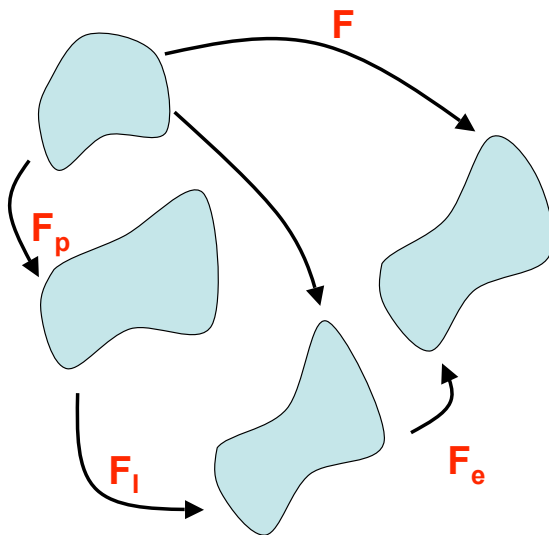
Lee -1967

$$F = F_e F_p$$

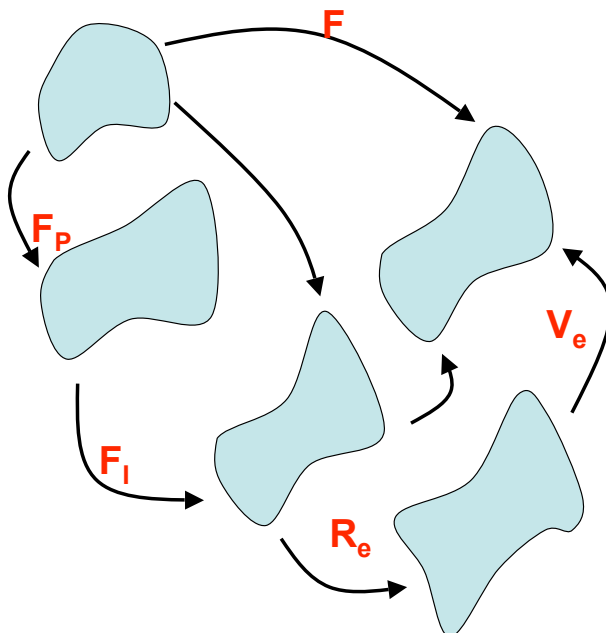


Bammann-2001

$$F = V_e R_e F_p$$



Clayton, McDowell - 2003
 $F = F_e F_i F_p$



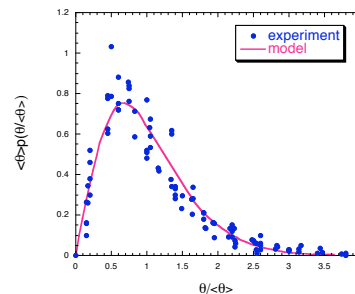
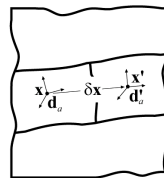
Clayton, McDowell,
 Bammann (2005,2006)
 $F = V_e R_e F_i F_p$

Modeling Approach

*Clayton, McDowell, Bammann, Int. J. Plasticity, **22** (2006) 210-256

- Kinematics, balance laws and general kinetic relations developed
 - Multiscale volume averaging of crystalline element containing translation and rotation defects (dislocations and disclinations)
- Macroscopic kinematics - 3 term multiplicative decomposition of the deformation gradient
- Microlevel - additive decomposition of affine connection into dislocations and disclinations to the distortion of lattice directors
- Standard macroscale balance laws
- Linear and angular momentum balances at microscale on first and second order moment stresses associated with geometrically necessary defects
- Micropolar rotations incorporated to capture physics of GNDs not captured by 1st order gradients of elastic deformation
 - of defect structure at multiple length scales
 - Incompatible lattice misorientation gradients arising in ductile single crystals under nominally homogeneous deformations

The Problem: Disclinations - grain fragmentation/subdivision

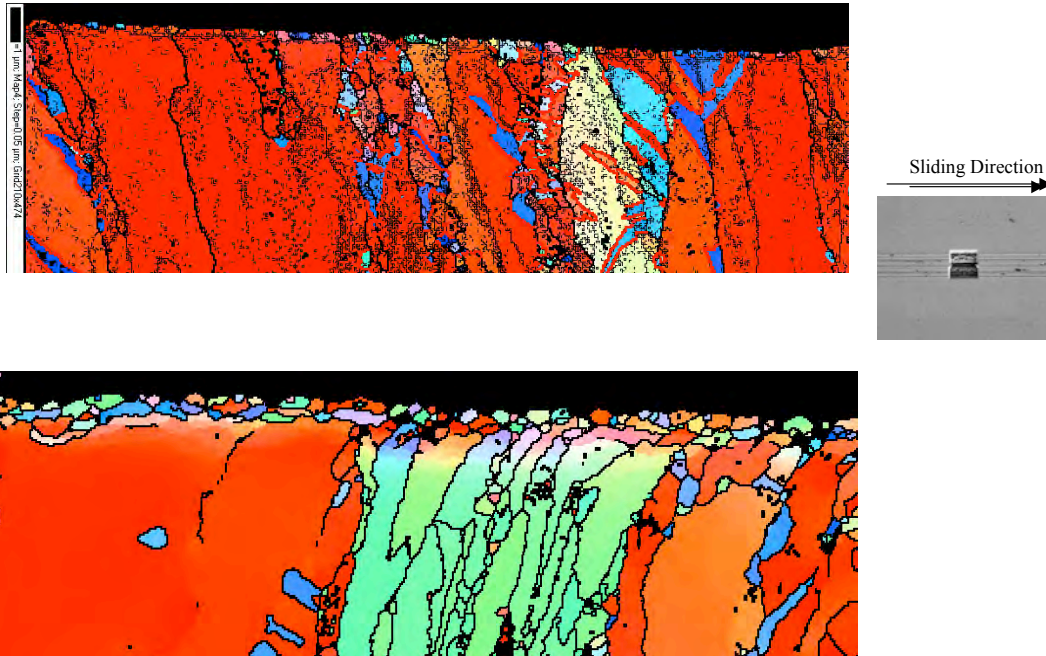


Defect substructure in FCC metals
(Pantleon, 1996; Hughes et al., 1997;
Butler & McDowell, 1998;
Kuhlmann-Wilsdorf, 1999)

Misorientation vs strain

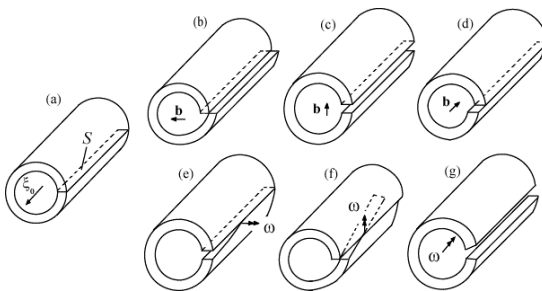
- Formation of cells of relatively small orientation organized collectively into larger cell blocks
- Average misorientations between blocks significantly greater than those between cells
- Increase strain \Rightarrow cell block sizes decrease faster than cell sizes
- Disclinations capture gradients of lattice rotation at cell block boundaries that arise from organization and superposition of small orientations between cells (represented by GNDs)
- Coupled kinetics of evolution of SSDs, GNDs and disclinations \Rightarrow cells and cell blocks will form under homogeneous loading
- Local minimum in free energy (lack of “cross-convexity” - Carstensen et al. 2002)

Formation of misoriented cells during contact sliding

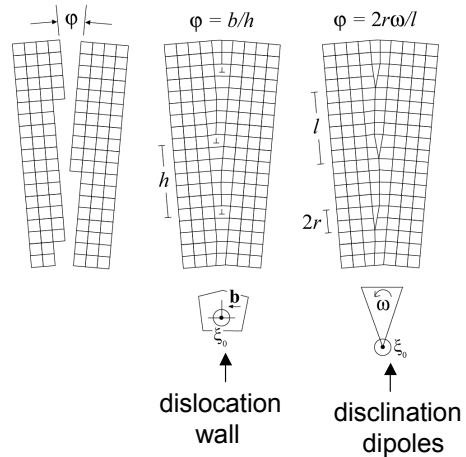


Disclination defects: background

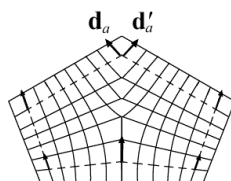
Volterra's elastic model (1907)



Li's grain boundary model (1972)



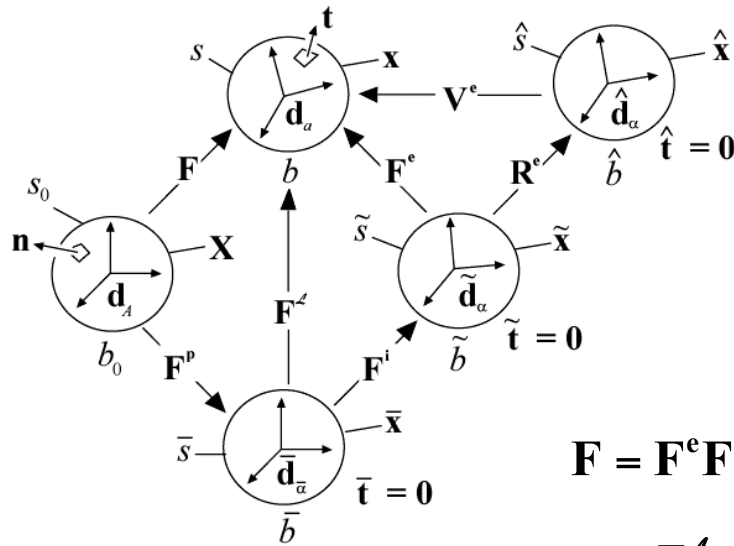
60° wedge disclination (De Wit, 1970; Lardner, 1974)



Disclinations:

- Can represent self-organized arrays of dislocations
- Introduce another length scale into the continuum theory, along with that of GNDs
- Popular for modeling liquid crystals (Cermelli & Fried, 2002)

General kinematics

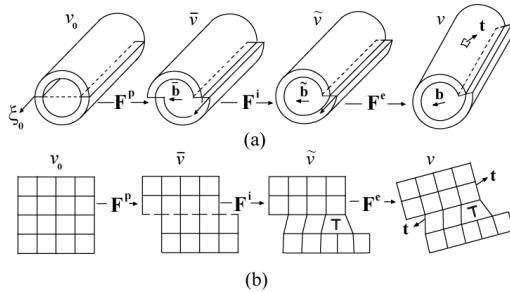


Disclinations: micropolar kinematics

Deformation gradient

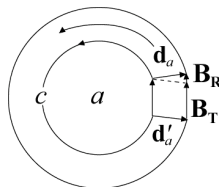
$$\mathbf{F} = \mathbf{F}^e \mathbf{F}^i \mathbf{F}^p$$

$$\mathbf{F}^L \equiv \mathbf{F}^e \mathbf{F}^i$$



Total Burgers vector

$$\begin{aligned} B^a &= \frac{1}{2} \varepsilon^{dbc} \int_a (T_{bc}^{..a} - R_{ecb}^{..a} x^e) n_d da \\ &= \int_a (\alpha^{ad} + C^{L-1af} \varepsilon_{fjb} \theta^{gd} x^b) n_d da \\ &= \underbrace{B_T^a}_{\text{dislocations}} + \underbrace{B_R^a}_{\text{disclinations}} \end{aligned}$$



Lattice directors

$$\mathbf{d}_a = (F^{L-1})_{..a}^{\bar{a}} \bar{\mathbf{d}}_{\bar{a}}$$

$$\nabla_b \mathbf{d}_a = \mathbf{d}_{a,b} - \Gamma_{ba}^{..c} \mathbf{d}_c$$

Connection

$$\Gamma_{cb}^{..a} \equiv F_{..a}^{Lc} F_{..b,c}^{L-1\bar{a}} + Q_{cb}^{..a} = \bar{\Gamma}_{cb}^{..a} + Q_{cb}^{..a}$$

Torsion tensor: net dislocations

$$T_{cb}^{..a} \equiv \Gamma_{cb}^{..a} - \Gamma_{bc}^{..a} = \bar{T}_{cb}^{..a} + 2Q_{[cb]}^{..a}$$

$$2\alpha^{ad} \equiv \varepsilon^{dbc} T_{bc}^{..a} \quad \alpha = \sum_j (\rho_+^j - \rho_-^j) \mathbf{b}_+^j \otimes \xi^j$$

Curvature tensor: net disclinations

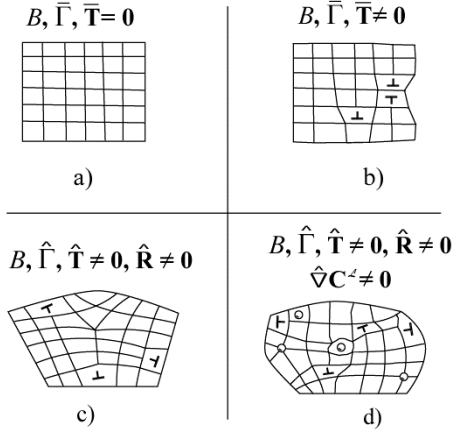
$$R_{bcd}^{..a} = 2\nabla_{[c} Q_{d]}^{..a} + Q_{ce}^{..a} Q_{db}^{..e} - Q_{de}^{..a} Q_{cb}^{..e} + T_{cd}^{..e} Q_{eb}^{..a}$$

$$4\theta^{gd} \equiv \varepsilon^{gba} \varepsilon^{dce} R_{abce} \quad \theta = \sum_k (\eta_+^k - \eta_-^k) \tilde{\omega}_+^k \otimes \xi_0^k$$

Kinematics of general lattice defects

Linear connection for lattice vectors:

$$\hat{\Gamma}_{cb}^{..a} = \underbrace{F_{..a}^{..c} F_{..c}^{..b}}_{\text{crystal connection (GNDs)}} + \underbrace{C^{..ad} Q_c[bd]}_{\text{micro-rotation (disclinations)}} + \underbrace{\delta_b^a Q_c}_{\text{micro-expansion (isotropic point defects)}} + \underbrace{C^{..ad} (Q_c(bd) - Q_c C^{..ad}_{bd})}_{\text{micro-strain (Somigliana dislocations)}}$$



Differential-geometric interpretation
(spatial configuration)

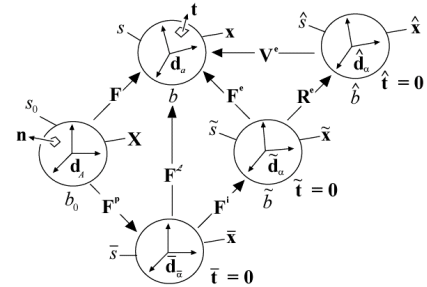
- a) Defect-free (or SSDs), Euclidean space
- b) GNDs, Asymmetric space with Cartan's torsion
- c) Disclinations, curved space
- d) General defects, non-metric space

Disclinations: micropolar kinematics

Defect densities satisfy additive relations on configuration

$$\begin{aligned} \tilde{\alpha}^{\alpha\beta} &\equiv J^e F^{e-1\alpha}_{..a} \alpha^{ab} F^{e-1\beta}_{..b} \\ &= J^e F^{e-1\alpha}_{..a} \varepsilon^{bcd} F_{..a}^{..c} F_{..c}^{..b} F^{e-1\beta}_{..b} + J^e F^{e-1\alpha}_{..a} \varepsilon^{bcd} Q_{[dc]}^{..a} F^{e-1\beta}_{..b} \end{aligned}$$

$$\begin{aligned} \tilde{\theta}^{\alpha\beta} &\equiv J^e F^{e-1\alpha}_{..a} \theta^{ab} F^{e-1\beta}_{..b} \\ &= \frac{1}{4} J^e F^{e-1\alpha}_{..a} \varepsilon^{adg} \varepsilon^{bce} R_{[gd][ce]} F^{e-1\beta}_{..b} \end{aligned}$$



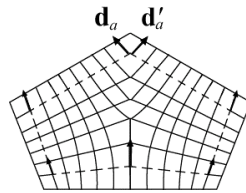
$$\tilde{\alpha}_p^{\alpha\beta} \equiv -\tilde{J}^{-1} \tilde{F}_{..A}^{\alpha} \varepsilon^{BCD} F^{p-1A}_{..a} F^{p\bar{\alpha}}_{D,C} \tilde{F}_{..B}^{\beta} - \tilde{J}^{-1} \tilde{F}_{..A}^{\alpha} \varepsilon^{BDC} \hat{Q}_{[DC]}^{..A} \tilde{F}_{..B}^{\beta}$$

$$\begin{aligned} \tilde{\theta}_p^{\alpha\beta} &\equiv -\tilde{J}^{-1} \tilde{F}_{..A}^{\alpha} \hat{\theta}^{AB} \tilde{F}_{..B}^{\beta} \\ &= -\frac{1}{4} \tilde{J}^{-1} \tilde{F}_{..A}^{\alpha} \varepsilon^{ADG} \varepsilon^{BCE} \hat{R}_{[GD][CE]} \tilde{F}_{..B}^{\beta} \end{aligned}$$

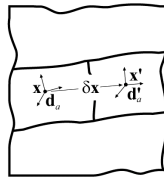
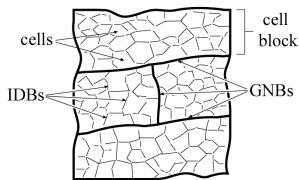
$$\begin{aligned} \tilde{\alpha}_T &\equiv \tilde{\alpha} + \tilde{\alpha}_p = 0 \\ \tilde{\theta}_T &\equiv \tilde{\theta} + \tilde{\theta}_p = 0 \end{aligned}$$

Rotational part of F^i can be associated
with disclination density (Lardner, 1973).

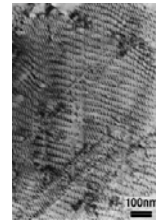
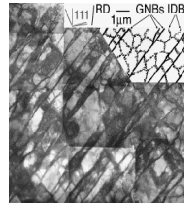
$$R_{\bar{\beta}}^{i\alpha} = \delta_{\bar{\beta}}^{\alpha} + \underbrace{\delta_a^{\alpha} \delta_{\bar{\beta}}^e C^{\mathcal{L}-1ab} \epsilon_{beg} \left(\frac{\ell_{ref}^2}{k} \sum_{i=1}^k \theta^{gh} (m^i)_h \right)}_{\text{average Frank vector over active slip planes}}$$



Disclinations: grain fragmentation/subdivision



(Hughes, Hansen, & Bammann, 2003)



Our framework:

- IDBs = dislocations (shorter range defect structures)
- GNBs = disclinations (longer range defect structures)

$$\mathbf{d}'_a = \mathbf{d}_a + \mathbf{d}_{a,b} dx_b = \mathbf{d}_a + Q_{bac} dx_b \mathbf{d}_c = \left(\delta_{ac} + Q_{b[ac]} dx_b \right) \mathbf{d}_c = \Phi_{ac} \mathbf{d}_c \Rightarrow \mathbf{Q}$$

Measures gradients of
lattice rotation

$$Q_{ca}^{\cdot d} = F^{\mathcal{L}d}_{\cdot \bar{a}} \left(\frac{\left(F^{\mathcal{L}'-1} \right)_{\cdot a}^{\bar{a}} - \left(F^{\mathcal{L}-1} \right)_{\cdot a}^{\bar{a}}}{\left(x'^c - x^c \right)} - \left(F^{\mathcal{L}-1} \right)_{\cdot a,c}^{\bar{a}} \right) \Rightarrow$$

Q accounts for lattice misorientations
that first order gradients fail to describe

For small misorientation
gradients,

$$4\theta^{gd} = \epsilon^{gba} \epsilon^{dce} 2\mathbf{R}_{abce} \approx 2\epsilon^{gba} \epsilon^{dce} \partial_{[c} Q_{e][ba]} = 2\epsilon^{gba} \epsilon^{dce} Q_{eba,c}$$

Disclinations: momentum balance

Macroscale

$$\Sigma^{ab}_{|b} + \rho \bar{f}^a = \rho \dot{x}^a$$

$$\varepsilon_{abc} \Sigma^{bc} = 0 \quad \left. \vphantom{\Sigma^{bc}} \right\} \text{angular momentum}$$

$$t^a = \Sigma^{ab} n_b \quad \left. \vphantom{\Sigma^{ab}} \right\} \text{macro-traction vector}$$

Standard non-polar dynamic continuum.
Cauchy stress is symmetric.

$$\left. \begin{aligned} \mathbf{S} &= \frac{1}{v_0} \int_{s_0} \mathbf{X} \otimes \mathbf{t}_0 ds_0 \\ \Sigma^{ab} &\equiv J^{-1} F^a_{\cdot A} S^{Ab} \end{aligned} \right\} \text{average stress}$$

Microscale

$$\left. \begin{aligned} \sigma^{ab}_{|b} &= 0 \\ \varepsilon^{abc} \sigma_{bc} + \mu^{ab}_{|b} &= 0 \end{aligned} \right\} \text{micro-momentum}$$

$$\left. \begin{aligned} (t_\sigma)^a &= \sigma^{ab} n_b \\ (t_\mu)^a &= \mu^{ab} n_b \end{aligned} \right\} \text{micro-traction}$$

$$\left. \begin{aligned} \sigma^{ab} &\equiv J^{e-1} F^{ea}_{\cdot \alpha} \tilde{g}^{\alpha\chi} \tilde{\sigma}_{\chi\delta} \tilde{g}^{\beta\delta} F^{eb}_{\cdot \beta} \\ \mu^{ab} &\equiv J^{e-1} F^{ea}_{\cdot \alpha} \tilde{g}^{\alpha\chi} \tilde{\mu}_{\chi\delta} \tilde{g}^{\beta\delta} F^{eb}_{\cdot \beta} \end{aligned} \right\} \text{spatial frame}$$

Micropolar elastic continuum.
Derived from static equilibrium of
higher order moments, assuming
decoupling with Cauchy stress.

Disclinations: thermodynamics

Energy balance (First Law)

$$\underbrace{\dot{U}_0}_{\text{internal energy}} = \underbrace{S^{Aa} g_{ab} \dot{F}^b_{\cdot A}}_{\text{stress power}} - \underbrace{q|_A}_{\text{heat flux}} + \underbrace{H_0}_{\text{heat sources}}$$

Free energy potential (intermediate configuration)

$$\tilde{\psi} = \tilde{\psi} \left(\underbrace{\tilde{\mathbf{C}}^e}_{\text{recoverable elasticity}}, \underbrace{\mathbf{V}^i}_{\text{micro-heterogeneity (moments of defects)}}, \underbrace{\tilde{\alpha}}_{\text{geom. nec. dislocations}}, \underbrace{\tilde{\theta}}_{\text{geom. nec. disclinations}}, \right. \\ \left. , \underbrace{\tilde{\varepsilon}_\rho, \tilde{\varepsilon}_\eta}_{\text{statistically-stored defects}}, \underbrace{T}_{\text{temperature}}, \underbrace{\tilde{\mathbf{g}}}_{\text{intermediate metric (energy coupling)}} \right)$$

Entropy inequality (Second Law)

$$\begin{aligned}
 & \underbrace{\langle \tilde{\mathbf{P}}, \tilde{\mathbf{L}}^p \rangle}_{\text{Dissipation from plastic defect fluxes (e.g. dislocation glide)}} + \underbrace{\langle \tilde{\mathbf{P}} \mathbf{V}^{i-1}, \dot{\mathbf{V}}^i \rangle}_{\text{Dissipation from microscopic heterogeneity (e.g. dislocation clustering)}} + \underbrace{\langle \mathbf{V}^i \tilde{\mathbf{P}} \mathbf{V}^{i-1}, \tilde{\mathbf{W}}^i \rangle}_{\text{Dissipation from microscopic heterogeneity (e.g. disclination spin)}} + \underbrace{\langle \tilde{\boldsymbol{\chi}}^T, \dot{\tilde{\boldsymbol{\alpha}}}_p \rangle + \langle \tilde{\boldsymbol{\xi}}^T, \dot{\tilde{\boldsymbol{\theta}}}_p \rangle}_{\text{Dissipation from geometrically necessary defect densities}} \\
 & \geq \underbrace{\left\langle \frac{\partial \tilde{\psi}}{\partial \mathbf{V}^i}, \dot{\mathbf{V}}^i \right\rangle}_{\text{Energy storage from microscopic heterogeneity}} + \underbrace{\frac{\partial \tilde{\psi}}{\partial \tilde{\boldsymbol{\varepsilon}}_\rho} \dot{\tilde{\boldsymbol{\varepsilon}}}_\rho + \frac{\partial \tilde{\psi}}{\partial \tilde{\boldsymbol{\varepsilon}}_\eta} \dot{\tilde{\boldsymbol{\varepsilon}}}_\eta}_{\text{Energy storage from statistically stored defect densities}} + \underbrace{\left\langle \frac{\partial \tilde{\psi}}{\partial \tilde{\mathbf{g}}}, \dot{\tilde{\mathbf{g}}} \right\rangle}_{\text{Choice of intermediate metric}}
 \end{aligned}$$

Eshelby stress is driving force for plasticity

$$\tilde{\mathbf{P}} \equiv \tilde{\mathbf{M}}^T - \tilde{\psi} \tilde{\mathbf{I}} = J^e \mathbf{F}^{e-1} \underbrace{(\boldsymbol{\Sigma} \mathbf{g} - \psi \mathbf{I})}_{\mathbf{P}} \mathbf{F}^e = \tilde{J}^{-1} \tilde{\mathbf{F}} \underbrace{(\mathbf{F}^T \hat{\mathbf{T}} \mathbf{G} - \psi_0 \mathbf{I}_0)}_{\mathbf{P}} \tilde{\mathbf{F}}^{-1}$$

Conjugate microforces (moment- and hyper-stresses)

$$\tilde{\boldsymbol{\sigma}} = \frac{\partial \tilde{\psi}}{\partial \tilde{\boldsymbol{\alpha}}} \quad \tilde{\boldsymbol{\mu}} = \frac{\partial \tilde{\psi}}{\partial \tilde{\boldsymbol{\theta}}}$$

Thermodynamics of mixed defect fields

Energy minimization of a non-convex potential drives evolution of microstructure (Ball & James, 1987; Carstensen et al., 2002)

$\psi(\mathbf{F})$ is not convex

→ heterogeneous $\mathbf{F}(\mathbf{X})$ is energetically favorable.

Convexity of free energy can be inhibited by competing mechanisms, even if energy is convex with respect to each individual mechanism

The challenge remains to postulate specific non-convex potentials for elastic-plastic materials and develop mathematical and computational techniques to evolve plastic flow and internal variables following energy minimization principles under arbitrary 3D deformation histories.

Free energy and non-convexity

Simple 1D Example:

$$\begin{aligned}\tilde{\psi}^S &= \frac{1}{2} \mu \left[\left(c_\rho \tilde{\epsilon}_\rho \right)^4 + \left(c_\eta \tilde{\epsilon}_\eta \right)^4 \right] \\ &= \frac{1}{2} \mu \left[\left(bc_\rho \right)^4 \tilde{\rho}_s^2 + \left(r\omega c_\eta \right)^4 \tilde{\eta}_s^2 \right]\end{aligned} \quad \left. \begin{array}{l} \text{energy quadratic (convex) in each} \\ \text{statistically stored defect density} \end{array} \right\}$$

$$\begin{array}{ll} \frac{\partial \tilde{\rho}_s}{\partial \gamma} = A - B\tilde{\eta}_s & \frac{\partial \tilde{\eta}_s}{\partial \gamma} = C \\ \downarrow & \downarrow \\ \tilde{\rho}_s = A\gamma - \frac{BC}{2}\gamma^2 & \tilde{\eta}_s = C\gamma \end{array} \quad \left. \begin{array}{l} \text{conceivable evolution equations and} \\ \text{solutions under monotonic straining } \gamma \end{array} \right\}$$

Leads to...

$$\begin{aligned}\tilde{\psi}^S &= \frac{1}{2} \mu \left[\left(bc_\rho \right)^4 \left(A^2 \gamma^2 - ABC\gamma^3 - \left(\frac{BC}{2} \right)^2 \gamma^4 \right) + \left(r\omega c_\eta \right)^4 C^2 \gamma^2 \right] \\ \frac{\partial^2 \tilde{\psi}^S}{\partial \gamma^2} &= \frac{1}{2} \mu \left[\left(bc_\rho \right)^4 \left(2A^2 - 6ABC\gamma - 12 \left(\frac{BC}{2} \right)^2 \gamma^2 \right) + 2 \left(r\omega c_\eta \right)^4 C^2 \right]\end{aligned}$$

Energy is strictly convex when...

$$A^2 + \left(\frac{r\omega c_\eta}{bc_\rho} \right)^4 C^2 > 3ABC\gamma + 6 \left(\frac{BC}{2} \right)^2 \gamma^2 \quad \left. \begin{array}{l} \text{free energy is convex in strain} \\ \text{for } A = B = 0, \text{ or } C = 0, \\ \text{but not for all } A, B, C \neq 0 \end{array} \right\}$$

Conclusion: competing dislocation/disclination mechanisms can destroy global convexity, even when free energy is ²⁰⁴convex in each individual variable.

Neglecting disclinations, for a single crystal, the equations are summarized as

Linear elasticity

$$\dot{\tilde{\sigma}} = 2\mu(\theta)(\tilde{\mathbf{D}}' - \tilde{\mathbf{D}}_p)$$

Plastic slip
and spin

$$\tilde{\mathbf{D}}_p = \sum_i \dot{\gamma}^{(i)} (\tilde{\mathbf{m}}^{(i)} \otimes \tilde{\mathbf{s}}^{(i)} + \tilde{\mathbf{s}}^{(i)} \otimes \tilde{\mathbf{m}}^{(i)})$$

$$\tilde{\mathbf{W}}_p = \sum_i \dot{\gamma}^{(i)} (\tilde{\mathbf{m}}^{(i)} \otimes \tilde{\mathbf{s}}^{(i)} - \tilde{\mathbf{s}}^{(i)} \otimes \tilde{\mathbf{m}}^{(i)})$$

Flow rule

$$\dot{\gamma}^{(i)} = \dot{\gamma}_0^{(i)} \left[\frac{(\tilde{\sigma} - \tilde{\alpha}) \mathbf{m} \cdot \mathbf{s}}{\tilde{\tau}} \right]^{\frac{1}{n}}$$

Internal stresses

$$\tilde{\tau} = c_\tau \mu(\Theta) \varepsilon_{ss} = c_\tau \mu(\Theta) b \sqrt{\rho_{ss}}$$

$$\tilde{\chi} = c_\chi \mu(\Theta) \tilde{\kappa}_e$$

Evolution of state

$$\dot{\rho}_{ss}^{(i)} = \left(\frac{c_1}{L_s^{(i)}} + \frac{c_2}{L_g^{(i)}} \right) \left| \dot{\gamma}^{(i)} \right| - c_3 \rho_{ss}^{(i)} \left| \dot{\gamma}^{(i)} \right|$$

Effect of GNDs on mean
free path of dislocations

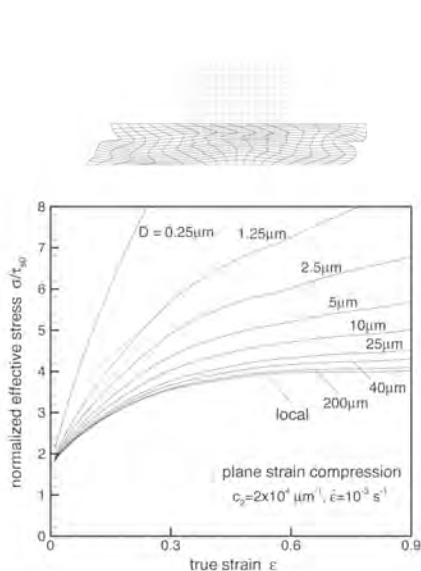
Evolution of \mathbf{R}_e

$$\dot{\mathbf{R}}_e = (\tilde{\mathbf{W}} - \tilde{\mathbf{W}}_e - \tilde{\mathbf{W}}_p) \mathbf{R}_e^T$$

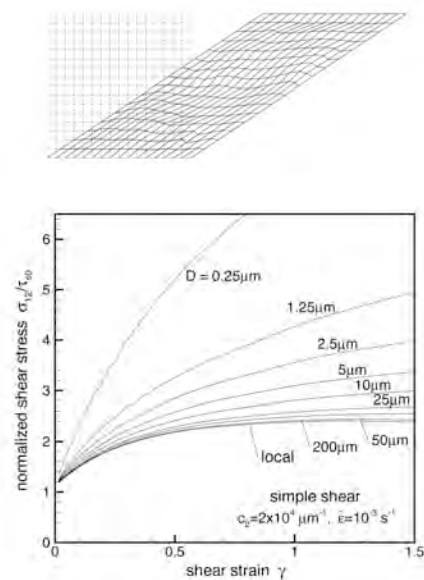
Plane Strain Compression/ Simple Shear

Deformed mesh at $\varepsilon = -0.9$

Deformed mesh at $\gamma = 1.5$

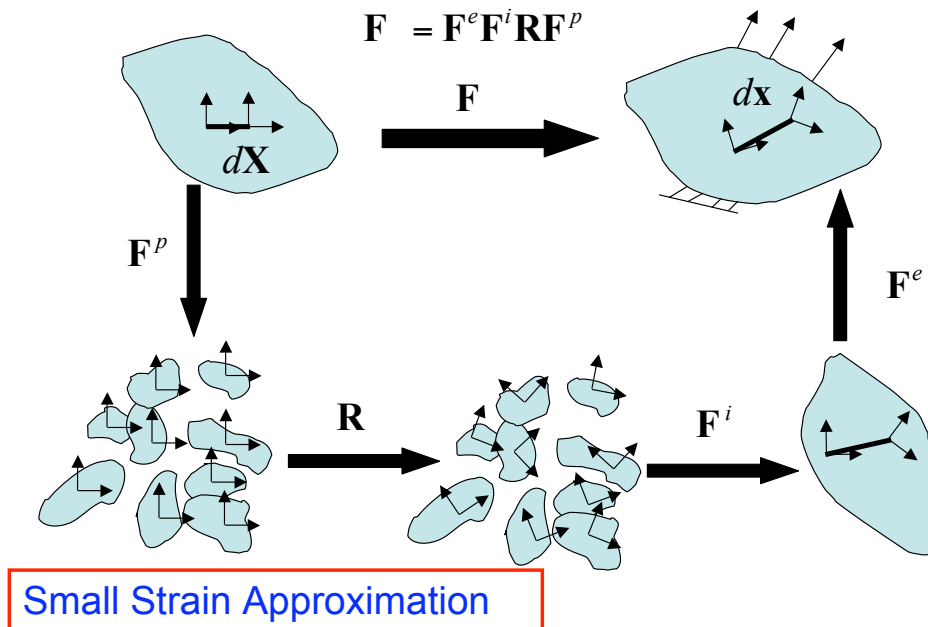


Effect of grain size “D”



Effect of grain size “D”

Crystal Plasticity Kinematics Including Disclinations



$$\mathbf{F} = \mathbf{F}^e \mathbf{F}^i \mathbf{R} \mathbf{F}^p = (\mathbf{I} + \bar{\mathbf{u}} \nabla)(\mathbf{I} + \hat{\mathbf{u}} \nabla) = \mathbf{I} + \bar{\mathbf{u}} \nabla + \hat{\mathbf{u}} \nabla + \vartheta^2$$

Linearized Equations

$$u = \bar{u} + \hat{u}$$

Bilby Problem
Eringen - 1969

MACRO

$$\bar{\boldsymbol{\varepsilon}} = \frac{1}{2}(\nabla \bar{\mathbf{u}} + \nabla \bar{\mathbf{u}}^T)$$

MESO

$$\hat{\boldsymbol{\varepsilon}} = \nabla \hat{\mathbf{u}} - e \nabla \phi$$

$$\hat{\boldsymbol{\varepsilon}} = \hat{\boldsymbol{\varepsilon}}_e + \hat{\boldsymbol{\varepsilon}}_p$$

$$\hat{\boldsymbol{\kappa}} = \nabla \phi = \hat{\boldsymbol{\kappa}}_e + \hat{\boldsymbol{\kappa}}_p$$

$$\nabla \times \boldsymbol{\varepsilon}_e - \hat{\boldsymbol{\kappa}}_e + \text{Tr} \hat{\boldsymbol{\kappa}}_e = \hat{\boldsymbol{\alpha}}_e$$

$$\nabla \times \hat{\boldsymbol{\kappa}}_e = \hat{\boldsymbol{\Omega}}_e$$

$$\hat{\boldsymbol{\sigma}} = \hat{\mathbf{C}} \hat{\boldsymbol{\varepsilon}}_e$$

$$\hat{\boldsymbol{\pi}} = \hat{\mathbf{C}} \hat{\boldsymbol{\kappa}}_e$$

curvature

Dislocation density

Disclination density

Kinematics

Hookes Law

Balance Laws

$$\bar{\boldsymbol{\sigma}} = \bar{\mathbf{C}} : \bar{\boldsymbol{\varepsilon}}$$

$$\text{div} \bar{\boldsymbol{\sigma}} = 0$$

$$\bar{\boldsymbol{\sigma}}^T = \bar{\boldsymbol{\sigma}}$$

$$\text{div} \hat{\boldsymbol{\sigma}} = 0$$

$$\text{div} \hat{\boldsymbol{\pi}} + e \cdot \hat{\boldsymbol{\sigma}} = 0$$

216

Flow rules

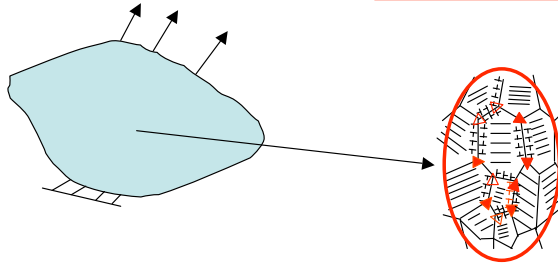
$$\dot{\hat{\boldsymbol{\varepsilon}}}^p = \sum_{\alpha} \dot{\gamma}^{\alpha} \bar{\mathbf{s}}^{\alpha} \otimes \bar{\mathbf{m}}^{\alpha}$$

$$\dot{\hat{\boldsymbol{\kappa}}}^p = \sum_{\beta} \dot{\lambda}^{\beta} \mathbf{Q}^{\beta}$$

Macro Balance Laws

$$\text{div} \bar{\sigma} = 0$$

$$\bar{\sigma} = \bar{\sigma}^T$$



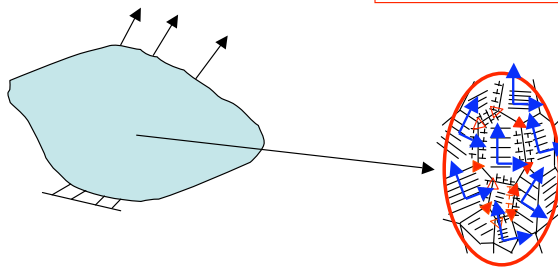
Crystal Plasticity - Dawson

- 256 grains at a point
- Taylor - no equilibrium
- Sachs - no compatibility
- Self consistent - approximate compatibility and equilibrium
- No boundaries

Macro Balance Laws

$$\text{div} \bar{\sigma} = 0$$

$$\bar{\sigma} = \bar{\sigma}^T$$

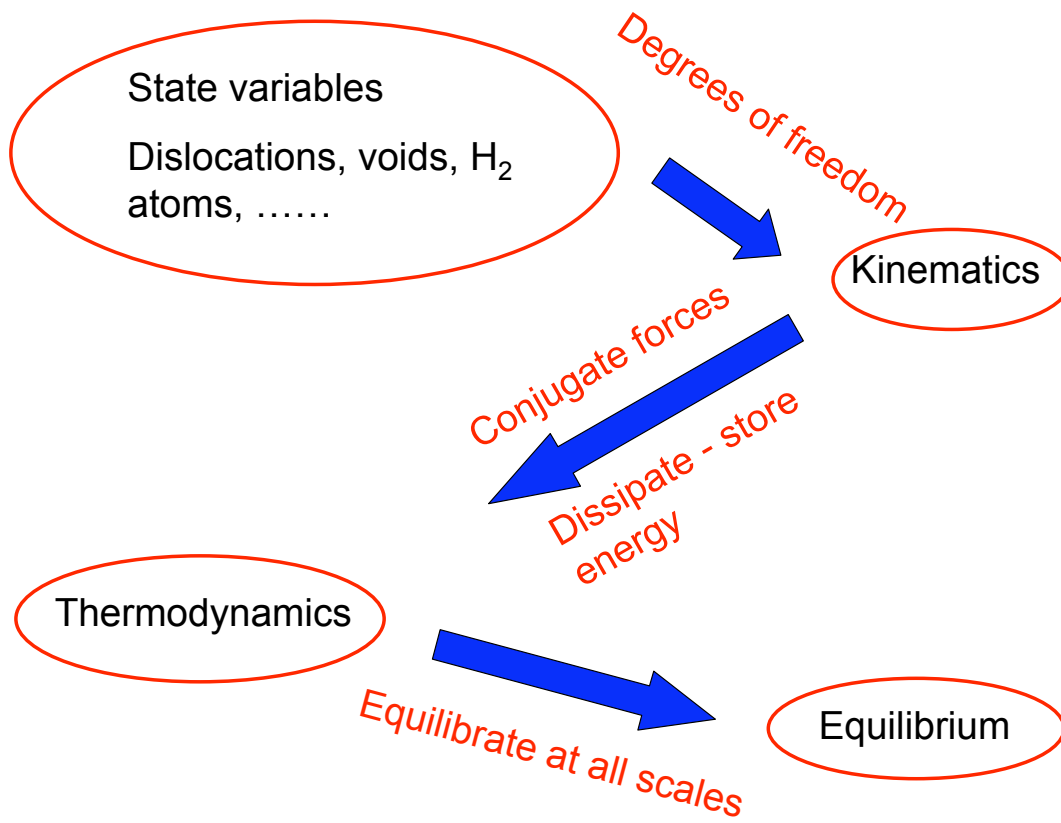


Current Model

- # grains/cells at a point
- Equilibrium
- Solve BVP
- No approximations
- Grain boundaries and cell walls included

$$\text{div} \hat{\sigma} = 0$$

$$\text{div} \hat{\pi} + e \cdot \hat{\sigma} = 0$$



Chapter 7

Summary

Principal Author: Jonathan A. Zimmerman

As stated in the abstract to this report, the goal of our project was to develop a consistent manifold model capable of accurately predicting both the evolution of disclinations and their kinetics as relevant to the deformation of nanocrystalline materials. Additionally, we sought to develop approaches to extract continuum mechanical information from nanoscale structure to verify any developed continuum theory that includes dislocation and disclination behavior. To those ends, we have successfully accomplished the following:

- We have developed a small-strain, micropolar continuum crystal plasticity model to account for the size-dependent mechanical response in nanocrystalline materials. This model contains an enhanced treatment of grain boundaries (GBs) and the role they play in slip obstruction, absorption and transmission of dislocations. The proposed model attempts to account for the geometry of the incoming/outgoing slip planes, the GB orientation and structure, and the evolution of the boundary's resistance to slip through an appropriate choice of internal state variables. In contrast to current approaches of modeling GBs, which tend to describe the increased slip resistance solely in terms of the presence of excess geometrically necessary dislocations, we are motivated by experimental observations to propose a non-associative plasticity model to describe the slip transmission process.

This model represents advancements in both the development and understanding of a class of generalized (micropolar) crystal plasticity models. Through its development, we have provided guidance on which type of micropolar formulation may be worth further pursuing as an alternative to the more common types of slip-gradient based approaches to crystal plasticity. Moreover, a novel methodology describing the effectiveness of GBs against initial slip transfer as well as boundary strength evolution is presented in terms of slip system geometry and GB structure. The model is amenable for inclusion within arbitrary crystal plasticity models, and can accept information from more detailed simulations of dislocation/GB interactions.

- We have developed expressions for evaluating an atomic-scale deformation gradient and related kinematic variables within an atomistic simulation framework. We have characterized and shown the usefulness of this metric through analysis of one-dimensional atomic chain, a biaxially stretched thin film containing a surface ledge, and a FCC metal subject to indentation loading from a nanometer-scale indenter. We have shown that our atomic-scale deformation gradient is consistent with its continuum mechanical counterpart, which is known to have a zero curl for compatible deformations, in most instances. While the concept of the multiplicative decomposition of the deformation gradient within the context

of plasticity theory was considered, our simulation results show zero values of curl within material containing defects such as dislocation loops and stacking faults. As such, it appears that our atomic-scale metric captures the full, compatible deformation field that the material is subject to. The deformation gradient expression itself produces discontinuities reflective of material that contain defects such as partial dislocations and stacking faults.

- We have derived a material frame formulation for calculating the continuum mechanical variables of stress and heat flux based on atomic scale quantities native to molecular simulation. In the context of this project's goal and approach, we expanded the formulation to define continuum variables from micromorphic continuum theory. Our formulation also includes expressions for kinematic variables including the microdeformation gradient and the gyration tensor. These quantities will be essential for future analysis of atomistic simulations for the purpose of providing input to micropolar and micromorphic continuum theories.
- We have used our expertise in molecular simulation, along with some of the metrics developed in the course of this project, to examine bicrystal grain boundaries subjected to shear loading (in both 2 and 3 dimensions) and single crystals subjected to uniaxial compression. With regard to the bicrystal system, our simulations reveal pronounced deformation fields that exist in small regions surrounding the grain boundary, and demonstrate the influence of interfacial structure on mechanical behavior for the thin models investigated. Specifically, our simulation results show specific mechanisms of grain boundary migration, sliding and dissociation. These mechanisms are not fully incorporated into the small-strain micropolar theory and indicate future development of that model needs to include such mechanisms. Our simulations of single crystal compression display a complex evolution of partial dislocations, full dislocations and stacking faults. Although some analysis was performed using the kinematic metrics developed during this project, future work is required to isolate the effectiveness of the various metrics in detecting and visualizing specific types of defects, and to develop a means to use these metrics to quantify dislocation and other defect densities.
- Finally, we have done some preliminary development on a finite (*i.e.* large) strain deformation theory capable of predicting lattice distortions due to tilt, twist and other types of interfacial boundaries, which contains physically reasonable forms of constitutive relations that govern the evolution of dislocations and disclinations. We have made some innovations including the reformulation of the deformation gradient decomposition to include separate portions for disclinations and geometrically necessary dislocations, and the identification of elastic strain fields as the proper internal state variables for such a theory. While much more work needs to be done before our theory is useful in an engineering analysis, we have developed and presented some of the initial formulation for the kinematics, thermodynamics, momentum balance, and energy balance of a finite deformation theory.

Ultimately, our goal was to develop our manifold models to a sufficient state as comparisons could be made with existing experimental data[119] on nanocrystalline materials and thin films to determine the applicability of the continuum model at these very small length scales. While this degree of development was not accomplished in this project, we have nonetheless completed a body of work that will assist model developers to achieve such a goal at some point in the future.

Chapter 8

Publications and Presentations

The following manuscripts and presentations have been produced as a result of the work for this project:

“A Material Frame Approach for Evaluating Continuum Variables in Atomistic Simulations”, Jonathan A Zimmerman, Reese E. Jones and Jeremy A. Templeton, *Journal of the Mechanics and Physics of Solids*, In Review, 2008.

“Deformation Gradients for Continuum Mechanical Analysis of Atomistic Simulations”, Jonathan A. Zimmerman, Douglas J. Bammann and Huajian Gao, *International Journal of Solids and Structures*, Accepted, 2008.

“An Internal State Variable Model of Micropolar Elasto-Viscoplasticity”, Douglas Bammann, Jason Mayeur David McDowell, and John Clayton, Presented at the TMS 2007 Annual Meeting & Exhibition, Orlando, Florida, USA, February 25 - March 1, 2007.

“An Internal State Variable Model of Micropolar Elasto-Viscoplasticity”, Douglas Bammann, Presented at the 1st World Symposium on Multiscale Material Mechanics and Engineering Sciences, Thessaloniki, Greece, April 29 - May 1, 2007.

“Calculation of Thermo-Mechanical Quantities in Atomistic Simulations”, Jonathan A. Zimmerman, Edmund B. Webb III and Steven C. Seel, Presented at the SEM XI Congress & Exposition on Experimental and Applied Mechanics, Orlando, Florida, USA, June 2 - 5, 2008.

“An Internal State Variable Model of Micropolar Elasto-Viscoplasticity”, Douglas Bammann, Jason Mayeur David McDowell, Presented at the 2nd International Conference on Heterogeneous Materials Mechanics (ICHMM-2008), Huangshan, China, June 3 - 8, 2008.

“Deformation Gradients for Continuum Mechanical Analysis of Atomistic Simulations”, J.A. Zimmerman, D.J. Bammann and H. Gao, To be presented at the International Symposium on Plasticity 2009, Frenchman’s Reef and Morning Star Marriott Beach Resort, St. Thomas, U.S. Virgin Islands, January 3- 8, 2009.

“A Material Frame Approach for Evaluating Continuum Variables Within Atomistic Simulations”, J.A. Zimmerman, R.E. Jones and J.A. Templeton, To be presented at the International Symposium on Plasticity 2009, Frenchman’s Reef and Morning Star Marriott Beach Resort, St. Thomas, U.S. Virgin Islands, January 3- 8, 2009.

“Atomic-Scale Deformation Kinematics for Simulations of Dislocation Nucleation and Bicrystal Grain Boundary Evolution”, J.A. Zimmerman, G.J. Tucker and D.L. McDowell, To be presented at the TMS 2008 Annual Meeting & Exhibition, San Francisco, California, USA, February 15-19, 2009.

“Atomic-Scale Deformation Kinematics for Bicrystal Grain Boundaries under Shear Loading”, G.J. Tucker, D.L. McDowell and J.A. Zimmerman, To be presented at the 12th International Conference on Fracture, Ottawa, Canada, July 12-17, 2009.

References

- [1] ABAQUS, Version 2006, 2006.
- [2] A Acharya and J L Bassani. Lattice incompatibility and a gradient theory of crystal plasticity. *Journal of the Mechanics and Physics of Solids*, 48:1565–1595, 2000.
- [3] K E Aifantis and A H W Ngan. Modeling dislocation - grain boundary interactions through gradient plasticity and nanoindentation. *Materials Science and Engineering A - Structural Materials Properties, Microstructure and Processing*, 459:251–261, 2007.
- [4] K E Aifantis, W A Soer, J T M De Hosson, and J R Willis. Interfaces within strain gradient plasticity: Theory and experiments. *Acta Materialia*, 54:5077–5085, 2006.
- [5] K E Aifantis and J R Willis. The role of interfaces in enhancing the yield strength of composites and polycrystals. *Journal of the Mechanics and Physics of Solids*, 53:1047–1070, 2005.
- [6] R K Abu Al-Rub. Interfacial gradient plasticity governs scale-dependent yield strength and strain hardening rates in micro/nano structured metals. *International Journal of Plasticity*, 24:1277–1306, 2008.
- [7] R K Abu Al-Rub. Modeling the interfacial effect on the yield strength and flow stress of thin metal films on substrates. *Mechanics Research Communications*, 35:65–72, 2008.
- [8] R K Abu Al-Rub, G Z Voyiadjis, and D J Bammann. A thermodynamic based higher-order gradient theory for size dependent plasticity. *International Journal of Solids and Structures*, 44:2888–2923, 2007.
- [9] M I Alsaleh, G Z Voyiadjis, and K A Alshibli. Modelling strain localization in granular materials using micropolar theory: Mathematical formulations. *International Journal of Numerical and Analytical Methods in Geomechanics*, 30:1501–1524, 2006.
- [10] K A Alshibli, M I Alsaleh, and G Z Voyiadjis. Modelling strain localization in granular materials using micropolar theory: Numerical implementation and verification. *International Journal of Numerical and Analytical Methods in Geomechanics*, 30:1525–1544, 2006.
- [11] P C Andia, F Costanzo, and G L Gray. A lagrangian-based continuum homogenization approach applicable to molecular dynamics simulation. *International Journal of Solids and Structures*, 42:6409–6432, 2005.
- [12] Pedro C Andia, Francesco Costanzo, and Gary L Gray. A classical mechanics approach to the determination of the stress-strain response of particle systems. *Modelling and Simulation in Materials Science and Engineering*, 14:741–757, 2006.

- [13] K-H Anthony. Crystal disclinations versus continuum theory. *Diffusion and Defect Data Part B: Solid State Phenomena*, 87:15–46, 2002.
- [14] R Armstrong, R M Douthwaite, I Codd, and N J Petch. Plastic deformation of polycrystalline aggregates. *Philosophical Magazine*, 7(73):45, 1962.
- [15] A Arsenlis and D M Parks. Crystallographic aspects of geometrically-necessary and statistically-stored dislocation density. *Acta Materialia*, 47:1597–1611, 1999.
- [16] A Arsenlis and D M Parks. Modeling the evolution of crystallographic dislocation density in crystal plasticity. *Journal of the Mechanics and Physics of Solids*, 50:1979–2009, 2002.
- [17] A Arsenlis, D M Parks, R Becker, and V V Bulatov. On the evolution of crystallographic dislocation density in non-homogeneously deforming crystals. *Journal of the Mechanics and Physics of Solids*, 52:1213–1246, 2004.
- [18] R J Asaro. Crystal plasticity. *Journal of Applied Mechanics - Transactions of the ASME*, 50:921–934, 1983.
- [19] M F Ashby. The deformation of plastically non-homogeneous materials. *Philosophical Magazine*, 21(170):399–424, 1970.
- [20] W M Ashmawi and M A Zikry. Effects of grain boundaries and dislocation density evolution on large strain deformation modes in fcc crystalline materials. *Journal of Computer-Aided Materials Design*, 7:55–62, 2000.
- [21] W M Ashmawi and M A Zikry. Prediction of grain-boundary interfacial mechanisms in polycrystalline materials. *Journal of Engineering Materials and Technology - Transactions of the ASME*, 124:88–96, 2002.
- [22] W M Ashmawi and M A Zikry. Grain boundary effects and void porosity evolution. *Mechanics of Materials*, 35:537–552, 2003.
- [23] W M Ashmawi and M A Zikry. Grain-boundary interfaces and void interactions in porous aggregates. *Philosophical Magazine*, 83:3917–3944, 2003.
- [24] T A Bamford, B Hardiman, Z Shen, W A T Clark, and R H Wagoner. Micromechanism of slip propagation through a high angle boundary in alpha-brass. *Scripta Metallurgica*, 20(2):253–258, 1986.
- [25] Douglas J Bammann. A model of crystal plasticity containing a natural length scale. *Materials Science and Engineering A*, 309-310:406–410, 2001.
- [26] D J Benson, H H Fu, and M A Meyers. On the effect of grain size on yield stress: extension into nanocrystalline domain. *Materials Science and Engineering A - Structural Materials Properties, Microstructure and Processing*, 319:854–861, 2001.
- [27] D Besdo. Some remarks on material laws of elastomechanics of cosserat continua. *Z. Angew. Math. Mech.*, 54:T70–T71, 1974.

- [28] B A Bilby, R Bullough, and E Smith. Continuous distributions of dislocations - a new application of the methods of non-riemannian geometry. *Proceedings of the Royal Society of London, Series A - Mathematical and Physical Sciences*, 231(1185):263–273, 1955.
- [29] M Born and K Huang. *Dynamical Theories of Crystal Lattices*. Clarendon Press, Oxford, 1956.
- [30] C E Carlton and P J Ferreira. What is behind the inverse hall-petch effect in nanocrystalline materials? *Acta Materialia*, 55:3749–3756, 2007.
- [31] P Cermelli and M E Gurtin. Geometrically necessary dislocations in viscoplastic single crystals and bicrystals undergoing small deformations. *International Journal of Solids and Structures*, 39:6281–6309, 2002.
- [32] P P Chattopadhyay, S K Pabi, and I Manna. On the inverse hall-petch relationship in nanocrystalline materials. *Z. Metallk.*, 91:1049–1051, 2000.
- [33] H Chen, X N Liu, and G Hu. Overall plasticity of micropolar composites with interface effect. *Mechanics of Materials*, 40:721–728, 2008.
- [34] Y Chen and J Lee. Atomistic formulation of a multiscale field theory for nano/micro solids. *Philosophical Magazine*, 85(33-35):4095–4126, 2005.
- [35] Youping Chen. Local stress and heat flux in atomistic systems involving three-body forces. *Journal of Chemical Physics*, 124:054113, 2006.
- [36] Youping Chen and James D Lee. Connecting molecular dynamics to micromorphic theory. (I). instantaneous and averaged mechanical variables. *Physica A*, 322:359–376, 2003.
- [37] Youping Chen and James D Lee. Connecting molecular dynamics to micromorphic theory. (II). balance laws. *Physica A*, 322:377–392, 2003.
- [38] K S Cheung and S Yip. Atomic-level stress in an inhomogeneous system. *Journal of Applied Physics*, 70(10):5688–5690, 1991.
- [39] A H Chokshi, A Rosen, J Karch, and H Gleiter. On the validity of the Hall-Petch relationship in nanocrystalline materials. *Scripta Metallurgica*, 23(10):1679–84, 1989.
- [40] W A T Clark, R H Wagoner, Z Y Shen, T C Lee, I M Robertson, and H K Birnbaum. On the criteria for slip transmission across interfaces in polycrystals. *Scripta Metallurgica et Materialia*, 26:203–206, 1992.
- [41] R J E Clausius. On a mechanical theorem applicable to heat. *Philosophical Magazine*, 40:122–127, 1870.
- [42] J D Clayton, D J Bammann, and D L McDowell. Anholonomic configuration spaces and metric tensors in finite elastoplasticity. *International Journal of Non-Linear Mechanics*, pages 1039–1049, 2004.

- [43] J D Clayton, D J Bammann, and D L McDowell. A geometric framework for the kinematics of crystals with defects. *Philosophical Magazine*, pages 3983–4010, 2005.
- [44] J D Clayton and D L McDowell. Finite polycrystalline elastoplasticity and damage: multi-scale kinematics. *International Journal of Solids and Structures*, 40:5669–5688, 2003.
- [45] J D Clayton and D L McDowell. A multiscale multiplicative decomposition for elastoplasticity of polycrystals. *International Journal of Plasticity*, 19:1401–1444, 2003.
- [46] J D Clayton, D L McDowell, and D J Bammann. A multiscale gradient theory for single crystalline elastoviscoplasticity. *International Journal of Engineering Science*, 42:427–457, 2004.
- [47] J D Clayton, D L McDowell, and D J Bammann. Modeling dislocations and disclinations with finite micropolar elastoplasticity. *International Journal of Plasticity*, 22:210–256, 2006.
- [48] H Conrad and J Narayan. On the grain size softening in nanocrystalline materials. *Scripta Materialia*, 42:1025–1030, 2000.
- [49] J Cormier, J M Rickman, and T J Delph. Stress calculation in atomistic simulations of perfect and imperfect solids. *Journal of Applied Physics*, 89(1):99–104, 2001.
- [50] F Costanzo, G L Gray, and P C Andia. On the definitions of effective stress and deformation gradient for use in md: Hill’s macro-homogeneity and the virial theorem. *International Journal of Engineering Science*, 43:533–555, 2005.
- [51] Francesco Costanzo, Gary L Gray, and Pedro C Andia. On the notion of average mechanical properties in md simulation via homogenization. *Modelling and Simulation in Materials Science and Engineering*, 12:S333–S345, 2004.
- [52] A H Cottrell. The 1958 institute of metals division lecture - theory of brittle fracture in steel and similar metals. *Transactions of the American Institute of Mining and Metallurgical Engineers*, 212:192–203, 1958.
- [53] W A Counts, M V Braginsky, C C Battaile, and E A Holm. Polycrystalline kinematics: An extension of single crystal kinematics that incorporates initial microstructure. *International Journal of Solids and Structures*, 44:5742–5751, 2007.
- [54] W A Counts, M V Braginsky, C C Battaile, and E A Holm. Predicting the hall-petch effect in fcc metals using non-local crystal plasticity. *International Journal of Plasticity*, 24:1243–1263, 2008.
- [55] S L Creighton, R A Regueiro, K Garikipati, P A Klein, E B Marin, and D J Bammann. A variational multiscale method to incorporate strain gradients in a phenomenological plasticity model. *Computer Methods in Applied Mechanics and Engineering*, 193:5453–5475, 2004.
- [56] M de Koning, R Miller, V V Bulatov, and F F Abraham. Modelling grain-boundary resistance in intergranular dislocation slip transmission. *Philosophical Magazine A - Physics of Condensed Matter Structure, Defects and Mechanical Properties*, 82:2511–2527, 2002.

- [57] R Deborst. Numerical modeling of bifurcation and localization in cohesive-frictional materials. *Pure Applied Geophysics*, 137:367–390, 1991.
- [58] R Deborst. A generalization of j2-flow theory for polar continua. *Computer Methods in Applied Mechanics and Engineering*, 103:347–362, 1993.
- [59] T J Delph. Conservation laws for multibody interatomic potentials. *Modelling and Simulation in Materials Science and Engineering*, 13:585–594, 2005.
- [60] M P Dewald and W A Curtin. Multiscale modelling of dislocation/grain-boundary interactions: I. edge dislocations impinging on sigma 11 (113) tilt boundary in al. *Modelling and Simulation in Materials Science and Engineering*, 15:S193–S215, 2007.
- [61] M P Dewald and W A Curtin. Multiscale modelling of dislocation/grain boundary interactions. ii. screw dislocations impinging on tilt boundaries in al. *Philosophical Magazine*, 87:4615–4641, 2007.
- [62] W Diepolder, V Mannl, and H Lippmann. The cosserat continuum, a model for grain rotations in metals. *International Journal of Plasticity*, 7:313–328, 1991.
- [63] A Dietsche, P Steinmann, and K Willam. Micropolar elastoplasticity and its role in localization. *International Journal of Plasticity*, 9:813–831, 1993.
- [64] W Ehlers and W Volk. On shear band localization phenomena of liquid-saturated granular elastoplastic porous solid materials accounting for fluid viscosity and micropolar solid rotations. *Mechanics of Cohesive-Friction Materials*, 2:301–320, 1997.
- [65] W Ehlers and W Volk. On theoretical and numerical methods in the theory of porous media based on polar and non-polar elasto-plastic solid materials. *International Journal of Solids and Structures*, 35:4597–4617, 1998.
- [66] A C Eringen. Theory of micropolar elasticity. In H Lubowitz, editor, *Fracture, an advanced treatise*, volume 2, chapter 7, pages 621–728. Academic Press, London, UK, 1968.
- [67] A C Eringen. *Microcontinuum Field Theories I: Foundations and Solids*. Springer-Verlag, New York, 1999.
- [68] A Cemal Eringen and Charles B Kafadar. Polar field theories. In A Cemal Eringen, editor, *Continuum Physics: Volume IV - Polar and Nonlocal Field Theories*. Academic Press, New York, 1969.
- [69] J D Eshelby. The force on an elastic singularity. *Philosophical Transactions of the Royal Society of London, Series A - Mathematical and Physical Sciences*, 244(877):87–112, 1951.
- [70] L P Evers, W A M Brekelmans, and M G D Geers. Non-local crystal plasticity model with intrinsic ssd and gnd effects. *Journal of the Mechanics and Physics of Solids*, 52:2379–2401, 2004.

- [71] L P Evers, W A M Brekelmans, and M G D Geers. Scale dependent crystal plasticity framework with dislocation density and grain boundary effects. *International Journal of Solids and Structures*, 41:5209–5230, 2004.
- [72] L P Evers, D M Parks, W A M Brekelmans, and M G D Geers. Enhanced modeling of hardening in crystal plasticity for fcc metals. *Journal of Physics IV*, 11:179–186, 2001.
- [73] L P Evers, D M Parks, W A M Brekelmans, and M G D Geers. Crystal plasticity model with enhanced hardening by geometrically necessary dislocation accumulation. *Journal of the Mechanics and Physics of Solids*, 50:2403–2424, 2002.
- [74] J Fatemi, P R Onck, G Poort, and F Van Keulen. Cosserat moduli of anisotropic cancellous bone: A micromechanical analysis. *Journal of Physics IV*, 105:273–280, 2003.
- [75] S M Foiles, M I Baskes, and M S Daw. Embedded-atom-method functions for the fcc metals Cu, Ag, Au, Ni, Pd, Pt, and their alloys. *Phys. Rev. B*, 33:7983–7991, 1986.
- [76] S Forest. Modeling slip, kink and smear banding in classical and generalized single crystal plasticity. *Acta Materialia*, 46:3265–3281, 1998.
- [77] S Forest, F Barbe, and G Cailletaud. Cosserat modelling of size effects in the mechanical behaviour of polycrystals and multi-phase materials. *International Journal of Solids and Structures*, 37:7105–7126, 2000.
- [78] S Forest, P Boubidi, and R Sievert. Strain localization patterns at a crack tip in generalized single crystal plasticity. *Scripta Materialia*, 44:953–958, 2001.
- [79] S Forest, G Cailletaud, and R W Sievert. A cosserat theory for elastoviscoplastic single crystals at finite deformation. *Archives of Mechanics*, 49:705–736, 1997.
- [80] S Forest, F Pradel, and K Sab. Asymptotic analysis of heterogeneous cosserat media. *International Journal of Solids and Structures*, 38:4585–4608, 2001.
- [81] S Forest and R Sievert. Elastoviscoplastic constitutive frameworks for generalized continua. *Acta Mechanica*, 160:71–111, 2003.
- [82] L P Franca. An algorithm to compute the square root of a 3 x 3 positive definite matrix. *Computers Math. Applic.*, 18(5):459–466, 1989.
- [83] P Fredriksson and P Gudmundson. Size-dependent yield strength and surface energies of thin films. *Materials Science and Engineering A - Structural Materials Properties, Microstructure and Processing*, 400:448–450, 2005.
- [84] P Fredriksson and P Gudmundson. Size-dependent yield strength of thin films. *International Journal of Plasticity*, 21:1834–1854, 2005.
- [85] P Fredriksson and P Gudmundson. Competition between interface and bulk dominated plastic deformation in strain gradient plasticity. *Modelling and Simulation in Materials Science and Engineering*, 15:S61–S69, 2007.

- [86] P Fredriksson and P Gudmundson. Modelling of the interface between a thin film and a substrate within a strain gradient plasticity framework. *Journal of the Mechanics and Physics of Solids*, 55:939–955, 2007.
- [87] H H Fu, D J Benson, and M A Meyers. Analytical and computational description of effect of grain size on yield stress of metals. *Acta Materialia*, 49:2567–2582, 2001.
- [88] H H Fu, D J Benson, and M A Meyers. Computational description of nanocrystalline deformation based on crystal plasticity. *Acta Materialia*, 52:4413–4425, 2004.
- [89] P Germain. Method of virtual power in continuum mechanics .2. microstructure. *SIAM Journal of Applied Mathematics*, 25:556–575, 1973.
- [90] P Germain. Virtual power method in mechanics of elastic-materials .1. second gradient theory. *Journal De Mecanique*, 12(2):235–274, 1973.
- [91] V Y Gertsman, A A Nazarov, A E Romanov, R Z Valiev, and V I Vladimirov. Disclination structural unit model of grain-boundaries. *Philosophical Magazine A - Physics of Condensed Matter Structure, Defects and Mechanical Properties*, 59:1113–1118, 1989.
- [92] P Grammenoudis, C Sator, and C Tsakmakis. Micropolar plasticity theories and their classical limits. part ii: Comparison of responses predicted by the limiting and a standard classical model. *Acta Mechanica*, 189:177–191, 2007.
- [93] P Grammenoudis and C Tsakmakis. Hardening rules for finite deformation micropolar plasticity: Restrictions imposed by the second law of thermodynamics and the postulate of il’iushin. *Continuum Mechanics and Thermodynamics*, 13:325–363, 2001.
- [94] P Grammenoudis and C Tsakmakis. Finite element implementation of large deformation micropolar plasticity exhibiting isotropic and kinematic hardening effects. *International Journal of Numerical Methods in Engineering*, 62:1691–1720, 2005.
- [95] P Grammenoudis and C Tsakmakis. Predictions of microtorsional experiments by micropolar plasticity. *Proceedings of the Royal Society of London, Serials A - Mathematical and Physical Sciences*, 461:189–205, 2005.
- [96] P Grammenoudis and C Tsakmakis. Micropolar plasticity theories and their classical limits. part i: Resulting model. *Acta Mechanica*, 189:151–175, 2007.
- [97] P Grammenoudis and C Tsakmakis. Incompatible deformations - plastic intermediate configuration. *ZAMM-Z. Angew. Math. Mech.*, 88:403–432, 2008.
- [98] I Groma. Link between the microscopic and mesoscopic length-scale description of the collective behavior of dislocations. *Physical Review B*, 56:5807–5813, 1997.
- [99] I Groma, F F Csikor, and M Zaiser. Spatial correlations and higher-order gradient terms in a continuum description of dislocation dynamics. *Acta Materialia*, 51:1271–1281, 2003.
- [100] D Guan-Suo. Determination of the rotation tensor in the polar decomposition. *Journal of Elasticity*, 50:197–208, 1998.

- [101] P M Gullett, M F Horstemeyer, M I Baskes, and H Fang. A deformation gradient tensor and strain tensors for atomistic simulations. *Modelling and Simulation in Materials Science and Engineering*, 16:015001, 2008.
- [102] M E Gurtin. *Configurational Forces as Basic Concepts of Continuum Physics*. Springer-Verlag, New York, 2000.
- [103] M E Gurtin. On the plasticity of single crystals: free energy, microforces, plastic-strain gradients. *Journal of the Mechanics and Physics of Solids*, 48:989–1036, 2000.
- [104] M E Gurtin. A theory of grain boundaries that accounts automatically for grain misorientation and grain-boundary orientation. *Journal of the Mechanics and Physics of Solids*, 56:640–662, 2008.
- [105] M E Gurtin and A Needleman. Boundary conditions in small-deformation, single-crystal plasticity that account for the burgers vector. *Journal of the Mechanics and Physics of Solids*, 53:1–31, 2005.
- [106] Morton E Gurtin. A gradient theory of single-crystal viscoplasticity that accounts for geometrically necessary dislocations. *Journal of the Mechanics and Physics of Solids*, 50:5–32, 2002.
- [107] E O Hall. The deformation and ageing of mild steel .3. discussion of results. *Proceedings of the Physical Society of London, Section B*, 64(381):747–753, 1951.
- [108] C-S Han, H Gao, Y Huang, and W D Nix. Mechanism-based strain gradient crystal plasticity — I. Theory. *Journal of the Mechanics and Physics of Solids*, 53:1188–1203, 2005.
- [109] R J Hardy. Formulas for determining local properties in molecular-dynamics simulations: Shock waves. *Journal of Chemical Physics*, 76(1):622–628, 1982.
- [110] R J Hardy and A M Karo. Stress and energy flux in the vicinity of a shock front. In *Shock Compression of Condensed Matter*, Proceedings of the American Physical Society Topical Conference, pages 161–164. American Physical Society, 1990.
- [111] R J Hardy, S Root, and D R Swanson. Continuum properties from molecular simulations. In *12th International Conference of the American-Physical-Society-Topical-Group on Shock Compression of Condensed Matter*, volume 620, Pt. 1 of *AIP Conference Proceedings*, pages 363–366. American Institute of Physics, 2002.
- [112] C S Hartley. A method for linking thermally activated dislocation mechanisms of yielding with continuum plasticity theory. *Philosophical Magazine*, 83:3783–3808, 2003.
- [113] A Hoger and D E Carlson. Determination of the stretch and rotation in the polar decomposition of the deformation gradient. *Quarterly of Applied Mathematics*, 42(1):113–117, 1984.
- [114] M F Horstemeyer and M I Baskes. Atomistic finite deformation simulations: A discussion on length scale effects in relation to mechanical stresses. *Journal of Engineering Materials and Technology*, 121:114–119, 1999.

- [115] M F Horstemeyer and M I Baskes. Strain tensors at the atomic scale. In *Multiscale Phenomena in Materials - Experiments and Modeling*, volume 578 of *Materials Research Society Symposium Proceedings*, pages 15–20. Materials Research Society, 2000.
- [116] M F Horstemeyer, M I Baskes, V C Prantil, J Philliber, and S Vonderheide. A multi-scale analysis of fixed-end simple shear using molecular dynamics, crystal plasticity, and a macroscopic internal state variable theory. *Modelling and Simulation in Materials Science and Engineering*, 11(3):265–286, 2003.
- [117] M F Horstemeyer and D L McDowell. Modeling effects of dislocation substructure in polycrystal elastoviscoplasticity. *Mechanics of Materials*, 27:145–163, 1998.
- [118] K Huang. On the atomic theory of elasticity. *Proc. Roy. Soc. London*, A203:178–94, 1950.
- [119] D A Hughes, N Hansen, and D J Bammann. Geometrically necessary boundaries, incidental dislocation boundaries and geometrically necessary dislocations. *Scripta Materialia*, 48:147–153, 2003.
- [120] H Inoue, Y Akahoshi, and S Harada. A molecular dynamics-aided fracture mechanics parameter and its application to a tensile problem. *Computational Mechanics*, 16:217–222, 1995.
- [121] J H Irving and J G Kirkwood. The statistical mechanical theory of transport processes. iv. the equations of hydrodynamics. *Journal of Chemical Physics*, 18(6):817–829, 1950.
- [122] Y Jin and F G Yuan. Atomistic simulations of j-integral in 2d graphene nanosystems. *Journal of Nanoscience and Nanotechnology*, 5:2099–2107, 2005.
- [123] C B Kafadar and A C Eringen. Micropolar media - I the classical theory. *Int. J. Engng. Sci.*, 9:271–305, 1971.
- [124] T Kameda and M A Zikry. Intergranular and transgranular crack growth at triple junction boundaries in ordered intermetallics. *International Journal of Plasticity*, 14:689–702, 1998.
- [125] T Kameda, M A Zikry, and A M Rajendran. Modeling of grain-boundary effects and intergranular and transgranular failure in polycrystalline intermetallics. *Metallurgical and Materials Transactions A - Physical Metallurgy and Materials Science*, 37A:2107–2115, 2006.
- [126] C L Kelchner, S J Plimpton, and J C Hamilton. Dislocation nucleation and defect structure during surface indentation. *Physical Review B*, 58(17):11085–11088, 1998.
- [127] P A Klein. *A Virtual Internal Bond Approach to Modeling Crack Nucleation and Growth*. PhD thesis, Stanford University, 1999.
- [128] U F Kocks. Laws for work hardening and low temperature creep. *Transactions of the ASME: Journal of Engineering Materials and Technology*, 98:76–85, 1976.
- [129] K Kondo. On the analytical and physical foundations of the theory of dislocations and yielding by the differential geometry of continua. *International Journal of Engineering Science*, 2:219–252, 1964.

- [130] D A Konstantinidis and E C Aifantis. On the “anomalous” hardness of nanocrystalline materials. *Nanostructured Materials*, 10:1111–1118, 1998.
- [131] H Kotera, M Sawada, and S Shima. Cosserat continuum theory to simulate microscopic rotation of magnetic powder in applied magnetic field. *International Journal of Mechanical Science*, 42:129–145, 2000.
- [132] J Kratochvil. *Foundations of Plasticity*, pages 401–415. Noordhoff-Leyder, Warsaw, 1972.
- [133] E. Kroner. Allgemeine kontinuumstheorie der versetzungen und eigenspannungen. *Archive for Rational Mechanics and Analysis*, 4(4):273–334, 1960.
- [134] N P Kruyt and L Rothenburg. Micromechanical definition of the strain tensor for granular materials. *Journal of Applied Mechanics*, 118:706–711, 1996.
- [135] M Kuroda and V Tvergaard. Studies of scale dependent crystal viscoplasticity models. *Journal of the Mechanics and Physics of Solids*, 54:1789–1810, 2006.
- [136] P Lancaster and K Salkauskas. Surfaces generated by moving least squares methods. *Mathematics of Computation*, 37:141–158, 1981.
- [137] K C Le and H Stumpf. Strain measures, integrability condition and frame indifference in the theory of oriented media. *International Journal of Solids and Structures*, 35:783–798, 1998.
- [138] T C Lee, I M Robertson, and H K Birnbaum. Prediction of slip transfer mechanisms across grain-boundaries. *Scripta Metallurgica*, 23(5):799–803, 1989.
- [139] T C Lee, I M Robertson, and H K Birnbaum. An insitu transmission electron-microscope deformation study of the slip transfer mechanisms in metals. *Metallurgical Transactions A - Physical Metallurgy and Materials Science*, 21(9):2437–2447, 1990.
- [140] T C Lee, I M Robertson, and H K Birnbaum. Tem insitu deformation study of the interaction of lattice dislocations with grain-boundaries in metals. *Philosophical Magazine A - Physics of Condensed Matter Structure, Defects and Mechanical Properties*, 62(1):131–153, 1990.
- [141] T C Lee, I M Robertson, and H K Birnbaum. Interaction of dislocations with grain-boundaries in Ni₃Al. *Acta Metallurgica et Materialia*, 40:2569–2579, 1992.
- [142] T C Lee, R Subramanian, I M Robertson, and H K Birnbaum. Dislocation-grain boundary interactions in Ni₃Al - effects of structure and chemistry. *Scripta Metallurgica et Materialia*, 25:1265–1270, 1991.
- [143] M Legros, B R Elliott, M N Rittner, J R Weertman, and K J Hemker. Microsample tensile testing of nanocrystalline metals. *Philosophical Magazine A*, 80(4):1017–1026, 2000.
- [144] J C M Li and Y T Chou. Role of dislocations in flow stress grain size relationships. *Metallurgical Transactions*, 1:1145, 1970.

- [145] A Lion. Constitutive modelling in finite thermoviscoplasticity: a physical approach based on nonlinear rheological models. *International Journal of Plasticity*, 16:469–494, 2000.
- [146] H Lippmann. A cosserat theory of plastic flow. *Acta Mechanica*, 8:255, 1969.
- [147] X N Liu and G K Hu. A continuum micromechanical theory of overall plasticity for particulate composites including particle size effect. *International Journal of Plasticity*, 21:777–799, 2005.
- [148] J F Lutsko. Stress and elastic constants in anisotropic solids: Molecular dynamics techniques. *Journal of Applied Physics*, 64(3):1152–1154, 1988.
- [149] A Ma, F Roters, and D Raabe. A dislocation density based constitutive model for crystal plasticity fem including geometrically necessary dislocations. *Acta Materialia*, 54:2169–2179, 2006.
- [150] A Ma, F Roters, and D Raabe. On the consideration of interactions between dislocations and grain boundaries in crystal plasticity finite element modeling - theory, experiments, and simulations. *Acta Materialia*, 54:2181–2194, 2006.
- [151] H S Ma and G K Hu. Influence of fiber’s shape and size on overall elastoplastic property for micropolar composites. *International Journal of Solids and Structures*, 43:3025–3043, 2006.
- [152] H S Ma, X N Liu, and G K Hu. Overall elastoplastic property for micropolar composites with randomly oriented ellipsoidal inclusions. *Computational Materials Science*, 37:582–592, 2006.
- [153] L E Malvern. *Introduction to the Mechanics of a Continuous Medium*. John Wiley & Sons, Inc., New York, 1969.
- [154] J Mandel. Equations constitutives et directeurs dans les milieux plastiques et viscoplastiques. *International Journal of Solids and Structures*, 9:725–740, 1973.
- [155] G Marc and W G McMillan. The virial theorem. *Advances in Chemical Physics*, 58:209–361, 1985.
- [156] J E Marsden and T J R Hughes. *Mathematical Foundations of Elasticity*. Prentice-Hall, Englewood Cliffs, New Jersey, 1983.
- [157] G A Maugin. Method of virtual power in continuum-mechanics - application to coupled fields. *Acta Mechanica*, 35:1–70, 1980.
- [158] G A Maugin. *Material Inhomogeneities in Elasticity*. Chapman and Hall, London, 1993.
- [159] J C Maxwell. On reciprocal figures, frames and diagrams of forces. *Transactions of the Royal Society Edinburgh*, XXVI:1–43, 1870.
- [160] J C Maxwell. Van der waals on the continuity of the gaseous and liquid states. *Nature*, pages 477–480, 1874.

- [161] D L McDowell. Materials design: A useful research focus for inelastic behavior of structural metals. *Theoretical and Applied Fracture Mechanics*, 37(1-3):245 – 259, 2001.
- [162] H Mecking and U F Kocks. Kinetics of flow and strain hardening. *Acta Metallurgica*, 29:1865–1875, 1981.
- [163] F T Meissonnier, E P Busso, and N P O’Dowd. Finite element implementation of a generalised non-local rate-dependent crystallographic formulation for finite strains. *International Journal of Plasticity*, 17:601–640, 2001.
- [164] M A Meyers and E Ashworth. A model for the effect of grain-size on the yield stress of metals. *Philosophical Magazine A - Physics of Condensed Matter Structure, Defects and Mechanical Properties*, 46:737–759, 1982.
- [165] M A Meyers, A Mishra, and D J Benson. The deformation physics of nanocrystalline metals: Experiments, analysis, and computations. *Jom*, 58:41–48, 2006.
- [166] C Miehe and J Schroder. A comparative study of stress update algorithms for rate-independent and rate-dependent crystal plasticity. *International Journal of Numerical Methods in Engineering*, 50:273–298, 2001.
- [167] Y Mishin, M J Mehl, D A Papaconstantopoulos, A F Voter, and J D Kress. Structural stability and lattice defects in copper: Ab initio, tight-binding, and embedded-atom calculations. *Physical Review B*, 6322(22), 2001.
- [168] A Ian Murdoch. On the microscopic interpretation of stress and couple stress. *Journal of Elasticity*, 71:105–131, 2003.
- [169] A Ian Murdoch. A critique of atomistic definitions of the stress tensor. *Journal of Elasticity*, 88:113–140, 2007.
- [170] P M Naghdi and A R Srinivasa. A dynamical theory of structured solids .1. basic developments. *Proceedings of the Royal Society of London, Serials A - Mathematical, Physical and Engineering Sciences*, 345:425–458, 1993.
- [171] P M Naghdi and A R Srinivasa. A dynamical theory of structured solids .2. special constitutive-equations and special cases of the theory. *Proceedings of the Royal Society of London, Serials A - Mathematical, Physical and Engineering Sciences*, 345:459–476, 1993.
- [172] K Nakatani, A Nakatani, Y Sugiyama, and H Kitagawa. Molecular dynamics study on mechanical properties and fracture in amorphous metal. *AIAA Journal*, 38(4):695–701, 2000.
- [173] A A Nazarov, A E Romanov, and R Z Valiev. On the structure, stress-fields and energy of nonequilibrium grain-boundaries. *Acta Metallurgica et Materialia*, 41:1033–1040, 1993.
- [174] A A Nazarov, O A Shenderova, and D W Brenner. Elastic models of symmetrical $\langle 002 \rangle$ and $\langle 011 \rangle$ tilt grain boundaries in diamond. *Physical Review B*, 61:928–936, 2000.

- [175] P Neff. A geometrically exact cosserat shell-model including size effects, avoiding degeneracy in the thin shell limit. part i: Formal dimensional reduction for elastic plates and existence of minimizers for positive cosserat couple modulus. *Continuum Mechanics and Thermodynamics*, 16:577–628, 2004.
- [176] P Neff. The cosserat couple modulus for continuous solids is zero viz the linearized cauchy-stress tensor is symmetric. *ZAMM-Z. Angew. Math. Mech.*, 86:892–912, 2006.
- [177] P Neff. A finite-strain elastic-plastic cosserat theory for polycrystals with grain rotations. *International Journal of Engineering Science*, 44:574–594, 2006.
- [178] P Neff and K Chelminski. Infinitesimal elastic-plastic cosserat micropolar theory. modelling and global existence in the rate-independent case. *Proceedings of the Royal Society of Edinburgh Section A - Mathematics*, 135:1017–1039, 2005.
- [179] P Neff and K Chelminski. Well-posedness of dynamic cosserat plasticity. *Applied Mathematics and Optimization*, 56:19–35, 2007.
- [180] P Neff, K Chelminski, W Muller, and C Weiners. A numerical solution method for an infinitesimal elasto-plastic cosserat model. *Mathematical Models and Methods in Applied Science*, 17:1211–1239, 2007.
- [181] T G Nieh and J Wadsworth. Hall-petch relation in nanocrystalline solids. *Scripta Metallurgica et Materialia*, 25(4):955–958, 1991.
- [182] J F Nye. Some geometrical relations in dislocated crystals. *Acta Metallurgica*, 1(2):153–162, 1953.
- [183] R W Ogden. *Non-Linear Elastic Deformations*. John Wiley & Sons, Inc., New York, 1984.
- [184] M Peach and J S Koehler. The forces exerted on dislocations and the stress fields produced by them. *Physical Review*, 80(3):436–439, 1950.
- [185] D Peirce, C F Shih, and A Needleman. A tangent modulus method for rate dependent solids. *Computers and Structures*, 18:875–887, 1984.
- [186] N J Petch. The cleavage strength of polycrystals. *Journal of the Iron and Steel Institute*, 174(1):25–28, 1953.
- [187] S Plimpton. Fast parallel algorithms for short-range molecular dynamics. *Journal of Computational Physics*, 117(1):1–19, 1995. lammmps.sandia.gov.
- [188] W H Press, S A Teukolsky, W T Vetterling, and B P Flannery. *Numerical Recipes in Fortran: the art of scientific computing*. Cambridge University Press, New York, 2nd edition, 1992.
- [189] V Randle. *The Role of the Coincident Site Lattice in Grain Boundary Engineering*. The University Press, Cambridge, 1996.

- [190] W T Read and W Shockley. Dislocation models of crystal grain boundaries. *Physical Review*, 78(3):275–289, 1950.
- [191] R A Regueiro, D J Bammann, E B Marin, and K Garikipati. A nonlocal phenomenological anisotropic finite deformation plasticity model accounting for dislocation defects. *Journal of Engineering Materials and Technology*, 124:380–387, 2002.
- [192] M Ristinmaa and M Vecchi. Use of couple-stress theory in elasto-plasticity. *Computer Methods in Applied Mechanics and Engineering*, 136(3-4):205–224, 1996.
- [193] P Rodriguez and R W Armstrong. Strength and strain rate sensitivity for hcp and fcc nanopolycrystal metals. *Bulletin of Materials Science*, 29(7):717–720, 2006.
- [194] O Rodríguez de la Fuente, J A Zimmerman, M A González, J de la Figuera, J C Hamilton, W W Pai, and J M Rojo. Dislocation emission around nanoindentations on a (001) fcc metal surface studied by scanning tunneling microscopy and atomistic simulations. *Physical Review Letters*, 88(3):036101, 2002.
- [195] A E Romanov and V I Vladimirov. Disclinations in solids. *Physica Status Solidi A*, 78(1):11–34, 1983.
- [196] S Root, R J Hardy, and D R Swanson. Continuum predictions from molecular dynamics simulations: Shock waves. *Journal of Chemical Physics*, 118(7):3161–3165, 2003.
- [197] J S Rowlinson and B Widom. *Molecular Theory of Capillarity*. Clarendon Press, Oxford, 1989.
- [198] P Rozenak, I M Robertson, T C Lee, G M Bond, and H K Birnbaum. Dynamic observations of the transfer of slip across a grain-boundary. *Ultramicroscopy*, 32:192–193, 1990.
- [199] P G Sanders, J A Eastman, and J R Weertman. Elastic and tensile behavior of nanocrystalline copper and palladium. *Acta Materialia*, 45(10):4019–4025, 1997.
- [200] LAMMPS, Sandia National Laboratories: <http://lammps.sandia.gov>, 2008.
- [201] ParaDyn, Sandia National Laboratories: <http://www.cs.sandia.gov/~sjplimp/>, 2008.
- [202] C Sansour. A theory of the elastic-viscoplastic cosserat continuum. *Archives of Mechanics*, 50:577–597, 1998.
- [203] F Sansoz and J F Molinari. Incidence of atom shuffling on the shear and decohesion behavior of a symmetric tilt grain boundary in copper. *Scripta Materialia*, 50(10):1283–8, 2004.
- [204] A Sawczuk. On yielding of cosserat continua. *ARCHIWUM MECHANIKI STOSOWANEJ*, 19(3):471, 1967.
- [205] K Sawyers. Comments on the paper “determination of the stretch and rotation in the polar decomposition of the deformation gradient”. *Quarterly of Applied Mathematics*, 44(2):309–311, 1986.

- [206] J Schiøtz, F D Di Tolla, and K W Jacobsen. Softening of nanocrystalline metals at very small grain sizes. *Nature*, 391(6667):561–3, 1998.
- [207] Jakob Schiøtz and Karsten W Jacobsen. A maximum in the strength of nanocrystalline copper. *Science*, 301:1357–1359, 2003.
- [208] P Schofield and J R Henderson. Statistical mechanics of inhomogeneous fluids. *Proceedings of the Royal Society of London A*, 379:231–240, 1982.
- [209] R Sedlacek, W Blum, J Kratochvil, and S Forest. Subgrain formation during deformation: Physical origin and consequences. *Metallurgical Transactions A - Physical Metallurgy and Materials Science*, 33:319–327, 2002.
- [210] R Sedlacek, J Kratochvil, and W Blum. Deformation induced misorientations: Initial stage of subgrain formation as a plastic instability. *Physics Status Solidi A - Applied Research*, 186:1–16, 2001.
- [211] M Seefeldt, L Delannay, B Peeters, S R Kalidindi, and P Van Houtte. A disclination-based model for grain subdivision. *Materials Science and Engineering A - Structural Materials Properties, Microstructure and Processing*, 319:192–196, 2001.
- [212] S Sengupta, P Nielaba, M Rao, and K Binder. Elastic constants from microscopic strain fluctuations. *Physical Review E*, 61(2):1072–1080, 2000.
- [213] Z Shen, R H Wagoner, and W A T Clark. Dislocation pile up and grain-boundary interactions in 304 stainless-steel. *Scripta Metallurgica*, 20(6):921–926, 1986.
- [214] Z Shen, R H Wagoner, and W A T Clark. Dislocation and grain-boundary interactions in metals. *Acta Metallurgica*, 36(12):3231–3242, 1988.
- [215] K Shizawa and H M Zbib. A thermodynamical theory of gradient elastoplasticity with dislocation density tensor. i: Fundamentals. *International Journal of Plasticity*, 15:899–938, 1999.
- [216] J Y Shu and N A Fleck. Strain gradient crystal plasticity: size-dependent deformation of bicrystals. *Journal of the Mechanics and Physics of Solids*, 47(2):297–324, 1999.
- [217] R Sievert, S Forest, and R Trostel. Finite deformation cosserat-type modelling of dissipative solids and its application to crystal plasticity. *Journal of Physics IV*, 8:357–364, 1998.
- [218] D E Spearot. *Interface cohesion relations based on molecular dynamics simulations*. PhD thesis, Georgia Institute of Technology, 2005.
- [219] P Steinmann. An improved fe expansion for micropolar localization analysis. *Communications in Numerical Methods in Engineering*, 10:1005–1012, 1994.
- [220] P Steinmann. A micropolar theory of finite deformation and finite rotation multiplicative elastoplasticity. *International Journal of Solids and Structures*, 31:1063–1084, 1994.

- [221] P Steinmann. Theory of finite micropolar elastoplasticity. *ZAMM - Z. Angew. Math. Mech.*, 74:T245–T247, 1994.
- [222] P Steinmann. Theory and numerics of ductile micropolar elastoplastic damage. *International Journal of Numerical Methods in Engineering*, 38:583–606, 1995.
- [223] P Steinmann. Views on multiplicative elastoplasticity and the continuum theory of dislocations. *International Journal of Engineering Science*, 34(15):1717–1735, 1996.
- [224] P Steinmann, A Elizondo, and R Sunyk. Studies of validity of the cauchy-born rule by direct comparison of continuum and atomistic modelling. *Modelling and Simulation in Materials Science and Engineering*, 15:S271–S281, 2007.
- [225] P Steinmann and E Stein. A unifying treatise of variational principles for two types of micropolar continua. *Acta Mechanica*, 121:215–232, 1997.
- [226] F H Stillinger and T A Weber. Computer simulation of local order in condensed phases of silicon. *Physical Review B*, 31:5262–5271, 1985.
- [227] S Sun, B L Adams, and W E King. Observations of lattice curvature near the interface of a deformed aluminium bicrystal. *Philosophical Magazine A - Physics of Condensed Matter Structure, Defects and Mechanical Properties*, 80:9–25, 2000.
- [228] S Sun, B L Adams, C Shet, S Saigal, and W King. Mesoscale investigation of the deformation field of an aluminum bicrystal. *Scripta Materialia*, 39:501–508, 1998.
- [229] R Sunyk and P Steinmann. On higher gradients in continuum-atomistic modelling. *International Journal of Solids and Structures*, 40:6877–6896, 2003.
- [230] Bob Svendsen. Continuum thermodynamic models for crystal plasticity including the effects of geometrically-necessary dislocations. *Journal of the Mechanics and Physics of Solids*, 50:1297–1329, 2002.
- [231] E B Tadmor, G S Smith, N Bernstein, and E Kaxiras. Mixed finite element and atomistic formulation for complex crystals. *Physical Review B*, 59:235–45, 1999.
- [232] J Tejchman. Behaviour of granular bodies in induced shear zones. *Granulated Matter*, 2:77–96, 2000.
- [233] J Tejchman. Patterns of shear zones in granular bodies within a polar hypoplastic continuum. *Acta Mechanica*, 155:71–94, 2002.
- [234] J Tejchman. Fe analysis of contractant shear zones in loose granular materials. *Granulated Matter*, 9:49–67, 2007.
- [235] J Tersoff. New empirical model for the structural properties of silicon. *Physical Review Letters*, 56:632–635, 1986.
- [236] J Tersoff. Modeling solid-state chemistry: interatomic potentials for multicomponent systems. *Physical Review B*, 39:R5566–R5568, 1989.

- [237] T C T Ting. Determination of $\mathbf{C}^{1/2}$, $\mathbf{C}^{-1/2}$ and more general isotropic tensor functions of \mathbf{C} . *Journal of Elasticity*, 15:319–323, 1985.
- [238] D H Tsai. The virial theorem and stress calculation in molecular dynamics. *J. Chem. Phys.*, 70:1375–1382, 1979.
- [239] M A Tschopp, G J Tucker, and D L McDowell. Structure and free volume of $\langle 110 \rangle$ symmetric tilt grain boundaries with the E structural unit. *Acta Materialia*, 55:3959–3969, 2007.
- [240] R Z Valiev, R K Islamgaliev, and A N Tumentsev. The disclination approach for nanostructured SPD materials. *Diffusion and Defect Data Part B: Solid State Phenomena*, 87:255–264, 2002.
- [241] H Van Swygenhoven and P M Derlet. Grain boundary sliding in nanocrystalline fcc metals. *Physical Review B*, 64:224105:1–8, 2001.
- [242] H Van Swygenhoven, P M Derlet, and A Hasnaoui. Atomistic modeling of strength of nanocrystalline metals. *Advanced Engineering Materials*, 5(5):345–50, 2003.
- [243] A Voter. Embedded atom method potentials for seven FCC metals: Ni, Pd, Pt, Cu, Ag, Au and Al. Technical Report LA-UR 93-3901, Los Alamos National Laboratories, 1993.
- [244] G Z Voyiadjis, M I Alsaleh, and K A Alshibli. Evolving internal length scales in plastic strain localization for granular materials. *International Journal of Plasticity*, 21:2000–2024, 2005.
- [245] G J Wagner, R E Jones, J A Templeton, and Parks M L. An atomistic-to-continuum coupling method for heat transfer in solids. *Computer Methods in Applied Mechanics and Engineering*, 197:3351–3365, 2008.
- [246] S D C Walsh and A Tordesillas. Element methods for micropolar models of granular materials. *Applied Mathematics and Modeling*, 30:1043–1055, 2006.
- [247] D H Warner and J F Molinari. A semi-discrete and non-local crystal plasticity model for nanocrystalline metals. *Scripta Materialia*, 54:1397–1402, 2006.
- [248] Edmund B Webb III, Jonathan A Zimmerman, and Steven C Seel. Reconsideration of continuum thermomechanical quantities in atomic scale simulations. *Mathematics and Mechanics of Solids*, 13:221–266, 2008.
- [249] J H Weiner. *Statistical Mechanics of Elasticity*. Dover Publications, Inc., Mineola, New York, 2nd edition, 2002.
- [250] D Wolf. Structure-energy correlation for grain boundaries in FCC metal. III. Symmetrical tilt boundaries. *Acta Metallurgica*, 38(5):781–790, 1990.
- [251] F Xun, G K Hu, and Z P Huang. Size-dependence of overall in-plane plasticity for fiber composites. *International Journal of Solids and Structures*, 41:4713–4730, 2004.

- [252] M Zhou. A new look at the atomic level virial stress: on continuum-molecular system equivalence. *Proceedings of the Royal Society of London, Series A*, 459:2347–2392, 2003.
- [253] M Zhou. Thermomechanical continuum representation of atomistic deformation at arbitrary size scales. *Proceedings of the Royal Society of London, Series A*, 461:3437–3472, 2006.
- [254] M Zhou and D L McDowell. Equivalent continuum for dynamically deforming atomistic particle systems. *Philosophical Magazine A*, 82:2547–2574, 2002.
- [255] M A Zikry and T Kameda. Inelastic three dimensional high strain-rate dislocation density based analysis of grain-boundary effects and failure modes in ordered intermetallics. *Mechanics of Materials*, 28:93–102, 1998.
- [256] J A Zimmerman. *Continuum and Atomistic Modeling of Dislocation Nucleation at Crystal Surface Ledges*. PhD thesis, Stanford University, 2000.
- [257] J A Zimmerman, R E Jones, P A Klein, D J Bammann, E B Webb III, and J J Hoyt. Continuum definitions for stress in atomistic simulation. Technical Report SAND2002-8608, Sandia National Laboratories, 2002.
- [258] J A Zimmerman, C L Kelchner, P A Klein, J C Hamilton, and S M Foiles. Surface step effects on nanoindentation. *Physical Review Letters*, 87(16):165507, 2001.
- [259] J A Zimmerman, E B Webb III, J J Hoyt, R E Jones, P A Klein, and D J Bammann. Calculation of stress in atomistic simulation. *Modelling and Simulation in Materials Science and Engineering*, 12:S319–S332, 2004.

DISTRIBUTION:

- 1 D.L. McDowell, Georgia Institute of Technology, Atlanta, GA 30332
- 1 J.R. Mayeur, Georgia Institute of Technology, Atlanta, GA 30332
- 1 G.J. Tucker, Georgia Institute of Technology, Atlanta, GA 30332
- 1 D.J. Bammann, Mississippi State University, Mississippi State, MS 39762
- 1 H. Gao, Brown University, Providence, RI 02912
- 1 MS 0157 H.S. Morgan, 1030
- 1 MS 0351 H.E. Fang, 1000
- 1 MS 0372 J. Pott, 1524
- 1 MS 0384 A.C. Ratzel, 1500
- 1 MS 0824 T.Y. Chu, 1500
- 1 MS 0824 M.R. Prairie, 1500
- 1 MS 0825 C.W. Peterson, 1510
- 1 MS 1320 R.B. Lehoucq, 1414
- 1 MS 1320 M.L. Parks, 1414
- 1 MS 1322 J.B. Aidun, 1435
- 1 MS 1322 P.S. Crozier, 1435
- 1 MS 1322 H.P. Hjalmarson, 1435
- 1 MS 1322 S.A. Silling, 1435
- 1 MS 1322 A.P. Thompson, 1435
- 1 MS 1411 R.A. Roach, 1814
- 1 MS 1411 C.C. Battaile, 1814
- 1 MS 1411 L.N. Brewer, 1814
- 1 MS 1411 R. Dingreville, 1814
- 1 MS 1411 S.M. Foiles, 1814
- 1 MS 1411 A.L. Frischknecht, 1814
- 1 MS 1411 E.A. Holm, 1814
- 1 MS 1411 E.B. Webb III, 1814
- 1 MS 9001 P.J. Hommert, 8000
- 1 MS 9035 P.A. Spence, 8239
- 1 MS 9035 D.K. Balch, 8239
- 1 MS 9042 D.M. Kwon, 8770
- 1 MS 9042 E.P. Chen, 8770
- 1 MS 9042 C.A. Le Gall, 8774
- 1 MS 9042 A.A. Brown, 8774

1	MS 9042	M.L. Chiesa, 8776
1	MS 9042	J.W. Foulk III, 8776
1	MS 9042	T.J. Vogler, 8776
1	MS 9403	T.J. Shepodd, 8778
1	MS 9403	B.M. Wong, 8778
1	MS 9403	L.A. Domeier, 8778
1	MS 9404	R.E. Jones, 8776
1	MS 9404	A. Mota, 8776
1	MS 9404	X. Zhou, 8776
1	MS 9404	J.A. Zimmerman, 8776
1	MS 9405	R.W. Carling, 8700
1	MS 9409	C.D. Moen, 8757
1	MS 9409	M. Grace, 8757
1	MS 9409	J.A. Templeton, 8757
1	MS 9409	G.J. Wagner, 8757
1	MS 0899	Technical Library, 8944 (electronic)
1	MS 0123	D. Chavez, LDRD Office, 1011

